Delft University of Technology

Document Version
Final published version

Citation (APA)
van Velde, P. F. (2026). *Quantitative Fluorescence Microscopy for RNA Imaging: From Single Molecules to Tissue* . [Dissertation (TU Delft), Delft University of Technology]. https://doi.org/10.4233/uuid:84e5c3d2-911a-4b99-b6f4-a2bc6fe51dd7

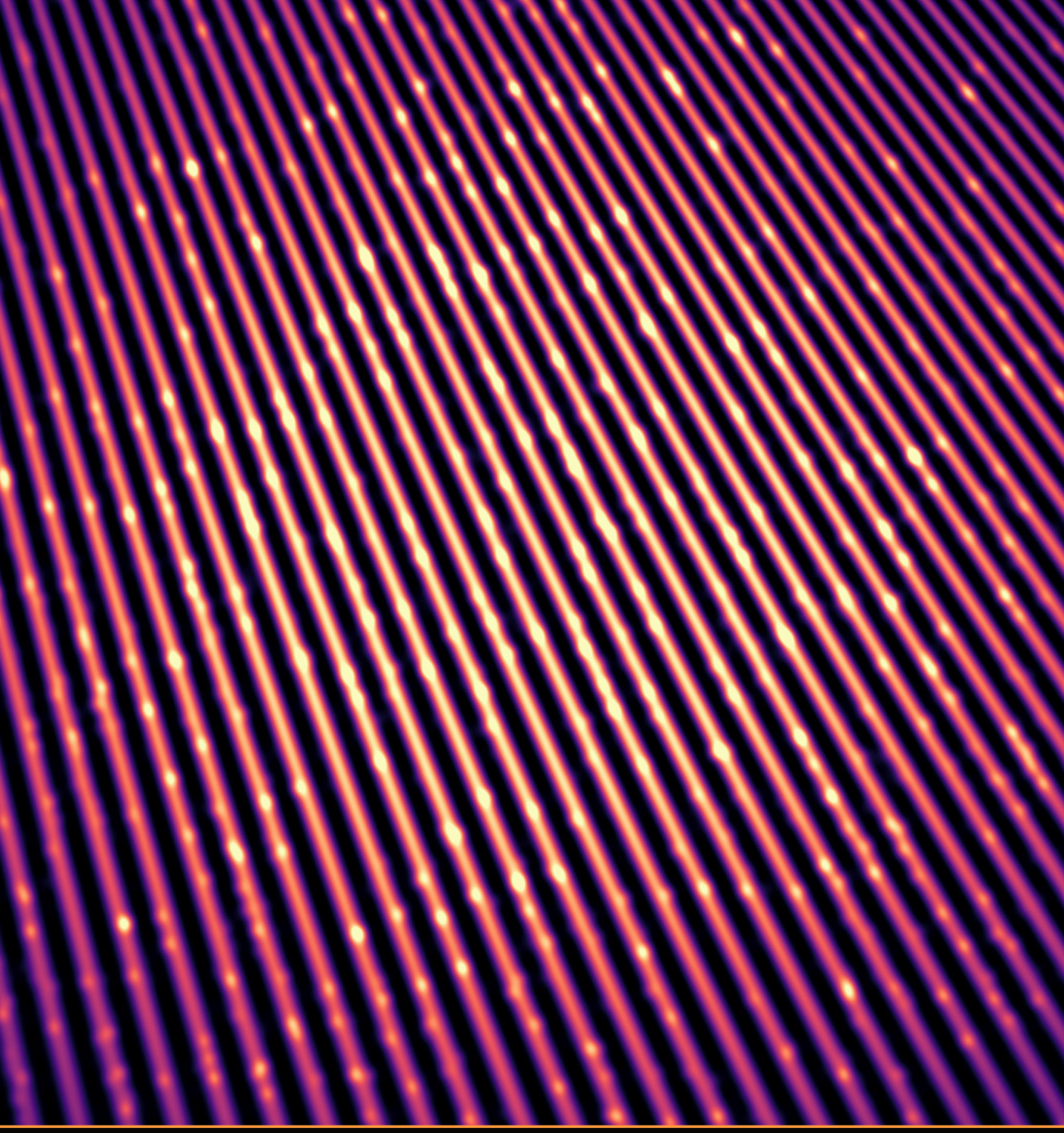
Important note
To cite this publication, please use the final published version (if applicable).
Please check the document version above.

Copyright
In case the licence states “Dutch Copyright Act (Article 25fa)”, this publication was made available Green Open Access via the TU Delft Institutional Repository pursuant to Dutch Copyright Act (Article 25fa, the Taverne amendment). This provision does not affect copyright ownership.
Unless copyright is transferred by contract or statute, it remains with the copyright holder.

Sharing and reuse
Other than for strictly personal use, it is not permitted to download, forward or distribute the text or part of it, without the consent of the author(s) and/or copyright holder(s), unless the work is under an open content license such as Creative Commons.

Takedown policy
Please contact us and provide details if you believe this document breaches copyrights.
We will remove access to the work immediately and investigate your claim.

This work is downloaded from Delft University of Technology.



Quantitative Fluorescence Microscopy for RNA Imaging

From Single Molecules to Tissue

Pieter Fop van Velde

QUANTITATIVE FLUORESCENCE MICROSCOPY FOR RNA IMAGING

FROM SINGLE MOLECULES TO TISSUE

Dissertation

for the purpose of obtaining the degree of doctor
at Delft University of Technology
by the authority of the Rector Magnificus,
Prof.dr.ir. H. Bijl,
chair of the Board for Doctorates
to be defended publicly on
Monday, 26 October 2026, 15:00

by

Pieter Fop VAN VELDE

This dissertation has been approved by the promotors.

Composition of the doctoral committee:

Rector Magnificus,	chairperson
Prof.dr. B. Rieger,	Delft University of Technology, promotor
Dr.ir. C.S. Smith,	Delft University of Technology, promotor
Dr. D. Grünwald,	University of Massachusetts Chan Medical School, USA, promotor

Independent Members:

Prof.dr. S. Stallinga,	Delft University of Technology
Prof.dr.rer.nat. J.C. Hohlbein,	Brandenburg University of Technology, Germany
Prof.dr. N. Grigorieff,	University of Massachusetts Chan Medical School, USA
Dr.rer.nat. K.S. Grußmayer,	Delft University of Technology
Prof.dr. S.M. Witte,	Delft University of Technology, *reserve member*



This work was supported by the Dutch Research Council (NWO) under the START-UP programme (project no. 740.018.015); by the National Science Foundation under Grant No. 1917206; by the CHDI Foundation (RecID A-19405); and by the National Institutes of Health (R01 NS104022, S10 OD020012, S10 OD036329).

Keywords:	single-molecule localization microscopy, fluorescence microscopy, mRNA imaging, nuclear pore complex, Huntington's disease, RNAscope, PSF engineering, structured illumination
Printed by:	Print Service Ede | www.proefschriftenprinten.nl
Cover by:	P.F. van Velde
Copyright:	© 2026 P.F. van Velde
ISBN:	978-94-6518-401-2

An electronic version of this dissertation is available at:
http://repository.tudelft.nl

CONTENTS

Summary vii

Samenvatting ix

Preface xi

1 Introduction 1
- 1.1 History of Fluorescence Microscopy . . . 1
  - 1.1.1 Introduction to Fluorescence Microscopy . . . 1
- 1.2 Resolution limit and Point Spread Function . . . 3
  - 1.2.1 Resolution Limit . . . 4
  - 1.2.2 Point-Spread Function (PSF) . . . 5
  - 1.2.3 Emergence of Super-Resolution . . . 5
- 1.3 Single Molecule Localization Microscopy . . . 6
  - 1.3.1 Switching mechanisms . . . 6
  - 1.3.2 Localization precision . . . 7
  - 1.3.3 Precision under real imaging conditions . . . 10
  - 1.3.4 Detection and estimation . . . 11
  - 1.3.5 Techniques for improving SMLM precision . . . 12
- 1.4 Biological context . . . 13
  - 1.4.1 mRNA transport through the nuclear pore complex . . . 13
  - 1.4.2 Huntington's disease and RNA pathology . . . 15
- 1.5 Scope of this thesis . . . 17

2 ZIMFLUX: Single molecule localization microscopy with patterned illumination in 3D 27
- 2.1 Introduction . . . 28
- 2.2 Theory . . . 29
  - 2.2.1 Imaging model . . . 29
  - 2.2.2 Supercritical angle fluorescence . . . 32
  - 2.2.3 Maximum likelihood estimation for ZIMFLUX . . . 32
- 2.3 Experimental setup and Methods . . . 35
  - 2.3.1 Experimental setup . . . 35
  - 2.3.2 Samples . . . 37
  - 2.3.3 Image acquisition & camera calibration . . . 37
  - 2.3.4 PSF calibration . . . 37
  - 2.3.5 Pattern estimation . . . 38
  - 2.3.6 Single-Molecule Localization Microscopy . . . 40

2.4 Results . . . 41
2.4.1 Simulation results . . . 41
2.4.2 Calibration of PSF model . . . 44
2.4.3 Illumination pattern measurement . . . 44
2.4.4 Proof of principle . . . 45
2.5 Discussion . . . 47
2.5.1 Imaging depth . . . 48
2.5.2 Computation time . . . 48
2.5.3 Point spread function model mismatch . . . 48
2.5.4 Lateral localization precision . . . 48
2.5.5 Outlook . . . 49
2.6 Disclosures . . . 49
2.7 Supplemental document . . . 49
2.8 Data availability . . . 49
2.9 Supplementary material . . . 49
2.10 Supplementary note 1: Illumination pattern . . . 49
2.11 Supplementary note 2: Axial pitch estimation from stage shift . . . 51
2.12 Supplementary note 3: DMD setup . . . 52
2.13 Supplementary figures . . . 53

3 Live cell mRNA imaging in yeast: framework for studying mRNA transport through the nuclear pore complex 63
3.1 Introduction . . . 65
3.2 Results . . . 66
3.2.1 Refractive Index Adjusted Media . . . 66
3.2.2 Nuclear Envelope Localization . . . 67
3.2.3 RNA Detection & Localization . . . 71
3.2.4 mRNA single molecule tracking . . . 74
3.2.5 mRNA transport through the NPC . . . 75
3.2.6 Failed Transport Events . . . 81
3.3 Discussion . . . 83
3.3.1 Nuclear Envelope Localization . . . 83
3.3.2 Impact of Non-Uniform Background Correction on RNA Imaging . . . 83
3.3.3 mRNA Transport through NPC . . . 85
3.3.4 Outlook . . . 86
3.4 Materials and methods . . . 86
3.4.1 Samples and treatment . . . 86
3.4.2 Microscope setup . . . 88
3.4.3 Image acquisition . . . 91
3.4.4 Image photon calibration . . . 92
3.4.5 Image Registration . . . 93
3.4.6 Drift Correction . . . 93
3.4.7 Nuclear envelope detection & localization . . . 94
3.4.8 Background estimation . . . 96
3.4.9 RNA localization . . . 97
3.4.10 Spot Detection . . . 98

3.4.11 Tracking . . . 99
3.4.12 Use of AI . . . 100
3.5 Data, code and protocol availability . . . 100
3.6 Supplementary material . . . 101
3.6.1 Supplementary Figures . . . 101
3.6.2 Supplemental Tables . . . 104
3.6.3 Supplemental Notes . . . 104

4 High-throughput quantification of huntingtin mRNA expression and aggregation in mouse brain using automated RNAscope imaging 115
4.1 Introduction . . . 117
4.2 Results . . . 119
4.2.1 Experimental design and data acquisition . . . 119
4.2.2 Establishing detection thresholds through negative control calibration . . . 120
4.2.3 PSF calibration and single-molecule identification . . . 121
4.2.4 Quantifying mRNA clusters: linear intensity-volume scaling . . . 124
4.2.5 Regional expression patterns and individual variation . . . 128
4.2.6 FOV-level analysis reveals heterogeneous mRNA accumulation . . . 131
4.2.7 Cluster properties distinguish extreme from normal FOVs . . . 134
4.2.8 Technical validation and control analyses . . . 136
4.3 Discussion . . . 136
4.3.1 Technical advances: quantitative mRNA counting through validated linearity . . . 137
4.3.2 Biological insights: heterogeneous mRNA accumulation . . . 138
4.3.3 Implications for therapeutic development . . . 140
4.3.4 Generalizability to other RNAscope applications . . . 140
4.3.5 Limitations and future directions . . . 141
4.3.6 Conclusion . . . 142
4.4 Materials and Methods . . . 142
4.4.1 Samples and Treatment . . . 142
4.4.2 Optical Setup & Image Acquisition . . . 144
4.4.3 Imaging Model . . . 145
4.4.4 Detection of Single Spots . . . 146
4.4.5 PSF Calibration Using RNAscope Data . . . 147
4.4.6 mRNA Cluster Detection . . . 148
4.4.7 Fluorescent Signal with RNAscope . . . 149
4.4.8 DAPI-based Nuclear Segmentation . . . 149
4.4.9 Distance to Nuclear Border . . . 149
4.4.10 Atlas Registration and Coordinate Assignment . . . 150
4.4.11 Statistical analysis . . . 150
4.4.12 Data and Code Availability . . . 151
4.4.13 Use of AI . . . 151
4.5 Supplementary material . . . 151

5 Conclusion **199**
5.1 Unifying approach . . . 199
5.2 Implications for quantitative computational microscopy . . . 200
5.2.1 Decision making supported by statistics . . . 200
5.2.2 Transferability of the hybrid approach . . . 201
5.3 Enabling impact of optical modeling . . . 202
5.3.1 Unbiased estimation using vectorial PSF modeling . . . 202
5.3.2 Simple models with carefully defined parameter bounds . . . 202
5.3.3 From feasibility to dependability . . . 203
5.3.4 Biological discoveries enabled by these methods . . . 203
5.4 Implications for society . . . 204
5.4.1 Toward understanding and treating Huntington's disease . . . 204
5.4.2 Advancing fundamental understanding . . . 204
5.4.3 Open science and accessibility . . . 205
5.5 Future perspectives . . . 205

Epilogue **213**

Acknowledgements **215**

Curriculum Vitæ **217**

List of Publications **219**

SUMMARY

Fluorescence microscopy has become an indispensable tool for studying biological processes at the molecular level. Quantitative measurements of RNA expression and location require continued innovation in optical methods and computational image analysis. This dissertation presents three contributions that advance quantitative fluorescence microscopy for RNA imaging at different biological scales.

Chapter 2 introduces ZIMFLUX, a method for three-dimensional single-molecule localization microscopy (SMLM) that combines astigmatic point-spread function (PSF) engineering with a structured illumination pattern in all three spatial dimensions. Existing modulation-enhanced techniques such as ModLoc improve axial localization precision, but a shorter axial pattern pitch means that emitters separated by more than one pitch period produce the same modulation phase. This phase ambiguity limits the usable axial range. These methods also require registration between separate camera regions. ZIMFLUX uses a single camera path, avoiding inter-camera registration. A vectorial PSF model accounts for optical aberrations, refractive index mismatch, and supercritical angle fluorescence (SAF). The illumination pattern is estimated directly from the acquired data, removing the need for external calibration and making the method robust to pattern distortions at greater imaging depths and to setup drift over time. Experimental validation on 80 nm DNA-origami nanostructures demonstrates unbiased three-dimensional localization with a 1.5-fold improvement in axial precision over conventional astigmatic SMLM. At imaging depths beyond a few micrometers, spherical aberration from refractive index mismatch gradually reduces the ellipticity of the astigmatic PSF, degrading axial precision. The structured illumination pattern in ZIMFLUX provides an independent source of axial information through the modulation phase, which can maintain axial precision even when ellipticity is reduced.

Chapter 3 presents a framework for two-dimensional live-cell mRNA imaging in budding yeast, designed to study messenger RNA transport through the nuclear pore complex (NPC). The approach uses low-power widefield fluorescence microscopy on intact cells, preserving the cell wall. This minimizes cellular stress while maintaining high throughput. Three mRNA transcripts (*GFA1*, *MYO2*, and *TRA1*) are labeled using an eGFP-PP7 (green) stem-loop construct and imaged alongside nucleoporins Nup60 and Nup82 labeled with mKate (red) at 20 ms time intervals.

A convolutional neural network (CNN) estimates the non-uniform background in the images. This reduces false positive mRNA detection from 40% to 16% compared to detection without background correction and improves localization precision by up to 800%. The nuclear envelope is localized with 13 nm precision using a ring model based on the generalized logistic function and a normal distribution. The combined localization precision, accounting for mRNA detection, nuclear envelope fitting, drift, and camera registration, is 49 nm.

The framework reveals distinct transport dynamics for different transcripts. *TRA1* exhibits different NPC interaction patterns, including re-entry closer to the nuclear side during failed transport events. Bimodal mRNA localization during NPC transit indicates nuclear and cytoplasmic docking sites, with characteristic distances measured for each transcript.

Chapter 4 quantifies huntingtin (*Htt*) mRNA expression and aggregation in mouse brain tissue. Huntington's disease (HD) is characterized by expanded CAG repeats in the *Htt* gene, which lead to mRNA clustering that may contribute to disease pathology. A high-throughput imaging pipeline combines RNAscope *in situ* hybridization with automated confocal imaging. It uses 3D Gaussian PSF fitting calibrated on fluorescent beads and pointillistic image features to establish per-slide intensity thresholds from negative controls. Validation operates at two scales: a linear relationship between spot size and intensity ($r^2 > 0.90$) for single molecules, and linear scaling between cluster volume and total intensity (mRNA content) ($R^2 > 0.98$) for multi-transcript clusters.

Applied to *Htt*Q111+/- knock-in mice (carrying ~111 CAG repeats), the analysis detects over 900,000 single mRNA molecules and segments over 1.9 million mRNA clusters across thousands of fields of view. Two probes targeting the spliced mutant transcript *Htt1a* and full-length *Htt* reveal considerable spatial heterogeneity. In Q111 mice, 16–62% of fields of view are classified as "extreme," defined as exceeding the 95th percentile of wildtype levels. The striatum shows consistently higher prevalence than the cortex. These extreme fields of view exhibit 2–6 times more clusters per nucleus, 1.3–1.7 times higher cluster density, and a shift from nuclear toward cytoplasmic localization. This shift is most pronounced for full-length *Htt*. Although the limited sample size of 11 mice precludes robust statistical inference at the animal level, the quantitative framework provides a foundation for evaluating therapeutic interventions in future studies with larger cohorts.

SAMENVATTING

Fluorescentiemicroscopie is een onmisbaar hulpmiddel geworden voor het bestuderen van biologische processen op moleculair niveau. Kwantitatieve metingen van de expressie en lokalisatie van RNA vereisen voortdurende innovatie in optische methoden en computationele beeldanalyse. Dit proefschrift presenteert drie bijdragen die kwantitatieve fluorescentiemicroscopie voor RNA-beeldvorming op verschillende biologische schalen verder ontwikkelen.

Hoofdstuk 2 introduceert ZIMFLUX, een methode voor driedimensionale single-molecule localization microscopy (SMLM) die astigmatische point spread function (PSF)-techniek combineert met een gestructureerd belichtingspatroon in alle drie de ruimtelijke dimensies. Bestaande modulatie-versterkte technieken zoals ModLoc verbeteren de axiale lokalisatieprecisie, maar een kortere axiale patroongolflengte betekent dat emitters die meer dan één periode uit elkaar liggen dezelfde modulatiefase opleveren. Deze fase-ambiguïteit beperkt het bruikbare axiale bereik. Deze methoden vereisen ook onderlinge uitlijning van afzonderlijke cameragebieden. ZIMFLUX maakt gebruik van een enkel camerapad, waardoor uitlijning tussen camera's niet nodig is. Een vectorieel PSF-model houdt rekening met optische aberraties, brekingsindexverschillen en fluorescentie onder superkritische hoek (SAF). Het belichtingspatroon wordt direct uit de meetdata geschat, waardoor externe kalibratie overbodig is en de methode robuust is tegen patroonverstoringen op grotere beeldvormingsdieptes en tegen drift van de opstelling over de tijd. Experimentele validatie op 80 nm DNA-origami-nanostructuren toont zuivere driedimensionale lokalisatie aan met een 1,5-voudige verbetering in axiale precisie ten opzichte van conventionele astigmatische SMLM. Op beeldvormingsdieptes groter dan enkele micrometers vermindert sferische aberratie door brekingsindexverschillen geleidelijk de ellipticiteit van de astigmatische PSF, waardoor de axiale precisie afneemt. Het gestructureerde belichtingspatroon in ZIMFLUX biedt een onafhankelijke bron van axiale informatie via de modulatiefase, waardoor de axiale precisie behouden kan blijven ook wanneer de ellipticiteit afneemt.

Hoofdstuk 3 presenteert een methode voor tweedimensionale mRNA-beeldvorming in levende gistcellen, ontworpen om het transport van boodschapper-RNA door het kernporiecomplex (NPC) te bestuderen. De aanpak maakt gebruik van breedveldfluorescentiemicroscopie met laag laservermogen op intacte cellen, waarbij de celwand behouden blijft. Dit minimaliseert cellulaire stress en behoudt een hoge doorvoer van data. Drie mRNA-transcripten (*GFA1*, *MYO2* en *TRA1*) worden gelabeld met een eGFP-PP7-stam-lusconstruct (groen) en afgebeeld naast nucleoporinen Nup60 en Nup82 gelabeld met mKate (rood), met tijdsintervallen van 20 ms.

Een convolutioneel neuraal netwerk (CNN) schat de niet-uniforme achtergrond in de beelden. Dit vermindert de foutpositieve mRNA-detectie van 40% naar 16% ten opzichte van detectie zonder achtergrondcorrectie en verbetert de lokalisatieprecisie met

tot 800%. De kernmembraan wordt gelokaliseerd met een precisie van 13 nm met behulp van een ringmodel op basis van de gegeneraliseerde logistische functie en een normale verdeling. De gecombineerde lokalisatieprecisie, inclusief mRNA-detectie, kernmembraanfitting, drift en camera-uitlijning, is 49 nm.

De methode onthult verschillende transportdynamieken voor de onderzochte transcripten. *TRA1* laat andere NPC-interactiepatronen zien, waaronder terugkeer dichter bij de nucleaire zijde tijdens mislukte transportgebeurtenissen. Bimodale mRNA-lokalisatie tijdens de passage door de NPC wijst op nucleaire en cytoplasmatische dockingplaatsen, met karakteristieke afstanden die voor elk transcript zijn gemeten.

Hoofdstuk 4 kwantificeert huntingtine (*Htt*) mRNA-expressie en -aggregatie in muizenhersenweefsel. De ziekte van Huntington (HD) wordt gekenmerkt door verlengde CAG-herhalingen in het *Htt*-gen, die leiden tot mRNA-clustering die kan bijdragen aan de ziektepathologie. Een pipeline met hoge doorvoer combineert RNAscope *in situ* hybridisatie met geautomatiseerde confocale beeldvorming. Deze maakt gebruik van 3D Gaussische PSF-fitting gekalibreerd op fluorescerende bolletjes en puntvormige beeldkenmerken om intensiteitsdrempels per objectglas vast te stellen vanuit negatieve controles. Validatie werkt op twee schalen: een lineair verband tussen spotvorm en intensiteit ($r^2 > 0{,}90$) voor enkele moleculen, en lineaire schaling tussen clustervolume en totale intensiteit (mRNA-inhoud) ($R^2 > 0{,}98$) voor multi-transcriptclusters.

Toegepast op *Htt*Q111+/- knock-in muizen (~111 CAG-herhalingen) detecteert de analyse meer dan 900.000 enkele mRNA-moleculen en segmenteert meer dan 1,9 miljoen mRNA-clusters over duizenden gezichtsvelden. Twee probes gericht op het gesplitste mutante transcript *Htt1a* en volledige *Htt* onthullen aanzienlijke ruimtelijke heterogeniteit. Bij Q111-muizen wordt 16–62% van de gezichtsvelden geclassificeerd als "extreem," gedefinieerd als boven het 95e percentiel van wildtype niveaus. Het striatum vertoont consequent een hogere prevalentie dan de cortex. Deze extreme gezichtsvelden vertonen 2–6 keer meer clusters per celkern, een 1,3–1,7 keer hogere clusterdichtheid en een verschuiving van nucleaire naar cytoplasmatische lokalisatie. Deze verschuiving is het duidelijkst voor volledige *Htt*. Hoewel de beperkte steekproefomvang van 11 muizen robuuste statistische inferentie op dierniveau verhindert, biedt de kwantitatieve methode een basis voor het evalueren van therapeutische interventies in toekomstige studies met grotere cohorten.

PREFACE

This dissertation presents work carried out during my doctoral research. It bridges optical physics, computational image analysis, and molecular biology. The research was mainly conducted at the RNA Therapeutics Institute at the University of Massachusetts Chan Medical School and Department of Imaging Physics at the Delft University of Technology.

The chapters reflect three interconnected projects. Their common thread is the development and application of quantitative fluorescence microscopy methods to study RNA biology at the single-molecule level. Chapter 1 presents ZIMFLUX, a method that advances three-dimensional single-molecule localization microscopy by combining astigmatic PSF engineering with structured illumination. Chapter 2 describes a framework for live-cell mRNA imaging in yeast to study mRNA transport through nuclear pore complexes. Chapter 3 applies automated high-throughput imaging to quantify huntingtin mRNA pathology in mouse brain tissue in the context of Huntington's disease.

Each project involved close collaboration with biologists, physicists, and computational scientists across multiple institutions. Working at this interface between disciplines has been both challenging and rewarding. I hope this thesis demonstrates the value of bringing quantitative imaging approaches to biological questions.

Pieter Fop van Velde
Delft, 2026

1

INTRODUCTION

Every cell in a human body contains the same DNA. Yet cells look and behave very differently. Much of this diversity originates from RNA: which genes are transcribed, how many copies are made, and where those transcripts end up. To understand gene regulation, we need to see individual RNA molecules inside cells and tissues.

Fluorescence microscopy makes this possible. A fluorescent label attached to a specific RNA sequence lights up under the correct excitation, revealing its position. Over the past two decades, advances in optics, labeling, and computation have pushed the boundaries of what can be resolved. Single molecules can now be localized with nanometer precision. Thousands of transcripts can be mapped across entire tissue sections.

This thesis develops and applies quantitative fluorescence microscopy to image fluorescent molecules at three scales: three-dimensional localization of single fluorophores, live-cell tracking of mRNA transport through nuclear pores, and tissue-wide quantification of mRNA pathology. Although each of these scales poses different challenges, the methods share a common foundation: accurate point spread function (PSF) modeling combined with statistical inference.

The following sections review the optical, computational, and biological foundations that these chapters build upon.

1.1. HISTORY OF FLUORESCENCE MICROSCOPY

Fluorescence microscopy, confocal microscopy, and super-resolution microscopy are now mainstays of biological research. The origins of microscopy trace back to the late 17th century, when Antonie van Leeuwenhoek developed microscopes capable of high magnification [1]. His work laid the foundation for microbiology.

1.1.1. INTRODUCTION TO FLUORESCENCE MICROSCOPY

Leeuwenhoek's microscopes relied on transmitted light. This enabled him to observe micro-organisms, including bacteria and protists [1]. Transmitted light microscopy re-

veals overall specimen structure, but it cannot highlight specific molecules or structures of interest. Fluorescence microscopy addressed this limitation by enabling researchers to selectively label and visualize specific targets.

In the early 20th century, Heinrich Lehmann and Otto Heimstädt introduced fluorescent dyes and markers into microscopy [2]. With these tools, researchers could label specific structures within cells and visualize individual molecules with high contrast. This shift from transmitted light to fluorescence made it possible to observe cellular processes and structures that were previously inaccessible [3].

FOUNDATIONS OF FLUORESCENCE

The phenomenon of fluorescence was first observed in the 16th century. Nicolás Monardes and Bernardino de Sahagún described the bluish glow emitted by the wood of a small tree called "lignum nephriticum" [4]. The term "fluorescence" was introduced in 1852 by George Gabriel Stokes. He described how shorter-wavelength light is absorbed and re-emitted at longer wavelengths, a process now called the Stokes shift [5, 4]. This characterization established key principles that would become essential in biological microscopy.

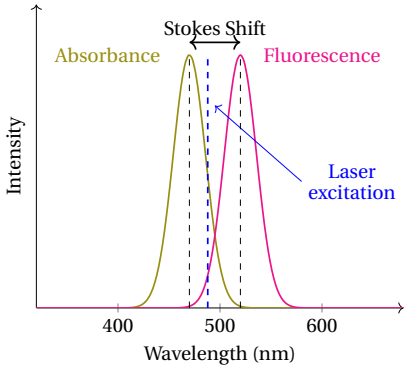


Figure 1.1: Stokes shift: emission of longer-wavelength light after exciting a fluorescent molecule with shorter-wavelength light.

The development of fluorescent dyes built on Stokes' work and played a crucial role in advancing fluorescence microscopy. In the late 19th century, Adolf von Baeyer synthesized the first fluorescent dye, Fluorescein [6]. In 1914, Stanislav von Provazek applied fluorescent dyes to visualize cells and tissue. This was the first use of a fluorescent dye as a stain in cell biology [7].

A transformative discovery was the Green Fluorescent Protein (GFP). It was first isolated from the jellyfish *Aequorea victoria* in 1961 [8] and later cloned in 1992 [9]. In 1994, scientists successfully co-expressed GFP with other genes [10, 11]. This led to the technique of "tagging" endogenous proteins. By fusing the gene encoding GFP with the gene encoding the target protein, researchers could visualize protein localization directly in living cells [12].

EVOLUTION OF FLUORESCENCE MICROSCOPY TECHNIQUES

Fluorescence microscopy has progressed alongside biological advancements. Early widefield microscopes, popular by the mid-20th century, are still used today but suffer from out-of-focus background light in thick specimens. Confocal microscopy, conceptualized by Marvin Minsky in 1957, reduces this unwanted background. It focuses excitation into a diffraction-limited spot and uses a pinhole to reject out-of-focus emission [13].

In the 1980s, Total Internal Reflection Fluorescence (TIRF) microscopy was developed for surface imaging. TIRF employs an excitation beam that reflects off the coverglass, generating an evanescent wave confined to about 100 nm from the surface. This selectively excites near-surface fluorophores, enabling high-contrast imaging of cell membranes and other surface-bound processes [14].

All fluorescence microscope techniques, whether widefield, confocal, or TIRF, rely on dichroic mirrors. These optical components selectively reflect specific wavelengths ($\lambda < \lambda_{\text{cut-off}}$) while transmitting others ($\lambda > \lambda_{\text{cut-off}}$), thereby separating excitation and emission light. A dichroic mirror with a cut-off wavelength between the excitation and emission spectra (fig. 1.1) isolates the sample signal from the excitation laser. Schematic layouts of widefield, confocal, and TIRF microscopy are shown in fig. 1.2.

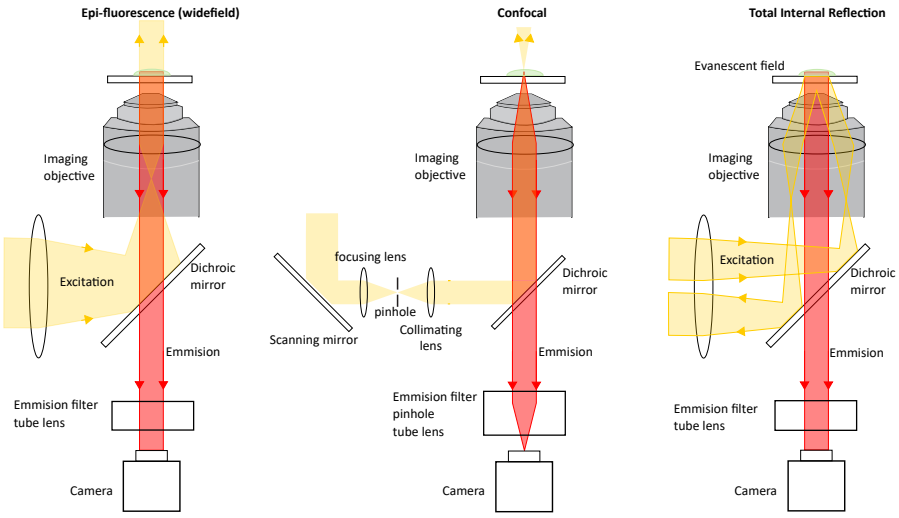


Figure 1.2: Schematic overview of fluorescence microscopy techniques: Widefield, Confocal, and TIRF microscopy. Each technique differs by selectively focusing on in-focus fluorescence, or limiting excitation to surface-bound fluorophores.

1.2. RESOLUTION LIMIT AND POINT SPREAD FUNCTION

With any microscope technique, the ability to distinguish fine details or different fluorophores is inherently limited by the physical properties of light and the microscope's optical system.

1

1.2.1. RESOLUTION LIMIT

Diffraction fundamentally limits microscope resolution. As light passes through the optical system, each point source in the specimen produces a blurred spot on the detector, known as the PSF [15].

Abbe's criterion quantifies this diffraction effect by linking the resolution limit to the highest spatial frequency that the objective lens can transmit. According to this criterion, the minimum distance d that can be resolved is given by

$$d = \frac{\lambda}{2\,\mathrm{NA}}, \tag{1.1}$$

where λ represents the wavelength of the emitted light and NA is the numerical aperture of the objective lens. The numerical aperture is defined as

$$\mathrm{NA} = n \sin\theta, \tag{1.2}$$

with n being the refractive index of the medium between the objective and the specimen, and θ the half-angle of the light cone entering the objective, as illustrated in fig. 1.3. Higher resolution requires either a shorter wavelength or a larger numerical aperture. The equation holds only when the refractive indices along the illumination path are uniform. The immersion fluid and the mounting medium surrounding the specimen must share the same n. If the indices differ, the effective NA is truncated by the lower refractive index. This mismatch also introduces depth-dependent spherical aberration and super-critical-angle fluorescence, both of which distort the PSF [16, 17, 18, 19]. For many applications in 2D widefield microscopy, the PSF can be approximated by a Gaussian for rapid localization [20, 21]:

$$\mathrm{PSF}_{\mathrm{Gauss}}(x, y) = \frac{1}{2\pi\sigma_{\mathrm{PSF}}^2} \exp\Big[-\frac{(x - x_0)^2 + (y - y_0)^2}{2\sigma_{\mathrm{PSF}}^2}\Big], \tag{1.3}$$

where (x_0, y_0) is the emitter position and σ_{PSF} its width. Many 3D astigmatic localization implementations use Gaussian models with empirical calibration curves. However, more accurate PSF descriptions can reduce systematic bias, particularly at greater imaging depths [17, 22].

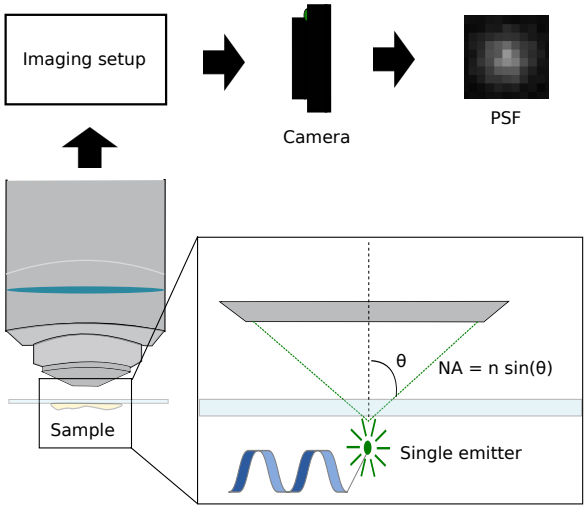


Figure 1.3: Illustration of a single emitter's light passing through the objective and forming a PSF on the camera.

1.2.2. POINT-SPREAD FUNCTION (PSF)

A fluorophore emits as an oscillating electric dipole. When it rotates freely during the acquisition time, its emission pattern averages out and can be approximated as isotropic [20]. The objective collects light within its numerical aperture and, together with the tube lens, forms an image on the detector as shown in fig. 1.3. The resulting intensity pattern from a single point emitter is the PSF. It characterizes how the microscope images a point source [23, 24]. Its width is related to the Abbe diffraction limit in eq. (1.1).
For high numerical apertures ($NA \gtrsim 0.5$), vectorial diffraction models are needed to accurately describe polarization effects and PSF shape [25, 26].

PSF engineering By placing a phase mask in the pupil plane, the PSF can be modified for specific applications. Examples include astigmatic, double-helix, and Tetrapod PSFs used for three-dimensional single-molecule localization [27, 28, 29]. These engineered PSFs encode axial position information in the shape of the PSF.

1.2.3. EMERGENCE OF SUPER-RESOLUTION

Conventional optical microscopy is constrained by the diffraction limit, which sets a lower bound on the resolvable structures. Super-resolution microscopy bypasses this limit using several strategies.
Some techniques modestly increase effective resolution (up to a factor of roughly 2) by incorporating prior information and image reconstruction algorithms. For example, structured illumination microscopy (SIM) [30, 31] uses a known illumination pattern, and deconvolution algorithms use knowledge of the PSF [32]. Other approaches achieve significantly higher resolution improvements:
Targeted super-resolution exploits nonlinear fluorophore responses under high-intensity light. Examples include stimulated emission depletion (STED) [33], ground-

state depletion (GSD) [34], and reversible saturable optical fluorescence transitions (RESOLFT) [35]. By switching fluorophores on or off in a controlled fashion, these methods reduce the effective PSF size.

Stochastic super-resolution leverages single-molecule blinking or switching to separate densely packed emitters in time. Techniques such as photoactivated localization microscopy (PALM) and stochastic optical reconstruction microscopy (STORM) localize individual fluorophores with high precision, exceeding the diffraction limit [36, 37].

These breakthroughs led to the 2014 Nobel Prize in Chemistry awarded to Eric Betzig, W.E. Moerner, and Stefan Hell for "the development of super-resolved fluorescence microscopy," starting a new era of molecular-scale optical imaging [38].

1.3. SINGLE MOLECULE LOCALIZATION MICROSCOPY

Single Molecule Localization Microscopy (SMLM) belongs to the class of stochastic super-resolution techniques. It localizes individual emitters within a densely labeled sample by temporally separating their emissions. This contrasts with conventional imaging where all fluorophores emit simultaneously, as shown in fig. 1.4a. By fitting the PSF of each isolated emitter in each time frame, spatial resolutions far beyond the Abbe limit can be achieved, as shown in fig. 1.4b.

1.3.1. SWITCHING MECHANISMS

The key requirement for SMLM is that only a sparse subset of emitters is active in each frame. Several strategies have been developed to achieve this temporal separation.

PALM uses photoactivatable or photoconvertible fluorescent proteins [36]. An activation laser stochastically converts a small fraction of molecules from a dark to a fluorescent state. Each activated molecule is imaged and localized before it bleaches. STORM uses organic dyes that switch between fluorescent and dark states at high excitation intensities in specific buffer conditions [37]. The combination of a thiol-containing reducing agent and an oxygen-scavenging system promotes controlled blinking. These two approaches were among the first to demonstrate nanometer-scale resolution in biological samples.

An alternative labeling strategy is DNA Points Accumulation for Imaging in Nanoscale Topography (DNA-PAINT). In DNA-PAINT, short fluorescently labeled oligonucleotides transiently bind to complementary strands attached to the target [39, 40]. The transient binding and unbinding creates the temporal separation needed for localization. Because the fluorophore is continuously replenished from solution, DNA-PAINT is not limited by photobleaching. This makes it well-suited for long acquisitions and quantitative imaging.

Each switching mechanism imposes trade-offs. PALM requires genetic fusion of a fluorescent protein, which may alter protein function. STORM achieves high photon counts from bright organic dyes but requires specific imaging buffers. DNA-PAINT achieves high localization precision and is inherently quantitative, but the binding kinetics must be carefully tuned to achieve sufficient temporal separation without excessive acquisition times.

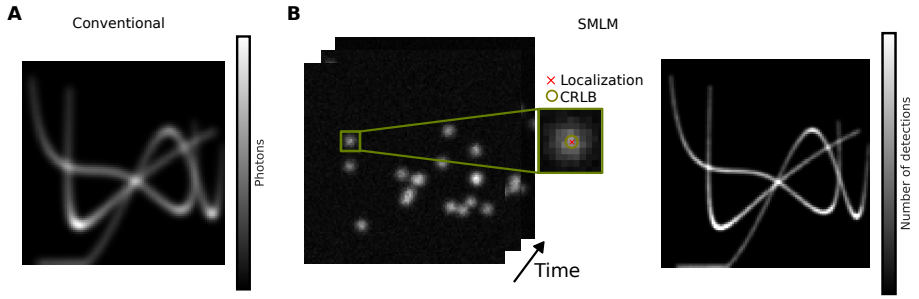


Figure 1.4: Conceptual and simulated illustration of Single Molecule Localization Microscopy (SMLM). (**a**) Image using conventional microscopy, in which all fluorophores are emitting simultaneously. (**b**) Fluorophores are switched on and off stochastically and imaged for many time frames, allowing individual localization events to be localized, with a precision defined by the Cramér–Rao lower bound, resulting in a reconstructed super-resolution image.

1.3.2. LOCALIZATION PRECISION

When an isolated emitter is observed in SMLM, multiple independent position measurements can be recorded. The variance of these measurements provides an experimental estimate of the localization precision, σ_{SMLM}, defined as the square root of this variance. The location of the emitter is then taken to be the mean of these localizations, with a standard error of the mean given by:

$$\delta_{\text{loc}} = \frac{\sigma_{\text{SMLM}}}{\sqrt{N_{\text{measurements}}}}, \tag{1.4}$$

where $N_{\text{measurements}}$ is the number of measurements. For a truly isolated emitter, it is theoretically possible to reduce the localization uncertainty arbitrarily by collecting sufficient data.

However, when two emitters lie closer than roughly σ_{SMLM}, their localization distributions overlap and become difficult to distinguish. In practice, this overlap constrains the achievable resolution to scales on the order of σ_{SMLM}. Ultimately, it is the interplay between labeling density and localization precision that governs the image resolution. A single metric that captures both effects is the Fourier ring correlation (FRC) [41].

A strategy to bypass this limitation is Resolution Enhancement by Sequential Imaging (RESI). RESI sequentially labels and images emitters located at distances much smaller than σ_{SMLM}. This approach fully exploits the $\sqrt{N_{\text{measurements}}}$ improvement and has enabled the localization of individual DNA bases separated by only 7 Å along a double helix [42, 43].

Another approach to resolve sub-nanometer structures is imaging at cryogenic temperatures. At cryogenic temperatures, fluorophores show increased stability and reduced photobleaching. This results in 1–2 orders-of-magnitude higher photon yield [44, 45, 46]. The higher photon yield directly improves the localization precision, as described in the following sections.

LATERAL LOCALIZATION PRECISION

The lateral localization precision in SMLM is determined by estimating the emitter coordinates (x_0, y_0) and can be expressed as

$$\sigma_{\text{lat}} = \sqrt{\sigma^2_{x,\text{CRLB}} + \sigma^2_{y,\text{CRLB}}},$$

where $\sigma_{x,\text{CRLB}}$ and $\sigma_{y,\text{CRLB}}$ denote the respective uncertainties in the x and y coordinates, to be distinguished from the PSF widths σ_x and σ_y used below in the discussion of astigmatic PSF encoding. These uncertainties are bounded from below by the Cramér–Rao lower bound (CRLB), which limits the variance of any unbiased estimator; maximum-likelihood estimation (MLE) attains this bound asymptotically. Assuming a Gaussian PSF model, the bound can be approximated as:

$$\sigma^2_{x,\text{CRLB}} = \frac{\sigma_a^2}{N_{\text{signal}}}\left(1 + 4\tau + \sqrt{\frac{2\tau}{1+4\tau}}\right) \tag{1.5}$$

in which $\tau = \frac{2\pi\sigma_a^2 N_{\text{bg}}}{N_{\text{signal}}\, a^2}$ and $\sigma_a^2 = \sigma^2_{\text{PSF}} + a^2/12$, where N_{signal} is the photon count of the emitter, N_{bg} the background photons per pixel, σ_{PSF} the width of the PSF (see eq. (1.3)) and a the camera pixel size [47]. This equation reveals two routes to improved precision: increasing the signal photon count or reducing the background.
In the low-background limit ($\tau \ll 1$), the expression simplifies to $\sigma_{x,\text{CRLB}} \approx \sigma_a/\sqrt{N_{\text{signal}}}$, and the precision scales as $1/\sqrt{N_{\text{signal}}}$. In the high-background regime ($\tau \gg 1$), precision degrades more rapidly with increasing background. This distinction is important for biological imaging, where background levels vary dramatically between controlled *in vitro* conditions and dense cellular or tissue environments.

THREE-DIMENSIONAL LOCALIZATION

An unaberrated PSF is symmetric around the focal plane. This symmetry makes it impossible to determine whether an emitter is above or below focus from a single image. To encode axial position, several PSF engineering strategies break this symmetry.

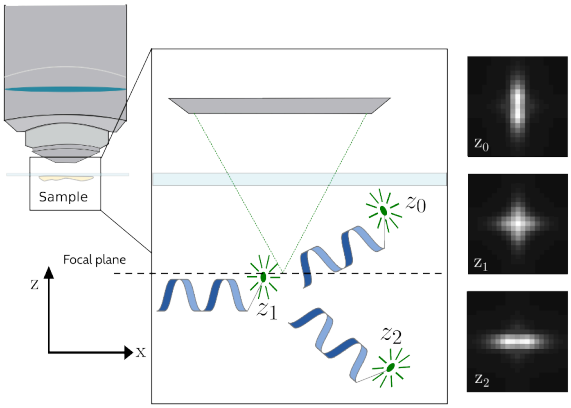


Figure 1.5: Example of 3D PSF engineering, where the shape of the PSF depends on the z-position of the emitter.

Astigmatic PSF. The most widely used approach places a cylindrical lens in the detection path [27]. This introduces astigmatism: the PSF becomes elliptical, with the orientation and ellipticity depending on the axial position of the emitter. Above focus the PSF is elongated along one axis, below focus along the other. The axial position is estimated by measuring the widths σ_x and σ_y of the elliptical PSF, as illustrated in fig. 1.5. The typical axial range is approximately 1 μm around the focal plane. Astigmatic PSF encoding is straightforward to implement and compatible with most microscope configurations.

Double-helix PSF. A phase mask in the back focal plane of the objective can create a PSF consisting of two lobes that rotate around each other as a function of axial position [28, 48]. The rotation angle encodes the z-coordinate. The double-helix PSF provides a larger axial range than astigmatism (up to 2 μm) and more uniform precision across depth. However, the two-lobe pattern spreads photons over a larger area, reducing the signal-to-noise ratio per lobe.

Other engineered PSFs. Several other phase profiles have been proposed. The Tetrapod PSF uses an optimized phase mask to generate four lobes, extending the axial range to several micrometers [29]. The self-bending PSF [49], corkscrew PSF [50], and saddle-point PSF [29] each offer different trade-offs between axial range and precision. The choice of engineered PSF depends on the application: short-range precision favors astigmatism, while large-range imaging benefits from extended-range designs.

Biplane and multi-plane detection. Alternatively, axial information can be obtained by splitting the detection path into two or more focal planes. In biplane SMLM, a beam splitter creates two images at different focal positions [51]. The relative sharpness of the emitter in the two planes encodes its axial position. This approach preserves the standard PSF shape and does not require pupil-plane modifications. However, the photon budget is divided between the planes, reducing the signal per plane.

Interferometric approaches. The highest axial precision is achieved by interferometric methods that use two opposing objectives to collect fluorescence from both sides of the sample. iPALM splits the combined beams into three interference channels using a three-way beam splitter [52, 53]. The relative intensities across the three channels encode the axial position, providing precision below 10 nm. 4Pi single-molecule switching microscopy uses a two-beam interference scheme instead [54]. Both approaches exploit the self-interference of emission from single emitters but differ in their optical layout and reconstruction algorithms. Recently, 4Pi detection has been combined with cryogenic imaging, and initial characterization on fluorescent beads demonstrated lateral precision of approximately 5 nm and axial precision of 2 nm [46]. These interferometric methods achieve outstanding axial resolution but require complex optical setups with two aligned objectives and are limited to thin, transparent samples.

Axial precision and PSF modeling. The axial localization precision σ_{ax} depends on the number of signal photons (N_{signal}), the background (N_{bg}), and the sensitivity of the PSF shape to axial displacement. Unlike the lateral case, an analytical approximation for

the axial CRLB is more complex and typically requires numerical computation from the Fisher information matrix.

Accurate PSF modeling is critical for unbiased 3D localization. A simple Gaussian model captures the PSF shape near the focal plane but neglects effects such as spherical aberration, supercritical angle fluorescence, and depth-dependent PSF changes [17, 22]. When emitters are located far from the coverslip, the refractive index mismatch between the immersion oil and the sample medium distorts the PSF [18, 19]. This distortion varies with depth and introduces systematic biases in position estimates if the PSF model does not account for it.

Vectorial PSF models provide a more accurate description by computing the electromagnetic field in the image plane from first principles [20, 16]. These models include the effects of polarization, high numerical aperture, and refractive index stratification. Although computationally more expensive than Gaussian fitting, vectorial models reduce localization bias, particularly for 3D imaging at depth and for emitters near the coverslip where supercritical angle fluorescence contributes.

1.3.3. PRECISION UNDER REAL IMAGING CONDITIONS

The CRLB in eq. (1.5) describes the best achievable precision for a given photon budget and background level. In practice, several factors degrade precision beyond this theoretical limit.

Background sources. In biological samples, background fluorescence arises from autofluorescence of cellular components, out-of-focus fluorescence in thick specimens, and non-specific binding of fluorescent labels. In widefield illumination, all fluorophores throughout the sample depth are excited simultaneously, producing a diffuse background that reduces the signal-to-background ratio. TIRF illumination mitigates this for surface-proximal emitters by confining excitation to an evanescent wave. For samples that cannot be imaged in TIRF geometry, such as intact cells or tissue sections, the background can be spatially varying and structured. Standard PSF fitting algorithms that assume a locally uniform background may then introduce biased position estimates [55, 56].

Several computational approaches address non-uniform background. Temporal median filtering can estimate slowly varying background from image sequences. Model-based approaches fit parametric background functions alongside the emitter PSF. More recently, convolutional neural networks (CNNs) have been trained to estimate spatially varying background directly from noisy images [56]. The estimated background map is then incorporated into the likelihood function for PSF fitting, restoring unbiased localization even when the background varies across the field of view.

Aberrations and refractive index mismatch. Refractive index differences between the immersion medium, coverslip, and sample introduce wavefront aberrations that distort the PSF [18, 19]. The dominant contribution is spherical aberration, which grows with imaging depth. At 5 μm to 10 μm into a water-mounted sample imaged with an oil-immersion objective, the PSF can broaden significantly and develop pronounced asymmetry. This leads to both degraded precision and systematic localization bias, particu-

larly in the axial direction [17, 22].
Adaptive optics can correct aberrations by measuring and compensating the wavefront distortion with a deformable mirror [16]. Alternatively, depth-dependent PSF models can account for the aberrations computationally during the fitting step. Both strategies require careful calibration and add experimental or computational complexity.

Sample drift. Mechanical drift of the sample stage during acquisition shifts all emitter positions by the same amount over time. Typical drift rates are on the order of nanometers per minute. If uncorrected, drift blurs the reconstructed super-resolution image. Fiducial markers, such as immobilized gold nanoparticles or fluorescent beads, can be tracked throughout the acquisition and used to register all frames to a common coordinate system. Alternatively, cross-correlation of intermediate reconstructions can estimate and correct drift without fiducial markers [57]. Drift correction is essential for any SMLM experiment that extends beyond a few minutes.

Emitter density and overlapping PSFs. When two emitters are simultaneously active within one diffraction-limited spot, their overlapping PSFs bias the individual position estimates [58]. Each emitter is pulled toward the other, creating artificial "bridging" between closely spaced structures. Reducing the emitter density avoids this problem but increases acquisition time. Multi-emitter fitting algorithms [59, 60] can fit multiple overlapping PSFs simultaneously, but the unknown number of active emitters remains a source of uncertainty.

1.3.4. DETECTION AND ESTIMATION

Localization begins with detection: identifying which regions of each frame contain a single-molecule signal. A common approach is to apply an intensity threshold after filtering the image with a bandpass or matched filter. The threshold is typically set by visual inspection or empirical tuning. This works well for bright emitters against low background but becomes unreliable when the signal-to-noise ratio drops.
A more principled approach is the Generalized Likelihood Ratio Test (GLRT). The GLRT compares two hypotheses: that a given image region contains only background, or that it contains background plus an emitter. The test statistic is the ratio of the maximum likelihoods under the two hypotheses [61, 55]. The detection threshold is set by the desired probability of false alarm, directly controlling the false positive rate. This provides a statistical guarantee that is independent of the specific image conditions. A test at level α fixes the probability of a false alarm at α and, among the tests that respect that limit, seeks the one that detects true emitters most often. For a pair of fully specified hypotheses the likelihood ratio test is optimal in this sense [61]; the GLRT extends the construction to the composite case encountered here, where the emitter position and intensity are unknown. It is particularly valuable for detecting dim emitters in structured background, where manual thresholding would either miss real signals or generate excessive false positives. Recently, an efficient implementation of the GLRT was shown to outperform commonly used detection filters such as difference-of-Gaussians and Laplacian-of-Gaussian [62].

1

1.3.5. TECHNIQUES FOR IMPROVING SMLM PRECISION

SMLM performed under widefield illumination achieves a localization precision that depends on the PSF, the signal photon count N_{signal}, and the background level N_{bg}. To improve precision without increasing the photon budget, several methods exploit structured or focused illumination patterns.

MINFLUX

MINFLUX employs a donut-shaped excitation beam with a central intensity null [63]. The fluorescence signal indicates how far the emitter is from the null. By scanning the donut around the emitter in an iterative fashion, the position can be refined to nanometer-scale precision with as few as 100 photons. The localization precision scales with L, the spatial extent of the illumination pattern. Reducing L in successive iterations improves precision, though the optimal scanning strategy depends on the photon budget per step [64].

MINFLUX has been extended to three dimensions using a 3D donut [65]. It has achieved multicolor nanometer resolution in cellular imaging and has also been applied to single-molecule tracking, enabling nanometer-scale spatial resolution at millisecond temporal resolution [66]. The main limitation is throughput: the scanning nature of MINFLUX restricts measurement to one or a few emitters at a time.

PATTERNED ILLUMINATION OVER THE FULL FIELD OF VIEW

SIMFLUX uses phase- and direction-switching sinusoidal patterns over the entire field of view [67]. The localization precision scales with the pattern pitch L_{lat}, similar to MINFLUX, but all emitters in the field of view benefit simultaneously. This enables higher throughput than MINFLUX. The minimum pitch is limited by the interference pattern generation and is typically larger than in MINFLUX.

ROSE-Z and ModLoc apply sinusoidal illumination patterns in the axial direction [68, 69]. These methods improve axial precision by encoding emitter position in the modulation phase. Accurate knowledge of the illumination pattern is essential for unbiased estimation. Small miscalibrations or sample-specific artifacts, such as refractive index mismatches or non-flat coverslips, can introduce systematic errors.

Extending patterned illumination to three dimensions combines the precision benefits in all three spatial dimensions. However, calibrating a 3D illumination pattern is more challenging than calibrating patterns along individual axes. Any mismatch between the assumed and actual pattern introduces bias that is difficult to diagnose from the localization data alone. Recently, 4Pi-SIMFLUX addressed this anisotropy by integrating structured illumination in the excitation path with 4Pi interferometric detection in the emission path [70]. The structured illumination doubles the lateral precision of 4Pi-SMLM, while the interferometric detection provides axial precision. Together they achieve near-isotropic localization precision of 2–3 nm in three dimensions. However, the 4Pi detection geometry requires two precisely aligned opposing objectives, making the system considerably more complex to build and calibrate than single-objective approaches.

1.4. BIOLOGICAL CONTEXT

The techniques described earlier provide increasingly powerful tools for imaging biological processes at the nanoscale. The value of these tools ultimately depends on the biological questions they address. The following sections introduce two such questions, each requiring a different imaging strategy: live-cell tracking of mRNA export through the nuclear pore complex, and spatial quantification of RNA in fixed tissue from Huntington's disease models.

1.4.1. mRNA TRANSPORT THROUGH THE NUCLEAR PORE COMPLEX

The transport of messenger RNA (mRNA) from the nucleus to the cytoplasm is a key event in gene expression. DNA is transcribed into mRNA in the nucleus, and the resulting mRNA is translated into protein in the cytoplasm [71], as illustrated in fig. 1.6A. The nuclear pore complex (NPC) acts as the selective gateway mediating this transport.

NPC STRUCTURE AND TRANSPORT PATHWAYS

The NPC is one of the largest protein complexes in the cell, composed of approximately 30 different nucleoporins (Nups) arranged with eight-fold rotational symmetry, so that each Nup is present in multiples of eight copies [72]. The nuclear envelope is a double membrane, and NPCs are embedded at the sites where the inner and outer nuclear membranes fuse. These nucleoporins form a channel between the nucleus and cytoplasm, with the inner ring positioned at this fusion point. The channel is lined with phenylalanine–glycine (FG) repeat proteins, which create a permeability barrier: small molecules diffuse through the pore freely, whereas larger cargo such as mRNA is excluded unless it is bound to a transport receptor. On the nuclear side, linker nucleoporins connect to a nuclear basket, while on the cytoplasmic side, filaments promote the docking or release of cargo [73, 74, 75], as shown in fig. 1.6B.

The transport of mRNA is a receptor-mediated process that extends beyond simple diffusion [76]. Multiple mRNA export pathways have been identified. The nuclear export factor 1 (NXF1)/NXT1 pathway is the primary route for most mRNAs and is closely tied to transcription [77]. A simplified diagram is shown in fig. 1.6C. This pathway relies on the transcription export (TREX) complex. TREX associates with the spliceosome and is recruited to mRNA during splicing. It comprises the multi-subunit THO complex and ALY. ALY links cargo mRNAs to NXF1/NXT1 to form export-competent mRNPs [78]. After export, GLE1 activates Dbp5-mediated mRNP remodeling at the cytoplasmic face of the NPC. This facilitates directional export and release into the cytoplasm [79]. Other pathways also exist, such as the CRM1/XPO1 pathway.

Increasing evidence suggests that the NPC plays an active role in gene regulation beyond acting as a conduit, affecting mRNA processing, translation, and export efficiency [80, 81, 82]. Defects in NPC function have been implicated in human diseases [83], including neurodegenerative disorders where mutant proteins disrupt nucleoporin function. In Huntington's disease, for example, mutant huntingtin protein mislocalizes nucleoporins and impairs nucleocytoplasmic transport [84], linking the two biological topics of this thesis.

SINGLE-MOLECULE STUDIES OF MRNA EXPORT

Many details of mRNA export remain unclear. These include the precise timing of protein recruitment, the composition of the nuclear messenger ribonucleoprotein particle (mRNP), the specific roles of each mRNP component, and the impact of cellular stress on export [85]. These questions are hard to answer because export is a transient single-molecule event: a transcript crosses a single pore in a few hundred milliseconds, so resolving it requires imaging individual molecules in living cells at high temporal resolution rather than averaging over a population. To study mRNA export mechanistically, a direct approach is to image individual mRNA molecules *in vivo*. Several studies have investigated mRNA translocation through the NPC using fluorescence microscopy.

These studies were enabled by RNA labeling methods developed in the late 1990s [86]. The MS2 and PP7 labeling techniques incorporate stem loop sequences into the mRNA of interest. These loops are recognized by coat proteins tagged with fluorescent markers, enabling real-time visualization of individual mRNA molecules, as illustrated in fig. 1.6D [87]. An alternative labeling strategy involves the PP7 system, which uses a different stem loop and coat protein with distinct binding properties [88, 89].

mRNA export has been studied in mammalian cells [90, 91, 92, 93] and yeast cells [94, 95, 96]. In mammalian cells, Grünwald et al. tracked MS2-labeled mRNAs through the NPC and measured export times of approximately 180 ms, with mRNPs spending additional time docked at the nuclear basket [90]. Subsequent studies refined these measurements and identified distinct kinetic phases of NPC transit [92]. Kaminski et al. used single-molecule tracking to study the interplay between Dbp5 and mRNA at the nuclear pore, revealing details of the remodeling step on the cytoplasmic side [93]. Most recently, Sau et al. used two-colour MINFLUX to resolve overlapping import and export pathways within the NPC central channel at nanometer resolution [66].

In yeast, Smith et al. imaged mRNA export using widefield microscopy combined with cell wall digestion to improve signal quality [94]. Saroufim et al. used a similar approach to measure export kinetics and found that export times in yeast are shorter than in mammalian cells [95]. Lari et al. studied the role of specific nucleoporins in export regulation [96]. However, all these yeast studies relied on either high-power confocal excitation or enzymatic cell wall digestion, both of which present limitations.

IMAGING CHALLENGES IN YEAST

Yeast cells provide a cost-effective and genetically tractable platform for high-throughput imaging. Core processes like mRNA export are conserved across species, enabling generalization between yeast and human biology [97, 98, 99]. However, the thick yeast cell wall (~200 nm) creates substantial challenges for fluorescence microscopy.

First, the refractive index mismatch between the cell wall ($n \approx 1.40$) and the growth medium ($n \approx 1.34$) introduces scattering and spherical aberrations [94]. These reduce the signal-to-noise ratio and distort the PSF. Second, the combination of short exposure times (tens of milliseconds) needed to capture rapid transport events and low laser powers needed to preserve cell viability produces dim signals against a structured, non-uniform background [100, 101, 102].

Existing strategies to address these challenges each have drawbacks. High-power confocal excitation improves signal detection but risks phototoxicity and may perturb the very processes under investigation. Enzymatic cell wall digestion reduces scattering but

introduces biological artifacts: the cell must expend energy to regenerate its wall, which may affect metabolism and transport dynamics. Digestion also limits the observation window and increases sample preparation complexity, reducing throughput. An ideal approach would preserve cell integrity while achieving sufficient signal-to-noise ratios for single-molecule detection. This remains an open challenge in the field [94, 103].

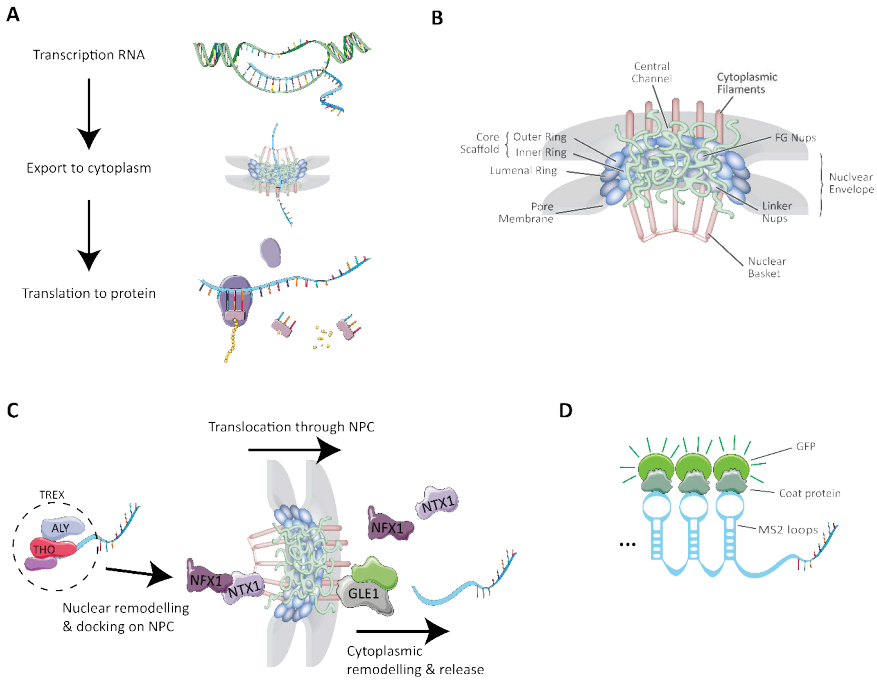


Figure 1.6: **mRNA export through the nuclear pore complex (NPC).** (**A**) A simplified representation of the pathway from DNA to protein, where RNA is transcribed from DNA, transported through the NPC, and translated into protein in the cytoplasm. (**B**) The structure of the NPC, which enables regulatory properties. (**C**) A simplified schematic of the NXF1/NXT1 mRNA export pathway, involving multiple remodeling and protein (un)binding events. (**D**) The MS2 tagging method enables *in vivo* mRNA tracking using fluorescent proteins. *Some figure elements adapted from Servier Medical Art licensed under CC BY 4.0.*

1.4.2. HUNTINGTON'S DISEASE AND RNA PATHOLOGY

The previous section examined mRNA transport in living cells. For tissue studies, the sample is typically fixed before imaging. This section reviews Huntington's disease (HD) as a context where quantitative RNA imaging in fixed tissue can provide spatial information that other methods cannot.

MOLECULAR BASIS OF HUNTINGTON'S DISEASE

HD is a fatal neurodegenerative disorder with an overall prevalence of 5.70 per 100,000 in Europe, North America, and Australia [104]. HD is caused by an expanded CAG repeat in the *Htt* gene, as shown in fig. 1.7A. All individuals with HD inherit a germline allele

containing 36 or more CAG repeats, compared to the typical range of 15–30 repeats [105]. In 98% of cases, the repeat count falls between 36 and 55.
Somatic expansion occurs throughout a person's lifetime, particularly in neurons. Individuals with an elevated baseline number of repeats eventually reach a tipping point. At this point, CAG expansions accelerate and lead to fatal disease progression, as illustrated in fig. 1.7B.
Once the repeat count exceeds 50, a cryptic splicing site is introduced. This causes improper splicing of the *Htt* mRNA [106]. The result is a truncated mutant transcript that includes *Htt* exon 1 and part of intron 1 at the 5' end, as shown in fig. 1.7C. This leads to the production of HTT1A protein. HTT1A levels correlate with CAG repeat length and have been observed in humans and in knock-in mouse models carrying 50 or more repeats [107].

mRNA CLUSTERING AND NUCLEAR RETENTION

Expanded-repeat mRNAs form stable secondary structures that sequester RNA-binding proteins. In HD, mutant *Htt* transcripts bind muscleblind-like 1 (MBNL1), contributing to nuclear retention and the formation of RNA foci [108, 109]. Similar MBNL1 sequestration by expanded CUG repeats occurs in myotonic dystrophy type 1 (DM1), where nuclear foci disrupt MBNL1 function [110]. Related RNA-mediated toxicity has been described in *C9orf72*-linked amyotrophic lateral sclerosis/frontotemporal dementia (ALS/FTD), where expanded G_4C_2 repeats form nuclear RNA foci [111]. These observations suggest that mRNA clustering through repeat expansion is a shared pathological mechanism across multiple neurodegenerative diseases [112, 113, 114].
The striatum is most affected in HD, with medium spiny neurons showing early vulnerability [115]. Within the striatum, neurodegeneration progresses along spatial gradients. *Htt1a* mRNA forms clusters that can only be resolved with microscopy. These clusters appear resistant to existing mRNA silencing strategies, while single cytoplasmic mRNAs are effectively silenced [116]. Understanding the spatial distribution, size, and molecular content of these clusters is therefore critical for developing effective therapeutics.

METHODS FOR SPATIAL RNA DETECTION IN TISSUE

Several approaches can quantify RNA expression in tissue, each with distinct strengths and limitations.
Single-cell RNA sequencing (scRNA-seq) yields quantitative gene expression profiles for hundreds of thousands of cells [115, 117]. However, it requires tissue dissociation and therefore does not provide spatial context [118]. Positional information can be vital, as disease processes may depend on where a transcript is localized within cells or across tissue regions [119].
Spatial transcriptomics methods such as MERFISH preserve spatial context and can image many transcripts simultaneously [120]. Yet they require complex probe design, specialized imaging protocols, and computationally intensive data analysis. The cost per experiment is substantially higher than for targeted single-gene approaches.
Single-molecule fluorescence *in situ* hybridization (smFISH) provides direct visualization of individual mRNA molecules in fixed tissue [121]. Conventional smFISH uses multiple short oligonucleotide probes that tile along the target mRNA. Each probe carries a single fluorophore, and the combined signal from 20–48 probes produces a diffraction-

limited spot whose intensity reflects the number of bound probes. smFISH achieves single-molecule sensitivity in cell culture but can be limited in tissue by probe penetration and background autofluorescence.

RNASCOPE TECHNOLOGY

RNAscope addresses the sensitivity-specificity trade-off through a branched signal amplification architecture [122]. Target probes are used in pairs, together called a "double Z". Each Z-shaped oligonucleotide binds the target RNA with its lower arm and carries only half of the pre-amplifier binding site on its upper arm. A complete binding site therefore exists only where two probes have hybridized to adjacent stretches of the same transcript; a probe that binds somewhere by chance leaves a half site, which is too short to retain the pre-amplifier. Non-specific binding cannot start the cascade, while a genuine target is recognized twice independently. Each bound pre-amplifier then recruits amplifiers that each carry multiple label probes, and roughly 20 probe pairs tiled along one transcript build an amplification tree bright enough to render a single mRNA as a diffraction-limited spot. RNAscope has become widely adopted for spatial RNA detection in tissue sections, including in the context of neurodegenerative diseases. However, quantifying transcripts in dense clusters, where multiple mRNAs co-localize within a diffraction-limited volume, remains a challenge for all fluorescence-based RNA detection methods [123].

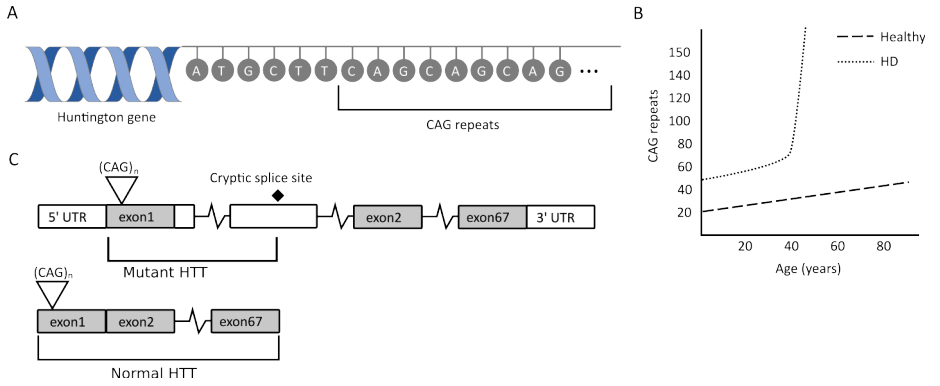


Figure 1.7: **Molecular genetics of Huntington's disease. (A)** The *Htt* gene contains a CAG repeat region whose length determines disease status. **(B)** Somatic CAG repeat expansion over a person's lifetime. In healthy individuals (dashed), repeat length grows only gradually. In HD (dotted), repeats undergo rapid expansion past a critical threshold, leading to disease onset. Trend adapted from [115]. **(C)** Gene structure of *Htt* showing the cryptic splice site in intron 1. When the CAG repeat count exceeds 50, aberrant splicing produces the truncated mutant *Htt1a* transcript. The regions corresponding to mutant *Htt1a* and normal full-length *Htt* are indicated. Exons and introns are not drawn to scale.

1.5. SCOPE OF THIS THESIS

Chapter 2 presents ZIMFLUX, a method for three-dimensional single-molecule localization microscopy. ZIMFLUX combines astigmatic PSF engineering with a three-dimensional sinusoidal illumination pattern generated by a digital micromirror device. A vectorial PSF model accounts for optical aberrations, refractive index mismatch, and

supercritical angle fluorescence. The illumination pattern is estimated directly from the acquired data. This avoids external calibration and reduces sensitivity to sample-specific artifacts. ZIMFLUX achieves a 1.5-fold improvement in axial precision over conventional astigmatic SMLM and remains unbiased at greater imaging depths.

Chapter 3 describes a framework for live-cell mRNA imaging in budding yeast to study mRNA transport through nuclear pore complexes. Three mRNA transcripts (*GFA1*, *MYO2*, and *TRA1*) are imaged using the PP7 labeling system in intact haploid cells. Low-power widefield microscopy preserves cell viability without cell wall digestion. A convolutional neural network estimates the spatially varying background. The GLRT then detects mRNA spots with controlled false positive rates. Automated nuclear envelope fitting enables precise localization of each NPC. The framework reveals transcript-specific transport dynamics, including differences in docking positions and NPC interaction patterns.

Chapter 4 presents a high-throughput RNAscope imaging pipeline for quantifying huntingtin mRNA in mouse brain tissue. The pipeline is applied to HttQ111+/- knock-in mice across three age groups. The analysis covers over 900,000 single mRNA molecules and 1.9 million clusters across cortex and striatum. A PSF-based calibration framework converts fluorescence intensity into absolute mRNA counts. This enables quantification of multi-transcript clusters that conventional dot counting cannot resolve. The striatum shows higher prevalence of extreme clustering than the cortex. The quantitative framework provides a foundation for evaluating RNA-targeted therapeutics for Huntington's disease.

Chapter 5 discusses the scientific and technical implications of these findings and outlines future perspectives.

BIBLIOGRAPHY

[1] Nick Lane. "The unseen world: reflections on Leeuwenhoek (1677)'Concerning little animals'". In: *Philosophical Transactions of the Royal Society B: Biological Sciences* 370.1666 (2015), p. 20140344.

[2] Francesca Cella Zanacchi, Paolo Bianchini, and Giuseppe Vicidomini. *Fluorescence microscopy in the spotlight*. 2014.

[3] Sviatlana Shashkova and Mark C Leake. "Single-molecule fluorescence microscopy review: shedding new light on old problems". In: *Bioscience Reports* 37.4 (2017), BSR20170031.

[4] Laura Marcu, Paul MW French, and Daniel S Elson. *Fluorescence lifetime spectroscopy and imaging: principles and applications in biomedical diagnostics*. CRC press, 2014.

[5] George Gabriel Stokes. "On the change of refrangibility of light". In: *Philosophical Transactions of the Royal Society of London* 142 (1852), pp. 463–562.

[6] Arianne Heinrichs. "Stains and fluorescent dyes". In: *Nature Cell Biology* 11.1 (2009), S7–S7.

[7] Olympus Life Science. *Basic Concepts in Fluorescence*. Accessed: 2024-10-16. 2024. URL: https://www.olympus-lifescience.com/en/microscope-resource/primer/techniques/fluorescence/fluorescenceintro/.

[8] Osamu Shimomura, Frank H Johnson, and Yo Saiga. "Extraction, purification and properties of aequorin, a bioluminescent protein from the luminous hydromedusan, Aequorea". In: *Journal of Cellular and Comparative Physiology* 59.3 (1962), pp. 223–239.

[9] Douglas C Prasher et al. "Primary structure of the Aequorea victoria green-fluorescent protein". In: *Gene* 111.2 (1992), pp. 229–233.

[10] Martin Chalfie et al. "Green fluorescent protein as a marker for gene expression". In: *Science* 263.5148 (1994), pp. 802–805.

[11] Satoshi Inouye and Frederick I Tsuji. "Aequorea green fluorescent protein: Expression of the gene and fluorescence characteristics of the recombinant protein". In: *FEBS Letters* 341.2-3 (1994), pp. 277–280.

[12] Roger Y Tsien. "The green fluorescent protein". In: *Annual Review of Biochemistry* 67.1 (1998), pp. 509–544.

[13] Marvin Minsky. "Memoir on inventing the confocal scanning microscope". In: *Scanning* 10.4 (1988), pp. 128–138.

[14] Daniel Axelrod. "Cell-substrate contacts illuminated by total internal reflection fluorescence." In: *Journal of Cell Biology* 89.1 (1981), pp. 141–145.

[15] S G Lipson, H Lipson, and D S Tannhauser. *Optical Physics*. 3rd. Cambridge: Cambridge University Press, 1995.

[16] Marijn Siemons et al. "High precision wavefront control in point spread function engineering for single emitter localization". In: *Optics Express* 26.7 (2018), pp. 8397–8416.

[17] Yiming Li et al. "Depth-dependent PSF calibration and aberration correction for 3D single-molecule localization". In: *Biomedical Optics Express* 10.6 (2019), pp. 2708–2718.

[18] Stefan Hell et al. "Aberrations in confocal fluorescence microscopy induced by mismatches in refractive index". In: *Journal of Microscopy* 169.3 (1993), pp. 391–405.

[19] Sheng Liu et al. "Three dimensional single molecule localization using a phase retrieved pupil function". In: *Optics Express* 21.24 (2013), pp. 29462–29487.

[20] S Stallinga and B Rieger. "Accuracy of the Gaussian point spread function model in 2D localization microscopy". In: *Optics Express* 18 (2010), pp. 24461–24476.

[21] Carlas S Smith et al. "Fast, single-molecule localization that achieves theoretically minimum uncertainty". In: *Nature Methods* 7.5 (2010), pp. 373–375.

[22] Marijn E Siemons, Lukas C Kapitein, and Sjoerd Stallinga. "Axial accuracy in localization microscopy with 3D point spread function engineering". In: *Optics Express* 30.16 (2022), pp. 28290–28300.

[23] E. Hecht. *Optics*. Pearson Education, Incorporated, 2017. ISBN: 9780133977226. URL: https://books.google.nl/books?id=ZarLoQEACAAJ.

[24] Joseph W Goodman. *Introduction to Fourier optics*. Roberts and Company publishers, 2005.

[25] Sjoerd Stallinga. "Axial birefringence in high-numerical-aperture optical systems and the light distribution close to focus". In: *Journal of the Optical Society of America A* 18.11 (2001), pp. 2846–2859.

[26] Bernard Richards and Emil Wolf. "Electromagnetic diffraction in optical systems, II. Structure of the image field in an aplanatic system". In: *Proceedings of the Royal Society of London. Series A. Mathematical and Physical Sciences* 253.1274 (1959), pp. 358–379.

[27] Bo Huang et al. "Three-dimensional super-resolution imaging by stochastic optical reconstruction microscopy". In: *Science* 319.5864 (2008), pp. 810–813.

[28] Mikael P Backlund et al. "The double-helix point spread function enables precise and accurate measurement of 3D single-molecule localization and orientation". In: *Single Molecule Spectroscopy and Superresolution Imaging VI*. Vol. 8590. Proceedings of SPIE. SPIE. 2013, pp. 121–131.

[29] Yoav Shechtman et al. "Optimal point spread function design for 3D imaging". In: *Physical Review Letters* 113.13 (2014), p. 133902.

[30] Mats GL Gustafsson. “Surpassing the lateral resolution limit by a factor of two using structured illumination microscopy”. In: *Journal of Microscopy* 198.2 (2000), pp. 82–87.

[31] Li-Hao Yeh, Lei Tian, and Laura Waller. “Structured illumination microscopy with unknown patterns and a statistical prior”. In: *Biomedical Optics Express* 8.2 (2017), pp. 695–711.

[32] Jean-Baptiste Sibarita. “Deconvolution microscopy”. In: *Microscopy Techniques*. Springer, 2005, pp. 201–243.

[33] Stefan W Hell and Jan Wichmann. “Breaking the diffraction resolution limit by stimulated emission: stimulated-emission-depletion fluorescence microscopy”. In: *Optics Letters* 19.11 (1994), pp. 780–782.

[34] Stefan Bretschneider, Christian Eggeling, and Stefan W Hell. “Breaking the diffraction barrier in fluorescence microscopy by optical shelving”. In: *Physical Review Letters* 98.21 (2007), p. 218103.

[35] Stefan W Hell. “Fluorescence nanoscopy: breaking the diffraction barrier by the RESOLFT concept”. In: *2005 IEEE LEOS Annual Meeting Conference Proceedings*. IEEE. 2005, p. 42.

[36] Eric Betzig et al. “Imaging intracellular fluorescent proteins at nanometer resolution”. In: *Science* 313.5793 (2006), pp. 1642–1645.

[37] Michael J Rust, Mark Bates, and Xiaowei Zhuang. “Sub-diffraction-limit imaging by stochastic optical reconstruction microscopy (STORM)”. In: *Nature Methods* 3.10 (2006), pp. 793–796.

[38] Nobel Prize. *The Nobel Prize in Chemistry 2014*. Accessed: 2024-04-27. 2014. URL: https://www.nobelprize.org/prizes/chemistry/2014/summary/.

[39] Ralf Jungmann et al. “Single-molecule kinetics and super-resolution microscopy by fluorescence imaging of transient binding on DNA origami”. In: *Nano Letters* 10.11 (2010), pp. 4756–4761.

[40] Ralf Jungmann et al. “Multiplexed 3D cellular super-resolution imaging with DNA-PAINT and Exchange-PAINT”. In: *Nature Methods* 11.3 (2014), pp. 313–318.

[41] Robert PJ Nieuwenhuizen et al. “Measuring image resolution in optical nanoscopy”. In: *Nature Methods* 10.6 (2013), pp. 557–562.

[42] Susanne CM Reinhardt et al. “Ångström-resolution fluorescence microscopy”. In: *Nature* 617.7962 (2023), pp. 711–716.

[43] Luciano Masullo et al. “Angstrom-resolution imaging of cell-surface glycans”. In: *bioRxiv* (2025), pp. 2025–02.

[44] Christiaan N Hulleman et al. “Photon yield enhancement of red fluorophores at cryogenic temperatures”. In: *ChemPhysChem* 19.14 (2018), pp. 1774–1780.

[45] Siegfried Weisenburger et al. “Cryogenic optical localization provides 3D protein structure data with Angstrom resolution”. In: *Nature Methods* 14.2 (2017), pp. 141–144.

[46] Q. Li. “Cryogenic 4Pi Single Molecule Localization Microscopy (Cryo-4Pi-SMLM): A 3D nanometer imaging technique”. PhD thesis. Delft University of Technology, 2025. ISBN: 978-94-6522-593-7. DOI: 10.4233/uuid:73be214e-ba16-4110-9ce4-4884310a539c.

[47] Bernd Rieger and Sjoerd Stallinga. “The Lateral and Axial Localization Uncertainty in Super-Resolution Light Microscopy”. In: *ChemPhysChem* 15.4 (2014), pp. 664–670.

[48] Sudhakar Prasad. “Rotating point spread function via pupil-phase engineering”. In: *Optics Letters* 38.4 (2013), pp. 585–587.

[49] S Jia, J Vaughan, and X. Zhuang. “Isotropic three-dimensional super-resolution imaging with a self-bending point spread function”. In: *Nature Photonics* 8 (2014).

[50] Matthew D Lew et al. “Corkscrew point spread function for far-field three-dimensional nanoscale localization of pointlike objects”. In: *Optics Letters* 36.2 (2011), pp. 202–204.

[51] Manuel F Juette et al. “Three-dimensional sub-100 nm resolution fluorescence microscopy of thick samples”. In: *Nature Methods* 5.6 (2008), pp. 527–529.

[52] Gleb Shtengel et al. “Interferometric fluorescent super-resolution microscopy resolves 3D cellular ultrastructure”. In: *Proceedings of the National Academy of Sciences* 106.9 (2009), pp. 3125–3130.

[53] Guanshi Wang et al. “Single-molecule real-time 3D imaging of the transcription cycle by modulation interferometry”. In: *Cell* 167.7 (2016), pp. 1839–1852.

[54] Daniel Aquino et al. “Two-color nanoscopy of three-dimensional volumes by 4Pi detection of stochastically switched fluorophores”. In: *Nature Methods* 8.4 (2011), pp. 353–359.

[55] Carlas S Smith et al. “Probability-based particle detection that enables threshold-free and robust in vivo single-molecule tracking”. In: *Molecular Biology of the Cell* 26.22 (2015), pp. 4057–4062.

[56] Leonhard Möckl et al. “Accurate and rapid background estimation in single-molecule localization microscopy using the deep neural network BGnet”. In: *Proceedings of the National Academy of Sciences* 117.1 (2020), pp. 60–67.

[57] Jelmer Cnossen et al. “Drift correction in localization microscopy using entropy minimization”. In: *Optics Express* 29.18 (2021), pp. 27961–27974.

[58] Mickaël Lelek et al. “Single-molecule localization microscopy”. In: *Nature Reviews Methods Primers* 1.1 (2021), p. 39.

[59] Fang Huang et al. “Simultaneous multiple-emitter fitting for single molecule super-resolution imaging”. In: *Biomedical Optics Express* 2.5 (2011), pp. 1377–1393.

[60] Artur Speiser et al. “Deep learning enables fast and dense single-molecule localization with high accuracy”. In: *Nature Methods* 18.9 (2021), pp. 1082–1090.

[61] Steven M. Kay. *Fundamentals of Statistical Signal Processing*. Englewood Cliffs, N.J.: Prentice-Hall PTR, 1993.

[62] Miroslav Hekrdla et al. "Optimized molecule detection in localization microscopy with selected false positive probability". In: *Nature Communications* 16 (2025), p. 601. DOI: 10.1038/s41467-025-55952-5.

[63] Francisco Balzarotti et al. "Nanometer resolution imaging and tracking of fluorescent molecules with minimal photon fluxes". In: *Science* 355.6325 (2017), pp. 606–612.

[64] Dylan Kalisvaart et al. "Precision in iterative modulation enhanced single-molecule localization microscopy". In: *Biophysical Journal* 121.12 (2022), pp. 2279–2289.

[65] Klaus C Gwosch et al. "MINFLUX nanoscopy delivers 3D multicolor nanometer resolution in cells". In: *Nature Methods* 17.2 (2020), pp. 217–224.

[66] Abhishek Sau et al. "Overlapping nuclear import and export paths unveiled by two-colour MINFLUX". In: *Nature* 640.8059 (2025), pp. 821–827. DOI: 10.1038/s41586-025-08738-0.

[67] Jelmer Cnossen et al. "Localization microscopy at doubled precision with patterned illumination". In: *Nature Methods* 17.1 (2020), pp. 59–63.

[68] Lusheng Gu et al. "Molecular-scale axial localization by repetitive optical selective exposure". In: *Nature Methods* 18.4 (2021), pp. 369–373.

[69] Pierre Jouchet et al. "Nanometric axial localization of single fluorescent molecules with modulated excitation". In: *Nature Photonics* 15.4 (2021), pp. 297–304.

[70] Qian Wang et al. "4Pi-SIMFLUX: 4Pi single-molecule localization microscopy with structured illumination". In: *Nature Methods* (2025), pp. 1–8.

[71] Francis Crick. "Central dogma of molecular biology". In: *Nature* 227.5258 (1970), pp. 561–563.

[72] Stefan Petrovic et al. "Architecture of the linker-scaffold in the nuclear pore". In: *Science* 376 (2022), eabm9798.

[73] Javier Fernandez-Martinez and Michael P Rout. "One ring to rule them all? Structural and functional diversity in the nuclear pore complex". In: *Trends in Biochemical Sciences* 46.7 (2021), pp. 595–607.

[74] Anthony P Schuller et al. "The cellular environment shapes the nuclear pore complex architecture". In: *Nature* 598.7882 (2021), pp. 667–671.

[75] Daniel H Lin et al. "Structural and functional analysis of mRNA export regulation by the nuclear pore complex". In: *Nature Communications* 9.1 (2018), p. 2319.

[76] Sami Hocine, Robert H Singer, and David Grünwald. "RNA processing and export". In: *Cold Spring Harbor Perspectives in Biology* 2.12 (2010), a000752.

[77] Vihandha O Wickramasinghe and Ronald A Laskey. "Control of mammalian gene expression by selective mRNA export". In: *Nature Reviews Molecular Cell Biology* 16.7 (2015), pp. 431–442.

[78] Shintaro Aibara et al. “The principal mRNA nuclear export factor NXF1: NXT1 forms a symmetric binding platform that facilitates export of retroviral CTE-RNA”. In: *Nucleic Acids Research* 43.3 (2015), pp. 1883–1893.

[79] Andrew W Folkmann et al. “Gle1 functions during mRNA export in an oligomeric complex that is altered in human disease”. In: *Cell* 155.3 (2013), pp. 582–593.

[80] Pau Pascual-Garcia and Maya Capelson. “The nuclear pore complex and the genome: organizing and regulatory principles”. In: *Current Opinion in Genetics & Development* 67 (2021), pp. 142–150.

[81] Caterina Strambio-De-Castillia, Mario Niepel, and Michael P Rout. “The nuclear pore complex: bridging nuclear transport and gene regulation”. In: *Nature Reviews Molecular Cell Biology* 11.7 (2010), pp. 490–501.

[82] Arkaitz Ibarra and Martin W. Hetzer. “Nuclear pore proteins and the control of genome functions”. In: *Genes & Development* 29 (2015), pp. 337–349. DOI: 10.1101/gad.256495.114.

[83] Jessica A Hurt and Pamela A Silver. “mRNA nuclear export and human disease”. In: *Disease Models & Mechanisms* 1.2-3 (2008), pp. 103–108.

[84] J C Grima et al. “Mutant huntingtin disrupts the nuclear pore complex”. In: *Neuron* 94 (2017), 93–107.e6.

[85] Johanna Franziska Seidler and Katja Sträßer. “Understanding nuclear mRNA export: Survival under stress”. In: *Molecular Cell* 84.19 (2024), pp. 3681–3691.

[86] Edouard Bertrand et al. “Localization of ASH1 mRNA particles in living yeast”. In: *Molecular Cell* 2.4 (1998), pp. 437–445.

[87] Esther Braselmann et al. “Illuminating RNA biology: tools for imaging RNA in live mammalian cells”. In: *Cell Chemical Biology* 27.8 (2020), pp. 891–903.

[88] Jeffrey A. Chao et al. “Structural basis for the coevolution of a viral RNA–protein complex”. In: *Nature Structural & Molecular Biology* 15 (2008), pp. 103–105.

[89] Weihan Li et al. “An improved imaging system that corrects MS2-induced RNA destabilization”. In: *Nature Methods* 19 (2022), pp. 1558–1562.

[90] David Grünwald and Robert H Singer. “In vivo imaging of labelled endogenous β-actin mRNA during nucleocytoplasmic transport”. In: *Nature* 467.7315 (2010), pp. 604–607.

[91] Asaf Ashkenazy-Titelman et al. “RNA export through the nuclear pore complex is directional”. In: *Nature Communications* 13.1 (2022), p. 5881.

[92] Rakefet Ben-Yishay et al. “Imaging within single NPCs reveals NXF1’s role in mRNA export on the cytoplasmic side of the pore”. In: *Journal of Cell Biology* 218.9 (2019), pp. 2962–2981.

[93] Tim Kaminski, Jan Peter Siebrasse, and Ulrich Kubitscheck. “A single molecule view on Dbp5 and mRNA at the nuclear pore”. In: *Nucleus* 4.1 (2013), pp. 8–13.

[94] Carlas Smith et al. “In vivo single-particle imaging of nuclear mRNA export in budding yeast demonstrates an essential role for Mex67p”. In: *Journal of Cell Biology* 211.6 (2015), pp. 1121–1130.

[95] Mark-Albert Saroufim et al. “The nuclear basket mediates perinuclear mRNA scanning in budding yeast”. In: *Journal of Cell Biology* 211.6 (2015), pp. 1131–1140.

[96] Azra Lari et al. “Live-Cell Imaging of mRNP–NPC Interactions in Budding Yeast”. In: *Imaging Gene Expression: Methods and Protocols*. Springer, 2019, pp. 131–150.

[97] Bryan R Cullen. “Nuclear RNA export”. In: *Journal of Cell Science* 116.4 (2003), pp. 587–597.

[98] Jun Katahira et al. “The Mex67p-mediated nuclear mRNA export pathway is conserved from yeast to human”. In: *The EMBO Journal* 18.9 (1999), pp. 2593–2609.

[99] Robin Reed and Ed Hurt. “A conserved mRNA export machinery coupled to pre-mRNA splicing”. In: *Cell* 108.4 (2002), pp. 523–531.

[100] Peter M Carlton et al. “Fast live simultaneous multiwavelength four-dimensional optical microscopy”. In: *Proceedings of the National Academy of Sciences* 107.37 (2010), pp. 16016–16022.

[101] Michael Wagner et al. “Light dose is a limiting factor to maintain cell viability in fluorescence microscopy and single molecule detection”. In: *International Journal of Molecular Sciences* 11.3 (2010), pp. 956–966.

[102] Kalina L Tosheva et al. “Between life and death: strategies to reduce phototoxicity in super-resolution microscopy”. In: *Journal of Physics D: Applied Physics* 53.16 (2020), p. 163001.

[103] Tyler Boothe et al. “A tunable refractive index matching medium for live imaging cells, tissues and model organisms”. In: *eLife* 6 (2017), e27240.

[104] Tamara Pringsheim et al. “The incidence and prevalence of Huntington’s disease: a systematic review and meta-analysis”. In: *Movement Disorders* 27.9 (2012), pp. 1083–1091.

[105] James F Gusella, Jong-Min Lee, and Marcy E MacDonald. “Huntington’s disease: nearly four decades of human molecular genetics”. In: *Human Molecular Genetics* 30.R2 (2021), R254–R263.

[106] K Sathasivam et al. “Aberrant splicing of HTT generates the pathogenic exon 1 protein in Huntington disease”. In: *Proceedings of the National Academy of Sciences* 110 (2013), pp. 2366–2370.

[107] Andreas Neueder et al. “The pathogenic exon 1 HTT protein is produced by incomplete splicing in Huntington’s disease patients”. In: *Scientific Reports* 7.1 (2017), p. 1307.

[108] X Sun et al. “Nuclear retention of full-length HTT RNA is mediated by splicing factors MBNL1 and U2AF65”. In: *Scientific Reports* 5 (2015), p. 12521.

[109] A Hautke et al. “CAG-repeat RNA hairpin folding and recruitment to nuclear speckles with a pivotal role of ATP as a cosolute”. In: *Journal of the American Chemical Society* 145 (2023), pp. 9571–9583.

[110] K Yum, E T Wang, and A Kalsotra. “Myotonic Dystrophy: Disease Repeat Range, Penetrance, Age of Onset, and Relationship Between Repeat Size and Phenotypes”. In: *Current Opinion in Genetics & Development* 44 (2017), pp. 30–37.

[111] M DeJesus-Hernandez et al. “Expanded GGGGCC hexanucleotide repeat in noncoding region of C9ORF72 causes chromosome 9p-linked FTD and ALS”. In: *Neuron* 72 (2011), pp. 245–256.

[112] Veronique V Belzil, Tania F Gendron, and Leonard Petrucelli. “RNA-mediated toxicity in neurodegenerative disease”. In: *Molecular and Cellular Neuroscience* 56 (2013), pp. 406–419.

[113] Yuzo Fujino and Yoshitaka Nagai. “The molecular pathogenesis of repeat expansion diseases”. In: *Biochemical Society Transactions* 50.1 (2022), pp. 119–134.

[114] R Nalavade et al. “Mechanisms of RNA-induced toxicity in CAG repeat disorders”. In: *Cell Death & Disease* 4.8 (2013), e752–e752.

[115] Robert E Handsaker et al. “Long somatic DNA-repeat expansion drives neurodegeneration in Huntington disease”. In: *bioRxiv* (2024), pp. 2024–05.

[116] Sarah Allen et al. “mRNA nuclear clustering leads to a difference in mutant huntingtin mRNA and protein silencing by siRNAs in vivo”. In: *Nucleic Acid Therapeutics* 34.4 (2024), pp. 164–172.

[117] Osama Al-Dalahmah et al. “Single-nucleus RNA-seq identifies Huntington disease astrocyte states”. In: *Acta Neuropathologica Communications* 8 (2020), pp. 1–21.

[118] Valentine Svensson, Roser Vento-Tormo, and Sarah A Teichmann. “Exponential scaling of single-cell RNA-seq in the past decade”. In: *Nature Protocols* 13.4 (2018), pp. 599–604.

[119] Cameron G Williams et al. “An introduction to spatial transcriptomics for biomedical research”. In: *Genome Medicine* 14.1 (2022), p. 68.

[120] Kok Hao Chen et al. “Spatially resolved, highly multiplexed RNA profiling in single cells”. In: *Science* 348.6233 (2015), aaa6090.

[121] Arjun Raj et al. “Imaging individual mRNA molecules using multiple singly labeled probes”. In: *Nature Methods* 5.10 (2008), pp. 877–879.

[122] F Wang et al. “RNAscope: a novel in situ RNA analysis platform for formalin-fixed, paraffin-embedded tissues”. In: *The Journal of Molecular Diagnostics* 14 (2012), pp. 22–29.

[123] Advanced Cell Diagnostics. *RNAscope Frequently Asked Questions*. 2023. URL: https://acdbio.com/technical-support/solutions/faq.

2

ZIMFLUX: SINGLE MOLECULE LOCALIZATION MICROSCOPY WITH PATTERNED ILLUMINATION IN 3D

Pieter VAN VELDE, Bernd RIEGER, Taylor HINSDALE, Jelmer CNOSSEN, Daniel FAN, Shih-Te HUNG, David GRUNWALD, Carlas SMITH

Three dimensional modulation-enhanced single-molecule localization techniques, such as ModLoc, offer advancements in axial localization precision across the entire field of view and axial capture range, by applying phase shifting to the illumination pattern. However, this improvement is limited by the pitch of the illumination pattern that can be used and requires registration between separate regions of the camera. To overcome these limitations, we present ZIMFLUX, a method that combines astigmatic point-spread-function (PSF) engineering with a structured illumination pattern in all three spatial dimensions. In order to achieve this we address challenges such as optical aberrations, refractive index mismatch, Supercritical Angle Fluorescence (SAF), and imaging at varying depths within a sample, by implementing a vectorial PSF model. In scenarios involving refractive index mismatch between the sample and immersion medium, the astigmatic PSF loses its ellipticity at greater imaging depths, leading to a deterioration in axial localization precision. In contrast, our simulations demonstrate that ZIMFLUX maintains high axial localization precision even when imaging deeper into the sample. Experimental results show unbiased localization of 3D 80 nm *DNA-origami nanostructures in SAF conditions with a 1.5-fold improvement in axial localization precision when comparing ZIMFLUX to conventional SMLM methods that rely solely on astigmatic PSF engineering.*

This chapter has been published in Optics Express **31**(25), 42701–42722 (2023) [1].

2.1. INTRODUCTION

Single-molecule localization microscopy (SMLM) has emerged as a powerful imaging technique, providing nanoscale resolution for visualizing subcellular structures [2, 3, 4]. SMLM encompasses all microscopic techniques that achieve super-resolution by isolating individual emitters and fitting their images using the point spread function (PSF). This technique has revolutionized our understanding of cellular structures and facilitated the discovery of previously unobserved subcellular features [5, 6, 7]. However, the inherent limitations of light microscopy and traditional SMLM constrain the resolving power in the axial dimension, hindering comprehensive visualization of 3D structures.

To overcome these limitations, various techniques have been developed to manipulate the PSF and enhance axial resolution in 3D SMLM. These methods include the double-helix PSF [8, 9], TetraPod [10], self-bending PSF [11], phase ramp PSF [12], corkscrew PSF [13], saddle-point PSF [10], and the commonly used approach involving a cylindrical lens for astigmatic z-encoding. Each of these techniques has been applied in 3D SMLM [14, 15, 16]. Other techniques, such as photoactivated localization microscopy (iPALM) [17, 18] and 4Pi single-molecule switching nanoscopy [19, 20], offer superior resolution based on the coherence of a single emitter's fluorescence but are challenging to construct, align, and maintain. Another approach to improve the axial resolution is Supercritical Angle Fluorescence (SAF), which, however, is limited to emitters near the coverslip [21, 22].

Alternatively, modulation-enhanced single-molecule localization can be employed to enhance precision in SMLM [23]. For example, MINFLUX uses a scanning doughnut illumination spot [24], which has been extended to 3D imaging [25]. However, MINFLUX's limitation of localizing one molecule at a time hinders throughput. To address this drawback, sinusoidal patterns are used to obtain enhancement over the entire FOV simultaneously in 2D [26, 27] and 3D [28, 29]. For 3D imaging, ModLoc offers a significant advantage by employing a single objective, thereby reducing the complexity of the optical setup and sample mounting. On the other hand, ROSE-Z requires two objectives to create the illumination pattern, increasing the overall complexity, but enabling a smaller pattern pitch in the axial direction, and thus a better localization precision.

As an alternative, we introduce ZIMFLUX, a method that combines an astigmatic PSF with a sinusoidal illumination pattern, while employing a single objective. Unlike ModLoc, ZIMFLUX employs a 3D sinusoidal illumination pattern and captures different phases on a single camera region, resulting in an increased field of view (FOV) size and eliminating the need for registration. The inclusion of an astigmatic PSF alongside the sinusoidal illumination pattern in ZIMFLUX provides the ability to obtain a 3D estimate of the position without the use of the illumination patterns. This circumvents the problem of phase wrapping and enables the use of smaller pitches. We use 480 nm versus 1 μm of ModLoc, leading to an improved axial localization precision with a factor of approximately 1.5. Moreover, astigmatism enables the estimation of the applied illumination pattern directly from the acquired image data itself, avoiding the need for a calibration sample and mitigating biased localization due to sample-specific factors, such as refractive index mismatches, non-flat coverslips (in custom samples), and misalignments over time in the optical setup.

The optical layout ZIMFLUX utilizes a Digital Micromirror Device (DMD) to generate two

excitation beams that intersect at the sample plane, resulting in the interference pattern (Fig. 2.1a). Rapidly shifting the pattern on the DMD causes the illumination pattern to move, leading to variations in the emitted photon count from the fluorophore. To achieve more accurate position estimations, we employ a vectorial PSF model [30, 31, 32], effectively handling, aberrations, depth varying PSFs, and SAF conditions. The PSF and illumination pattern information are then integrated into a Maximum Likelihood Estimation (MLE) to achieve superior axial precision in emitter localization (Fig. 2.1b).
To summarize, in this paper we introduce ZIMFLUX, an advancement in modulation-enhanced single-molecule localization microscopy that alleviates some of the current limitations of existing methods. By integrating astigmatic PSF engineering with sinusoidal illumination, ZIMFLUX achieves enhanced axial resolution, expanding its potential applications in 3D imaging of nanostructures and biological samples.

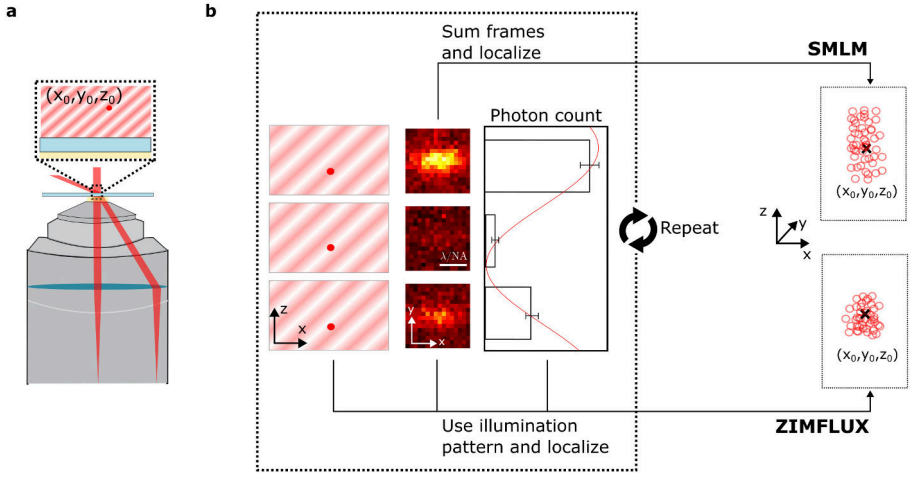


Figure 2.1: **a**, An interference pattern is generated by two beams entering the sample, illuminating the emitter located at (x_0, y_0, z_0). **b**, ZIMFLUX operates by recording three images with shifted patterns, and using the information of the illumination pattern, PSF and photon count for a maximum likelihood estimation. This method results in improved axial localization precision compared to conventional Single Molecule Localization Microscopy (SMLM) using an astigmatic PSF, where only the PSF obtained from the sum of the frames is used for localization of the emitter.

2.2. THEORY

2.2.1. IMAGING MODEL

The imaging model combines the illumination patterns and the PSF model to describe the expected photon count of a pixel, due to the presence of an emitter. The imaging model is given by

$$\mu_j^{lk} = NP\big(\phi_{lk}(\vec{r}_0)\big)H(\vec{r}_j - \vec{r}_0) + \frac{b}{LK} \tag{2.1}$$

where N is the photon count of the emitter, b represents the background photon count and $\vec{r}_0$ and $\vec{r}_j$ are the center positional vectors of the emitter and pixel j, respectively. H

is the PSF model, and P is the illumination pattern. $l = 1, 2, \ldots, L$ and $k = 1, 2, \ldots, K$ denote the indices representing the direction and phase step of the illumination pattern. $P(\phi_{lk}(\vec{r}_0))$ is the relative intensity of the phase ϕ_{lk} at position $\vec{r}_0$. For a more comprehensive understanding of the subject, the following sections will provide detailed descriptions of the illumination and PSF models.

ILLUMINATION MODEL

The sample undergoes excitation with a three-dimensional sinusoidal patterned electric field $\vec{E}_\mathrm{i}$ characterized by a lateral pitch of p_lat and an axial pitch of p_ax, given by

$$p_\mathrm{lat} = \frac{\lambda_0}{|n_0(\sin\alpha_1 + \sin\beta_1)|}, \tag{2.2}$$

$$p_\mathrm{ax} = \frac{\lambda_0}{|n_0(\cos\alpha_1 - \cos\beta_1)|}. \tag{2.3}$$

where λ_0 is the wavelength of the monochromatic light source, n_0 is the refractive index of the mounting medium, α_1 and β_1 are the angles of the two excitation beams $\vec{E}_1$ and $\vec{E}_2$, with respect to the optical axis in the mounting medium, as shown in Fig. 2.2. As shown in Supplementary Note 1, the intensity of the sinusoidal interfering electric field ($\vec{E}_i$) pattern can be modeled as

$$P(\phi_{lk}(\vec{r})) = \eta_{lk}(1 + m_{lk}\cos(\phi_{lk}(\vec{r}))), \tag{2.4}$$

where η_{lk} is the relative intensity per patterns, satisfying $\sum_{lk}^{LK}\eta_{lk} = 1$, m_{lk} is the modulation depth, and ϕ_{lk} is the phase at location $\vec{r}$, which is defined as

$$\phi_{lk}(\vec{r}) = 2\pi\vec{q}_l\cdot\vec{r} - \psi_{lk}, \tag{2.5}$$

here ψ_{lk} is the phase offset and $\vec{q}_l$ is the spatial frequency vector defined by

$$\vec{q}_l = \{\frac{\cos(\gamma_l)}{p_\mathrm{lat}}, \frac{\sin(\gamma_l)}{p_\mathrm{lat}}, \frac{1}{p_\mathrm{ax}}\}. \tag{2.6}$$

where γ_l is the azimuthal angle in the x, y plane.

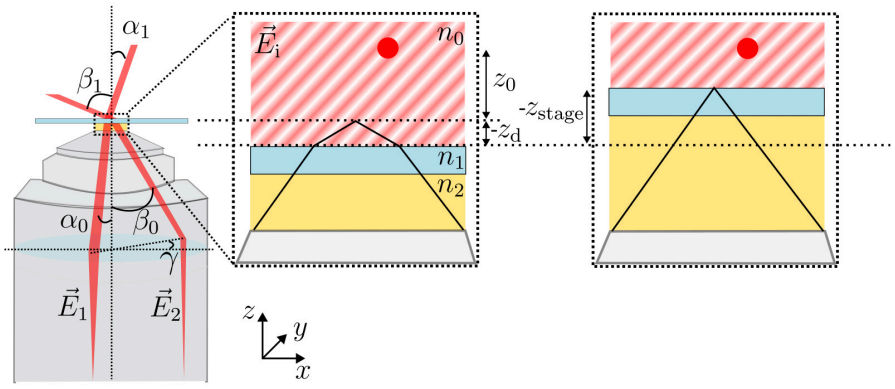


Figure 2.2: The figure illustrates the interference pattern $\vec{E}_i$ that is formed by two plane waves $\vec{E}_1$ and $\vec{E}_2$ originating from the objective, with incidence angles of α_0 and β_0, and with an azimuthal angle of γ. The light passes through the immersion media and cover glass, with refractive indices of n_2 and n_1. Due to the refractive index mismatch, the angles of the beams change to α_1 and β_1. The fluorophores are embedded in a medium with a refractive index of n_0. The imaging depth z_d corresponds to the distance from the cover glass to the focal plane, while z_0 represents the emitter's distance from the focal plane. z_stage is defined as the distance the stage has moved from the point at which the top of the cover glass is aligned with the focal plane.

Following a similar approach as described in previous research [27], we phase-shift the pattern equidistantly in $k = 1, 2, \ldots, K$ illuminations for various orientations $l = 1, 2, \ldots, L$, adhering to the following condition:

$$\sum_{l=1}^{L}\sum_{k=1}^{K} P(\phi_{lk}(\vec{r})) = 1. \tag{2.7}$$

POINT SPREAD FUNCTION MODEL

The freely-rotating dipole vectorial PSF model is employed in accordance with previous studies [30, 31, 33, 34, 32]. The emitted light from the dipole (E_dipole) propagates through the media with different refractive indices, which are the mounting media (n_0), cover-glass (n_1) and immersion medium (n_2). For an oil objective, the refractive index of the immersion oil and the coverglass are similar, hence we assume that $n_1 = n_2$. The objective collects the light and transfers it to the pupil plane (E_pupil). Subsequently, the electric field is focused on the detector by the tube lens. The electric field component $p = x, y$ in the pupil plane is proportional to the emission dipole component $q = x, y, z$ as follows:

$$E_{\mathrm{pupil},pq}(W, \vec{\rho}, z_\mathrm{d}, z_\mathrm{stage}) = A(\vec{\rho}) q_{pq}(\vec{\rho}) \exp\left[i W(\vec{\rho}) + i\left(z_\mathrm{d} k_{\mathrm{z},0}(\vec{\rho}) - z_\mathrm{stage} k_{\mathrm{z},2}(\vec{\rho}) \right) \right], \tag{2.8}$$

where $\vec{\rho}$ are the normalized pupil coordinates, $A(\vec{\rho})$ is the amplitude, including the well-known aplanatic correction factor [35, 36], $q_{pq}(\vec{\rho})$ are polarization vector components defined elsewhere [30], and z_d is the imaging depth, which is the distance between the focal plane and the coverglass, and z_stage is the corresponding position of the stage, and the z-component of the wave-vector in the i-th medium $k_{\mathrm{z},i}$ is

$$k_{\mathrm{z},i}(\vec{\rho}) = \frac{2\pi}{\lambda}\sqrt{n_i^2 - NA^2 ||\vec{\rho}||_2^2}, \tag{2.9}$$

with n_i, λ, and NA as the refractive index, wavelength, and numerical aperture respectively.

Finally, to calculate the incoherent PSF from the freely-rotating dipole, the six Fourier transforms of the electric field components in the pupil are quadratically added

$$\begin{aligned} H(\vec{r}_j - \vec{r}_0) = \frac{N}{3 w_\mathrm{n}} \sum_{p=x,y} \sum_{q=x,y,z} \Bigg| \int_{\xi_j} \int_{|\vec{\rho}|<1} & E_{\mathrm{pupil},pq}(W, \vec{\rho}, z_\mathrm{d}, z_\mathrm{stage}) \\ & \times \exp\left[-i \vec{k}(\vec{\rho}) \cdot (\vec{r}_j - \vec{r}_0) \right] d^2\rho d^2\xi_j \Bigg|^2, \end{aligned} \tag{2.10}$$

where ξ_j is the j-th pixel, $\vec{k}(\vec{\rho}) = \left(k_\mathrm{x}(\vec{\rho}), k_\mathrm{y}(\vec{\rho}), k_{\mathrm{z},0}(\vec{\rho})\right)$, N is the photon count of the signal, w_n is a normalizing factor defined elsewhere [37]. The lateral wavevectors are de-

fined as $k_x(\vec{\rho}) = 2\pi NA\rho_x/\lambda$ and $k_y(\vec{\rho}) = 2\pi NA\rho_y/\lambda$. The aberration function $W(\vec{\rho})$ is expressed as a sum of the Zernike polynomials.

2.2.2. SUPERCRITICAL ANGLE FLUORESCENCE

When the dipole is positioned close to the cover glass, the emitted evanescent wave will extend into the cover glass and becomes a propagating wave that can be captured by the objective. This phenomenon is referred to as supercritical angle fluorescence (SAF) and only occurs if $NA > n_0$ and $n_2 > n_0$ [38, 39]. SAF influences the PSF model and increases the effective NA. For pupil coordinates that satisfy $||\vec{\rho}||_2 > n_0/NA$, Eq. 2.9 and Eq. 2.8 become

$$k_{z,0}(\vec{\rho}) = \frac{2\pi}{\lambda} i\sqrt{NA^2||\vec{\rho}||_2^2 - n_0^2}, \tag{2.11}$$

$$E_{\text{pupil},pq}(W,\vec{\rho},z_d,z_{\text{stage}}) = A(\vec{\rho})q_{pq}(\vec{\rho})\exp\left[-\delta\frac{z_d}{\lambda} + i\left(W(\vec{\rho}) - z_{\text{stage}}k_{z,2}(\vec{\rho})\right)\right], \tag{2.12}$$

where $\delta = 2\pi\sqrt{NA^2||\vec{\rho}||_2^2 - n_0^2}$ is the attenuation constant. The SAF term decays exponentially with z_d/λ, indicating that the effect will decay to zero with $z_d \gg \lambda$.

2.2.3. MAXIMUM LIKELIHOOD ESTIMATION FOR ZIMFLUX

A maximum likelihood estimation is used to fit the parameters of the imaging model [40]. The parameters to be estimated are $\theta = \{x_0, y_0, z_0, N, b\}$. Other parameters that define the imaging model, such as z_d, z_{stage}, and W, are assumed to be known and measured a priori through calibration experiments (for details see section 2.3). The measured photon counts by state-of-the-art EMCCD and sCMOS cameras can accurately be modeled as realizations of a Poisson process [40, 41, 42]. The log-likelihood for a Poisson process is computed as

$$\log\mathscr{L} = \sum_{l=1}^{L}\sum_{k=1}^{K}\sum_{j=1}^{J}\left[n_j^{lk}\log(\mu_j^{lk}) - \mu_j^{lk}\right], \tag{2.13}$$

where we recall that K and L are the different pattern shifts and orientations respectively, J is the total amount of pixels in the ROI and n_j^{lk} is the photon count for pixel j. The maximum likelihood estimate is computed using the Levenberg-Marquardt algorithm, with the log-likelihood ($\log\mathscr{L}$) and its derivatives guiding the optimization process

$$\frac{\partial\log\mathscr{L}}{\partial\theta_i} = \sum_{l=1}^{L}\sum_{k=1}^{K}\sum_{j=1}^{J}\frac{n_j^{lk} - \mu_j^{lk}}{\mu_j^{lk}}\frac{\partial\mu_j^{lk}}{\partial\theta_i}. \tag{2.14}$$

The derivatives of μ_j^{lk} with respect to the relevant parameters are

$$\frac{\partial \mu_j^{lk}}{\partial \vec{r}_0} = NP(\phi_{lk}(\vec{r}_0))\frac{\partial H(\vec{r}_j - \vec{r}_0)}{\partial \vec{r}_0} + NH(\vec{r}_j - \vec{r}_0)\frac{\partial P(\phi_{lk}(\vec{r}_0))}{\partial \vec{r}_0}, \tag{2.15}$$

$$\frac{\partial \mu_j^{lk}}{\partial N} = P(\phi_{lk}(\vec{r}_0))H(\vec{r}_j - \vec{r}_0), \tag{2.16}$$

$$\frac{\partial \mu_j^{lk}}{\partial b} = \frac{1}{LK}. \tag{2.17}$$

where $\vec{r}_0 = \{x_0, y_0, z_0\}$ is the position of the emitter and the lateral component of $\vec{r}_j$ is the center position of pixel j, while the axial component is the focal plane. The derivative of the illumination field is given by

$$\frac{\partial P(\phi_{lk}(\vec{r}_0))}{\partial \vec{r}_0} = -2\pi\eta_{lk} m_{lk} \sin(\phi_{lk}(\vec{r}_0)), \tag{2.18}$$

The positional derivatives of the PSF are computed as follows [43]

$$\frac{\partial H(\vec{r}_j - \vec{r}_0)}{\partial \vec{r}_0} = \frac{N}{3w_\mathrm{n}} \sum_{p=x,y} \sum_{q=x,y,z} \frac{\partial}{\partial \vec{r}_0} U_{pq}(\vec{r}_j - \vec{r}_0)\, U_{pq}(\vec{r}_j - \vec{r}_0) \tag{2.19}$$

$$= \frac{2N}{3w_\mathrm{n}} \sum_{p=x,y} \sum_{q=x,y,z} \mathrm{Re}\left\{ U_{pq}(\vec{r}_j - \vec{r}_0) \frac{\partial U_{pq}(\vec{r}_j - \vec{r}_0)}{\partial \vec{r}_0} \right\}, \tag{2.20}$$

where we have introduced the following shorthand notation

$$U_{pq}(\vec{r}_j - \vec{r}_0) = \int_{\xi_j} \int_{|\vec{\rho}|<1} E_{\mathrm{pupil},pq}(W, \vec{\rho}, z_\mathrm{d}, z_\mathrm{stage}) \exp\left[-i\vec{k}(\vec{\rho}) \cdot (\vec{r}_j - \vec{r}_0) \right] d^2\rho\, d^2\xi_j, \tag{2.21}$$

so that the positional derivatives are

$$\begin{aligned} \frac{\partial U_{pq}(\vec{r}_j - \vec{r}_0)}{\partial x} = -i \int_{\xi_j} \int_{|\vec{\rho}|<1} & E_{\mathrm{pupil},pq}(W, \vec{\rho}, z_\mathrm{d}, z_\mathrm{stage}) k_\mathrm{x}(\vec{\rho}) \\ & \times \exp\left[-i\vec{k}(\vec{\rho}) \cdot (\vec{r}_j - \vec{r}_0) \right] d^2\rho\, d^2\xi_j, \end{aligned} \tag{2.22}$$

in which x can be interchanged with y and z by substituting k_y and $k_{\mathrm{z},0}$ for k_x, respectively. The Fisher matrix can be calculated as follows:

$$F_{rs} = \sum_{l=1}^{L} \sum_{k=1}^{K} \sum_{j=1}^{J} \frac{1}{\mu_j^{lk}} \frac{\partial \mu_j^{lk}}{\partial \theta_r} \frac{\partial \mu_j^{lk}}{\partial \theta_s}. \tag{2.23}$$

The Cramér-Rao Lower Bound (CRLB) is the inverse of the Fisher matrix.

MAXIMUM LIKELIHOOD ESTIMATION USING ONLY THE ILLUMINATION PATTERN OR PSF

The position of the emitter can also be estimated using only the illumination pattern or only the PSF model. This is used to in-situ refine the model for the illumination pattern

(see section 2.3.5). To obtain an imaging model that describes the data but only relies on the illumination pattern, we sum over all the pixels in the ROI as

$$\mu^{lk} = \sum_{j=1}^{J} NP\big(\phi_{lk}(\vec{r}_{\text{ill},0})\big)H(\vec{r}_j - \vec{r}_{\text{ill},0}) + \frac{b}{LK}, \tag{2.24}$$

$$\mu^{lk} = NP(\phi_{lk}(\vec{r}_{\text{ill},0})) + \frac{b}{LK}J. \tag{2.25}$$

where J is the total amount of pixels in the ROI and $\vec{r}_{\text{ill},0}$ the emitter position computed based on the illumination pattern. In analogy with Eq. 2.13, the log-likelihood is

$$\log \mathscr{L} = \sum_{l=1}^{L}\sum_{k=1}^{K}\left[n^{lk}\log(\mu^{lk}) - \mu^{lk}\right]. \tag{2.26}$$

Similarly, to obtain an imaging model that only relies on the PSF we sum over all the illumination patterns

$$\mu_j = \sum_{l=1}^{L}\sum_{k=1}^{K} NP\big(\phi_{lk}(\vec{r}_{\text{psf},0})\big)H(\vec{r}_j - \vec{r}_{\text{psf},0}) + \frac{b}{LK}, \tag{2.27}$$

$$\mu_j = NH(\vec{r}_j - \vec{r}_{\text{psf},0}) + b, \tag{2.28}$$

where $\vec{r}_{\text{psf},0}$ is the emitter position computed based on the PSF. The maximum likelihood and CRLB can be computed analogous to the previous section.

2.3. EXPERIMENTAL SETUP AND METHODS

2.3.1. EXPERIMENTAL SETUP

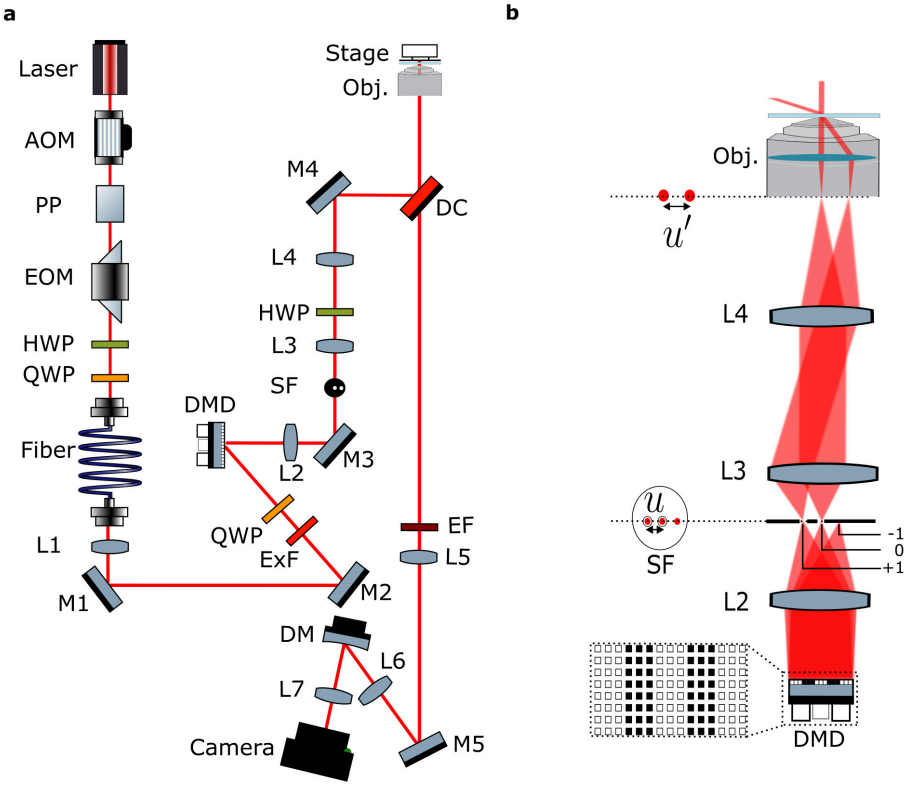


Figure 2.3: **a**, A schematic of the custom-built ZIMFLUX setup. Additional information is available in the main text. **b**, A simplified schematic of the excitation path. Incoming laser light is diffracted by a Digital Micromirror Device (DMD) on which a binary block wave is projected. The spatial filter (SF) permits only the zeroth and one first-order beam, with a spacing of u, to pass through. The spacing is then magnified to u' at the back focal plane, resulting in non-parallel beams that generate an interference pattern at the overlap in the sample plane. All abbreviations used in the figure are defined in the main text.

A customized setup was constructed to generate the interference pattern, illuminate, and image the sample, enabling ZIMFLUX localization (see Fig. 2.3a). The setup utilizes a 642 nm diode laser (MPB Communications, F-04306-107) to produce a monochromatic beam. The beam is modulated using an Acousto-Optic Modulator (AOM, G&H, 3080-125) to adjust the power and is set at 25% of the maximum power (250 mW), resulting in a total laser power of 3 mW at the sample plane over an area with a diameter of approximately 50 μm. Assuming a Gaussian laser profile, this translates to an energy density of ~ 300 W/cm^2 over the FOV (16.4 μm x 16.4 μm). A Glan-Taylor Polarization Prism (PP, Thorlabs, GT10-A) polarizes the light, and a voltage Electro-Optic Light Modulator (EOM, Leysop, EM400K) regulates the polarization angle. A Half Wave Plate (HWP, Thorlabs, WPH05M-633) and Quarter Wave Plate (QWP, Thorlabs, WPQ05M-633) are used

to align the polarization and correct for elliptical polarization induced by the reflective elements further in the setup. A polarization-maintaining optical fiber (Thorlabs, P1-488PM-FC-1) and a 0.13 NA objective (L1, Olympus, UplanFL N, 4x/0.13) collimate the beam.

Two mirrors (M1/M2, Thorlabs, BB1-E02) direct the beam through an excitation filter (ExF, Chroma, ET640/20m), and another quarter wave plate onto the Digital Micromirror Device (DMD, Texas Instruments, DLP7000BFLP). The DMD is controlled by a high-speed DLP subsystem (VIALUX GmbH, V4100 0.7 VIS + ALP-4.2). A telecentric relay lens system is established between the DMD and the objective to filter the diffraction pattern and control the spacing of the beams in the back focal plane of the objective (see Fig. 2.3b).

The first lens (L2, Thorlabs, AC254-150-A-ML, f=150 mm) and a mirror (M3, Thorlabs, BB2-E02) guide the light through the custom Spatial Filter (SF) positioned in the Fourier plane, which filters out everything but the zeroth and first-order diffraction patterns from the DMD. The next lens (L3, Thorlabs, AC508-080-AB, f=80 mm), Half Wave Plate (HWP, Thorlabs, AHWP10M-600), and another lens (L4, Thorlabs, AC508-180-A-ML, f=180 mm) align the polarization and magnify the spacing between the two orders. Another mirror (M4) and a long pass dichroic mirror (DC, Semrock, Di03-R660-t1-25.2x35.6) reflect the beams to the objective (Nikon, CFI Apo 1.49 total internal reflection (TIRF) 100XC Oil). The immersion oil (Nikon, immersion oil type F) used has a refractive index of 1.518 at 23°.

The stage (Physik Instrumente, Q-545 Q-Motion) is driven by E873 PIShift controllers and controlled by the PIMikroMove software. The emission light from the sample passes through the dichroic mirror. An Emission Filter (EF, Chroma, ET690/50) filters the light, and a mirror (M4, Thorlabs, BB1-E02) directs it through the objective tube lens (L5, Thorlabs, TTL200). The light is then guided through another 4F system with two lenses (L6/L7, Thorlabs, AC254-100-A). In the Fourier plane, a Deformable Mirror (DM, Boston Micromachines, Multi-3.5) is positioned to add an astigmatic aberration of approximately 90 mλ to the PSF. The emission light is finally imaged with a CMOS camera (Teledyne Kinetix Scientific CMOS, 01-KINETIX-M-C) with a pixel size of 6.5 µm x 6.5 µm in the sensor plane, resulting in a pixel size of 65 nm in the sample plane.

A simplified view of the excitation path is shown in Fig. 2.3b. In practice, the DMD is rotated by 45° because the micromirror's hinge is along the pixel's diagonal. The DMD is mounted so that its base is perpendicular to the incident beam. As shown in Supplementary Note 3, the placement and angle of the DMD influence the energy distribution over the different diffraction orders. With our alignment, assuming perfect polarization, the best achievable modulation depth is 0.96. The DMD pixel pitch is 13.68 µm, and the repeating pattern of three pixels on and off results in a DMD pitch $p_{\mathrm{DMD}} = 82.08\,\mu\mathrm{m}$.

The distance u, following the grating equation, between the zeroth order and the first order (Fig. 2.3b) is

$$u = \frac{\lambda_0 f}{p_{\mathrm{DMD}}} = 1.17\,\mathrm{mm} \tag{2.29}$$

in which the excitation wavelength λ_0 is 642 nm, and $f = 150\,\mathrm{mm}$, which corresponds to the focal length of L2. In the back focal plane of the objective, u is magnified to $u' = 2.63\,\mathrm{mm}$ by a factor of f4/f3. Considering that the effective focal length (EFL) of

the objective is 2 mm and assuming that α_0=0°, then β_0=60.6°.

2.3.2. SAMPLES

Three different types of samples have been used to calibrate the PSF model, validate the illumination pattern, and demonstrate the proof of concept. Gatta-beads (GATTAquant, ATTO 647N), embedded in a media with a refractive index of 1.46 and a diameter of 23 nm [44], were used for PSF calibration. A bead sample (Invitrogen™ FluoSpheres™ Carboxylate-Modified Microspheres, ex/em: 660/680nm, F8783) with a diameter of 20 nm, mounted on the coverslip and embedded in a 1% w/v agarose solution, was imaged for pattern validation. For the proof of concept, the GATTA-PAINT 3D HiRes 80R Expert Line (GATTAquant, ATTO655) sample was employed. This sample consists of DNA origami nanopillars, attached to the coverslip. The nanopillars are randomly oriented in all three dimensions, and both ends have a binding site for fluorescent probes with a spacing of 81(21) nm [45].

2.3.3. IMAGE ACQUISITION & CAMERA CALIBRATION

The samples are imaged using one pattern direction (L=1) with three phase shifts (K=3), and each frame has an exposure time of 10 ms for a total of 40×10^3 frames. The observed camera counts, represented as Analog-to-Digital Units (ADU), are converted into photons by measuring the gain and camera offset. This calibration process involves acquiring 2000 bright and 200 dark calibration images [46]. Performing this calibration is essential for achieving the theoretical maximum possible localization precision [40].

2.3.4. PSF CALIBRATION

We defined a fully vectorial PSF model for the optical system. The model's parameters were derived from the optical system's specifications, which included a numerical aperture (NA) of 1.49, immersion oil and coverslip with a refractive index of 1.515, and a mounting medium with a refractive index of 1.33 (unless stated otherwise). The upper limit of the emission filter, a wavelength of 715 nm, was set as the emission wavelength for the PSF. With our optical setup, we capture a portion of emission arising from SAF for emitters close to the coverslip. To achieve an unbiased estimation, it is necessary to consider this in the PSF model.

ABERRATION ESTIMATION

The Gatta-beads (section 2.3.2) are used to make a through-focus image stack of 40 slices, shifted by increments of 20 nm. The camera gain and offset are determined for the imaging conditions (section 2.3.3), which resulted in an average signal from the beads of 2×10^4 photons. Using the through-focus image stack, an MLE is employed to determine the aberration coefficients of the Zernike polynomials. In total 12 Zernike polynomials (Noll index 5-16) are used to construct the abberated wavefront W [47]. More details on the MLE framework can be found in the protocol by Siemons et al. [34].

SAF CALIBRATION

Before the maximum likelihood estimation (section 2.2.3) can be performed, the imaging depth z_d and stage position z_{stage} need to be determined. Using the found aberra-

tions W from the previous section, z_d can be computed from z_stage by maximizing the relative Strehl ratio, as proposed in earlier work [31]. The following metric function is maximized to find z_d for a given z_stage

$$z_\mathrm{d}^* = \arg\max_{z_\mathrm{d}} \left(\frac{\sum_{p=x,y}\sum_{q=x,y,z}\left|\int_{|\vec{\rho}|<1} E_{\mathrm{pupil},pq}(W_1,\vec{\rho},z_\mathrm{d},z_\mathrm{stage})d^2\rho\right|^2}{\sum_{p=x,y}\sum_{q=x,y,z}\left|\int_{|\vec{\rho}|<1} E_{\mathrm{pupil},pq}(W_2,\vec{\rho},z_\mathrm{d},z_\mathrm{stage})d^2\rho\right|^2} \right). \tag{2.30}$$

where $W_1(\vec{\rho}) = W(\vec{\rho})$, $W_2(\vec{\rho}) = W(\vec{\rho}) + z_\mathrm{d}k_{z,0}(\vec{\rho}) - z_\mathrm{stage}k_{z,2}(\vec{\rho})$, and we follow the the same notation as in section 2.2. The relation for our imaging conditions, between z_d and z_stage is shown in Fig. 2.4.

The stage position (z_stage) needs to be known in order to use the right distance from the cover glass to the focal plane (z_d). Before the ZIMFLUX data of the DNA PAINT nanorulers is acquired, the stage position is estimated using the following procedure:

1. The focus plane is initially set by hand, using the stage, on the emitters attached to the coverslip, which is considered as $z_\mathrm{d} = 0$. Using $z_\mathrm{d} = 0$, $z_{\mathrm{stage},0}$ can be computed by maximizing the relative Strehl ratio for z_stage, analogous to Eq. 2.30.

2. The stage is moved by a desired amount Δz_stage from $z_\mathrm{d} = 0$ in order to move the focal plane towards the binding sites of the DNA PAINT nanorulers, that are not attached to the coverglass.

3. Then $z_\mathrm{stage} = z_{\mathrm{stage},0} + \Delta z_\mathrm{stage}$ and z_d can be computed using Eq. 2.30.

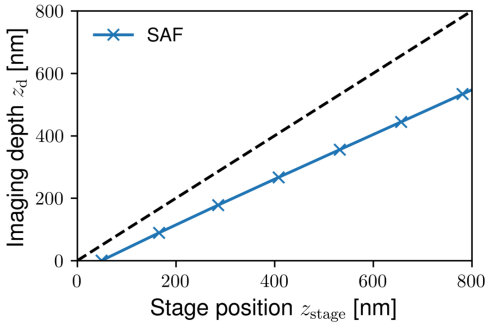


Figure 2.4: The relation between the imaging depth and the stage position in SAF conditions for the setup used in this research, which is obtained from Eq. 2.30 for multiple values of z_stage.

2.3.5. PATTERN ESTIMATION

INITIAL PATTERN ESTIMATION

The illumination pattern is estimated from the recorded data to avoid potential systematic errors in the illumination pattern parameters, thereby minimizing localization errors. First, all the positions $\vec{r}_{\mathrm{psf},\upsilon}$ are estimated from all emitters ignoring the pattern information, by summing over the different phases and directions ($L \times K$ applied patterns, see section 2.2.3 and 2.3.6), implying that the total number of acquired frames is

$L \times K \times V$. Then, for each individual frame, the photon count per emitter N^{lk} is estimated while keeping the previously estimated positions fixed. For each l and k, a SMLM reconstruction is made (S^{lk}), where the pixel size is 6 times smaller than the original image. Here 2D Gaussian spot are rendered with a width of 20 nm and an intensity scaled to N^{lk}. The lateral components of the spatial frequency vector $\vec{q}_{lk}$ are detected by finding the peak in the Fourier domains of S^{lk} [27]. The spatial frequency vector for each direction $\vec{q}_l$ is then calculated as the average over all phase steps of $\vec{q}_{lk}$. To reduce the effect of z deviation of the emitters, the z height variations of 200 nm in which most emitters are found is used to estimate the lateral components of $\vec{q}_l$. The axial component of $\vec{q}_l$ is initially set based upon the setup. The angle of the off-center beam (Eq. 2.29) is calculated, to compute the axial pitch p_{ax} (Eq. 2.3), to finally the determine axial component of $\vec{q}_l$ (Eq. 2.6).

THE PHASE, MODULATION DEPTH, AND RELATIVE INTENSITY ESTIMATION

The found spatial frequency vectors $\vec{q}_l$, the emitter positions $\vec{r}_{\text{psf},v}$, photon counts per frame N_v^{lk}, and photon counts of the summed frames N_v from the previous section are used to estimate other parameters of the illumination pattern: the phase ψ_{lk}, modulation depth m_{lk} and relative intensity η_{lk} (section 2.2.1). These parameters are estimated by minimizing the error metric Ω_{lk}, which is defined as the difference between the measured photon count and the expected photon count based on the pattern, phase and position [27]:

$$\Omega_{lk} = \sum_v^V \left| N_v^{lk} - \eta_{lk} \frac{N_v}{LK} (1 + m_{lk} \cos(\phi_{lk}(\vec{r}_{\text{psf},v})) \right|^2. \tag{2.31}$$

The error metric is minimized by setting the derivative with respect to the zeroth and first-order Fourier coefficients $\{\eta_{lk}, \eta_{lk} m_{lk} \cos(\psi_{lk}), \eta_{lk} m_{lk} \sin(\psi_{lk})\}$ to zero. This results in the following set of equations:

$$\begin{pmatrix} \sum_v \frac{N_v^2}{K^2} & \sum_v \frac{N_v^2}{K^2} \cos(2\pi \vec{q}_l \cdot \vec{r}_{\text{psf},v}) & \sum_v \frac{N_v^2}{K^2} \sin(2\pi \vec{q}_l \cdot \vec{r}_{\text{psf},v}) \\ \sum_v \frac{N_v^2}{K^2} \cos(2\pi \vec{q}_l \cdot \vec{r}_{\text{psf},v}) & \sum_v \frac{N_v^2}{K^2} \cos(2\pi \vec{q}_l \cdot \vec{r}_{\text{psf},v})^2 & \sum_v \frac{N_v^2}{K^2} \cos(2\pi \vec{q}_l \cdot \vec{r}_{\text{psf},v}) \sin(2\pi \vec{q}_l \cdot \vec{r}_{\text{psf},v}) \\ \sum_v \frac{N_v^2}{K^2} \sin(2\pi \vec{q}_l \cdot \vec{r}_{\text{psf},v}) & \sum_v \frac{N_v^2}{K^2} \cos(2\pi \vec{q}_l \cdot \vec{r}_{\text{psf},v}) \sin(2\pi \vec{q}_l \cdot \vec{r}_{\text{psf},v}) & \sum_v \frac{N_v^2}{K^2} \sin(2\pi \vec{q}_l \cdot \vec{r}_{\text{psf},v})^2 \end{pmatrix} \begin{pmatrix} \eta_{lk} \\ \eta_{lk} m_{lk} \cos(\psi_{lk}) \\ \eta_{lk} m_{lk} \sin(\psi_{lk}) \end{pmatrix} = \begin{pmatrix} \sum_v \frac{N_v N_v^{lk}}{K} \\ \sum_v \frac{N_v N_v^{lk}}{K} \cos(2\pi \vec{q}_l \cdot \vec{r}_{\text{psf},v}) \\ \sum_v \frac{N_v N_v^{lk}}{K} \sin(2\pi \vec{q}_l \cdot \vec{r}_{\text{psf},v}) \end{pmatrix} \tag{2.32}$$

which can be solved for ψ_{lk}, η_{lk} and m_{lk} for all emitters. However, to check and correct for any variations over time, we employ data binning. Specifically, we divide the data into 10 time bins (each containing approximately 4000 frames).

PATTERN REFINEMENT

An error in the spatial frequencies $\vec{q}_l$ and the phase ψ_{lk} of the illumination pattern will lead to a bias in the ZIMFLUX position estimates. In order to mitigate this error we minimize the mean square difference $\Delta\vec{r}_\nu$ between the position estimates obtained with only the PSF $\vec{r}_{\text{psf},\nu}$ and with only the illumination pattern $\vec{r}_{\text{ill},\nu}$ (see section 2.2.3). The phase at a specific position is defined as $\phi_{lk}(\vec{r}_\nu) = 2\pi\vec{q}_l \cdot \vec{r}_\nu - \psi_{lk}$. We proceed to determine the systematic phase error for each direction

$$\Delta\vec{r}_\nu = \vec{r}_{\text{psf},\nu} - \vec{r}_{\text{ill},\nu}, \tag{2.33}$$

$$\Delta\phi_l(\vec{r}_{\text{psf},\nu}, \vec{r}_{\text{ill},\nu}) = 2\pi\vec{q}_l \cdot \Delta\vec{r}_\nu + 2\pi\Delta\vec{q}_l \cdot \vec{r}_{\text{psf},\nu} - \Delta\psi_l, \tag{2.34}$$

in which $\Delta\vec{q}_l$ and $\Delta\psi_l$ are the unknown errors in the spatial frequency and phase, respectively. To minimize the phase error (R_l), we employ least square estimation, which is defined as follows:

$$R_l = \sum_{\nu=1}^{V} |\Delta\phi_l(\vec{r}_{\text{psf},\nu}, \vec{r}_{\text{ill},\nu})|^2, \tag{2.35}$$

which is minimized to yield

$$\sum_\nu 2\pi(\Delta\vec{q}_l \cdot \vec{r}_{\text{psf},\nu}) - \sum_\nu \Delta\psi_l = -\sum_\nu 2\pi(\vec{q}_l \cdot \Delta\vec{r}_{\text{psf},\nu}). \tag{2.36}$$

which can be solved for $\Delta\vec{q}_l$ and $\Delta\psi_l$, by fitting a linear line through $\Delta\vec{r}_{\text{psf},\nu}$ versus $\vec{r}_{\text{psf},\nu}$ for each dimension and all ν. From the found slope and offset, $\Delta\vec{q}_l$ and $\Delta\psi_l$ are updated. We found that the phase estimation described earlier already determines $\frac{\Delta\psi}{\psi_l} < 10^{-4}$ and does not need to be refined. Starting with the initial estimate of spatial frequency vector of the pattern, the following iterative procedure for pattern refinement is used:

1. Phase estimation (section 2.3.5).
2. Estimate and $\vec{r}_{\text{ill},\nu}$ and compute $\Delta\vec{r}_\nu$.
3. Update $\vec{q}'_l = \vec{q}_l + \Delta\vec{q}_l$

The procedure is stopped if the fraction $\frac{\Delta\vec{q}_l}{\vec{q}_l}$ is smaller than 10^{-4}.

2.3.6. SINGLE-MOLECULE LOCALIZATION MICROSCOPY

ASTIGMATIC PSF ESTIMATION

After acquiring the patterned illuminated frames ($L \times K \times V$), we generate uniform illuminated frames by summing the applied patterns ($L \times K$) corresponding to all phase steps and directions. For ZIMFLUX $L = 1$ and $K = 3$. Regions of interest (ROIs) measuring 16×16 pixels, which contain candidate emitters, are detected using a thresholding algorithm based on local maxima in a feature-enhancing difference of Gaussian filtered image [48]. The position (x, y, and z), signal photon count N, and background photon count per pixel b of the candidate emitters in the identified ROIs are estimated using the Maximum Likelihood Estimation (MLE) (section 2.2.3), without considering the illumination field information. Any non-converging estimations within the ROI, excluding the 2-pixel width border, are filtered out. The results obtained from the summed frames are henceforth referred to astigmatic PSF estimation.

ZIMFLUX ESTIMATION

Using the knowledge about illumination patterns, obtained via the previous step, the ZIMFLUX localization is performed. If the emitter was not in its 'on state' during all phase shifts, it affects the accuracy and precision of the localization. To mitigate this effect, all spots which have maximum modulation error ϵ_{mod} larger than a user defined threshold are filtered out. The maximum modulation error is

$$\epsilon_{\text{mod}} = \max\left(\frac{N_{\text{exp}}^{lk} - N_{\text{est}}^{lk}}{N_{\text{exp}}^{lk}}\right) \quad \forall \quad 0 \leq l \leq L \quad \text{and} \quad 0 \leq k \leq K \tag{2.37}$$

where N_{exp}^{lk} represents the expected signal of the emitter based on the illumination pattern, while N_{est}^{lk} is the estimated signal of the emitter in that frame. We have found that $\epsilon_{\text{mod}} < 0.3$ works to ensure an accurate ZIMFLUX estimation.

DRIFT CORRECTION

Finally, drift correction is performed based on the astigmatic PSF localizations to maximize the information. The drift correction is based on entropy minimization as described previously [49]. The found drift correction is applied to both the astigmatic PSF and ZIMFLUX estimates.

2.4. RESULTS

Firstly, we investigate the impact of astigmatism on the precision of ZIMFLUX in comparison to using only the astigmatic PSF through simulations. We analyze how the precision varies depending on the emitter's position relative to the focal plane under SAF and Undercritical Angle Fluorescence (UAF) conditions, using the CRLB. Secondly, we examine the influence of the axial pitch and modulation depth of the illumination pattern on the CRLB of ZIMFLUX, once again under UAF and SAF conditions. Thirdly, we present the experimental PSF obtained from the optical setup and demonstrate the impact of SAF on the electric field in the pupil plane. Fourthly, we image the illumination pattern using a fluorescent bead sample and confirm that it corresponds to the expected pattern from the optical setup. Lastly, we provide a proof of concept for ZIMFLUX by utilizing 3D nanorulers, demonstrating its effectiveness and potential applications.

2.4.1. SIMULATION RESULTS

We conducted simulations assuming perfect alignment of the center beam with the optical axis and no optical aberrations, except for vertical astigmatism Z_2^2. Our goal is to assess the effects of astigmatism and SAF on using solely the astigmatic PSF and ZIMFLUX by simulating emitters at various depths, as illustrated in Fig. 2.5. We used Zernike coefficients of $-30\,\text{m}\lambda$, $-60\,\text{m}\lambda$, and $-90\,\text{m}\lambda$ to represent varying degrees of astigmatism. For the ZIMFLUX simulation, the phases for each emitter are randomly assigned and the illumination pattern exhibits an axial pitch of 492 nm and a lateral pitch of 452 nm, with a modulation depth of 0.85.

Firstly, we simulated emitters at an imaging depth of $z_{\text{d}} = 300\,\text{nm}$, where SAF is present. It can be seen that the astigmatic PSF is non-symmetric, due to the SAF conditions, and that the PSF changes significantly over its z position (Fig. 2.5a). This results in a

low CRLB for the z position estimation of the astigmatic PSF and it shows that stronger astigmatism is favourable for higher precision (Fig. 2.5b). For ZIMFLUX, the effect of astigmatism on the CRLB of the z position estimation is much smaller, compared to the astigmatic PSF estimation (Fig. 2.5c). Looking at Fig. 2.5b and Fig. 2.5c, it can be seen that the improvement in the axial localization of ZIMFLUX over the astigmatic PSF is roughly a factor 2.

Secondly, we simulated emitters at $z_d = 1300\,\text{nm}$, whereas SAF has a negligible effect. At this depth, the PSF barely changes, particularly for negative z-values (Fig. 2.5d), leading to a high CRLB for the axial localization for the astigmatic PSF (Fig. 2.5e). This effect has been more extensively covered in previous work [50]. However, ZIMFLUX demonstrates a significantly lower CRLB (Fig. 2.5f), by comparing it to the CRLB of the astigmatic PSF (Fig. 2.5e). Since the PSF barely changes for negative z-values at $z_d = 1300\,\text{nm}$, the improvement factor in the CRLB of ZIMFLUX compared to the astigmatic PSF can reach a factor of roughly 10, while for positive z values, the improvement factor goes down to approximately 2. This indicates that ZIMFLUX maintains superior axial localization precision at greater imaging depths compared to SMLM using an astigmatic PSF.

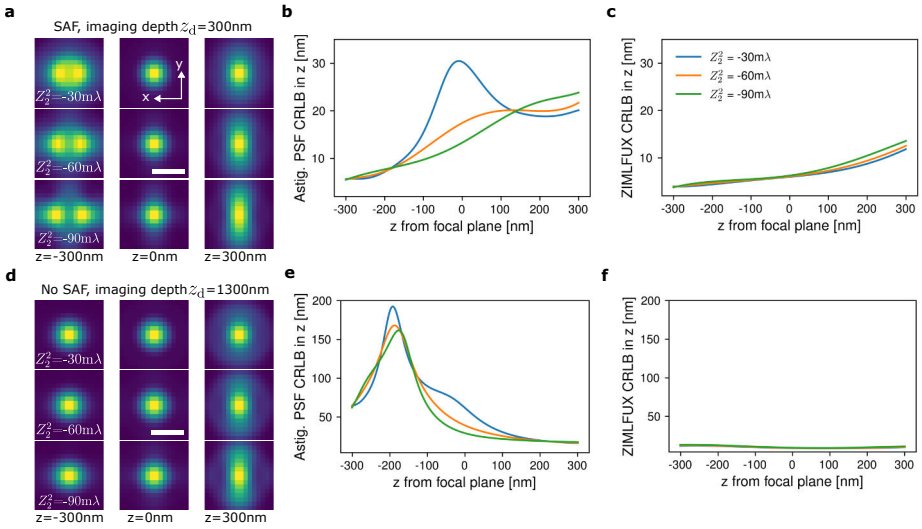


Figure 2.5: **a**, PSF at various z distances from the focal plane for different values of the astigmatic Zernike coefficient Z_2^2 ($-30\,\text{m}\lambda$, $-60\,\text{m}\lambda$, $-90\,\text{m}\lambda$) at an imaging depth of 300 nm. The parameters used are similar to the experimental conditions (an oil immersion objective, refractive index mounting medium of 1.33, and signal and background photon count of 2800 and 8). **b, c**, The CRLB of the astigmatic PSF and ZIMFLUX axial localization are shown as a function of different distances from the focal plane at an imaging depth of $z_d = 300\,\text{nm}$. SAF occurs due to refractive index mismatch, which lowers the CRLB near the coverslip and decreases with increasing distance from the coverslip. The illumination pattern has a modulation depth of 0.85 and an axial and lateral pitch of 492 nm and 452 nm, respectively. The CRLB of ZIMFLUX is nearly independent of the level of astigmatism and is approximately half of the CRLB of the astigmatic PSF. **d-f**, Similar to **a-c** but at $z_d = 1300\,\text{nm}$, where the effect of SAF is negligible. The refractive index mismatch significantly affects the axial localization precision of the astigmatic PSF (**e**), but ZIMFLUX enables a higher precision when imaging deeper into the sample, which is a 10-fold improvement for negative z values, that goes down to approximately 2-fold for positive z values (**f**). The y-axis of the plots are scaled such that the CRLB of the astigmatic PSF and ZIMFLUX can be compared easily, for a scale that is suitable for the individual plots, see Fig. 2.15.

To investigate how the pattern and SAF affect the performance of ZIMFLUX, emitters were randomly simulated over an axial distance of 600 nm at imaging depths of 300 nm and 1300 nm. Generally, a lower axial pattern pitch improves the CRLB of the z-position estimation, as depicted in Fig. 2.6. The simulation area of the emitters, where SAF is expected, is illustrated in Fig. 2.6a. The CRLB of the z-estimation of ZIMFLUX is slightly affected by the modulation depth of the pattern (Fig. 2.6b). The impact of different levels of astigmatism on the ZIMFLUX CRLB was examined with a modulation depth of 0.85. The results suggest that the level of astigmatism does not noticeably enhance the precision and may even impair it when the axial pitch is less than 1000 nm (Fig. 2.6c). At an imaging depth of 300 nm, the improvement factor in the CRLB of ZIMFLUX over the astigmatic PSF ranges from 1.5 to 3.5, depending on the level of astigmatism and axial pitch (Fig. 2.6d). At an imaging depth of 1300 nm (Fig. 2.6e-h), the trends are similar, but the improvement factor of ZIMFLUX over the astigmatic PSF reaches 3 to 8, depending on the astigmatism and axial pitch.

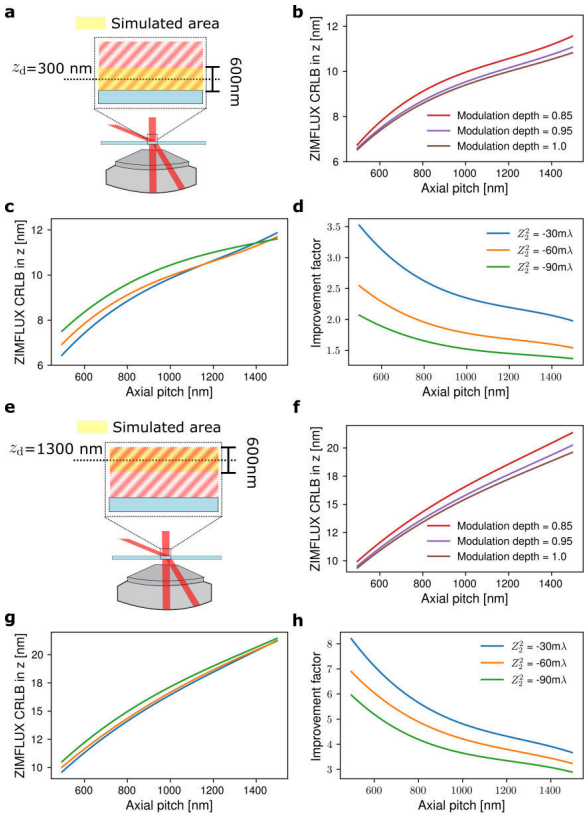


Figure 2.6: **a**, The schematic shows that the CRLB in **b**-**d** is computed for emitters randomly generated between −300 nm and 300 nm away from the focal plane at an imaging depth of 300 nm. **b**, The CRLB for estimating the z-position as a function of the axial pitch for different modulation depths m, assuming the center beam is perfectly parallel to the optical axis and the astigmatism is set with the Zernike mode Z_2^2 of −60 mλ. **c**, The effect of different levels of astigmatism on the CRLB, with a modulation depth of 0.85. It can be observed that the degree of astigmatism does not significantly improve the precision and can even deteriorate it for an axial pitch lower than 1000 nm. **d**, The improvement factor of the CRLB in z-estimation for ZIMFLUX compared to the astigmatic PSF is shown for different levels of astigmatism and axial pitches. **e**, the CRLB in **f**-**h** is computed CRLB similarly as for the **b**-**d**, but at an imaging depth of 1300 nm, at which the effect of SAF is negligible. **f**-**h**, Similar to **b**-**d**, but with an imaging depth of 1300 nm. The improvement factor of the CRLB for ZIMFLUX over the astigmatic PSF z estimation is about 2 times higher at this depth compared to an 300 nm imaging depth.

2.4.2. CALIBRATION OF PSF MODEL

In order to successfully use the vectorial PSF model in experimental conditions, it is necessary to determine the aberrations of the system. A through-focus PSF scan of fluorescent beads embedded in a medium with a refractive index of 1.46 was performed to retrieve the aberrations. The fluorescent beads were assumed to be attached to the coverslip and to be point sources because the diameter (23 nm) is much smaller than the diffraction limit. The 12 (Noll index 5-16) Zernike coefficients defining the aberrated wavefront were obtained from 11 beads with an average precision of 2 mλ. The Zernike coefficient of the vertical astigmatism induced by the deformable mirror in the emission path was −87(3) mλ, while the others are around 0 mλ (Fig. 2.16c). The calibration PSF, the Zernike modes, the aberrated wavefront and the effect of SAF are shown in Fig. 2.16.

2.4.3. ILLUMINATION PATTERN MEASUREMENT

The illumination pattern is imaged by analyzing a bead sample embedded in agarose as described in section 2.3.2. The pattern phase is kept constant while the stage is moved. From the intensity of the emitters, based on the stage position, the lateral and axial pattern pitches are estimated.

To find the axial pattern pitch, the stage is moved in the axial direction and the lateral position of the PSF is fixed at the center of the ROI, which is found from a maximum intensity projection. The other parameters, z, photons N, and background photons b are then estimated for each ROI. As the stage is shifted in steps of 30 nm in the axial direction, the intensity of the emitter varies according to the pitch of the pattern in the immersion oil, p'_z, as depicted in Fig. 2.7a (see Supplementary note 2 for the derivation). A sinusoidal function with a linear offset (to incorporate bleaching) is fitted to the estimated PSF signal as a function of the stage shift, to determine p'_z. This process is repeated for 99 beads, and p'_z and the standard error of the mean (SEM) is found to be 835(12) nm (SEM).

For estimating the lateral illumination pattern, the stage is shifted in both the x and y directions by one pixel (65 nm) for 25 steps. Unlike the axial stage shift, the PSF remains unchanged, so the ROIs containing a bead are summed after shifting, and the position of the bead within the ROI is determined. Using the estimated position for each individual ROI, the signal is estimated, and the intensity profiles are fitted to determine the pitches of the pattern in the x and y directions, denoted by p_x and p_y. The pitch of the sinusoidal fit is estimated for 111 different beads shifted in the x-direction and 110 beads in the y-direction, with values of p_x = 646(3) nm (SEM) and p_y = 663(3) nm (SEM), as shown in

Fig. 2.7c,d. Computing the lateral wave vector using p_x and p_y gives a lateral pitch p_{lat} of 462(3) nm (SEM).
Eq. 2.2 and Eq. 2.59 are solved using the found pitches p'_z and p_{lat} to determine the two unknown beam angles and their uncertainties. This yields $\alpha_0 = 3(2)°$ and $\beta_0 = 60(1)°$ and a spacing u' in the back focal plane between the two beams arising from those angles are 2.8(3) mm, which is within the expected range based on the optical setup and the pitch of the DMD. In the case of perfect alignment, the expected u' is calculated to be 2.63 mm (section 2.3.1).

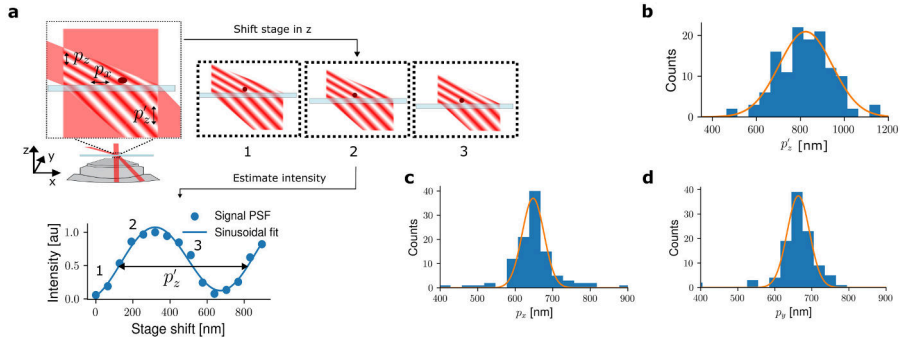


Figure 2.7: **a**, By shifting the stage and measuring the signal of a single emitter while keeping the pattern constant, the lateral pitches p_x and p_y in a sample can be determined. Due to a refractive index mismatch between the sample and coverslip, there is a difference in the pattern below and above the coverslip. Thus, when the stage is moved in the z-direction, the intensity profile of the emitter represents the pitch in z within the immersion oil, as explained in the Theory section and depicted in the schematic. For the lateral directions, the found pitch corresponds to the pitch of the pattern within the sample. **b**, The axial pitch p'_z and standard error of the mean (SEM) obtained from the stage shift is 835(12) nm (SEM, n=99) (bin width 50 nm). **c, d**, Histograms of the estimated lateral pitches of the sinusoidal function reveal values of 646(3) nm (SEM, n=111) and 663(3) nm (SEM, n=110) for p_x and p_y, respectively (bin width 30 nm).

2.4.4. PROOF OF PRINCIPLE

We conducted an experiment to demonstrate the feasibility of our method by imaging randomly oriented 3D DNA-origami nanorulers with a length l of 81(21) nm, as provided by the manufacturer (details in section 2.3.2). The field of view (FOV) was 16.6 µm × 16.6 µm, as depicted in Fig. 2.8a. Before image acquisition, we displaced the stage position z_{stage} such that the imaging depth z_{d} is approximately 60 nm (Fig. 2.4), which is used in the astigmatic PSF model. Due to a relatively low axial deviation of 80 nm, the lateral pitch could be estimated using 2D Fourier domain peak finding, and the corresponding spatial spectrum and the peak (Fig. 2.11a) correspond to a lateral pitch p_{lat} of 454 nm, with an azimuthal angle of the pattern of 42°. The initial axial pitch p_{ax} was set to 500 nm based on pattern validation. We further refined p_{ax} as described in section 2.3.5, which resulted in p_{ax} = 481 nm, to which it converged within 4 iterations (Fig. 2.11b). With the found pattern, no systematic bias in the localization for all three dimensions has been found between using only the astigmatic PSF and only the illumination pattern (Fig. 2.11c-f).
Subsequently, the phases, modulation depths and illumination power were estimated (Fig. 2.12a-c). The estimated intensities relative to the expected pattern intensity for the

emitters are provided in Fig. 2.12d-f and the localizations with a $\epsilon_{\text{mod}} > 0.3$ are filtered out.

In Fig. 2.8b, a zoomed-in display of the boxes in Fig. 2.8a is presented, in which the localizations are convolved with a Gaussian kernel of size 10 nm. The histograms of the z-projection are also depicted for the individual nanorulers, and the enhancement in precision can be observed. To verify the consistency of the astigmatic PSF and ZIMFLUX estimation for different z-positions, the Euclidean distance l between the binding sites versus the polar angle of the nanoruler with respect to the coverslip is shown in Fig. 2.8c, where only minor deviations from a horizontal line can be observed, indicating that the PSF model is accurate. The lenght of the nanorulers is displayed differently in Fig. 2.8d, with mean values of 83(7) nm and 83(8) nm for the astigmatic PSF estimation and ZIMFLUX, respectively. The experimentally obtained precisions and the corresponding CRLBs are shown in Fig. 2.8e, and the median values for the clusters are 18.8 nm for the astigmatic PSF estimation and 12.6 nm for the ZIMFLUX estimation. The corresponding CRLB values are 11.7 nm and 6.0 nm for the astigmatic PSF and ZIMFLUX estimation, respectively.

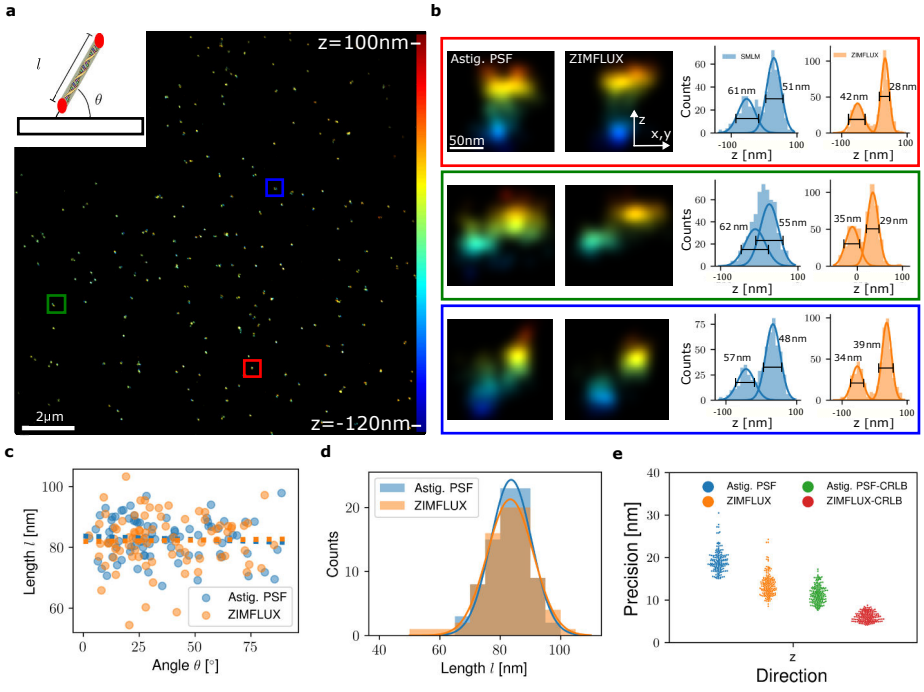


Figure 2.8: **a**, The field of view (FOV) is captured from a sample containing randomly oriented 3D DNA origami nanorulers that are attached to the coverslip. The polar angle, θ, denotes the angle between the nanoruler of length l and the coverslip, as illustrated in the upper left corner. **b**, The colored boxes in **a** are zoomed in to display the results of the astigmatic PSF and ZIMFLUX on the same underlying data. To aid visualization, the localizations are convolved with a Gaussian kernel of size 10 nm and the color corresponds to the z position. The histograms show the estimated z-positions of the individual localizations. The two binding sites are identified by K-means clustering, and the fit of each cluster is shown in the histograms with the Full Width Half Maximum (FWHM) noted. **c**, The positions of the binding sites are calculated as the mean of all localizations in each cluster. The Euclidean distance between the binding sites, l, as a function of the polar angle θ is plotted. **d**, The histogram of length l has mean values of 83(7) nm and 83(8) nm for the astigmatic PSF and ZIMFLUX, respectively. The bin width of the histograms in **b** and **d** is 5 nm. **e**, The median values of the found precision of the clusters are 18.8 nm and 12.6 nm for the astigmatic PSF and ZIMFLUX and 11.7 nm and 6.0 nm for the CRLB. The CRLB is computed with the mean values of the estimated parameters of each cluster.

The experimentally observed precision σ_{exp} is worse than the theoretical CRLB σ_{crlb} by a margin σ_{e}. By applying the relationship $\sigma^2_{\text{exp}} = \sigma^2_{\text{crlb}} + \sigma^2_{\text{e}}$, it is calculated that σ_{e} is 14.7 nm for the astigmatic PSF estimation and 11.1 nm for ZIMFLUX estimation. This deviation may be attributed in part to imprecisions in the drift correction, as well as the fact that a single PSF model is employed for estimating the measured PSF, despite that any slope of the cover glass and axial drift that can alter imaging depth and influence the PSF, and gives a model mismatch, particularly given the significant variability of the SAF effect over small distances. As we are using the lateral pitch of 452 nm that is relatively large compared to the spot width, there is no improvement visible for the lateral directions. The experimentally observed precision is worse than the theoretical CRLB for the lateral localization by a similar margin as for the axial localization (Fig. 2.14).

2.5. DISCUSSION

The presented approach offers an effective way to improve the axial localization precision in standard SMLM experimental settings by incorporating the vectorial PSF model with a sinusoidal illumination pattern. Although a similar technique using a two-beam excitation, which uses a different type of setup, has been previously demonstrated in ModLoc [28], the addition of PSF information and astigmatism allows for the use of smaller axial pitches and eliminates phase wrapping issues. This overcomes the lower limit of the axial pitch to be at least the depth of focus of the imaged sample. Our simulations show that using a pitch of 500 nm improves axial localization precision by a factor of ~ 1.5 compared to using a pitch of 1 μm as ModLoc is using. Additionally, incorporating the astigmatic PSF model provides better control over the estimation of pattern parameters and results in unbiased estimations, since the imaging setup can have misalignments over time, which affects the pattern, but also the pattern can deviate per sample due to a changing coverslip angle or refractive index of the mounting medium.

Our experimental results show that the vectorial PSF model can effectively handle SAF conditions. In previous work, it has been shown that solely using an astigmatic PSF model in the presence of SAF leads to relative axial localization errors between 30% and 50% over a range of several hundreds of nanometers [31]. Therefore, the vectorial PSF model can provide more accurate and reliable results in such experimental conditions.

2.5.1. IMAGING DEPTH

The maximum achievable imaging depth with ZIMFLUX varies depending on the specific optical system. As the imaging depth increases, the axial localization precision (σ_{ax}) of the astigmatic PSF decreases, because of depth-dependent aberrations [51, 50]. For instance, if σ_{ax} is bigger than the axial pitch of the illumination pattern (p_{ax}), it becomes unfeasible to reliably estimate the illumination pattern. Considering the Nyquist-Shannon sampling theorem, which dictates that the sampling frequency should be at least twice the signal frequency, one could argue that ZIMFLUX is applicable up to imaging depths where $\sigma_{ax} < p_{ax}/2$.

2.5.2. COMPUTATION TIME

Estimating parameters with the vectorial PSF model takes significantly longer computational time compared to only using an astigmatic PSF, making it less practical. Computing the MLE for both models has a linear computational time complexity for increasing iterations and the MLE for the vectorial PSF model is ~ 135 times slower than using solely an astigmatic PSF on a standard commercial graphics processing unit (NVIDIA GeForce RTX 3060), as shown in Fig. 2.17. The total time to run the whole pipeline takes approximately 2.5 hours for 180000 spots.

2.5.3. POINT SPREAD FUNCTION MODEL MISMATCH

The determination of the imaging depth z_d and stage position z_{stage} is not very precise, because it is difficult to precisely determine when the spots are in focus and a sample with emitters attached to the coverslip is needed in order to use the method described in this research. Additionally, axial sample drift has a significant effect on the PSF, especially in SAF conditions. For this study, a single model was used for the entire data acquisition, resulting in a model mismatch. In future research, a more variable vectorial PSF model could be preferable.

2.5.4. LATERAL LOCALIZATION PRECISION

With the setup used in ZIMFLUX and a perfect alignment of the center beam, a minimum lateral pitch p_{lat} of approximately 480 nm can be achieved; otherwise, the off-center beam will enter the TIRF regime. Theoretically, assuming zero background and neglecting the dependence on the global phase, the improvement factor for lateral precision using a sinusoidal illumination pattern, compared to conventional SMLM, is given by $\sqrt{1+2\pi^2\left(\frac{m^2}{1+\sqrt{1-m^2}}\cdot\frac{\sigma^2}{p_{lat}^2}\right)}$, where m is the modulation depth and $\sigma \approx \lambda/4\text{NA}$ is the spot width if astigmatism is neglected [27]. In our setup, with $m = 0.85$, the sinusoidal illumination pattern would result in a 1.35-fold improvement in lateral precision compared to using only the PSF. For an astigmatic PSF, σ increases depending on the z position, and a higher improvement factor for the lateral position would be expected in ZIMFLUX. However, this has not been observed under experimental conditions, as shown in Fig. 2.14.

2.5.5. OUTLOOK

In our study, we have demonstrated the effectiveness of a rapidly shifting illumination pattern in combination with a high NA oil objective (NA = 1.49) and an aberrated PSF. For future research, it could be worthwhile to explore alternative illumination patterns to improve the resolution of SMLM, such as the counter-propagating beams as proposed in ROSE-Z [29], which results in an axial pitch of approximately 240 nm of the illumination pattern, using an excitation wavelength of 640 nm. Including an astigmatic PSF will prevent phase wrapping and allows to image samples with a broader axial range (>240 nm) of emitters. This could be combined with with two off-center beams with opposing angles, which could reduce the lateral pitch of the illumination pattern up to 240 nm as well. This combined approach holds the potential to achieve enhanced precision in all dimensions.

2.6. DISCLOSURES

The authors declare no conflicts of interest.

2.7. SUPPLEMENTAL DOCUMENT

See supplementary document for supporting content.

2.8. DATA AVAILABILITY

Code and example data is available at https://github.com/qnano/zimflux. A standalone implementation for a vectorial PSF fitting tool, including a graphical user interface, is available at https://github.com/qnano/VectorialPSF.

2.9. SUPPLEMENTARY MATERIAL

2.10. SUPPLEMENTARY NOTE 1: ILLUMINATION PATTERN

The illumination pattern that excites the sample is generated by the interference field ($\vec{E}_i$) at the intersection of two plane waves $\vec{E}_1$ and $\vec{E}_2$, as shown in fig. 2.9. It is assumed that all media is isotropic and non-conducting. The illumination model is defined by the spatial frequency vector of $\vec{E}_i$, which is computed from the axial and lateral pitches of the interference pattern, which are derived based on the wavevectors of $\vec{E}_1$ and $\vec{E}_2$ in this section.

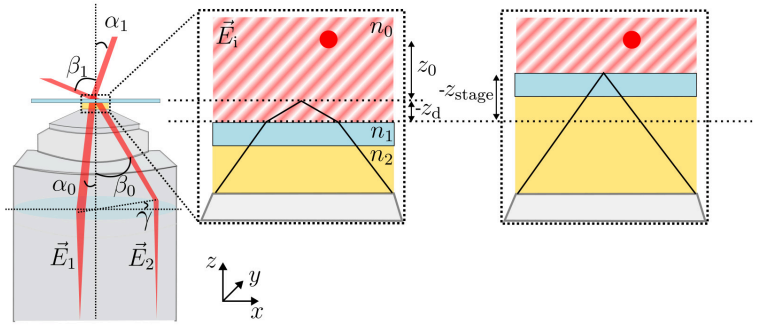


Figure 2.9: The figure illustrates the interference pattern $\vec{E}_i$ that is formed by two plane waves $\vec{E}_1$ and $\vec{E}_2$ originating from the objective, with incidence angles of α_0 and β_0. The light passes through the immersion media and cover glass, with refractive indices of n_2 and n_1, respectively. Due to the refractive index mismatch, the angles of the beams change to α_1 and β_1. The fluorophores are embedded in a medium with a refractive index of n_0. The imaging depth z_d corresponds to the distance from the cover glass to the focal plane, while z_0 represents the emitter's distance from the focal plane. z_{stage} is defined as the distance the stage has moved from the point at which the top of the cover glass is aligned with the focal plane.

The interference field $\vec{E}_i$ is

$$\vec{E}_i(\vec{r},t) = \vec{A}_1 e^{i(\vec{k}_1\cdot\vec{r}-\omega t+\phi_1)} + \vec{A}_2 e^{i(\vec{k}_2\cdot\vec{r}-\omega t+\phi_2)}, \tag{2.38}$$

with the fields of the two plane waves $\vec{E}_1$ and $\vec{E}_2$ as

$$\vec{E}_1(\vec{r},t) = \vec{A}_1 e^{i(\vec{k}_1\cdot\vec{r}-\omega t+\phi_1)}, \tag{2.39}$$
$$\vec{E}_2(\vec{r},t) = \vec{A}_2 e^{i(\vec{k}_2\cdot\vec{r}-\omega t+\phi_2)} \tag{2.40}$$

where $\vec{r}$ is the position vector, $\vec{A}_1$ and $\vec{A}_2$ are the electric field amplitudes, t is the time, ω is the angular frequency, ϕ_1 and ϕ_2 are the initial phases. The wave vectors $\vec{k}_1$ and $\vec{k}_2$ are

$$\vec{k}_1 = \{k\sin\alpha_1\cos\gamma, k\sin\alpha_1\sin\gamma, k\cos\alpha_1\}, \tag{2.41}$$
$$\vec{k}_2 = \{-k\sin\beta_1\cos\gamma, -k\sin\beta_1\sin\gamma, k\cos\beta_1\}. \tag{2.42}$$

where α_1 and β_1 are the angles of $\vec{k}_1$ and $\vec{k}_2$ with respect to the optical axis in the mounting medium and γ is the angle in the x,y plane (Fig. 2.2). The intensity pattern of $\vec{E}_i$ is

$$P(x,y,z) = \frac{1}{2}\epsilon_0 c n_0 \vec{E}_i\cdot\vec{E}_i^* \tag{2.43}$$
$$= \frac{1}{2}\epsilon_0\left[||\vec{A}_1||_2^2 + ||\vec{A}_2||_2^2 + 2\vec{A}_1\cdot\vec{A}_2 e^{i((\vec{k}_1-\vec{k}_2)\cdot\vec{r}+\phi_1-\phi_2)}\right] \tag{2.44}$$
$$= \frac{1}{2}\epsilon_0\left[||\vec{A}_1||_2^2 + ||\vec{A}_2||_2^2 + 2\vec{A}_1\cdot\vec{A}_2\cos((\vec{k}_1-\vec{k}_2)\cdot\vec{r}+\phi_1-\phi_2)\right] \tag{2.45}$$
$$= \frac{1}{2}\epsilon_0\{||\vec{A}_1||_2^2 + ||\vec{A}_2||_2^2 + 2\vec{A}_1\cdot\vec{A}_2\cos\big[xk(\sin\alpha_1\cos\gamma+\sin\beta_1\cos\gamma) + yk(\sin\alpha_1\sin\gamma+\sin\beta_1\sin\gamma) + zk(\cos\alpha_1 - cos\beta_1)+\phi_1-\phi_2\big]\}. \tag{2.46}$$

where ϵ_0 is the vacuum permittivity and c the speed of light. The lateral and axial pitch, p_{lat} and p_{ax}, of the interference pattern can be computed from eq. (2.46) as

$$p_{\text{lat}} = \frac{1}{|k(\sin\alpha_1 + \sin\beta_1)|} = \frac{\lambda_0}{|n_0(\sin\alpha_1 + \sin\beta_1)|}, \tag{2.47}$$

$$p_{\text{ax}} = \frac{1}{|k(\cos\alpha_1 - \cos\beta_1)|} = \frac{\lambda_0}{|n_0(\cos\alpha_1 - \cos\beta_1)|}. \tag{2.48}$$

where λ_0 is the wavelength of the monochromatic light source, and n_0 is the refractive index of the mounting medium. When introducing ψ, $\vec{q}$, η, m and ϕ, the interference term P in Eq. 2.46 can be rewritten as an amplitude modulated signal

$$\psi = \phi_1 - \phi_2, \tag{2.49}$$

$$\vec{q} = \{\frac{\cos(\gamma)}{p_{\text{lat}}}, \frac{\sin(\gamma)}{p_{\text{lat}}}, \frac{1}{p_{\text{ax}}}\}, \tag{2.50}$$

$$\phi(\vec{r}) = 2\pi\vec{q}\cdot\vec{r} - \psi, \tag{2.51}$$

$$m = \frac{2\vec{A}_1\cdot\vec{A}_2}{||\vec{A}_1||_2^2 + ||\vec{A}_2||_2^2} \tag{2.52}$$

$$\eta = \frac{1}{2}\epsilon_0 c n_0 (||\vec{A}_1||_2^2 + ||\vec{A}_2||_2^2) \tag{2.53}$$

$$P(\phi(\vec{r})) = \eta\big(1 + m\cos(\phi(\vec{r}))\big). \tag{2.54}$$

where m is the modulation depth, that only can reach 1 if $\vec{A}_1$ and $\vec{A}_2$ have the same amplitude and polarization, and η is the intensity. The absolute intensity of the pattern is not crucial in our analysis. Instead, we focus on the intensity fluctuations between multiple patterns, and to quantify the relative intensity among them, we use the parameter η.

2.11. SUPPLEMENTARY NOTE 2: AXIAL PITCH ESTIMATION FROM STAGE SHIFT

A 2D fluorescent sample is used to estimate p_{ax} experimentally. Shifting the stage in the axial direction alters the optical path length of the beams. To observe a full modulation in the intensity profile of an emitter, the distance moved by the stage does not correspond to p_{ax}, but rather to p'_{ax}, which is derived in the rest of this section. Assuming that the lateral coordinates remain constant, the interference intensity pattern from eq. (2.46) is

$$P(\Delta z) = \frac{1}{2}\epsilon_0\left[||\vec{A}_1||_2^2 + ||\vec{A}_2||_2^2 + 2\vec{A}_1\cdot\vec{A}_2\cos(\xi_1(\Delta z) - \xi_2(\Delta z))\right]. \tag{2.55}$$

where Δz is the axial stage shift. Taking into account the difference in optical path length of beams $\vec{E}_1$ and $\vec{E}_2$ resulting from the stage shift Δz, the corresponding phase differences are

$$\xi_1(\Delta z) = \frac{2\pi}{\lambda_0} n_2 \Delta z \cos\alpha_0, \tag{2.56}$$

$$\xi_2(\Delta z) = \frac{2\pi}{\lambda_0} n_2 \Delta z \cos\beta_0, \tag{2.57}$$

where n_0 is the refracting index of the immersion medium, and α_1 and β_1 are the angles of $\vec{k}_1$ and $\vec{k}_2$ with respect to the optical axis in the immersion medium. Substituting the phases in eq. (2.55) gives

$$P(\Delta z) \sim 2\vec{A}_1 \cdot \vec{A}_2 \cos\left(\frac{2\pi}{\lambda_0} n_2 \Delta z(\cos\alpha_0 - \cos\beta_0)\right). \tag{2.58}$$

The observed pitch, denoted as p'_{ax}, when shifting the stage is

$$p'_{\mathrm{ax}} = \frac{\lambda_0}{n_2(\cos\alpha_0 - \cos\beta_0)}. \tag{2.59}$$

2.12. SUPPLEMENTARY NOTE 3: DMD SETUP

The reflective grating model of the Digital Micromirror Device (DMD) allows simulation of its diffraction pattern based on its physical properties and alignment, as well as the wavelength used. This influences, besides the position of the diffraction orders, also the intensity distribution between the orders, which influences the modulation depth of the illumination pattern.

Unlike transparent gratings or Spatial Light Modulators (SLMs), where the reflection angle β is opposite to the incident angle α with respect to the normal of the array plane, the DMD behaves differently. Individual mirrors are tilted at an angle θ, leading to a phase difference between two consecutive mirrors, like a blazed grating. The individual mirrors rotate along the diagonal axis, requiring rotation of the DMD base by 45° to match the direction of the travelling wave. In a 1D scenario where all mirrors are directed in the same direction, the phase difference is expressed as

$$\phi(x) = \exp\left(ix\left[\frac{2\pi p_{\mathrm{px}}}{\lambda_0}, (\sin(\alpha) + \sin(\beta))\right]\right) \tag{2.60}$$

where λ_0 is the wavelength of the light and p_{px} is the pitch of a single mirror. A previously developed model and publicly available code is used to simulate the diffraction pattern of the DMD in this setup [52]. The DMD was positioned such that the incident beam was perpendicular and the reflected beam had an angle of $\gamma = 2\theta$ with respect to the base of the DMD (fig. 2.10a). Using a micromirror pitch of 13.68 µm, a repeating pattern of three pixels on and off, and a wavelength of 638 nm, the diffraction pattern in the Fourier plane behind a lens with focal length f was simulated (fig. 2.10b). The intensity of the zeroth and first orders are shown in fig. 2.10c, with corresponding relative intensity values of 0.81 for the zeroth order, and 0.18 and 0.44 for the first orders. The difference in intensity affects the maximum modulation depth m_{max} of the illumination pattern that can be achieved, if a perfect polarization is assumed. In case the relative intensity peaks of 0.81 and 0.44 are used for illumination, $m_{\mathrm{max}} = 0.96$. If the relative intensity of 0.18 as the first order is used, $m_{\mathrm{max}} = 0.77$,

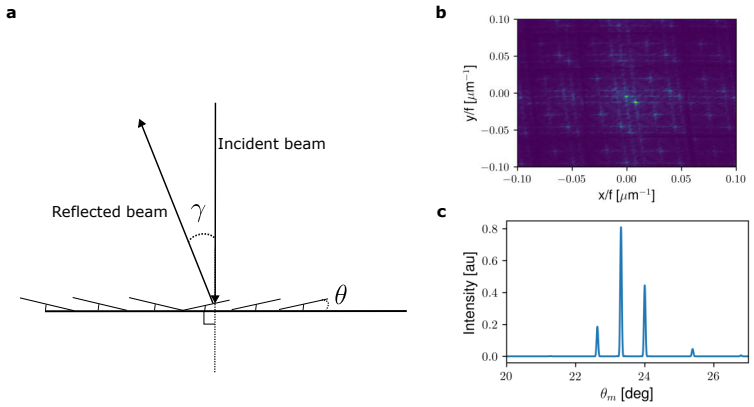


Figure 2.10: **a**, The layout of the DMD in our setup. θ is the angle of the individual mirrors with respect to the base, which can be $-12°$ or $12°$. The setup is designed such that the incidence beam is perpendicular to the base of the DMD. With this design the reflected beam has an angle of $\gamma = 2\theta$ with the normal of the mirror. **b**, The simulated diffraction pattern, after a lens with focal length f, of the light reflected onto the DMD used in this experiment. **c**, The relative intensity values of the zeroth and first orders are plotted as a function of the reflected angle. The zeroth order has an intensity value of 0.81, while the first orders have values of 0.18 and 0.44.

2.13. SUPPLEMENTARY FIGURES

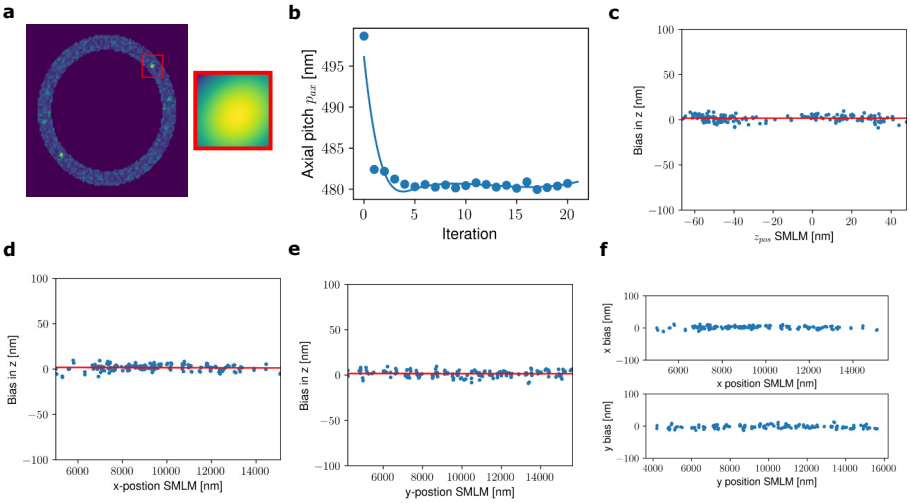


Figure 2.11: **a**, The spatial spectrum obtained from the Fourier peak finding algorithm. The position of the peak corresponds to a lateral pitch p_{lat} of 454 nm, located at an azimuthal angle of 42°. The zoomed-in red box shows the upsampled area around the peak for more precise estimation. **b**, The value for the axial pitch p_{ax} as a result of the pattern refinement, p_{ax} converges to 481 nm. **c-e**, The bias, defined as the difference between the SMLM MLE and the MLE only using the illumination pattern, for the z-position of detection clusters, as a function of the x,y and z position of that cluster found in the SMLM results. **f**, The bias, defined similarly as in **c-e**, but of the x and y position estimation. All bias plots show straight linear behaviour around a bias of 0, which indicates there is no systematic error in the pattern estimation.

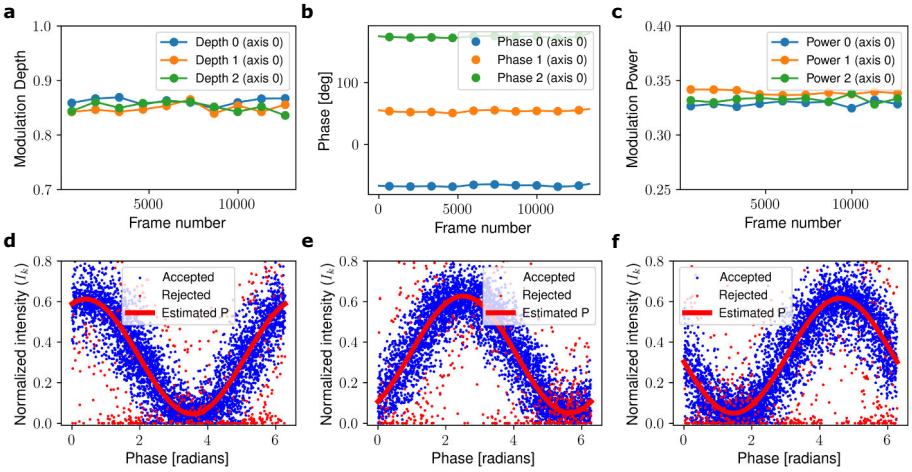


Figure 2.12: **a-c**, the estimated phases ψ_{lk}, modulation depths m_{lk} and illumination power η_{lk} for each pattern phase, as a function over time. **d-f**, The intensities of a random subset of all localizations as a function of their position projected on a single period. The red line corresponds to the estimated pattern for that each phase step and all blue-coloured spots satisfy the maximum modulation error condition and are used in the ZIMFLUX estimation.

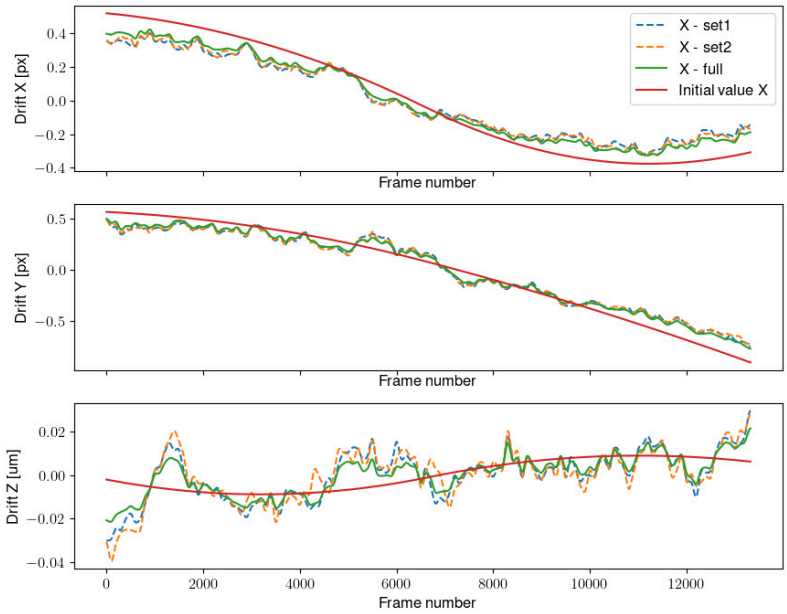


Figure 2.13: The estimated drift [49] based on all N SMLM localizations (full set) and on random subsets with a size $N/2$ localizations (set 1, set 2). The precision of the full set drift estimation is determined by taking the standard deviation of the difference between both drift estimations from set 1 and set 2, divided by $\sqrt{2}$, assuming that the precision of the drift scales with $1/\sqrt{N}$ localizations. The precision of the drift estimations are 1 nm for the x and y direction and 4 nm for the z-direction.

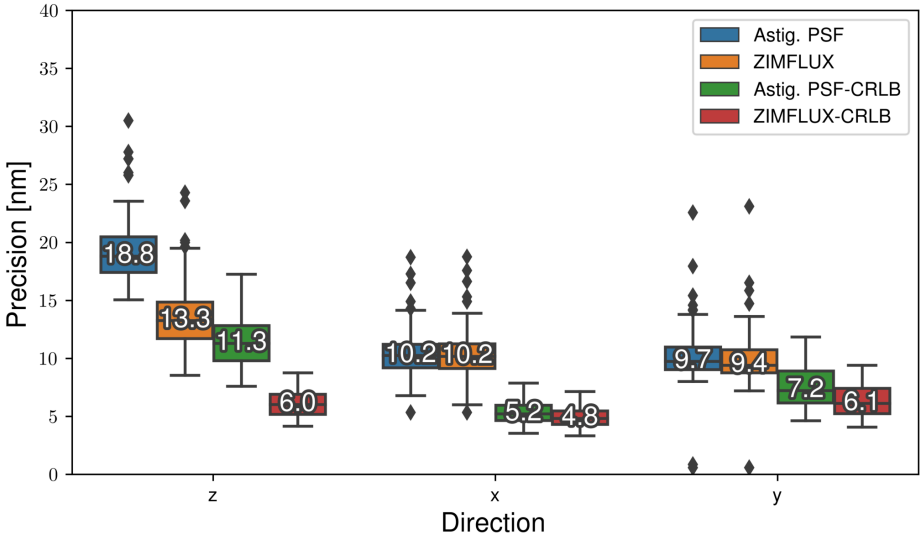


Figure 2.14: The found precision and the CRLB for all directions for the proof of concept ZIMFLUX and SMLM estimations, with the median values listed in the boxes.

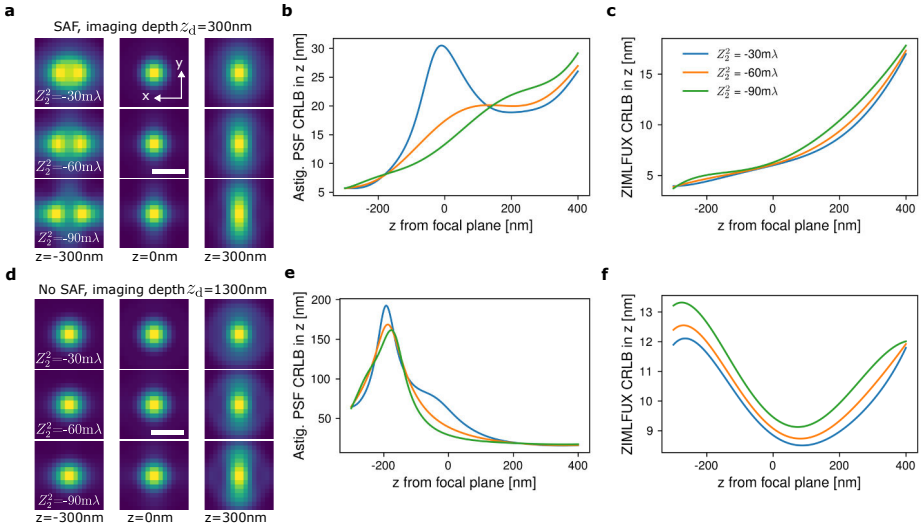


Figure 2.15: **a**, The PSF is shown at various z distances from the focal plane for different values of the astigmatic Zernike coefficient Z_2^2 ($-30\,\mathrm{m}\lambda$, $-60\,\mathrm{m}\lambda$, $-90\,\mathrm{m}\lambda$) at an imaging depth of 300 nm. The parameters used are similar to the experimental conditions (an oil immersion objective, refractive index mounting medium of 1.33, and signal and background photon count of 2800 and 8). **b, c**, The CRLB of the astigmatic PSF and ZIMFLUX axial localization are shown as a function of different distances from the focal plane at an imaging depth of 300 nm. SAF occurs due to refractive index mismatch, which lowers the CRLB near the coverslip and decreases with increasing distance from the coverslip. The illumination pattern has a modulation depth of 0.85 and an axial and lateral pitch of 492 nm and 452 nm, respectively. The CRLB of ZIMFLUX is nearly independent of the level of astigmatism and is approximately half of the CRLB of the astigmatic PSF. **d**-**f**, Similar to **a**-**c** but at an imaging depth of 1300 nm, where the effect of SAF is negligible. The refractive index mismatch significantly affects the axial localization precision of the astigmatic PSF (**e**), but ZIMFLUX enables a higher precision when imaging deeper into the sample, which is a 10-fold improvement for negative z values, that goes down to approximately 2-fold for positive z values (**f**).

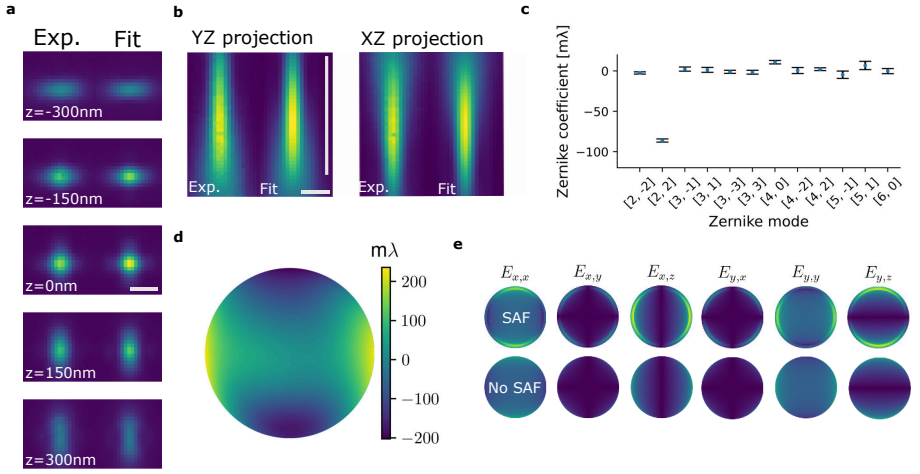


Figure 2.16: **a**, A through-focus scan of a bead sample embedded in a medium with a refractive index of 1.46. The measured and fitted Point Spread Functions (PSF) are displayed on the left-hand side and right-hand side, respectively. **b**, The YZ and XZ projection of the same bead as in **a**. Scale bars in **a** and **b**, 500 nm. **c**, The fitted Zernike aberration coefficients that comprise the aberrated wavefront are presented, using the notation [radial degree, azimuthal degree]. The astigmatic Zernike coefficient Z_2^2 is found to be $-87(3)\,\mathrm{m}\lambda$. **d**, The experimental aberrated wavefront, retrieved by constructing it from the determined Zernike coefficients, has an RMS of $87.4\,\mathrm{m}\lambda$. **e**, The electric field components at the pupil plane, which are normalized and exclude phase aberrations, are simulated for experimental conditions involving an emitter at the focal plane with an imaging depth of 150 nm. In the upper row (SAF), the mounting medium had a refractive index of 1.33, while in the lower row (No SAF) the refractive index was matched to the immersion oil, at 1.518. The subscript notation for the electric fields corresponds to the theory section.

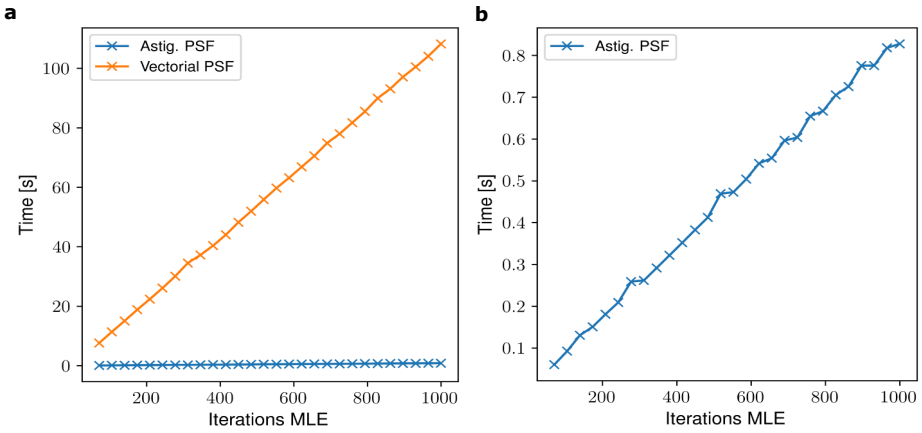


Figure 2.17: **a**, The computational time for the maximum likelihood estimation (MLE) for the vectorial PSF as implemented in this paper and solely an astigmatic PSF, which is defined in previous work [40], is shown as a function of iterations (It). The computations are performed on the NVIDIA GeForce RTX 3060 GPU using PyTorch and on pre-compiled code using TorchScript. The MLE is conducted on a batch of 100 spots. The slope of the curves is 108 ms/It for the vectorial PSF and 0.8 ms/It for the astigmatic PSF. **b**, The computational time for the astigmatic PSF is presented on a different y-scale to enhance visualization.

BIBLIOGRAPHY

[1] Pieter Van Velde et al. “ZIMFLUX: Single molecule localization microscopy with patterned illumination in 3D”. In: *Optics Express* 31.25 (2023), pp. 42701–42722.

[2] Mickaël Lelek et al. “Single-molecule localization microscopy”. In: *Nature Reviews Methods Primers* 1.1 (2021), p. 39.

[3] Stefan W Hell. “Microscopy and its focal switch”. In: *Nature Methods* 6.1 (2009), pp. 24–32.

[4] Bo Huang, Hazen Babcock, and Xiaowei Zhuang. “Breaking the diffraction barrier: super-resolution imaging of cells”. In: *Cell* 143.7 (2010), pp. 1047–1058.

[5] Ke Xu, Guisheng Zhong, and Xiaowei Zhuang. “Actin, spectrin, and associated proteins form a periodic cytoskeletal structure in axons”. In: *Science* 339.6118 (2013), pp. 452–456.

[6] Ylli Doksani et al. “Super-resolution fluorescence imaging of telomeres reveals TRF2-dependent T-loop formation”. In: *Cell* 155.2 (2013), pp. 345–356.

[7] Adish Dani et al. “Superresolution imaging of chemical synapses in the brain”. In: *Neuron* 68.5 (2010), pp. 843–856.

[8] Mikael P Backlund et al. “The double-helix point spread function enables precise and accurate measurement of 3D single-molecule localization and orientation”. In: *Single Molecule Spectroscopy and Superresolution Imaging VI*. Vol. 8590. Proceedings of SPIE. SPIE. 2013, pp. 121–131.

[9] Sudhakar Prasad. “Rotating point spread function via pupil-phase engineering”. In: *Optics Letters* 38.4 (2013), pp. 585–587.

[10] Yoav Shechtman et al. “Optimal point spread function design for 3D imaging”. In: *Physical Review Letters* 113.13 (2014), p. 133902.

[11] S Jia, J Vaughan, and X. Zhuang. “Isotropic three-dimensional super-resolution imaging with a self-bending point spread function”. In: *Nature Photonics* 8 (2014).

[12] David Baddeley, Mark B Cannell, and Christian Soeller. “Three-dimensional sub-100 nm super-resolution imaging of biological samples using a phase ramp in the objective pupil”. In: *Nano Research* 4 (2011), pp. 589–598.

[13] Matthew D Lew et al. “Corkscrew point spread function for far-field three-dimensional nanoscale localization of pointlike objects”. In: *Optics Letters* 36.2 (2011), pp. 202–204.

[14] Andrey Aristov et al. “ZOLA-3D allows flexible 3D localization microscopy over an adjustable axial range”. In: *Nature Communications* 9.1 (2018), p. 2409.

[15] Yiming Li et al. “Real-time 3D single-molecule localization using experimental point spread functions”. In: *Nature Methods* 15.5 (2018), pp. 367–369.

[16] Bo Huang et al. “Three-dimensional super-resolution imaging by stochastic optical reconstruction microscopy”. In: *Science* 319.5864 (2008), pp. 810–813.

[17] Gleb Shtengel et al. “Interferometric fluorescent super-resolution microscopy resolves 3D cellular ultrastructure”. In: *Proceedings of the National Academy of Sciences* 106.9 (2009), pp. 3125–3130.

[18] Guanshi Wang et al. “Single-molecule real-time 3D imaging of the transcription cycle by modulation interferometry”. In: *Cell* 167.7 (2016), pp. 1839–1852.

[19] Daniel Aquino et al. “Two-color nanoscopy of three-dimensional volumes by 4Pi detection of stochastically switched fluorophores”. In: *Nature Methods* 8.4 (2011), pp. 353–359.

[20] Fang Huang et al. “Ultra-high resolution 3D imaging of whole cells”. In: *Cell* 166.4 (2016), pp. 1028–1040.

[21] Anindita Dasgupta et al. “Direct supercritical angle localization microscopy for nanometer 3D superresolution”. In: *Nature Communications* 12.1 (2021), pp. 1–9.

[22] Martin Oheim, Adi Salomon, and Maia Brunstein. “Supercritical angle fluorescence microscopy and spectroscopy”. In: *Biophysical Journal* 118.10 (2020), pp. 2339–2348.

[23] Dylan Kalisvaart et al. “Precision in iterative modulation enhanced single-molecule localization microscopy”. In: *Biophysical Journal* 121.12 (2022), pp. 2279–2289.

[24] Francisco Balzarotti et al. “Nanometer resolution imaging and tracking of fluorescent molecules with minimal photon fluxes”. In: *Science* 355.6325 (2017), pp. 606–612.

[25] Klaus C Gwosch et al. “MINFLUX nanoscopy delivers 3D multicolor nanometer resolution in cells”. In: *Nature Methods* 17.2 (2020), pp. 217–224.

[26] Loïc Reymond et al. “SIMPLE: Structured illumination based point localization estimator with enhanced precision”. In: *Optics Express* 27.17 (2019), pp. 24578–24590.

[27] Jelmer Cnossen et al. “Localization microscopy at doubled precision with patterned illumination”. In: *Nature Methods* 17.1 (2020), pp. 59–63.

[28] Pierre Jouchet et al. “Nanometric axial localization of single fluorescent molecules with modulated excitation”. In: *Nature Photonics* 15.4 (2021), pp. 297–304.

[29] Lusheng Gu et al. “Molecular-scale axial localization by repetitive optical selective exposure”. In: *Nature Methods* 18.4 (2021), pp. 369–373.

[30] S Stallinga and B Rieger. “Accuracy of the Gaussian point spread function model in 2D localization microscopy”. In: *Optics Express* 18 (2010), pp. 24461–24476.

[31] Marijn E Siemons, Lukas C Kapitein, and Sjoerd Stallinga. "Axial accuracy in localization microscopy with 3D point spread function engineering". In: *Optics Express* 30.16 (2022), pp. 28290–28300.

[32] Carlas Smith et al. "Simultaneous measurement of emission color and 3D position of single molecules". In: *Optics Express* 24.5 (2016), pp. 4996–5013.

[33] Christiaan N Hulleman et al. "Simultaneous orientation and 3D localization microscopy with a Vortex point spread function". In: *Nature Communications* 12.1 (2021), pp. 1–14.

[34] Marijn Siemons et al. "High precision wavefront control in point spread function engineering for single emitter localization". In: *Optics Express* 26.7 (2018), pp. 8397–8416.

[35] Tony Wilson, R Juškaitis, and P Higdon. "The imaging of dielectric point scatterers in conventional and confocal polarisation microscopes". In: *Optics Communications* 141.5-6 (1997), pp. 298–313.

[36] Peter Török, Paul D Higdon, and Tony Wilson. "Theory for confocal and conventional microscopes imaging small dielectric scatterers". In: *Journal of Modern Optics* 45.8 (1998), pp. 1681–1698.

[37] Tobias Liaudat et al. "Rethinking data-driven point spread function modeling with a differentiable optical model". In: *Inverse Problems* 39.3 (2023), p. 035008.

[38] Sheng Liu et al. "Three dimensional single molecule localization using a phase retrieved pupil function". In: *Optics Express* 21.24 (2013), pp. 29462–29487.

[39] Jörg Enderlein, Thomas Ruckstuhl, and Stefan Seeger. "Highly efficient optical detection of surface-generated fluorescence". In: *Applied Optics* 38.4 (1999), pp. 724–732.

[40] Carlas S Smith et al. "Fast, single-molecule localization that achieves theoretically minimum uncertainty". In: *Nature Methods* 7.5 (2010), pp. 373–375.

[41] Carlas S Smith et al. "Probability-based particle detection that enables threshold-free and robust in vivo single-molecule tracking". In: *Molecular Biology of the Cell* 26.22 (2015), pp. 4057–4062.

[42] Fang Huang et al. "Video-rate nanoscopy using sCMOS camera–specific single-molecule localization algorithms". In: *Nature Methods* 10.7 (2013), pp. 653–658.

[43] CS Smith et al. "Iterative linear focal-plane wavefront correction". In: *Journal of the Optical Society of America A* 30.10 (2013), pp. 2002–2011.

[44] GATTAquant. *Technical FAQ*. https://www.gattaquant.com/faq. [Online; accessed 29-March-2023]. 2023.

[45] Jürgen J Schmied et al. "DNA origami nanopillars as standards for three-dimensional superresolution microscopy". In: *Nano Letters* 13.2 (2013), pp. 781–785.

[46] James C Mullikin et al. "Methods for CCD camera characterization". In: *Image Acquisition and Scientific Imaging Systems*. Vol. 2173. Spie. 1994, pp. 73–84.

[47] Robert J Noll. “Zernike polynomials and atmospheric turbulence”. In: *Journal of the Optical Society of America* 66.3 (1976), pp. 207–211.

[48] Fang Huang et al. “Simultaneous multiple-emitter fitting for single molecule super-resolution imaging”. In: *Biomedical Optics Express* 2.5 (2011), pp. 1377–1393.

[49] Jelmer Cnossen et al. “Drift correction in localization microscopy using entropy minimization”. In: *Optics Express* 29.18 (2021), pp. 27961–27974.

[50] Marijn Siemons et al. “Comparing strategies for deep astigmatism-based single-molecule localization microscopy”. In: *Biomedical Optics Express* 11.2 (2020), pp. 735–751.

[51] Shih-Te Hung et al. “Adaptive optics in single objective inclined light sheet microscopy enables three-dimensional localization microscopy in adult Drosophila brains”. In: *Frontiers in Neuroscience* 16 (2022), p. 954949.

[52] Peter T Brown et al. “Multicolor structured illumination microscopy and quantitative control of polychromatic light with a digital micromirror device”. In: *Biomedical Optics Express* 12.6 (2021), pp. 3700–3716.

3

LIVE CELL MRNA IMAGING IN YEAST: FRAMEWORK FOR STUDYING MRNA TRANSPORT THROUGH THE NUCLEAR PORE COMPLEX

Pieter VAN VELDE, Mathias HAMMER, Ammeret ROSSOUW, Brian TRAN, Anyee E. LI, Graham LATINO, Azra LARI, Bernd RIEGER, Ben MONTPETIT, David GRUNWALD

Messenger RNA (mRNA) export in yeast cells occurs through nuclear pores, large nanomachines serving as gateways between the nucleus and cytoplasm. While there is extensive knowledge on the structure and composition of the nuclear pore complex (NPC), the dynamics and selectivity of mRNA transport through NPCs in yeast remain poorly understood. This study presents a comprehensive framework for 2D live cell mRNA imaging in yeast, utilizing low laser power widefield fluorescence microscopy and avoiding cell wall digestion. This approach ensures minimal stress on cells and provides an accessible and cost-effective method for studying mRNA transport dynamics. This method has a time resolution of 20 ms, allowing the capture of highly transient interactions in living yeast cells.

The fluorescently tagged NE is automatically localized by fitting the intensity profile with a ring model consisting of the generalized logistic function and a normal distribution, yielding a precision measure of 13 nm for NE localization. Biological validation of the

This chapter is based on a manuscript in preparation.

*NE localization is achieved by measuring distances between different nuclear pore complex components, which are consistent with the known structure. We labeled nucleoporins (Nups) Nup60 and Nup82 with mKate for NE localization. Alongside the Nups, we imaged three mRNA transcripts (*GFA1*,* MYO2*, and* TRA1*) using an eGFP-PP7 stem-loop construct. For mRNA detection and localization, we utilized a Convolutional Neural Network (CNN) to estimate non-uniform background in images, which improved spot detection accuracy and localization precision. This reduced the false positive detection for mRNA from 40% to 16% and enhancing localization precision by up to 800%, depending on the non-uniformity of the background. The total precision, including stage drift over time, registration of the two-color channels, NE, and RNA localization, is calculated to be 49 nm.*

Zooming into the mRNA traces that traverse the NPC, we revealed distinct transport dynamics for different transcripts. The presence of docking sites within the NPC is visible as a bimodal probability of mRNA localization during transport, with a peak on the nuclear side and the cytoplasmic side. The mean position of nuclear binding site with respect to the labelled Nups were determined to be -76 ± 5 *nm for* GFA1, -80 ± 4 *nm for* MYO2, *and* -67 ± 5 *nm for* TRA1. *The mean cytoplasmic binding site locations were determined to be* 84 ± 5 *nm for* GFA1, 74 ± 4 *nm for* MYO2, *and* 71 ± 4 *nm for* TRA1.

Failed transport events provided further insights, showing that (mRNA) TRA1 *tends to re-enter the NPC closer to the nuclear side by a factor of 30% compared to the other mRNAs. Together with the nuclear binding site of* TRA1 *lying closer to the NPC during transport, this suggests a different interaction with the NPC. These findings suggest interactions variability between NPCs and messenger ribonucleoprotein (mRNP) granules amongst different transcripts, which may be due to differences in mRNP complex formation or NPC structural adaptations.*

3.1. INTRODUCTION

In eukaryotic cells, transcription occurs in the nucleus and translation in the cytoplasm, separated by the nuclear envelope (NE). To bridge this divide, mRNA is transported through the nuclear pore complex (NPC), a protein structure made of about 30 different nucleoporins (Nups) arranged in multiples of eight, forming a channel between the nucleus and cytoplasm [1]. Increasing evidence suggests that the NPC plays an active role in gene regulation, affecting mRNA processing, translation, and export efficiency [2, 3, 4, 5, 6]. Studying mRNA interactions with the NPC sheds light on selective transport mechanisms and the emergence of transport inefficiencies or abnormalities, which have been linked to diseases [7].

mRNA-NPC interactions have been extensively studied using live-cell imaging in both yeast and mammalian cells with MS2 or PP7 fluorescent labeling systems [8, 9, 10, 11, 12, 13, 14, 15, 16, 17]. Mammalian cells generally offer better imaging conditions, but yeast provides a cost-effective and genetically accessible alternative to study and challenge mRNA transport properties. A major challenge in both cell types has been imaging enough events, with the major bottleneck historically being data analysis. A high-throughput, verified analysis pipeline would enable studying several types of transcripts, or other more complex situations with multiple factors to manipulate, which has been impossible so far [18, 19, 20, 21, 22].

Traditional imaging methods in yeast, such as widefield and confocal microscopy, introduce stress. Widefield microscopy requires cell wall digestion to generate enough signal while confocal microscopy uses high-power lasers to increase signal, risking phototoxicity [12, 13, 23]. To minimize stress conditions, we explored optical clearing through adjusting the refractive index of the imaging media instead of cell wall digestion, combined with widefield imaging (low power density) [12, 24]. However, RI adjustments with substances like Sorbitol, Glycerol, Iohexol, or Iodixanol, among others, may affect viability and vitality of the cells [25, 26, 27, 28, 29]. We developed an imaging buffer with optimal RI for yeast cells, maintaining viability and vitality like SC-His medium.

Even then, the combination of short exposure times (10's of ms), low excitation power density and remaining signal scatter caused by (1) the difference between the R.I. of the intact cell wall and the imaging-growth media that matching the average R.I. of the yeast cells, and (2) the remaining R.I. mismatch between immersion oil and imaging-growth media, result in low signal-to-noise ratios (SNR) further complicated by non-uniform background. To address this vexing situation, we apply a convolutional neural network (CNN) to estimate local background [30]. This estimated background is incorporated into the imaging model to detect mRNA with high sensitivity. We use the Generalized Likelihood Ratio Test (GLRT) to detect low-SNR spots with high sensitivity and control false positives, enabling automatic single-molecule tracking [31, 32]. The GLRT is the most powerful among all level-α tests, enabling detection of low signal-to-noise ratio spots, using a non-arbitrary threshold based on significance level α. The efficient detection and the low density of labelled mRNA per frame per cell allow fully automatic single-molecule tracking, enabling high-throughput analysis.

Robust localization of the NE in yeast has been impossible in the past, severely limiting the detailed analysis of export traces compared to mammalian cells [12]. We solved this problem by estimating the intensity profile of the NE using a Gaussian distribution

combined with the generalized logistic function [33]. This approach can account for the differences in background fluorescent signal inside and outside of the nucleus and the highly variable NE fluorescent signal allowing the automated analysis of multiple cells in the field of view. This method was validated by measuring in vivo distances between Dbp5 and Nup82/Nup170/Nup60, consistent with the yeast NPC structure [1].
Using the PP7 RNA labeling system, we imaged three mRNA transcripts (*GFA1*, *MYO2*, and *TRA1*) in living, intact haploid yeast. Our results suggest NPC-mRNP interactions vary for different transcripts. We measured export times and found transcript-specific binding site differences along the NPC axis. Precise NE localization enabled us to observe mRNA acceleration through the center of the pore. This motion was confined to a path perpendicular to the NE, consistent with movement through the narrow central channel of the NPC. Notably, failed transport events showed *TRA1* mRNA localizing near the nuclear side of the NPC, indicating transcript-specific NPC interactions.

3.2. RESULTS

3.2.1. REFRACTIVE INDEX ADJUSTED MEDIA

Spherical aberration from refractive index (RI) differences between cell walls, culture medium, and cover glasses can be minimized by digesting cell walls or adjusting the RI of the immersion or culture medium [24]. The digestion of the yeast cell wall can be physically interpreted as an adjustment of the overall RI of the yeast cell, especially since Sorbitol, which is used to adjust the osmolarity of the buffer in which the spheroplasts are kept, does also impact the RI of the buffer [12]. This method has a limited window for observation; until the cell wall recovers, which adds an anomalous energetic effort for the cells metabolism and hence might impact observed processes, or limit targets to components of the cell wall building machinery of the cell.
Matching the R.I. of the culture or imaging media therefore seem favorable, but effective refractive indices for yeast cell walls have only been estimated (1.45–1.46) in the literature so far [34] or were based on Rayleigh-Gauss scattering measurements of effective refractive indices for whole bacterial cells (1.42, *Staphylococcus aureus*) with the caveat of applying a method for homogenous substances to cells [35].
We hence established the effective R.I. of live yeast cells through optical clearing experiments (see Material and Methods, section 3.4.1) to be 1.393 in log-phase, 1.395 during exponential growth and 1.401 in the post-diauxic phase. The R.I. of L-Histidine dropout growth medium (SC-His) at 30 °C is 1.3350, 1.5H cover glasses have a R.I. of 1.5255 and the immersion medium (Olympus Type F) has a R.I. of 1.5180. Both, adjusting the R.I. of the immersion media and of the culture media has been used in the literature [36, 24]. We decided against adjusting the immersion media as changes of its composition and its R.I. can compromise the objective performance including its color correction (ISO 8255-1).

Table 3.1: Osmolarity, viability and vitality of yeast media with adjusted refractive index.

Media		RI at 30 °C ($\pm 2.5 \times 10^{-4}$)	Avg. osmolarity (mOsm/kg)	Viability (%)	Vitality (%)
SC-His		1.3350	163 ± 16	79.95 ± 8.21	83.49 ± 3.22
Glycerol		1.3984	6413 ± 190	45.30 ± 0.28	21.30 ± 2.12
Sorbitol		1.4015	2770 ± 30	19.90 ± 27.1	12.00 ± 8.34
Iohexol	low	1.4012	660 ± 39	91.93 ± 1.50	92.97 ± 4.54
	high	1.4782	1034 ± 20	81.90 ± 2.55	90.85 ± 3.61
Iodixanol	low	1.4012	374 ± 15	85.57 ± 4.49	91.27 ± 1.25
	high	1.5150	515 ± 45	93.90 ± 0.71	79.30 ± 5.94

The R.I. of yeast culture medium can be adjusted by adding higher R.I. reagents. Sorbitol [27], Glycerol [28], dimethyl sulfoxide [29], Iohexol (Histodenz) and Iodixanol (OptiPrep) [25, 26] have been used for this purpose. Adding R.I. adjusting reagents to any growth media comes with the concern of changing the osmolality and viscosity of the media, both of which can impact cell growth, or their viability and vitality. Such negative impacts could theoretically be mitigated by limiting the duration of exposure of the cells to the adjusted media. For yeast cells, with a cell cycle duration in the range of an hour, however, even an unrealistic short imaging time frame of 10 minutes would represent a significant portion of the cell cycle. Maintaining growth conditions therefore is imperative for R.I. adjusted media.
The target range for the R.I. of the ideal imaging media lies between 1.395 (the R.I. of yeast cells in log phase) and 1.5180 (the R.I. of immersion oil). Table 3.1 lists the range of adjustable R.I., viability, vitality and osmolality for several reagents. As to be expected, lower molecular mass reagents like Sorbitol and Glycerol have a limited range of R.I. that can be realized while also featuring high osmolality values. Higher molecular mass reagents like Iohexol (Histodenz, typically used in gradient centrifugation) and Iodixanol (OptiPrep, an FDA approved contrast media) allow for a larger range of R.I. adjustment at lower osmolality ranges. We found that Iohexol and Iodixanol provided comparable viability and vitality for yeast growth compared to L-Histidine dropout growth medium (SC-His) with Iodixanol allowing for the largest range of R.I. adjustment at the lowest osmolality values, making Iodixanol the reagent of choice.

3.2.2. NUCLEAR ENVELOPE LOCALIZATION

To study translocation of mRNAs across the nuclear envelope (NE) an approximation of the position of the NE is essential. In mammalian cells either fluorescent labels [37] or transmitted light images [38] were used for this purpose. In yeast fluorescent labels were used [12], but determining the peak position was limited by weak signal, high background and strong curvature of the yeast NE. For this work we developed a method that allows analytical determination of the NE position enabling post analysis of tracking data similar to prior work in mammalian cells [8]. As before [12] we found the signal to background dynamic in yeast cells to be complex with the expected intensity profile gradually changing to the background intensity as distance from the NE increases. This provided two challenges: (1) generating a robust estimate or mask of the NE for initiating a fitting

routine, and (2) finding a model-bias free fitting function.
We solved the mask finding problem (1) by applying a Convolutional Neural Network (CNN) to an averaged image of the NE acquisition channel (1000 images per movie) to produce a mask (fig. 3.1B), which is applied to make an initial estimate of the NE position (fig. 3.1A). For details on the CNN, including training data, and the estimation procedure, see section 3.4.7. The model bias problem (2) was solved by changing from the traditionally used combination of a Gaussian function and linear background [37] to a more complex model.

We tested both the traditional linear function and a sigmoid function as well as generalized logistic function [33] in conjunction with a Gaussian curve and found the generalized logistic function was the bias free model with the lowest mean square error (section 3.4.7). Therefore, we selected the sum of a generalized logistic function and Gaussian curve as fitting model.

$$I(n) = \text{Generalized logistic function} + \text{Gaussian distribution}, \tag{3.1}$$

where I is the intensity profile normal to the initially estimated NE location and n the position along that normal (section 3.4.7). $I(n)$ was then estimated at every position of the initially estimated NE location (fig. 3.1A), and the NE position was updated to match the estimated peak of the Gaussian distribution. An example of the raw data, the model fitted data, the overlap, and updated fit are shown (fig. 3.1C). The NE position was updated using this process for all the masks found in the FOV (fig. 3.1D).
We repeat this procedure to determine our localization precision for the NE based on 2140 cells. To this end we used the first 250 odd and even frames of the NE channel movie. The distribution of the difference between the estimated peaks from both sets of frames (even and odd) is centered around zero, with a standard deviation $\sigma_{\text{NE}} = 13\,\text{nm}$. We find that the relative mean error E for all n (see fig. 3.1C), is centered around zero, within a standard deviation of E smaller than 2%, which indicates that there are no systematic errors (fig. 3.7B). The mean squared error (MSE) between the fitted model and the data is found to be lower than 8 photons^2 for all n (fig. 3.7C). For the definition of eq. (3.1) and the details of the estimation procedure, we refer to section 3.4.7.

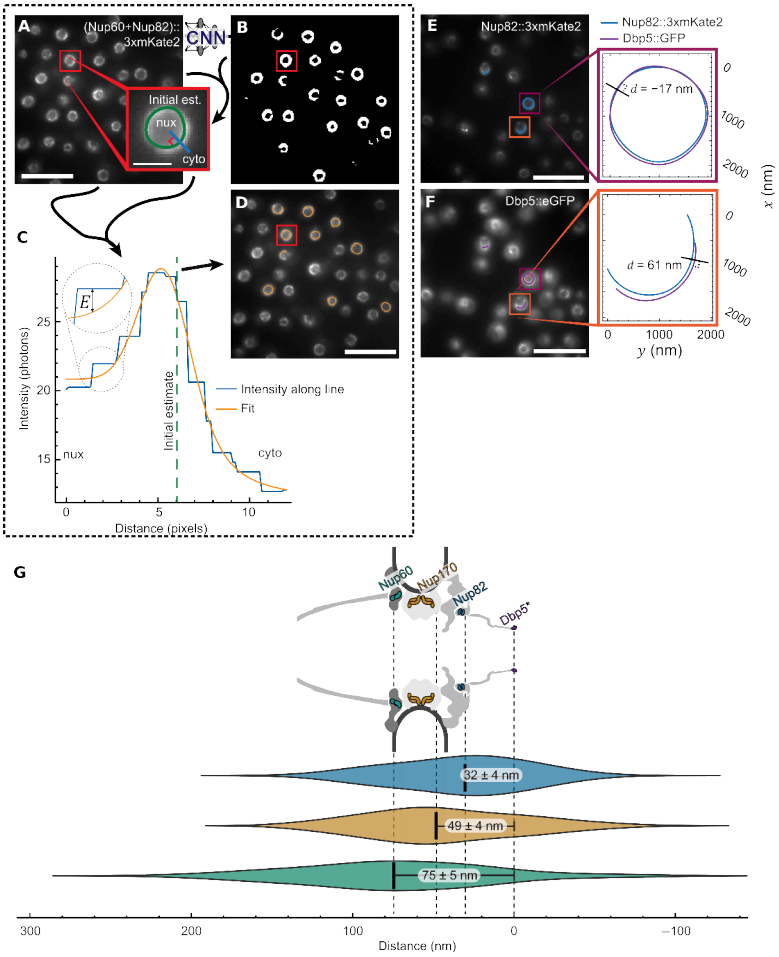


Figure 3.1: **Localization of the Nuclear Envelope (NE). (A–D, dashed box)** The NE fitting procedure. **(A)** Field of view (FOV) of an image representing the averaged first 250 frames of (Nup60+Nup82)::3xmKate2, and **(B)** the associated convolutional neural network (CNN) generated mask. Highlighted single cell (A, blowout) depicting the initial NE position estimation (green) based on the mask (B), with a normal line extending 12 pixels from the nucleus (n) to the cytoplasm (c) (scale bar = 2 µm). **(C)** Intensity profile (blue) along the normal line in (A), with the intensity fit (orange) compared to the initial estimation (green). To quantify the goodness of the fit, we introduce E, the error between the fitted model and observed data. **(D)** Presents the NE localizations within a FOV. **(E, F)** Provide an FOV example with dual-labeled Nuclear Pore Complex (NPC) components 3xmKate2::Nup82 (E) and GFP::Dbp5 (F), including two cases of NE position estimations for both color channels and their inter-distance denoted as d. The dotted line represents a perpendicular angle to the Dbp5::GFP fit. **(G)** Displays the distribution distances across the entire NE circumference between Dbp5::eGFP and Nup60, Nup82, or Nup170::3xmKate2 localizations (90 to 110 cells per distribution), in which the values listed are the mean ± the standard error (SE) of that mean (calculated as the square root of the corresponding diagonal element of the covariance matrix returned when fitting a normal distribution through least squares minimization using SciPy curve fit [39]); note that this error reflects the precision of the mean and not the width of the distribution itself. The one-way ANOVA revealed significant differences between the strains ($p \ll 10^{-5}$). Scale bars are 10 µm, unless otherwise noted.

BIOLOGICAL VALIDATION NE LOCALIZATION

To validate the NE localization, we measured the relative positions of three Nups (Nup60; Nup82; Nup170) against the same reference (Dbp-5) and compared our findings to the expected distances based on structural information. The expected values were derived from a combined interpretation of PDB structures 7TBI and 8ZZC [1, 40]. PDB structure 8ZZC includes a comprehensive set of proteins but lacks coordinate data necessary for distance measurements. Therefore, we used PDB structure 7TBI for this purpose. Since Nup60 is absent in 7TBI, we substituted it with Nup145 (TYR 324 [auth 415]), which borders the coordinates closest to the C-terminus of Nup60 in 8ZZC. All Nup pairs were measured from C-terminus to C-terminus. By selecting proteins within the same NPC spoke, we found the distances shown in table 3.2.

We aimed to measure these distances in our experiment as follows: From a strain that contained Dbp-5 labeled with eGFP (Dbp-5::eGFP) we constructed three strains each labeled with one additional mKate2 (NupX::3xmKate2) tagged nucleoporin, either Nup60, Nup82 or Nup170 (fig. 3.1E,F). We repeated the NE localization procedure described in section 3.2.2 for each individual channel and calculated the distance between the NE localization indicated by NupX::3xmKate2 and that indicated by the Dbp-5::eGFP (a total of three localization pairs). The channels are physically registered as described in section 3.4.5, with a registration precision of 17 nm.

The distance d between the estimated NE location from both color channels was computed by constructing a line perpendicular to the tangent at the Dbp-5 NE location and calculating d from that location to the Nup NE location (fig. 3.1E,F) on that line. This procedure can be applied to any Dbp-5 NE location. This calculation was repeated for 90 to 110 cells; the resulting distributions of the distances d between Dbp-5::eGFP and NupX::3xmKate2 NE localizations are shown in fig. 3.1G. The fluorescent tags have a finite size and we do not exactly know how these impact the NPC structure, compared to the crystal structure. However, the match of the distances between the Nups support the efficacy of our approach for accurately estimating the NE position.

The distances found between Dbp-5 and Nup60, Nup82, and Nup170 are 75 nm (SE, 5 nm), 32 nm (SE, 4 nm), and 49 nm (SE, 4 nm), respectively, where SE is the standard error of the fitted mean; the distributions themselves are much broader (SD of about 50 nm, see fig. 3.1G). Comparing the experimental distances between Nup60, Nup82, and Nup170 against the known crystal structure of the nuclear pore complex yielded comparable results [1]. These results support the efficacy of the described approach for accurate estimation of the NE position.

Table 3.2: Comparison of experimentally derived distances between Nup60[a], Nup82, and Nup170 with crystalline structures of the nuclear pore complex. Experimental values are the mean, with the standard error (SE) of that mean propagated from the errors on the individual Dbp-5–Nup distances (90 to 110 cells per distance).

Nup Pair	Structural Coordinates	Crystalline (nm)	Experimental (nm)
Nup82, Nup170	Nup82 (GLN 713), Nup170 (ASP 1316)	19	17 (SE, 6)
Nup170, Nup60	Nup170 (ASP 1316), Nup145 (TYR 324)[a]	21	26 (SE, 7)
Nup82, Nup60	Nup82 (GLN 713), Nup145 (TYR 324)[a]	40	43 (SE, 7)

[a] Nup145 is used as a substitute for Nup60

IMPACT OF NUP60 AND NUP82 DUAL LABEL OF NE LOCALIZATION

For our mRNA export measurements, we engineered a strain in which the NE is defined by dual labeling with Nup60::mKate2 and Nup82::mKate2. This dual labeling affects our NE positioning as follows:
Assuming Pom152 represents the center of the NPC, structural data indicate that Nup60 and Nup82 are equidistant from Nup57 (24 nm and 26 nm, respectively), which lies in the same central plane as Pom152 [40]. Both Nup60 and Nup82 are approximately 20 nm from the central plane. Therefore, the combined fluorescence signal from Nup60::mKate2 and Nup82::mKate2 would localize around this central plane.
Assuming the signal is diffraction-limited, the theoretical Gaussian width is:

$$\sigma_{\text{mKate2}} \approx \frac{\lambda_{\text{mKate2}}}{4\,\text{NA}} = 109\,\text{nm}, \tag{3.2}$$

using $\lambda_{\text{mKate2}} = 633\,\text{nm}$ [41] and the numerical aperture NA = 1.45 of the objective (section 3.4.2).
The combined signal width becomes:

$$\sigma_{\text{combined}} = \sqrt{\sigma_{\text{mKate2}}^2 + \left(\frac{d}{2}\right)^2}, \tag{3.3}$$

where d is the distance between Nup60 and Nup82 (40 nm). Equation (3.3) tells us that for this construct the increase in σ_{combined} compared to σ_{mKate2} is less than 2%. Therefore, we do not expect the dual label to significantly affect the fitting procedure, compared to the single label used in the validation. These considerations ensure that the combined signal from the dual labeling represents the center of the NPC and does not adversely impact the accuracy of our NE localization in mRNA export studies.

3.2.3. RNA DETECTION & LOCALIZATION

The nature of the background signal while imaging stem loop tagged mRNA in yeast was found to be challenging in the past [12]. We originally provided a statistical framework utilizing a Generalized Likelihood Ratio Test or GLRT to address the low signal to background ratio for *in vivo* imaging of mRNAs in yeast [32]. However, the same way that NE localization could be improved we recognized that explicit treatment of local background, possible through the utilization of CNNs, could further improve particle detection. We found that improved GLRT methodology allowed us to utilize detection probabilities in the tracking process.

BACKGROUND ESTIMATION

The varying refractive indices (RI) of the imaging medium, yeast cell wall, and structures within the cell scatter light, even if the RI of the imaging media is optimized. Together with unbound coat protein GFP complex (CP-GFP), this light creates images with non-uniform backgrounds. The background is especially non-uniform for spots located at the edges of the nucleus with a relatively sharp drop in background signal between the nucleus and the cytoplasm (fig. 3.2A). The conventional single-molecule imaging model adopts a Gaussian point-spread function (PSF) that assumes a uniform background [42,

43]:

$$\mu(x,y) = \mathrm{PSF}(x,y) + bg_{\mathrm{co}}, \tag{3.4}$$

where $\mu(x,y)$ represents the expected photon count for a pixel at (x,y), and bg_{co} denotes the uniform background photon count per pixel. However, in our cellular environment, the background is non-uniform, which led to inaccuracies in spot detection and localization when the conventional model was deployed. To address this, we estimate a non-uniform background bg_{NN} from Poisson noise-corrupted images using a Convolutional Neural Network (CNN) with a U-Net++ architecture (see section 3.4.8), resulting in:

$$\mu(x,y) = \mathrm{PSF}(x,y) + \theta_{bg}\, bg_{\mathrm{NN}}(x,y), \tag{3.5}$$

where θ_{bg} is the mean background level (photons per pixel) estimated by MLE, while $bg_{\mathrm{NN}}(x,y)$ is *a priori* information from the CNN [30, 44]. For an example of normalized bg_{NN} across an entire cell see fig. 3.2A. Incorporating the non-uniform background $bg_{\mathrm{NN}}(x,y)$ into the imaging model rather than subtracting it prevented artifact creation when applying MLE (section 3.4.9). A more detailed version of the background-inclusive imaging model is presented in section 3.4.9.

To assess the level of background non-uniformity in our experiments, we define δ_{bg} as the standard deviation of photon counts per pixel within a Region of Interest (ROI) from the estimated $bg_{\mathrm{NN}}(x,y)$, which does not include Poissonian shot noise. Across ~37,000 evaluated candidate emitters, δ_{bg} exhibited a range of 0 to 20 photons (fig. 3.2B). The presence of δ_{bg} induces a model mismatch that affects conventional methods for spot localization and detection.

SPOT DETECTION AND LOCALIZATION

Our method for spot detection is detailed in section 3.4.10. To summarize, we segmented the nucleus (section 3.2.2), create a rectangular bounding box, with at least 2000 nm of space between the box and the NE on the cytoplasmic site, that included the nucleus, and applied the GLRT to each pixel within the bounding box. Each pixel was considered within the context of a 9×9 pixel ROI. The GLRT—recognized as the most effective test for a given significance (α-level) according to the Neyman–Pearson lemma [31, 32]—compares the maximum likelihood ($\mathscr{L}_{\max}$) of two models, one with a labeled mRNA molecule (signal + bg) and one without an mRNA molecule (bg only). The model used for the GLRT includes the estimated non-uniform background as described in section 3.2.3. The test statistic T_G is given by:

$$T_G(x,y) = 2\log\left(\frac{\mathscr{L}_{\max}(\text{signal}+\text{bg})}{\mathscr{L}_{\max}(\text{bg})}\right), \tag{3.6}$$

where (x,y) denotes the pixel position. For ROIs lacking signal, T_G aligns with a central chi-squared (χ^2) distribution, whereas for signal-present ROIs, it follows a non-central χ^2 distribution, with one degree of freedom in both cases [32]. Given that T_G for ROIs without signal follows the central χ^2 distribution, we set a threshold for T_G to establish a false positive probability (P_{FA}) of 5%. Given the large number of pixels in a 1,000-frame movie (2.5×10^6 for a 50×50 pixels bounding box), we adjust this rate to 5% using the Benjamini–Yekutieli method [32, 43] (see section 3.4.10). This False Discovery Rate

(FDR) control procedure is used to correct for multiple hypothesis testing. While the False Positive Rate (FPR) refers to the probability of falsely rejecting a single null hypothesis, the FDR specifically controls the expected proportion of false positives among all the rejected hypotheses (detected spots). By controlling the FDR, we limit the rate of incorrectly identifying spots (false positives) among the detected spots to 5%, thus increasing the reliability and validity of our detection results.

For our experiment, a case of non-uniform background, the conventional model's assumption of uniformity led to discrepancies between the T_G distribution for signal-absent ROIs and the χ^2 distribution, invalidating the established P_{FA} threshold (fig. 3.2C). Conversely, when the GT background was used, we saw that the T_G distribution for signal-absent ROIs matched the χ^2 distribution (fig. 3.2D).

To quantify the effect of this mismatch on the P_{FA} as well as the improvement demonstrated when an estimated background bg_{NN} was included (section 3.2.3), we simulate 2×10^5 ROIs with randomly generated backgrounds as outlined in section 3.4.8. The ROIs were corrupted with Poissonian shot noise to mimic experimental data and the actual false positive rate (P'_{FA}) is computed while aiming for a 5% P_{FA}. As shown in fig. 3.2E, with the ground truth background knowledge included, P'_{FA} equaled the expected P_{FA}. Using a uniform background model, P'_{FA} increased up to 40%, varying with δ_{bg}. Conversely, utilizing the estimated non-uniform background mitigated the model mismatch, keeping P'_{FA} below 16%.

Additionally, employing a uniform background model dramatically deteriorates the localization precision, causing it to increase as much as 8-fold that of the ground truth precision, depending on δ_{bg} (fig. 3.2F). This high value arises from the model mismatch for each ROI, which introduces a bias for each localization. Alternatively, we examined the impact of non-uniform background on localization precision. It was observed that when including bg_{NN}, the mean localization precision deteriorates by less than 20% (depending on δ_{bg}) compared to the precision achieved with the GT background knowledge for the same spots.

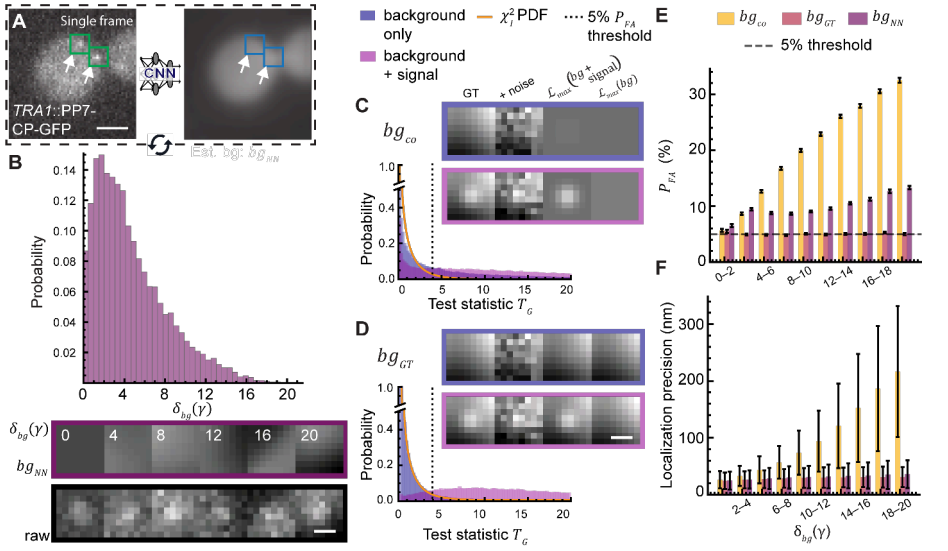


Figure 3.2: **Background Estimation for Non-uniform Backgrounds.** **(A)** A single time frame of (mRNA) *TRA1*::PP7-CP-GFP, illustrating the estimation of the non-uniform background bg_{NN} via a CNN. Light scattering due to the cell wall, varying refractive indices within the cell, and the presence of GFP-fused unbound coat protein (CP-GFP) results in this non-uniform background (scale bar is 2 µm). **(B)** The probability distribution (PDF) of δ_{bg}, defined as the standard deviation of photon counts within bg_{NN}, for each ROI across ~37,000 candidate emitters. The strip beneath the histogram shares its δ_{bg} axis and shows, for representative δ_{bg} values, the corresponding CNN background estimate bg_{NN} and the raw ROI. **(C)** Distribution of test statistics (T_G) for simulated ROIs including those devoid of signal (blue) and those with signal (magenta), using a uniform background bg_{co}. **(D)** Analogous to (C), but employing the ground truth (GT) background, showing distributions that align with theoretical expectations. **(E)** The actual false positive probability (P'_{FA}) set at 5%, analyzed across different δ_{bg} values for the scenarios using bg_{co}, bg_{NN}, and GT backgrounds. **(F)** Similar to (E) but focuses on localization precision.

3.2.4. MRNA SINGLE MOLECULE TRACKING

To study the dynamics of mRNA translocating the NE, we tagged and imaged three mRNA transcripts: *GFA1* (2154 nt), *MYO2* (4725 nt) and *TRA1* (11235 nt), length excluding PP7 cassette (24 repeats – 1,500 nt), (see section 3.4.1). The estimation of the drift over time, the registration of the two-color channels, and NE and RNA localization each have a corresponding precision defined as σ_{drift}, σ_{reg}, σ_{NE}, and σ_{RNA}, respectively. Each precision calculation is described in section 3.4, with the exception of σ_{NE}, which is defined in section 3.2.2. The combination of these precisions is the co-localization precision σ_{CoLoc}:

$$\sigma_{\mathrm{CoLoc}} = \sqrt{\sigma^2_{\mathrm{NE}} + \sigma^2_{\mathrm{drift}} + \sigma^2_{\mathrm{reg}} + \sigma^2_{\mathrm{RNA}}} = \sqrt{13^2 + 7^2 + 17^2 + 43^2} = 49\,\mathrm{nm}. \tag{3.7}$$

We imaged a total of 4,208 cells with tagged *GFA1*, *MYO2*, and *TRA1* mRNA, resulting in a total of 285,812 trajectories with an average observation time of approximately 275 ms, as detailed in table 3.3.

Table 3.3: Summary of the acquired single-molecule imaging data. Tracks are grouped by where they were observed: entirely on the nuclear side (Nux), entirely on the cytoplasmic side (Cyto), or crossing the NE (Crossing NE). That column counts every track that crosses the NE midplane, with no threshold applied. Cells are likewise grouped by whether any track in them crosses the NE. The subset of these tracks that is used for the transport analyses in this chapter is reported separately in table 3.6.

			Cells		Tracks from						
					without traces crossing NE			with traces crossing NE			
mRNA	Length (nt)	Movies	Without	With	Total	Nux	Cyto	Total	Nux	Cyto	Crossing NE
GFA1	2154	548	919	704	30777	2865	27325	86465	11472	67258	4612
MYO2	4725	505	758	599	24378	3050	20794	77251	11321	59777	3736
TRA1	11235	516	717	511	19498	2749	16325	47443	8786	33769	2890

256 × 256 pixel FoV; 128 nm pixel size; 20 ms frame rate; 20 s movie length

For tracking we used Trackpy [45, 46], given that the particle density was sparse below ~0.5 particles per frame. The tracking algorithm required a gap closing time, defined as the number of frames a particle can disappear (move out of focus) while still being "linked"—connected for the purposes of the search algorithm—to the same trace if it reappears. Missing spot positions were interpolated as start positions for GLRT detection. Links were removed if the false positive detection probability P_{FA} (section 3.4.10) surpassed a threshold of 20% (section 3.4.11) at any linearly interpolated position. The impact of this gap closing time on the nuclear and cytoplasmic binding sites is given in fig. 3.10. Across all gap closing distances (2 to 15 frames), the nuclear binding site of (mRNA) *TRA1* consistently remains closest to the center of the NPC compared to other mRNAs.

3.2.5. mRNA TRANSPORT THROUGH THE NPC

To study the transport dynamics of mRNA, we focus on traces of mRNA that have traversed an NPC; fig. 3.3A shows an exemplar trace. In prior studies varying criteria for a successful transport event were developed [9, 38, 37, 12, 8, 47, 48, 49]. Broadly speaking these criteria combined structural expectations with measurement imprecisions to reason for a distance on both sites of the NE that would suffice to identify a transport event. A uniform definition has not evolved and experimentally realized spatial and temporal measurement scales vary enough to question the value of a single, uniform distance being used as an *a priori* transport criteria. Furthermore, in living cells it is to be assumed that the NPC has at least some flexibility, limiting the use of structure-based transport thresholds.

For these reasons, we evaluated if a data-driven approach could be used to define a transport threshold. Data-driven methods demand much larger data sets (2–3 orders of magnitude) than available for prior published works that typically range around hundreds of traces. Our methodology advances of NE detection, explicit treatment of background in the GLRT framework and extension of GLRT probabilities to the gap closing problem in tracking mRNAs—allowed us to develop automated analysis pipelines that withstand visual inspection of traces and scaled our available trace data accordingly.

THRESHOLDS FOR IDENTIFYING TRANSPORT EVENTS

A signifying feature of mRNA export has been the finding of a bi-modal localization probability distribution there the peaks on either site of the NPC were interpreted as

binding sites for mRNAs pre- and post-transition through the central channel of the NPC [8]. To filter out stationary mRNA stuck in an NPC, we only selected traces which crossed the NPC midplane less than four times. We found that varying the distance at which a trace is classified as a transport event ($TH_{\text{transport}}$, fig. 3.3B) directly affects the sample size of transport traces and the resulting identification of binding sites. For instance, if $TH_{\text{transport}}$ was set equal to the colocalization precision of our measurements (49 nm), we find 3025 transport traces for *GFA1* mRNA. The resulting localization probability distribution followed a bimodal distribution with means $\mu_{\text{binding,nux}} = -67\,\text{nm}$ and $\mu_{\text{binding,cyto}} = 68\,\text{nm}$. Choosing $TH_{\text{transport}} = 2\sigma_{\text{CoLoc}} = 98\,\text{nm}$, resulted in 1390 transport traces and a shift in the bimodal localization probability distribution, now with means of $\mu_{\text{binding,nux}} = -86\,\text{nm}$ and $\mu_{\text{binding,cyto}} = 90\,\text{nm}$ (fig. 3.3C).

One inherent feature of past $TH_{\text{transport}}$ criteria is that they imposed symmetry on both sides of the NPC, although NPC structure does not imply symmetry between cytoplasmic filaments and nuclear basket features. We reason that the peak positions of the bimodal localization probability distribution provide a better measure for $TH_{\text{transport}}$ and can be defined by varying $TH_{\text{transport}}$ independently on the nuclear and cytoplasmic site of the NPC so that the difference between $TH'_{\text{transport}}$ and the resulting binding site μ_{binding} (aka peak position of the bimodal localization probability distribution) is zero (fig. 3.3D; see also fig. 3.10).

The calculated points $TH'_{\text{transport}}$ were used as threshold distance beyond which an mRNA transcript must be recorded traversing on both sides of an NPC for a trace to be classified as a transport trace. Track length statistics for the resulting trace populations are summarized in table 3.4.

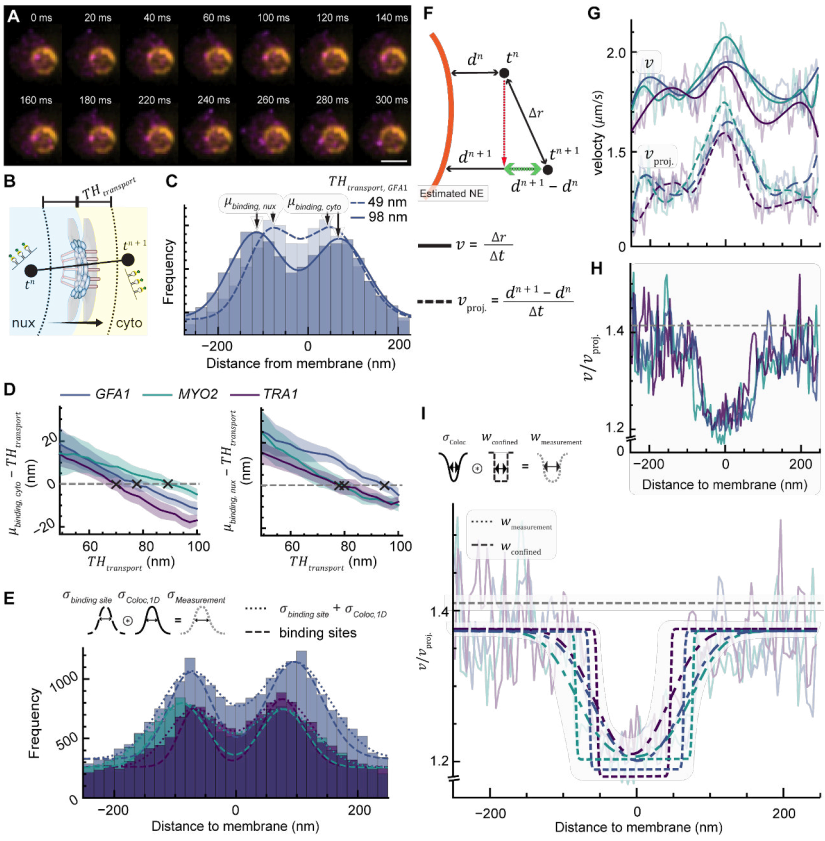


Figure 3.3: **mRNA transport analysis through the NPC. (A)** Exemplar time-lapse of mRNA translocating through the NPC. **(B)** Schematic of a transport trace crossing the NE from the nucleus (nux) to the cytoplasm (cyto), with the transport threshold $TH_{\text{transport}}$ indicated on either side. **(C)** Histogram of mRNA localization during transport as a function of distance from the membrane for different transport thresholds. **(D)** Transport threshold optimization: difference between $TH_{\text{transport}}$ and binding site position for nuclear and cytoplasmic sides. **(E)** Bimodal probability density function of mRNA localization during transport, indicating nuclear and cytoplasmic binding sites for *GFA1*, *MYO2*, and *TRA1*. **(F)** Definitions of the velocity v and the projected velocity v_{proj} of a trace relative to the estimated NE. **(G)** Velocities of mRNA transporting through the NPC as a function of distance from the NE. **(H)** The ratio between v and v_{proj}, compared to the expected value of $\sqrt{2}$ for a freely moving particle. **(I)** Confinement analysis: the inverted block pulse modeled using two sigmoids for the confined region, with deconvolved and experimental data for each strain.

Table 3.4: Track length summary statistics.

	Cells without transport events						Cells with transport events								
	nux			cyto			nux			cyto			transport		
mRNA	mean	med.	mode	mean	med.	mode	mean	med.	mode	mean	med.	mode	mean	med.	mode
GFA1	13.0	9	5	13.7	10	5	13.2	10	5	13.5	10	5	16.0	12	5
MYO2	12.3	9	5	13.7	10	5	13.3	10	5	13.8	10	5	14.9	12	5
TRA1	11.8	9	5	13.5	10	5	13.2	10	5	14.0	10	5	15.6	12	5

NPC BINDING SITES

Using $TH'_{\text{transport}}$ with differing values per transcript as well as for the nuclear and cytoplasmic side, we examined the bimodal probability density function (PDF) of $TH'_{\text{transport}}$ filtered mRNA transport traces for *GFA1*, *MYO2*, and *TRA1* mRNA. The observed distribution reflects the biological distribution of NPC binding sites convolved with the measurement imprecision, which we model as a normal distribution with $\sigma_{\text{CoLoc}}/\sqrt{2}$ (fig. 3.3E). The mean nucleoplasm binding site locations $\mu_{\text{binding,nux}}$ were determined to be -76 ± 5 nm for *GFA1*, -80 ± 4 nm for *MYO2*, -67 ± 5 nm for *TRA1*, and alongside standard deviations $\sigma_{\text{binding,nux}}$ of 42 ± 5 nm, 42 ± 5 nm, and 32 ± 5 nm, respectively.
In the cytoplasm, the mean binding site locations $\mu_{\text{binding,cyto}}$ were calculated as 84 ± 5 nm for *GFA1*, 74 ± 4 nm for *MYO2*, and 71 ± 4 nm for *TRA1*, along with the standard deviations $\sigma_{\text{binding,cyto}}$, 52 ± 5 nm, 41 ± 5 nm, and 41 ± 5 nm, respectively. These values are summarized in table 3.5.

MOBILITY CONSTRAINTS DURING NPC TRANSITION

Acceleration and confinement We also analyzed the velocities of the mRNA transport traces. The velocities v are in 2D Euclidean space (a microscope projects the 3D sample into a 2D image). For the 1D projected velocity v_{proj}, change in position is relative to the NE; v_{proj} is calculated using the shortest distance to the NE divided by Δt (fig. 3.3F). A positive change in velocity near the center of the NPC was observed (fig. 3.3G), suggesting that mRNA accelerates as it navigates through the central channel of the NPC. We anticipated a ratio of $\sqrt{2}$ when we plotted the ratio v/v_{proj}, which would be typical for a particle moving freely in 2D (fig. 3.3H, see also section 3.6.3). However, we observed a deviation from this ratio near the center of the NPC, suggesting confinement or non-isotropic movement in that region, which is likely caused by the NPC's structure. To model this, we used a simplified depiction of the NPC as a rigid structure with the confined region represented as an inverse block pulse, made from two sigmoids such that it was differentiable. This model allowed us to fit the confined region across all strains, yielding mean values and widths (fig. 3.3I and table 3.5). Although the center μ_{confined} is around zero for all the strains, the estimated width w_{confined} for *MYO2* is larger than for *GFA1* and *TRA1*, namely 139 ± 13 nm vs 121 ± 11 nm and 106 ± 16 nm, respectively, where the error on the width is propagated in quadrature from the errors on the two edges listed in table 3.5.

Table 3.5: Spatial description of transport events. All values are in nm; the number in parentheses is the standard error (SE) of the corresponding fitted parameter. Note that σ_{binding} is itself a distribution width, so its SE quantifies how well that width is determined.

mRNA	$\mu_{\text{binding,nux}}$	$\sigma_{\text{binding,nux}}$	$\mu_{\text{binding,cyto}}$	$\sigma_{\text{binding,cyto}}$	$x_{\text{confined,nux}} - x_{\text{confined,cyto}}$
GFA1	−76 (SE 5)	42 (SE 5)	84 (SE 5)	52 (SE 5)	(−63) – 57 (SE 8–8)
MYO2	−80 (SE 4)	42 (SE 5)	74 (SE 4)	41 (SE 5)	(−69) – 70 (SE 9–9)
TRA1	−67 (SE 5)	32 (SE 5)	71 (SE 4)	41 (SE 5)	(−57) – 49 (SE 11–11)

TRANSPORT STATES

To provide an overview of mRNA behavior near the NPC, we categorized all transport traces into three states (table 3.6). A trace counts as a transport trace when the mRNA is observed beyond $TH'_{\text{transport}}$ on *both* sides of the NE, that is, when its distance to the

NE reaches past the threshold on the nuclear side as well as on the cytoplasmic side. Within this set, a trace is an *export* when it starts on the nuclear side and ends beyond the threshold on the cytoplasmic side, and an *import* when it does the reverse. Every transport trace that is neither an export nor an import falls into the *undefined* category; these are traces for which the direction of travel could not be established, for example because the trace returned to the side it came from.
The total number of transport traces decreases with mRNA size: 1953 for *GFA1*, 1543 for *MYO2*, and 1356 for *TRA1*. Export events dominate over imports for all three transcripts, with 924 exports against 212 imports for *GFA1*, 768 against 157 for *MYO2*, and 640 against 100 for *TRA1*. This asymmetry is consistent with the expected directionality of mRNA transport. A considerable number of traces could not be assigned unambiguously and were classified as undefined.

Table 3.6: Transport states. A trace counts as a transport trace when it crosses the NE midplane and is observed beyond $TH'_{\text{transport}}$ on both sides of the NE; it is therefore a subset of the Crossing NE column of table 3.3, which applies no threshold. Within this set, export, import and undefined are mutually exclusive and together account for the total.

mRNA	Transport traces	Export	Import	Undefined
GFA1	1953	924	212	817
MYO2	1543	768	157	618
TRA1	1356	640	100	616

EXPORT TIMES

A key hallmark of cargo transport across the NPC is the time spent in transport. Generally transport times have been found to be fast with proteins spending (less than) 10's of ms associated with the NPC while mRNAs have been found to spend between roughly 200 ms to seconds at the NPC, correlating with the speed of image acquisition. We find the time spent by all three RNAs colocalizing with the NPC, or dwell time, to be very similar for all three mRNAs, largely independent of their size.

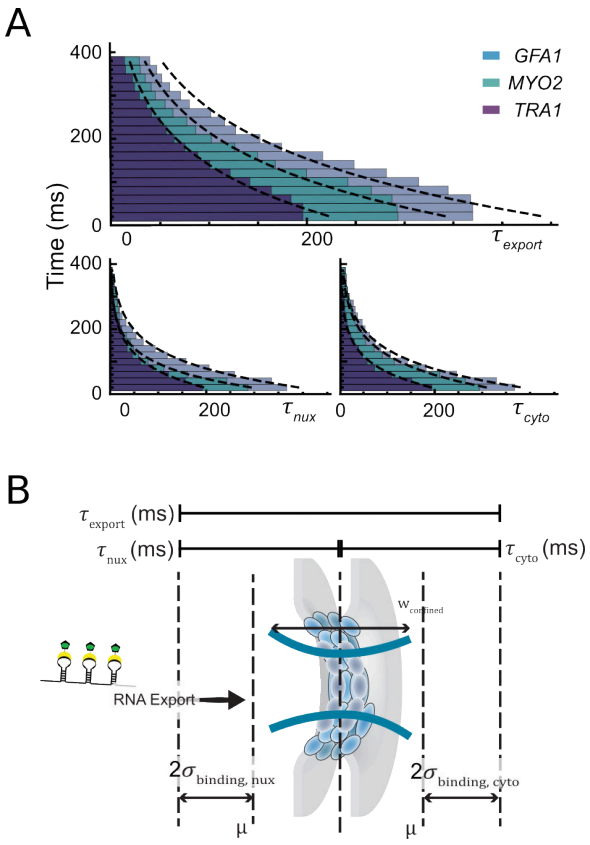


Figure 3.4: **Export times and NPC binding site overview. (A)** Export time distributions for *GFA1*, *MYO2*, and *TRA1*: the total export time τ_{export} (top) and the times spent on the nuclear and cytoplasmic side, τ_{nux} and τ_{cyto} (bottom left and right), each fitted with a cumulative exponential distribution function (dashed). **(B)** Schematic of the NPC showing the interval over which each dwell time is measured, together with the spatial definitions of the nuclear and cytoplasmic binding sites ($\mu_{\text{binding,nux}}$, $\mu_{\text{binding,cyto}}$), their widths ($\sigma_{\text{binding}}$), and the confined region (w_{confined}).

Dwell times were derived from the complementary cumulative distribution of the time spent within the annotated regions, for only the export traces found with the threshold criteria $TH'_{\text{transport}}$, travelling from the nucleus and ending up in the cytoplasm [12, 37]. Each trace contributes to every time bin up to its own duration, so that bin k contains the number of traces that resided in the region for at least k frames of 20 ms. This decaying distribution was fitted with a single exponential to obtain the characteristic dwell time. We categorized time spent on the nuclear side τ_{nux}, the cytoplasmic side τ_{cyto}, and the total export τ_{export}. The delineation of these regions varied based on the data-driven thresholds established, extending from $\mu_{\text{binding,nux}} - 2\sigma_{\text{binding,nux}}$ to $\mu_{\text{binding,cyto}} + 2\sigma_{\text{binding,cyto}}$ for τ_{export}. The dwell times τ_{nux} and τ_{cyto} were computed in the same way for their respective sides of the NE. The resulting export time distributions for all mRNAs are shown in fig. 3.4A, with the corresponding regions indicated schematically in fig. 3.4B. A trace ends not only when the mRNA genuinely leaves the

annotated region, but also when the label photobleaches or the mRNA moves out of the focal plane. Both truncate the observed residence time, so the reported dwell times represent lower limits [37]. At the gap closing time of 10 frames used for the main analysis (section 3.4.11), the fitted export times τ_{export} were 199 ± 6 ms for *GFA1*, 173 ± 6 ms for *MYO2* and 174 ± 5 ms for *TRA1*, despite their transcript lengths spanning a five-fold range. Of this time, $\tau_{\text{nux}} = 103 \pm 2$, 98 ± 2 and 81 ± 2 ms was spent on the nuclear side and $\tau_{\text{cyto}} = 100 \pm 2$, 78 ± 2 and 94 ± 2 ms on the cytoplasmic side for *GFA1*, *MYO2* and *TRA1*, respectively. Similarly, as for the binding sites, the impact of gap closing time on the export time was considered (table 3.8). The nuclear dwell time of *TRA1* was consistently the shortest of the three mRNAs, regardless of the gap closing time.

3.2.6. FAILED TRANSPORT EVENTS

When we analyzed failed transport events, we focused on mRNA molecules that transition back and forth through the NPC. Again, we only selected traces which crossed the NPC midplane less than four times, to filter out stationary mRNAs. We looked to all time-points of a trace in between two NE crossings. These data provide insight into the spatial limits of NPC functionality and identify specific zones where mRNA is less likely to re-enter the NPC. Our analysis simplified the potential influences on mRNA-NPC interactions by assuming that all mRNA, regardless of the transcript, followed the same a priori localization probability.

An example of such a trace is depicted in fig. 3.5A. To systematically map these zones, we established a uniform coordinate system adapted for any orientation of NPC failed transport. Initially, we identify traces crossing the NE twice. We then determine the 'center' of the NPC by finding the cross-sectional midpoint of the estimated NE where the trace doubles back on itself. To prevent mapping traces that crosses the NE through another NPC, we require the distance between cross points to be smaller than $\sqrt{2(3\sigma_{\text{CoLoc}})^2} + 40\,\text{nm} = 248\,\text{nm}$. After computing the normal vector at this point, we adjusted the coordinate system to align the normal vector with $x = (1,0)$ (with the cytoplasm in the positive direction), originating from $(x,y) = (0,0)$ (fig. 3.5B). We used this adjusted coordinate system to map 971, 756 and 563 aborted import events (nuclear side) and 748, 561 and 490 aborted export events (cytoplasmic side) for *GFA1*, *MYO2* and *TRA1*, respectively.

Subsequently, we applied kernel-density estimation using Gaussian kernels to represent the probability density function (PDF) of these events for all localizations of (mRNA) *GFA1*. Using the PDF, we determined the area where 68% of events are localized for *GFA1*, *MYO2* and *TRA1* (fig. 3.5C). Moreover, we compared the delay before the transcript of interest re-entered the NPC between strains, a similar methodology as that used for export times. This process involved fitting the cumulative distribution function of an exponential distribution to the dwell times for failed imports ($\tau_{\text{nux,fail}}$) and exports ($\tau_{\text{cyto,fail}}$) (fig. 3.5D,E). No significant differences were observed between the strains with respect to these re-entry times ($\tau_{\text{nux,fail}}$, $\tau_{\text{cyto,fail}}$) or the covered areas, except for the area covered in the nucleus for *TRA1* ($(1.50 \pm 0.05) \times 10^4$ nm^2) compared to *GFA1* and *MYO2* ($(2.05 \pm 0.06) \times 10^4$ and $(1.96 \pm 0.05) \times 10^4$ nm^2, respectively), which indicated a distinctive pattern in the failed transport events at the nuclear side.

This difference in spatial distribution, combined with the more confined binding sites

($\mu_{\text{binding,nux}}$ and $\sigma_{\text{binding,nux}}$), suggests that *TRA1* interacts more closely and directly with the NPC at the nuclear side compared to the other mRNAs.

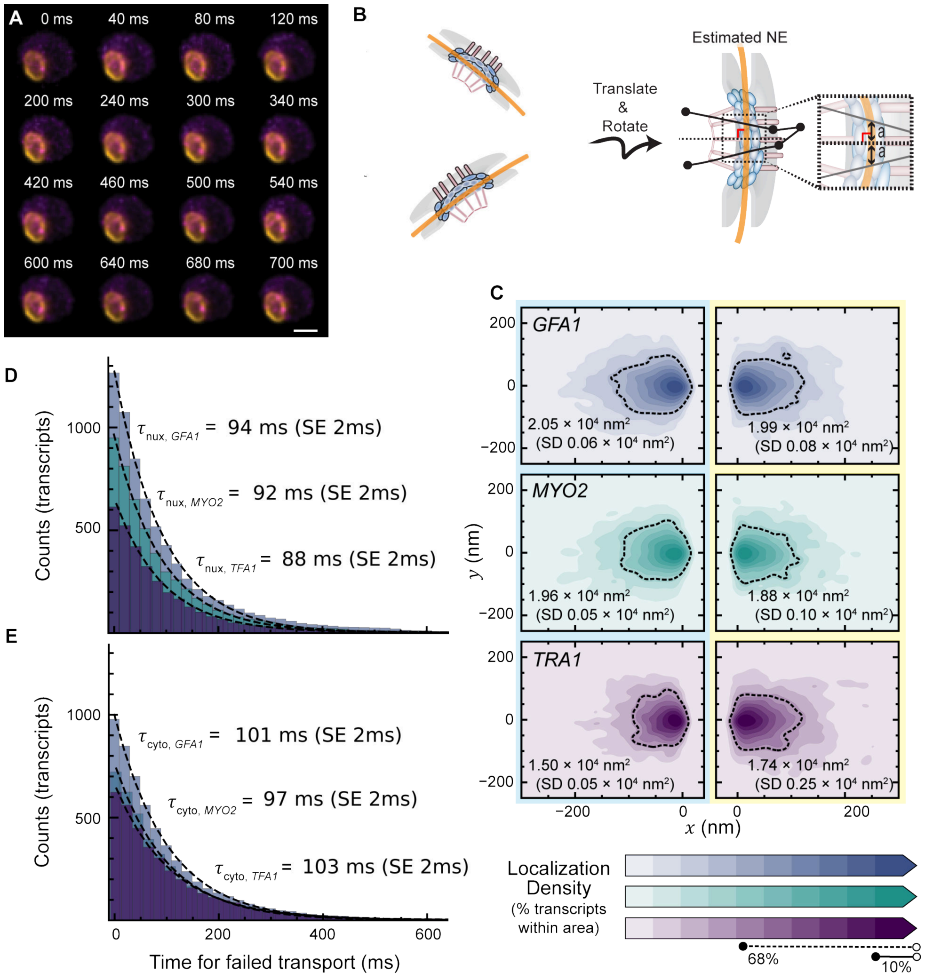


Figure 3.5: **Failed mRNA transport events through the NPC. (A)** A trace of mRNA (magenta) that failed to successfully traverse the NPC; the nuclear envelope is shown in yellow. Scale bar represents 2 µm. **(B)** The transformation applied to the coordinate system used to find the mRNA localization relative to a commonly defined center point. **(C)** Kernel-density estimation of the localization of failed transport events for *GFA1*, *MYO2* and *TRA1*, on the nuclear (left, blue) and cytoplasmic (right, yellow) side of the NPC. The dashed line denotes the border within which 68% of events occur; the area it encloses is listed in each panel. **(D, E)** Quantification of the time before mRNA re-enters the NPC using cumulative exponential distribution functions fit to the dwell times for failed imports and exports, respectively. Errors labelled SE are the square root of the corresponding diagonal element of the covariance matrix returned by the least-squares fit (SciPy curve fit [39]).

3.3. DISCUSSION

In this work, we presented a framework for studying mRNA transport through the NPC in live yeast cells. The framework encompasses nuclear envelope detection, non-uniform background correction, single-molecule localization and tracking, and automated transport classification. Each of these components was designed to operate without human intervention, which opens the possibility of analyzing thousands of movies efficiently.

3.3.1. NUCLEAR ENVELOPE LOCALIZATION

A previous method have measured the radial position of different NPC elements in vivo using nuclear radial intensity measurements. This method utilizes the nuclear center of mass and generates radial lines spanning 360°, which necessitates strictly circular shapes. In contrast, our method initially identifies shapes using a Convolutional Neural Network (CNN), allowing for the detection of any shape.

The previous approach fits a Gaussian distribution to the intensity data, which requires precise initial estimates and can result in model mismatches, especially in cases where there might be intensity differences between both sides of the NE, such as in yeast. Our proposed model, which combines a Generalized Logistic function with a Gaussian distribution, allows for a broader fitting range.

We have demonstrated that our model shows no bias between the model and the intensity data over a line of 1536 nm (12 pixels), enabling us to measure radial distances between Nup82, Nup170, and Nup60. Accurate estimation of the NE is crucial for investigating mRNP-NPC interactions in vivo. The precision achieved in NE localization, quantified at $\sigma_{\mathrm{NE}} = 13\,\mathrm{nm}$, sets a new standard for similar studies, facilitating more detailed investigations into nuclear processes.

An important assumption for measuring the radial distances of different Nups is that the focal plane is flat for all color channels at the same focal position and crosses the NE perpendicularly. In case of a refractive index mismatch between the immersion oil and sample medium, a flat field cannot be guaranteed at any imaging depth, we ensured flatness of the field using the MRS 4-2 calibration sample (Geller MicroAnalytical Laboratory) and brightfield illumination. This assumption can be confirmed as described in the methods section.

3.3.2. IMPACT OF NON-UNIFORM BACKGROUND CORRECTION ON RNA IMAGING

The advancements in background estimation presented in this study signify a substantial improvement in in vivo single-molecule imaging under realistic cellular conditions in yeast. While previous studies in Single Molecule Localization Microscopy (SMLM) have employed background subtraction techniques, our approach integrates the background directly into the imaging model. This integration circumvents the artifacts associated with simple background subtraction, maintaining the integrity of maximum likelihood estimations and enhancing the overall accuracy of localization (section 3.4.9) [30].

Our methodology incorporates the GLRT detection method, enabling us to establish a reliable false positive detection rate (P_{FA}) threshold. This capability is particularly ad-

vantageous for experiments with low signal-to-noise ratios, where traditional spot detection methods are prone to failure. In our experiments, the presence of a non-uniform background posed significant challenges. Traditional models, which assume uniform background, led to discrepancies in the theoretical distribution of the test statistic computed by the GLRT. In contrast, using the ground truth (GT) background, the test statistic obeys the theoretical distribution. This highlights the critical importance of accurate background estimation in maintaining reliable detection thresholds.

To further quantify the impact of background mismatches on P_{FA}, we simulated ROIs with parameters reflecting experimental conditions (section 3.4.8). These simulations, corrupted by Poissonian shot noise, revealed that with ground truth background knowledge, P'_{FA} matched the expected P_{FA}. However, assuming a uniform background led to an increase in P'_{FA} up to 40%, depending on δ_{bg}. In contrast, using our estimated background (bg_{NN}) significantly mitigated this issue, keeping P'_{FA} below 16% (fig. 3.2E). Detection approaches utilizing neural networks, which are trained on datasets inclusive of background noise, set their detection sensitivity based on the lowest signal-to-background ratio present in the training data, resulting in an arbitrary threshold. Our approach, by incorporating background into the imaging model, avoids these pitfalls and ensures more consistent detection sensitivity.

Additionally, the influence of non-uniform background on localization precision was examined. When using non-uniform background in the imaging model, the deterioration in mean localization precision was less than 20% compared to that achieved with GT background knowledge. Conversely, a uniform background model drastically reduced localization precision, increasing it by up to 800% compared to ground truth precision, due to the model mismatch for each ROI. This substantial degradation underscores the necessity of accurate background models to avoid introducing bias in localization.

The high degree of non-uniformity in the background observed in our GFP-tagged mRNA experiments in live yeast cells was primarily due to the high refractive index of yeast cell walls, light scattering between cellular compartments and the presence of unbound fluorescent proteins. Even though we tried to limit the scattering by using a refractive index adjusted imaging medium, traditional imaging models assuming uniform background across ROIs introduced considerable errors in both the detection and localization of RNA molecules, as evidenced by our results. Our advanced approach effectively mitigates these errors, underscoring the necessity of accommodating background non-uniformity for live cell imaging in yeast.

MRNA SINGLE MOLECULE TRACKING

Our study aimed to study the dynamics of mRNA translocation across the NE by tagging and imaging three different mRNA molecules: *GFA1*, *MYO2*, and *TRA1*. These mRNAs, varying in length from 2154 to 11235 base pairs, were tracked in yeast cells, revealing insights into their behavior and interaction with the NE. The precision of our measurements, encompassing drift, registration of color channels, NE localization, and RNA localization, culminated in a co-localization precision of approximately 49 nm. This high precision enabled us to track a significant number of trajectories, with over 60,000 tracks per mRNA type, providing a robust dataset for analyzing mRNA dynamics.

3.3.3. mRNA TRANSPORT THROUGH NPC

In summary, there is evidence of variability in mRNA-NPC interactions across strains. Binding site locations and confinement dimensions within the NPC differ among strains, suggesting potential variations in nuclear mRNP complex formations or NPC structural adaptations [18, 50]. At this stage, it is unclear whether these differences arise from strain-specific mRNP complexes, structural differences between NPC, or a combination of both.

BINDING SITES

Analyzing the transport dynamics of mRNA through the NPC revealed bimodal distributions of localization probability, indicating binding sites at the NPC as observed before [8]. The threshold for defining a transport event has been previously based on the size of the NPC [8, 12]. To circumvent this, we proposed a method to determine the threshold for calling a transport event by analyzing the localization probability of transporting transcripts relative to their distance from the NE. This method allows for a more precise determination of transport events based on the actual observed distances.

By examining these distributions, we observed shifts of the bimodal distribution, based on the transport threshold ($TH_{\text{transport}}$) defined as the minimum distance the mRNA must be observed on both sides of the NE to be considered a transport event. To identify the 'optimal' $TH_{\text{transport}}$, we calculated the differences between $TH_{\text{transport}}$ and the means of the bimodal distributions for various $TH_{\text{transport}}$ values, selecting the threshold where these differences converged to zero.

Moreover, the analysis of the bimodal probability density function (PDF) for (mRNA) *GFA1*, *MYO2*, and *TRA1*, considering our co-localization precision (σ_{CoLoc}), revealed inherent biological distributions of NPC binding sites. We examined the binding sites for the different mRNAs (section 3.2.5) and also the effect of the tracking parameters. We observed consistently that the nuclear binding site of *TRA1* is closer the NPC, compared to the other mRNAs.

ACCELERATION, DIRECTED MOTION AND EXPORT TIMES THROUGH THE NPC

Our analysis highlighted the acceleration of mRNA as it translocates through the NPC, as well as the directed motion in the radial direction. Specifically, we observed that mRNA speeds up as it navigates through the central channel of the NPC. This directed motion implies that the movement of the mRNA is restricted within the narrow central channel, which is approximately 40–60 nm wide [1].

FAILED TRANSPORT EVENTS

Investigating failed transport events provided further insights into the dynamics of mRNA-NPC interactions. By mapping the locations where mRNA traces failed to complete translocation, we identified the zone within the NPC where mRNA is likely to re-enter and where it is not. This gives insight at which point the NPC loses interaction with the mRNAs. This spatial distribution, coupled with differences in the time before an mRNA re-enters the NPC after a failed attempt, highlighted distinctive patterns for each mRNA, particularly for *TRA1*, which showed a closer interaction with the NPC at the nuclear side. Which is in line with the observations found for the independent dataset of the successful transport events.

3.3.4. OUTLOOK

This research established a framework for studying live cell mRNA imaging in yeast, without the need for cell wall digestion and using low laser power. This approach offers an accessible and relatively inexpensive method to study mRNA export. The fully automatic pipeline enables high-throughput analysis, although high-throughput data acquisition was not in place for this research. Implementing high-throughput data acquisition in the future will allow for detailed studies of mRNA-NPC interactions and the role of different transport factors.

Extending the imaging process to three or four colors and labeling multiple nucleoporins will facilitate the study of NPC rearrangement during transport. This will provide a more comprehensive understanding of the dynamics and rearrangements of the NPC.

An open question arises from the use of the PP7 labeling system at the 3' UTR. This implies that our observations reflect the movement of the 3' end rather than the entire mRNA molecule. Although it has been shown that mRNA exports primarily 5' end first [9], double labeling in live imaging would provide more insights into the transport time and conformation of the whole molecule.

3.4. MATERIALS AND METHODS

3.4.1. SAMPLES AND TREATMENT

YEAST STRAINS

The *Saccharomyces cerevisiae* strains examined were endogenously labeled with Nup82-3x mKate2::HIS and Nup60-3x mKate2::URA (ex_{max} = 588 nm, em_{max} = 633 nm) and eGFP-PCP::LEU2 (PP7 coat protein; ex_{max} = 488 nm, em_{max} = 507 nm). We derived three strains each carrying a 24x-PP7 stem loop cassette (approximately 1500 nt) in one allele for either *GFA1* (2154 nt), *MYO2* (4725 nt), or *TRA1* (11235 nt). The final size of each mRNA is given by the sum of PP7 tag and mRNA length. These strains were used to observed mRNA transport across the nuclear envelope.

To determine the overall precision of our methodology we stably labeled Dbp5, which localizes to the cytoplasmic face of the NPC with eGFP (eGFP-Dbp5::NAT) and derived three strains, each labeled with one additional fusion of a nucleoporin to 3x mKate2: (Nup82-3xmKate2::URA3), Nup170 (Nup170-3xmKate2::URA3), or Nup60 (Nup60-3xmKate2::URA3).

MEDIA AND GROWTH CONDITIONS

Each yeast strain was plated on solid agar plates (pre-imaging solid growth medium), incubated for 2 to 3 days at 25 °C, which can be stored in a 4 °C fridge. In preparation for observation under the microscope, the yeast strains were cultured in a liquid pre-imaging medium (pre-imaging liquid medium) at 25 °C in glass tubes placed in a spinning wheel at 200 rpm.

All imaging and pre-imaging media contain a high amount of adenine, typically an additional 2×; this additional adenine minimizes the autofluorescence caused by the red pigment accumulation associated with the adenine pathway of *S. cerevisiae* [51]. Furthermore, in the strains that use PP7-CP loops for mRNA labeling, 2× methionine was added to the pre-imaging and imaging media to prevent PP7-CP aggregation (pre-imaging PP7 medium). The PP7-CP expression is driven by the *MET25* promotor; high methionine

concentrations repress *MET25* expression, preventing overexpression and thus the aggregation thereof PP7-CP loops [14].

REFRACTIVE INDEX DETERMINATION BY OPTICAL CLEARING

The average RI of the yeast cells was determined through optical clearing experiments. In preparation for the experiment, yeast was preconditioned though dilution and growth time to sample from the log- (OD_{600} = 0.45), the exponential (OD_{600} = 1.5) and postdiauxic (OD_{600} = 2.5) phases. Each phase was verified through optical density (OD) measurements at λ = 600 nm in the growth medium. The OD_{600} was measured with a spectrophotometer (Molecular Devices SpectraMax m5) with a machine error of ± 0.003.
The phase-conditioned samples were pelleted (spun-down for 5 minutes at 500g) and re-suspended to an OD_{600} of one in SC-His yeast culture medium. Then 1 mL samples of the OD_{600} = 1 solution were pelleted and re-suspended in 1 mL media of different RIs that ranged from 1.335 (SC-His) to 1.423 (SC-His + 60 vol% Iohexol). The RI media were produced through a Iodexol concentration series in 5% volume increments and their RI measured with an Abbe refractometer (Zeiss, Jena) at a precision of $\pm\ 2.5 \times 10^{-4}$. The OD_{600} was measured with a spectrophotometer (Molecular Devices SpectraMax m5).
The average RI of the yeast corresponded with the minimum of the OD_{600} over RI curve, which was determined by the minimum of a locally fit quadratic function at p-values below 7×10^{-5}.

OSMOLALITY, VIABILITY AND VITALITY MEASUREMENT

For each R.I. adjusted media condition (see table 3.1) media suitability was assessed by comparing osmolarity, viability and vitality of cells grown to cells grown in standard SC-His media. The osmolarity measurements were performed with the μOsmette automatic osmometer (Precision Systems μOsmette model 5004, serial No 0006040), which was calibrated and used according to the manufacturer's operating manual.
A Nexcelom Cellometer (Nexcelom Bioscience Vision 10x, serial No. Vision-203-0039-10x) was used to determine the viability and the vitality of yeast cells. The viability was measured with the "Cellometer ViaStain kit" (Nexcelom Bioscience CSK-0102) and the vitality through the enzymatic activity (Nexcelom Bioscience CFDA-AM CS1-0125).

CONCANAVALINEA COATED COVER GLASSES

The yeast cells were immobilized on cover glasses prepared with ConA. To prepare the ConA cover glasses (#1.5H Warner Instruments CS-25R15), a plasma cleaned cover glass was placed in an imaging chamber and 1 mL ConA solution was added at a concentration of 1 g/L (Sigma-Aldrich C2272) and incubated for 10 minutes after which the ConA solution was removed. The cover glasses were ready for use after drying covered for a minimum of 20 minutes but can be stored for up to one week in closed container.

IMAGE SAMPLE PREPARATION

In preparation for microscopy, a colony picked from the solid stock plate was diluted in liquid pre-imaging medium and incubated at 25 °C overnight at 200 rpm. The fluid culture was diluted in fresh pre-imaging medium to an optical density of between 0.25 and 0.3 at 600 nm (OD_{600}; Molecular Devices SpectraMax M5) the next day. The diluted

sample was incubated for 3 to 4 hours at 25 °C and 200 rpm to reach an OD_{600} of 0.8 to 1.0, to maintain exponential growth.
To plate a sample into an imaging chamber (Attofluor Cell Chamber, Thermo Fisher Scientific, Cat#: A7816) with a ConcanavalineA (ConA, Sigma-Aldrich C2272) coated cover glass (#1.5H Warner Instruments CS-25R15), a 1.5 mL sample of the conditioned yeast was centrifuged in an Eppendorf tube at 500g for five minutes. After removing the supernatant, the pellet was re-diluted in 0.75 mL of pre-imaging medium. The filled chamber remained covered in an incubator at 25 °C for 10 minutes to allow cells to settle. After settling the cover glass was repeatedly washed to remove excess cell layers by slightly tilting the imaging chamber and carefully rinsing with 1 mL pre-imaging medium from the top and removing excess fluid at the bottom of the chamber. This procedure was repeated until a single layer of cells was left in the central region of the cover glass. This washing step resulted in decreased background fluorescence and created space for lateral growth, prolonging the observation time on the microscope.
After washing 1 mL of imaging medium was added to the imaging chamber which was then placed inside the preheated stage incubator (Warner Instruments TC-344C, set point 26.3 °C) and the cover glass brought in contact with the immersion medium of the heated objective (Warner Instruments TC124, set point 26.2 °C) to achieve temperature equilibrium at 25.1 °C at the sample plane, measured with a temperature probe in the sample plane (Thorlabs, TSP01). Temperature equilibrium was achieved at 25 °C before imaging.

RI ADJUSTED MEDIA

The RI of the imaging medium was adjusted with Iodixanol (Sigma Life Science, OptiPrep D1556) to 1.4155 to lower the gradient of the refractive index (RI) between the medium, the yeast cell wall (RI ~ 1.42–1.46) [34, 35], the cover glass (RI = 1.525), and the immersion oil (RI = 1.518, Olympus Type F).
A RI of 1.4155 is higher than the average RI of yeast cells (which lies between 1.3948 and 1.4014, (section 3.2.1)) but below the estimated RI of 1.45 for yeast cell walls [35] and found to be the best compromise for our imaging system as cells, at a RI of 1.4249, become invisible in brightfield or transmitted light illumination, which is used for channel registration (section 3.4.5).
Detailed recipes for all media, including those with refractive indices adjusted with Sorbitol (CalBioChem, Sorbitol 56755), Glycerol (Fisher Chemicals Glycerol G33) and Iohexol (Sigma Life Science, Histodenz D2158), can be found on protocols.io.

3.4.2. MICROSCOPE SETUP

All live cell imaging data was recorded using a custom build multi-camera microscope (fig. 3.6) that can perform transmitted light and fluorescence widefield microscopy and is optimized for live-cell single-molecule tracking experiments. In short, a 488 nm laser (Coherent Obis LS 488-20) and a 561 nm laser (Coherent Obis LS 561-20), are combined in a custom laser combiner into a single-mode, broadband fiber (KineFlex, FPC, 405–640 nm, QiOptiq) and coupled to the excitation beam path using a reflective collimator (Thorlabs RC12FC-P01). Laser power is adjusted using an Obis remote controller (Coherent Obis, 1234466) in combination with a custom build function generator. The

collimated fiber output was routed through a shutter (Thorlabs SHB05T), a square iris (Ealing, 74-1137) and reflected through an emission reflective multi-band dichroic mirror (Chroma, ZT405/488/561/640rpc) to the objective (Olympus UAPON150XOTIRF) by an achromatic $f = 100\,\text{mm}$ lens (Thorlabs ACA254-100-532). Transmitted light illumination was provided through a cold white LED (Thorlabs, MCWHL5 410–700 nm emission range) mounted above the sample incubator (Warner Instruments TC-344C) which features a transparent (cover glass) lid. The incubator was connected through a custom build sample holder to an xyz-stage (Thorlabs MMR601 with MBD602 and MST602) that combines stepper motors and nano-positioners. Emission light, reflected off the dichroic mirror was routed through 2 notch-filters (Semrock NF03-488E-25 & NF03-561E-25) and split by a single band dichroic (Semrock FF560-FDi02-t3) into a green and red emission channel. Each channel held an emission band path filter (Semrock FF03-525/50-25 green channel and Semrock FF02-628/40-25 red channel) before the light was focused onto two cameras (Andor iXon Ultra U-897U-CSO-#BV, green channel and Andor iXon3 U-897E-CSO-#BV-500 red channel) by an air-spaced achromatic doublet, $f = 150\,\text{mm}$ lens (Thorlabs ACA254-150-A). The green channel camera was mounted on an xyz-translation stage (Thorlabs PT3/M) and the red channel camera was mounted on a custom build 6-axis c-mount pivotal camera holder. The whole microscope was built on a custom ordered, 800 kg heavy floating air table (TMC Ametek). The pixel size of the camera (or dexel, detector element and/or detector pixel) was $16 \times 16\,\mu\text{m}^2$ and the total system magnification was $125\times$ resulting in a 128 nm side length pixel representation in the image plane close to the theoretical optimum for sampling diffraction limited spots in the anticipated photon count range.

This microscope design allows for very precise physical alignment of the cameras to the illumination area and each other, provides for the minimal number of surfaces in the emission beam path (sensitivity), diffraction limited wavefront error and excellent field flatness in the emission range, an excitation field flatness better 5% for the FoV, minimal light exposure and simultaneous multi-channel recording.

Details of the optical components according to the NBO-Q (4DN-BINA-OME-QUAREP) microscopy metadata specifications can be reviewed in the provided hardware file micOne-two_color.json and the channel assembly in combination with the settings, in the file micOne-two_color-Settings.json, with the MicroMeta app [52].

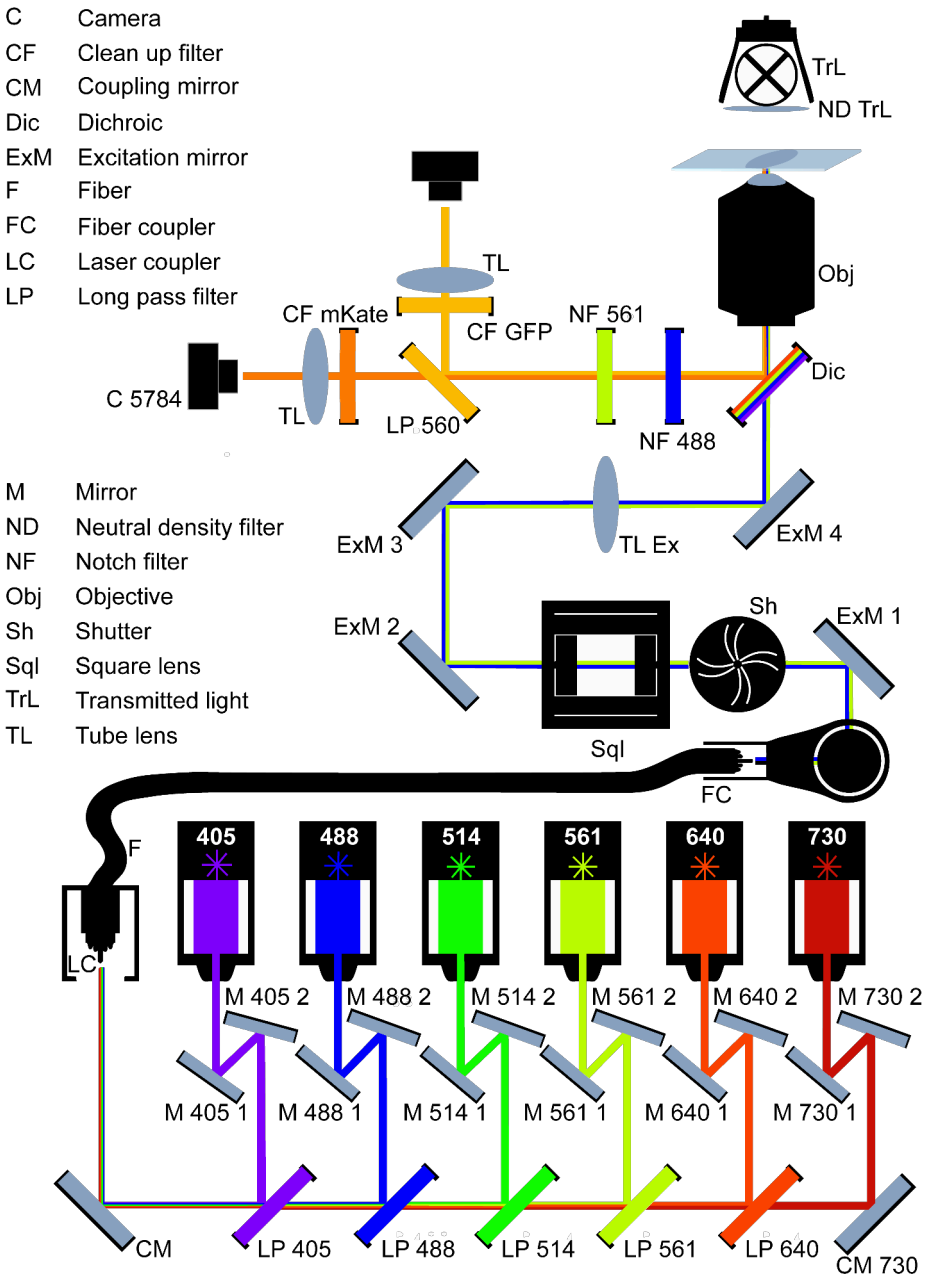


Figure 3.6: **Schematic drawing of MicOne.** The parts notation is aligned to the names used in the attached hardware file (micOne-two_color.json), which provides detailed information according to the NBO-Q microscopy metadata specification.

CAMERA ALIGNMENT PROCEDURES

Camera channel alignment minimizes the channel offsets and chromatic aberration, respectively. First, the cameras were aligned to the same focal plane using an Argolight SIM calibration slide (Argolight SIM SLG 217), that was centered with respect to the objective's FoV.

After the central target of the Argolight slide was in focus, the microscope stage was adjusted to position the slide's 3D crossing stairs in FOV of the cameras. A rough x, y-alignment of the cameras was performed such that the cross stairs were aligned with the center of both cameras' chips. The focal plane alignment was achieved when the middle pair of rings of the stairs were equally in focus and the intensity distribution of the neighboring rings was symmetric and equal on both cameras.

The precise adjustment of the x-y-axes as well as tip, tilt and rotation were performed using the 500 nm pitch pattern on an MRS-4.2 target (Geller MicroAnalytical Laboratory) that features a series of nested black lines/squares with a separation of approximately 200 nm and an edge variation of approximately 20 nm. This target was projected on the cameras through transmitted light. For the alignment process the Geller target was placed on the stage such that the nested squares were close to alignment with the rows and columns of the sensors. The resolution limited lines between the nested squares were visible on both cameras when the pattern was in focus.

For the alignment a nested square was chosen that roughly covers 2/3 of the FOV. The edges of that square were easily identified on both cameras due to the high contrast and the coordinates were captured.

For the following step, the camera (Andor iXon3 U-897E-CSO-#BV-500) that was attached to the x, y, z-translation stage (Thorlabs PT3/M) was the lead camera because its tip, tilt and rotation cannot be changed.

For the 4 edges, $i = 1, \ldots, 4$:

$$\Delta \mathbf{x}_i = x_{i,\text{leading}} - x_{i,\text{2nd camera}}, \tag{3.8}$$

and

$$\Delta \mathbf{y}_i = y_{i,\text{leading}} - y_{i,\text{2nd camera}}. \tag{3.9}$$

We plot the vectors $\Delta \mathbf{x}_i$ and $\Delta \mathbf{y}_i$ for all 4 edges. If all $\Delta \mathbf{x}_i$ and $\Delta \mathbf{y}_i$ pointed in the same direction, the offset was compensated through x and y translation on the 6-axis pivotal c-mount camera holder. If the vectors $\Delta \mathbf{x}_i$ and $\Delta \mathbf{y}_i$ appear as if they were tracing a circle—meaning $\Delta \mathbf{x}_n$ left, $\Delta \mathbf{y}_{n+1}$ down, $\Delta \mathbf{x}_{n+2}$ right, and $\Delta \mathbf{y}_{n+3}$ up, or, similarly, the same sequence of vectors with the direction inverted—the difference was eliminated by rotating around the z-axis. When the $\Delta \mathbf{x}_i$ in one row pointed in opposite directions and that was inverted in the other row, the difference was adjusted by rotating around the x-axis. In the same way, the tilt difference around the y-axis can be identified through comparison of $\Delta \mathbf{y}_i$ directions with respect to the columns.

The offsets were adjusted step-wise because all the different offsets are present simultaneously. This alignment procedure was repeated to minimize the offset of the cameras.

3.4.3. IMAGE ACQUISITION

Images were acquired by both cameras simultaneously at 20.0 ms time intervals with an 18 ms exposure time, as necessitated by the frame transfer between successive images

(2 ms). The camera EM gain was set to 60 for brightfield imaging to prevent saturation and set to 300 for fluorescence imaging.
The imaging process was initialized by activation of the brightfield lamp, which simultaneously closed the shutter in the excitation path (Thorlabs SHB05T). We acquired 250 brightfield images for registration of the color channels. Following brightfield imaging, the brightfield lamp was deactivated, which triggered the excitation shutter to open.
Then we acquired a series of 1000 fluorescence images simultaneously using 488 nm and 561 nm lasers to image the mRNA and NE, respectively. The lasers were triggered through a TTL signal from the cameras (Andor iXon) during exposure time (18 ms) and were turned off during the frame transfer of the cameras (2 ms) using an Obis remote controller (Coherent Obis, 1234466).
To minimize irradiation of the sample, the square iris was adjusted to 300 × 300 pixels which is matched with both cameras that are recording on a 256 × 256 pixel sub-frame to achieve the needed recording speed, resulting in a homogeneous illumination. This limiting of the illuminated area protected the unobserved areas of the sample and reduced the effects of illumination on any future imaging data acquired in the vicinity of current observations.
For tracking experiments the power output was nominally set to 6 mW for the 488 nm (Obis LS 488-20, 1178767) and 2.5 mW for the 561 nm (Obis LS 561-20, 1223779) laser. In the sample plane, after coupling through the fiber and over-illumination of the square iris this resulted in 0.19 mW power for the 488 nm laser, equal to a power density of 12.9 W/cm^2 and 0.09 mW power for the 561 nm laser, equal to a power density of 6.1 W/cm^2. For experiments with dual labelled NPCs only the 561 nm power was adjusted: now 0.11 mW in the sample plane, equivalent to a power density of 7.5 W/cm^2. Power densities reported are calculated for the 300 × 300 pixel illumination area. Power in the sample plane was measured using a suitable power meter (Thorlabs, PM400) and sensor (Thorlabs, S170C) for high N.A. oil immersion objectives.
To ensure the stability of the image acquisition process and assess any potential changes in channel registration over time, we captured an additional 250 brightfield images after the fluorescent imaging. This set of images, in combination with those 250 brightfield images taken prior to fluorescent imaging, was analyzed to evaluate the registration precision and verify the consistency of the acquisition process (see section 3.4.5).

3.4.4. IMAGE PHOTON CALIBRATION

To ensure accuracy of converting experimentally collected intensity values to photon counts, we calibrate the photon gain and camera offset. Both the 'red' and 'green' color channels were calibrated by capturing 2000 images that spanned a range of photon counts mimicking the conditions of our previously acquired experimental images using an out-of-focus MRS 4-2 target (Geller MicroAnalytical Laboratory) and brightfield illumination. These images were used to calculate photon gains of 0.046 and 0.0124 photons per analog-to-digital unit (ADU) for the 'green' and 'red' channel cameras, respectively [53]. The response of both cameras in this range was linear, ensuring accurate photon count conversion (see fig. 3.9A). Subsequently, we captured an additional 1000 dark images to establish camera offsets of 168 ADU and 396 ADU for the 'green' and 'red' channel cameras, respectively. Note that the cameras are different models (see section 3.4.2),

therefore the differences in the calibration values were not unexpected.

3.4.5. IMAGE REGISTRATION

To ensure accurate alignment across different color channels, we collected 250 bright-field images per channel, maintaining a consistent exposure time of 20 ms. The temporal mean image was computed for each set. A Difference of Gaussian (DoG) filter with standard deviations of 0.5 px and 1.5 px was applied to produce a filtered image that served to generate reference images for registration. By reducing noise and improving edge delineation, the use of these reference images effectively facilitated consistent registration.

We employed the Fast Fourier Transform (FFT) approach [54] to image registration to compute translation, rotation and scaling. The process entailed computing the rotation angle (α), scale factor (S) and translational vector ($\vec{r}$). Specifically, α and S are derived from phase cross-correlation applied to the log-polar transformed reference images [55], while $\vec{r}$ is obtained through phase cross-correlation of the original reference images with a 1000-fold upsampling for increased precision [56]. The whole registration process is schematically visualized in fig. 3.8 and the code can be found in our publicly available repository (see section 3.5).

REGISTRATION PRECISION

To gauge the registration precision (σ_{reg}) of our fluorescence imaging, registration images were captured both before and after data collection. The effects on the registration of the rotation angle (α) and scale factor (S) were small ($\alpha = 0.2°$ (SD, 0.1°), $S = 1.00$ (0.01), see fig. 3.8F). Therefore, α and S were omitted from the precision calculation. Using the previously described registration method, we calculated the translational difference vector $\vec{r}_{\text{diff}} = \vec{r}_{\text{after}} - \vec{r}_{\text{before}}$ across roughly 1000 field-of-views (FOVs). The standard deviations of $\vec{r}_{\text{diff}}$'s x and y components, denoted as $\sigma_{\text{reg,x}}$ and $\sigma_{\text{reg,y}}$, were measured to be 12.46 nm and 11.46 nm, respectively. Thus, the overall registration precision for our setup was:

$$\sigma_{\text{reg}} = \sqrt{\sigma_{\text{reg,x}}^2 + \sigma_{\text{reg,y}}^2} = 17\,\text{nm}. \tag{3.10}$$

For quality assurance, datasets where $\|\vec{r}_{\text{diff}}\| > 2\sigma_{\text{reg}}$ are excluded from further analysis.

3.4.6. DRIFT CORRECTION

During image acquisition, we captured images of the fluorescently labeled NE and mRNA simultaneously, resulting in a sequence of 1000 images taken at 20 ms intervals for both channels. To quantify and correct any drift in the system, we employed the following approach. First, we divided the 1000 frames into 4 bins by time, each containing 250 images, and compute the mean image for each bin. Subsequently, we determined the drift by computing the phase cross-correlation between these time bins [56]. The calculated drift data points were then interpolated using cubic splines with natural boundary conditions—i.e., the second derivative at curve ends are zero—ensuring smooth drift corrections. An example of drift estimation can be found in fig. 3.8D; for additional details we refer the reader to section 3.5.

DRIFT PRECISION

The precision of our drift estimation, denoted as σ_{drift}, is established by dividing the recorded images into two distinct sets by frame number, odd numbered frames and even numbered frames. The drift estimation procedure previously outlined was then executed for both sets, yielding drift estimations D_1 and D_2. To facilitate a direct comparison between the divided sets and the full set, we matched the bin size of the divided sets to that of the full set; each divided set into 2 bins of 250 frames each as the full set was portioned into 4 bins of 250 frame bins. The difference in drift, ΔD, between the two sets was calculated as:

$$\Delta D = D_1 - D_2. \tag{3.11}$$

This computation was repeated for roughly 1000 different image sets, and the normal probability density distributions for ΔD along the x- and y-axes are illustrated in fig. 3.8E, yielding precisions of $\sigma_{\text{drift,x}} = 4.87\,\text{nm}$ and $\sigma_{\text{drift,y}} = 4.65\,\text{nm}$. The precision of our drift estimation, σ_{drift}, was then computed as:

$$\sigma_{\text{drift}} = \sqrt{\sigma^2_{\text{drift,x}} + \sigma^2_{\text{drift,y}}} = 7\,\text{nm}. \tag{3.12}$$

3.4.7. NUCLEAR ENVELOPE DETECTION & LOCALIZATION

SEGMENTATION & INITIAL ESTIMATE

To determine the position of the NE, we used the images of the fluorescently labeled nuclear pore complexes. Initially, the mean of the first 250 frames was calculated to generate a single representative image depicting the NE. We segmented this image using a neural network trained on 60 different FOVs. A Feature Pyramid Network (FPN) with a ResNet-34 encoder was employed for this task; this architecture was adapted from publicly available software [57] and is available in our code repository (see section 3.5).
Subsequently, the segmented masks are 'skeletonized', a single-pixel width line was drawn through the center of each mask. This line was smoothed using cubic B-spline interpolation [39, 56, 58]. These cubic B-splines served as initial estimates of NE positions. For the more detailed implementation, we refer to the code repository section 3.5.

MODEL SELECTION FOR NE FITTING

Determining the peak position of the NE is traditionally done using a Gaussian function with a linear background [37]. We observed that this model introduces bias in the imaging data farther from the peak. To find an unbiased intensity profile model, we tested a sigmoid function, and a generalized logistic function [33] combined with a Gaussian curve. The mean ensemble errors, computed from fitting 1,000 NEs, along the fitting range for all models are shown; both the sigmoid and generalized logistic functions do not introduce strong biases (mean error < 0.5% along fitting region).
The key parameter is the fluorescence signal of the NE label, described by the Gaussian function, while the background is modeled by the linear, sigmoid, or generalized logistic functions. For the different models, the average mean squared errors (MSE) from fitting 1,000 NEs are 2.1 photons^2, 1.2 photons^2, and 0.8 photons^2, respectively. The lower MSE with the generalized logistic function is expected due to its greater number of parameters. Although an excessive number of parameters may introduce overfitting, we accept it in this context because we are solely interested in accurately modeling the

Gaussian part representing the NE signal. The complexity of the background model does not impact our analysis of the NE signal, so overfitting the background is not a concern. Therefore, we chose the model with the lowest MSE—the generalized logistic function combined with the Gaussian model.

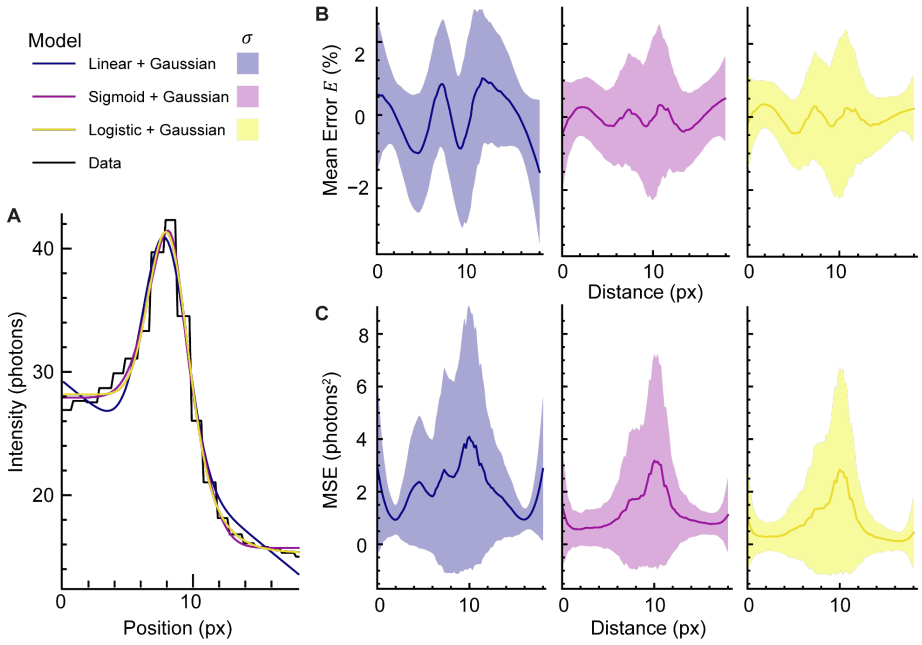


Figure 3.7: **Model selection for NE fitting.** **(A)** Comparison of three intensity profile models—Linear + Gaussian, Sigmoid + Gaussian, and Generalized Logistic + Gaussian—fitted to the same intensity profile. **(B)** Mean error E and **(C)** mean squared error (MSE) along the fitting range for each model, for 1,000 NEs.

NUCLEAR ENVELOPE LOCALIZATION

For the nuclear envelope localization underlying section 3.2.2, the intensity profile I, which is normal to the tangent of the initially estimated NE position, was modelled. The peak position of this model then replaces the initial estimate of the NE position. The resulting model was a composite of the generalized logistic function and Gaussian curve, as described by the following equation:

$$I(n) = A + \frac{K-A}{\left(C + Q \cdot e^{-B(n-M)}\right)^{1/\nu}} + a \cdot \exp\left(-\frac{(n-\mu_{\mathrm{NE}})^2}{2\sigma_{\mathrm{NE}}^2}\right) + b, \tag{3.13}$$

In this equation, n represents the position along the normal to the tangent of the initially estimated NE position, A denotes the left horizontal asymptote, C determines the right horizontal asymptote, M represents the translation of the curve, and B, K, ν, and Q determine the shape of the S-curve and are defined elsewhere in the literature [59]. Additionally, the amplitude a, width σ_{NE}^2, and center position μ_{NE} are parameters used to characterize the Gaussian function, while b serves as the offset of the combined curve.

The refined position of the NE is set as the estimated position μ_{NE} along the normal to the initial estimated position of the NE. We fit the curve by minimizing the least-squared error between the fit and data using a Levenberg-Marquardt algorithm and the partial derivatives below (eq. (3.14) to eq. (3.24)) [60]. Fits that did not converge were filtered out and those parts of the NE were excluded.

$$\frac{\partial I(n)}{\partial A} = 1 - \left(C + Q \cdot \exp(-B(n-M))\right)^{-1/\nu} \tag{3.14}$$

$$\frac{\partial I(n)}{\partial K} = \left(C + Q \cdot \exp(-B(n-M))\right)^{-1/\nu} \tag{3.15}$$

$$\frac{\partial I(n)}{\partial B} = \frac{(K-A)(n-M)Q\exp(-B(n-M))}{\nu\left(C + Q\exp(-B(n-M))\right)^{1/\nu+1}} \tag{3.16}$$

$$\frac{\partial I(n)}{\partial C} = \frac{(K-A)}{\nu\left(C + Q\exp(-B(n-M))\right)^{1/\nu+1}} \tag{3.17}$$

$$\frac{\partial I(n)}{\partial \nu} = \frac{(K-A)\log\left(C + Q\exp(-B(n-M))\right)}{\nu^2\left(C + Q\exp(-B(n-M))\right)^{1/\nu}} \tag{3.18}$$

$$\frac{\partial I(n)}{\partial Q} = \frac{(K-A)\exp(-B(n-M))}{\nu\left(C + Q\exp(-B(n-M))\right)^{1/\nu+1}} \tag{3.19}$$

$$\frac{\partial I(n)}{\partial M} = \frac{(K-A)QB\exp(-B(n-M))}{\nu\left(C + Q\exp(-B(n-M))\right)^{1/\nu+1}} \tag{3.20}$$

$$\frac{\partial I(n)}{\partial \mu_{\text{NE}}} = a \cdot \frac{(n-\mu_{\text{NE}})}{\sigma^2_{\text{NE}}} \cdot \exp\left(-\frac{(n-\mu_{\text{NE}})^2}{2\sigma^2_{\text{NE}}}\right) \tag{3.21}$$

$$\frac{\partial I(n)}{\partial \sigma_{\text{NE}}} = a \cdot \frac{(n-\mu_{\text{NE}})^2}{\sigma^3_{\text{NE}}} \cdot \exp\left(-\frac{(n-\mu_{\text{NE}})^2}{2\sigma^2_{\text{NE}}}\right) \tag{3.22}$$

$$\frac{\partial I(n)}{\partial a} = \exp\left(-\frac{(n-\mu_{\text{NE}})^2}{2\sigma^2_{\text{NE}}}\right) \tag{3.23}$$

$$\frac{\partial I(n)}{\partial b} = 1 \tag{3.24}$$

3.4.8. BACKGROUND ESTIMATION

To mitigate the influence of non-uniform background in yeast cell imaging, we utilize a Convolutional Neural Network (CNN) with a UNet++ architecture to estimate the non-uniform background [44]. Our CNN is trained on a dataset comprised of 5 million randomly generated regions of interest (ROIs), each 16×16 pixels. Of these ROIs, 50% feature randomly positioned emitters with Point Spread Functions (PSFs) as described in section 3.4.9. The PSFs have variable widths σ_{psf} between 100 nm and 140 nm, with photon counts spanning from 50 to 3000. The non-uniform background was simulated by combining a randomly positioned, oriented, 2D-sigmoid surface that represented the yeast

cell wall with random Perlin noise to replicate other sources of non-uniformity [61]. The resulting background exhibits random intensity values ranging from 0 to 190 photons per pixel. This synthetically generated background serves as the target, while the training ROIs are affected by Poissonian distributed shot noise. The background estimated by the network is denoted as $bg_{\mathrm{NN}}(x,y)$.
Our experimental conditions fell comfortably within this broad range of simulation parameters, which enhanced the robustness of our model.
In summary, the network received 20 consecutive images over time of a 16×16 pixel ROI, each potentially containing a PSF emitter. We then downsampled the dimensions until a 2×2 pixel resolution was reached while we simultaneously upsampled the channels. The dimensions of the downsampled image are then upsampled again. Up to this point, all the intermediate connections are made following the classic UNet++ approach. Here we introduce a minor adjustment by replacing the typically employed max pooling layer with a convolution layer with a 3×3 pixel kernel and a 2 pixel stride for downsampling. Since our ROIs were initially small, prioritize minimizing information loss during downsampling was prioritized over the computational speed that a max pooling layer would have offered.

3.4.9. RNA LOCALIZATION

RNA LOCALIZATION WITH UNIFORM BACKGROUND

We adopted a Gaussian PSF model to describe the PSF of a widefield fluorescence microscope [62, 42], given by

$$G(x,y)=\frac{1}{2\pi\sigma_{\mathrm{psf}}^2}\exp\left(-\frac{1}{2\sigma_{\mathrm{psf}}^2}\left[(x-\theta_x)^2+(y-\theta_y)^2\right]\right), \tag{3.25}$$

where (θ_x,θ_y) is the center and σ_{psf} the width of the PSF. The imaging model $\mu_k(x,y)$ is described by the integration of the PSF over a finite set of pixels:

$$\mu_k(x,y)=\theta_{I0}\int_{A_k}G(u,v)\,du\,dv+\theta_{bg}, \tag{3.26}$$

where θ_{bg} is the background photon count per pixel, θ_{I0} is the photon count of the PSF, and $\mu_k(x,y)$ is the expected photon count of the area A_k of the k^{th} pixel at position (x,y). The parameters $\theta=\{\theta_x,\theta_y,\theta_{I0},\theta_{bg}\}$ are estimated using a maximum likelihood estimation (MLE) as described in earlier work [62].

MODIFICATION POINT SPREAD FUNCTION MODEL NON-UNIFORM BACKGROUND

The estimated non-uniform background from the CNN, $bg_{\mathrm{NN}}(x,y)$, is included in the imaging model as

$$\mu_k(x,y)=\theta_{I0}\int_{A_k}G(u,v)\,du\,dv+\theta_{bg}\,bg_{\mathrm{NN}}(x,y), \tag{3.27}$$

where $bg_{\mathrm{NN,k}}$ is the estimated non-uniform background normalized to the mean.
A previous approach to estimation simply subtracted the CNN estimated background [30]. However, we noted that this method introduced artifacts into the probability-based

particle detection technique (section 3.4.10). These artifacts resulted in distributions that diverged from theoretical expectations (see fig. 3.9B). To further investigate this phenomenon, we simulated 40,000 spots against varying background scenarios as outlined prior (section 3.4.8). Our objective was to measure the actual false positive ratio (P_{FA}) when the theoretical $P_{\mathrm{FA,th}}$ threshold was set at 5%. As expected, utilizing the actual background data in our model (eq. (3.27)) yielded $P_{\mathrm{FA}} = 5.0\%$ (SD, 0.09%). By contrast, subtracting the non-uniform background led to a departure from the theoretical expectation, resulting in a P_{FA} of 7.5% (SD, 0.2%) (errors are standard deviations based on 40 repetitions).

We reason that this discrepancy originated in a departure from the basis for MLE, the Poisson distribution, as background subtraction results in a non-Poisson distribution of photon counts. This violation was evidence by a variance unequal to the mean, when the equality thereof is a defining characteristic of a Poisson distribution. To avoid this pitfall, instead of subtracting the background noise, it should be incorporated into the imaging model as demonstrated by our method.

LOCALIZATION PRECISION

To compute the localization precision of the RNA, we compute the Fisher matrix $\mathbf{F}$ as

$$\mathbf{F}_{i,j} = \sum_{k=1}^{K} \frac{1}{\mu_k} \frac{\partial \mu_k}{\partial \theta_i} \frac{\partial \mu_k}{\partial \theta_j}, \tag{3.28}$$

where K is the total number of pixels in the ROI and the derivatives with respect to μ can be computed similarly as described elsewhere [62]. The Cramér-Rao Lower Bound (CRLB) is the inverse of the Fisher matrix and lower bound of the variance of the estimator [62]. To compute the localization precision of the RNA, σ_{RNA}, we use

$$\sigma_{\mathrm{RNA}} = \sqrt{\mathrm{CRLB}_x + \mathrm{CRLB}_y}, \tag{3.29}$$

where CRLB_x and CRLB_y are the CRLB for the x and y position estimation of the emitter. The distribution of σ_{RNA} for ~37,000 emitters in our experiment can be found in fig. 3.9D, with a median value of $\sigma_{\mathrm{RNA}} = 43\,\mathrm{nm}$.

3.4.10. SPOT DETECTION

The detection of RNA spots is grounded in a probabilistic particle detection methodology, leveraging the GLRT as initially introduced for fluorescent spot detection by Smith et al. [32]. According to the Neyman-Pearson lemma [31], the GLRT stands out as the most powerful among all α-level tests. This characteristic enables effective detection while maintaining the lowest possible false positive rate for any chosen threshold.

To adapt this approach to our imaging framework, we incorporated provisions for a non-uniform background as described in eq. (3.27). A bounding box was established for each cell selected by prior segmentation. Within this defined area, for every pixel (x, y) an ROI spanning 9×9 pixels with a central pixel defined as (x, y) was generated for evaluating the maximum likelihood estimations for two nested models.

These models are constructed as per the parameters defined in eq. (3.27), with the location parameters θ_x and θ_y held constant at the central pixel (x, y). Under the null

hypothesis H_0, we assume the absence of signal, thereby constraining the parameter space to $\theta = \{\theta_{I0}, \theta_{bg}\} = \{0, \theta_{bg}\}$. Conversely, the alternative hypothesis H_1 allows for the presence of signal and is represented as $\theta = \{\theta_{I0}, \theta_{bg}\}$. For each hypothesis, the corresponding maximum likelihood, $\mathscr{L}_{\max}$, is computed, leading to the derivation of the GLRT statistic $T_G(x, y)$ for each pixel:

$$T_G(x,y) = 2\log\left(\frac{\mathscr{L}_{\max}(\theta_{I0}, \theta_{bg}; \mathbf{X})}{\mathscr{L}_{\max}(0, \theta_{bg}; \mathbf{X})}\right), \tag{3.30}$$

where $\mathbf{X}$ denotes the photon counts captured by pixels within the ROI. Under conditions without signal (H_0), $T_G(x, y)$ adheres to a central χ^2 distribution with one degree of freedom. In contrast, ROIs exhibiting a signal (H_1) follow a non-central χ^2 distribution.
Employing the properties of $T_G(x, y)$ under H_0, we established a threshold for $T_G(x, y)$ to govern the false-positive probability $P_{\text{FA}}(x, y)$. This metric quantifies the ratio of tests, across pixels, that falsely conclude a signal exists in the ROI [32]. To counterbalance the impact of conducting multiple hypothesis tests, we constrain the false discovery rate, FDR(x, y), by employing the Benjamini-Yekutieli method [43]. This allowed us to control the expected proportion of false positives among the detected spots instead of controlling the false positives across all tests. By applying this method, we ensured that the false discovery rate (FDR) remains at or below 5%. Limiting the rate of incorrect spot identification in the presence of multiple comparisons increased the reliability and validity of our detection results.
The inclusion of a non-uniform background model aims to minimize discrepancies between the found and expected false positive rates, as shown in fig. 3.2E. Finally, we set a threshold for $T_G(x, y)$ that corresponds to an FDR of 5% and generated a binary mask of the images, with true values for pixels that are likely in the proximity of an emitter. For those pixels, we localized the mRNA as described previously (section 3.4.9).

3.4.11. TRACKING

The mRNA localizations were used to construct trajectories by connecting the localizations across sequential frames. The sparse number of detected mRNA particles per frame (mean of 0.38 to 0.52 depending on labelled mRNA) was considered when selecting Trackpy for this task [45, 46]. This package uses recursive linking alongside a KDTree nearest neighbor search algorithm to connect ("link") localized spots. We set the search radius to 200 nm. This is the distance a particle covers in the maximum gap closing interval of 10 frames (200 ms) at a maximal average diffusive velocity of $1\,\mu\text{m}\,\text{s}^{-1}$, so that a spot that disappears for up to 10 frames can still be linked to the same trace.
In instances where a spot was not detected within a sequence of frames, we employed linear interpolation using the spot's known positions to determine its location when missing in a frame. Following interpolation, a GLRT was applied to each interpolated position. This step is crucial for maintaining the overall reliability of the trajectory; should the false positive probability P_{FA} surpass a threshold of 20% for any interpolated position, the spot is deemed unreliable and discarded, as visualized in fig. 3.9F.

SMOOTHING TRAJECTORIES

To calculate the velocity at any point on a given trajectory, we applied cubic B-spline interpolation to the identified traces using SciPy's 'Univariate Spline'. This interpola-

tion function allowed us to adjust the smoothness of the resulting spline by selecting the smoothing factor, which governs the appropriate number of junctions where piecewise polynomials meet [39]. Smoothing the trajectories can improve the accuracy of trajectory reconstruction [63] and mitigates the effect of sporadic wrong links made in the tracking algorithm.

To optimize the smoothing factor, we compared the mean squared error (MSE) of simulated trajectories after cubic B-spline interpolation that varied by smoothing factor. For this purpose, we conducted simulations on 20,000 traces with a localization precision of $\sigma_{\mathrm{RNA}} = 43\,\mathrm{nm}$, which is equal to the median localization precision observed in our experiments (section 3.4.9). These simulated traces are each comprised of 5 segments and have random lengths between 1 and 8 frames. Each segment is randomly assigned either diffusive or directed motion, featuring step sizes ranging from 0 to 150 nm. An example of such a trace—including a ground truth trace, a trace including σ_{RNA}, and a smoothed trace using a smoothing factor of 1.6—is shown in fig. 3.9C. The MSEs between the smoothed trajectories (inclusive of σ_{RNA}) and the ground truth trajectories (exclusive of σ_{RNA}) across various smoothing factors were calculated, as depicted in fig. 3.9E. The lowest MSE was yielded by a smoothing factor of 1.6, thus it was used in the analysis of our experimental data.

3.4.12. USE OF AI

Generative AI tools were used during the preparation of this chapter for writing assistance and grammar checking, and to help locate errors in the analysis code. No data and no images were generated by AI: all measurements, image processing and figures derive from the experiments and analysis described above. All AI-assisted text and code was reviewed and verified.

3.5. DATA, CODE AND PROTOCOL AVAILABILITY

The analysis code will be made publicly available after publication at:
https://github.com/grunwald-lab-umass/yeast-processing-pipeline

3.6. SUPPLEMENTARY MATERIAL

3.6.1. SUPPLEMENTARY FIGURES

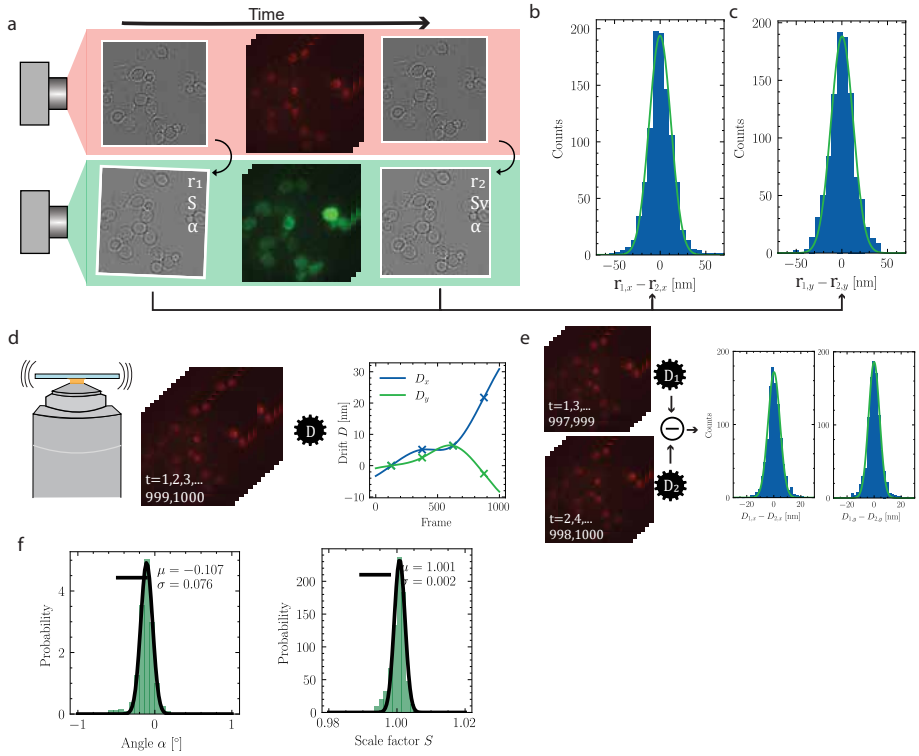


Figure 3.8: **Image Registration and Drift Correction Procedures and Precision.** (A) Representation of the image acquisition for both color channels. First 250 frames of brightfield images are acquired, then 1000 frames fluorescent images, after that another 250 brightfield images. All images are captured with an exposure time of 20 ms. The registration parameters, including rotation angle (α), scale factor (S), and translational vector ($\vec{r}$), are computed using phase cross-correlation. (B,C) Distributions of $\vec{r}_1 - \vec{r}_2$ for components in the x and y directions, yielding registration precisions of $\sigma_{\text{reg,x}} = 12.46\,\text{nm}$ and $\sigma_{\text{reg,y}} = 11.46\,\text{nm}$. The overall registration precision is $\sigma_{\text{reg}} = 17\,\text{nm}$. (D) Example of drift estimation, showing the drift data points from bins of 250 frames, interpolated using cubic splines. (E) Normal probability density distributions of drift differences in the x and y directions, obtained by dividing recorded images into odd and even sets. The drift precision is $\sigma_{\text{drift,x}} = 4.87\,\text{nm}$ and $\sigma_{\text{drift,y}} = 4.65\,\text{nm}$, with an overall drift precision of $\sigma_{\text{drift}} = 7\,\text{nm}$. (F) Distributions for the registration angle and scale with the mean (μ) and standard deviations (σ) listed.

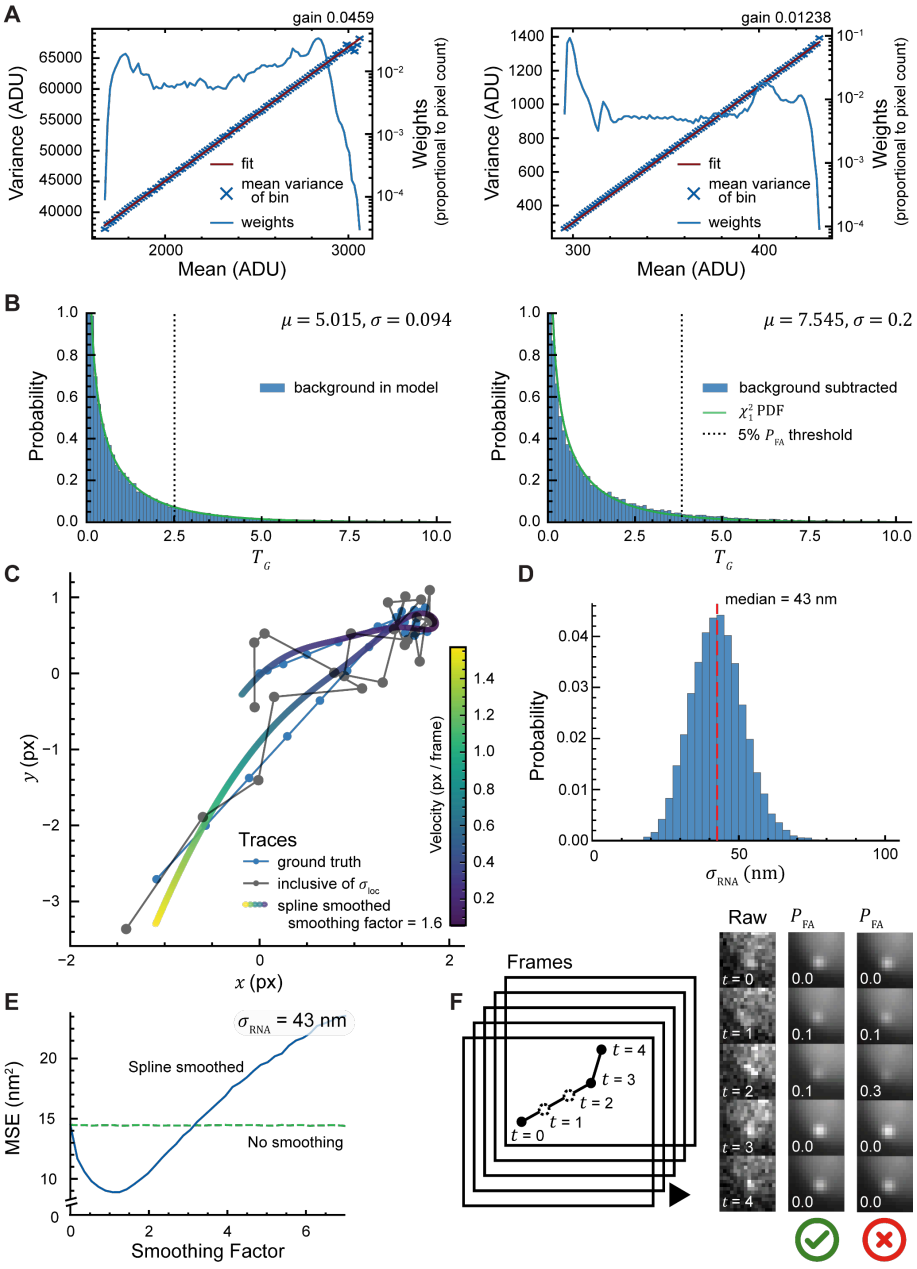

A
gain 0.0459
Variance (ADU)
Mean (ADU)
fit
mean variance of bin
weights
Weights (proportional to pixel count)
gain 0.01238
B
$\mu = 5.015, \sigma = 0.094$
background in model
Probability
T_G
$\mu = 7.545, \sigma = 0.2$
background subtracted
χ^2_1 PDF
5% P_{FA} threshold
C
Traces
ground truth
inclusive of σ_{loc}
spline smoothed
smoothing factor = 1.6
Velocity (px / frame)
y (px)
x (px)
D
median = 43 nm
σ_{RNA} (nm)
E
σ_{RNA} = 43 nm
Spline smoothed
No smoothing
MSE (nm²)
Smoothing Factor
F
Frames
t = 0
t = 1
t = 2
t = 3
t = 4
Raw
P_{FA}
P_{FA}

Figure 3.9: **Tracking, Image Calibration Procedures and Precision.** (A) Calibration of photon counts for the 'green' and 'red' channel cameras using an out-of-focus MRS 4-2 calibration sample and brightfield illumination, yielding gains of 0.046 and 0.0124 photons per ADU, respectively. The linear response of the camera in this range ensures accurate photon count conversion. (B) Comparison of incorporating the background in the imaging model (left) and background subtraction (right). Subtracting the background introduces artifacts into the probability-based particle detection technique, deviating from theoretical expectations. (C) The image shows a ground truth trace, a trace including σ_{RNA}, and a smoothed trace (spline) using a smoothing factor of 1.6. (D) Distribution of localization precision (σ_{RNA}) for approximately 37,000 emitters, with a median value of $\sigma_{\mathrm{RNA}} = 43\,\mathrm{nm}$. (E) Mean squared error (MSE) between smoothed trajectories (inclusive of σ_{RNA}) and the actual ground truth trajectories (exclusive of σ_{RNA}) across various smoothing factors. A smoothing factor of 1.6 yielded the lowest MSE. (F) Example of trajectory linking, with a gap closing time of 2 frames, and interpolation. Linear interpolation is employed when a spot is not detected within a sequence of frames, followed by a Generalized Likelihood Ratio Test (GLRT) to ensure reliability. Links where the false positive probability P_{FA} exceeds 20% are discarded, ensuring the reliability of the trajectories in which a gap over multiple frames is closed.

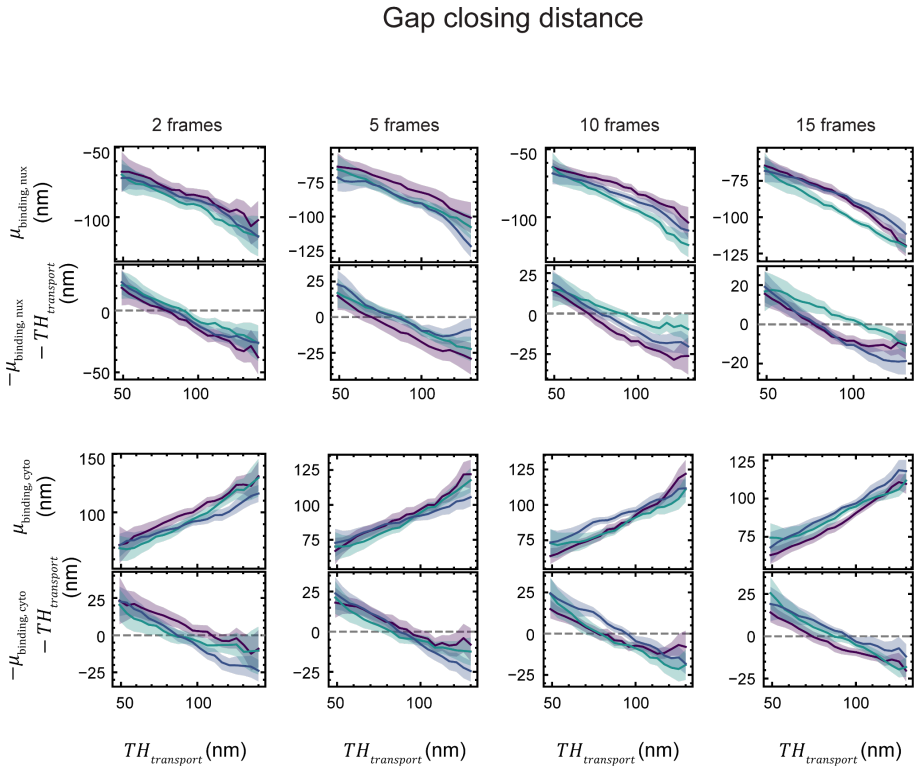


Figure 3.10: **Effect of gap closing time of the tracking algorithm on the binding sites.** Each column corresponds to one gap closing time (2, 5, 10 and 15 frames). Upper two rows, nuclear side: the fitted binding site $\mu_{\mathrm{binding,nux}}$ and the difference $-\mu_{\mathrm{binding,nux}} - TH_{\mathrm{transport}}$, both as a function of the transport threshold $TH_{\mathrm{transport}}$. Lower two rows, cytoplasmic side: the same two quantities for $\mu_{\mathrm{binding,cyto}}$. Dashed lines mark zero; the threshold at which the difference crosses zero defines $TH'_{\mathrm{transport}}$. Shaded bands indicate the uncertainty on the fitted binding site. Colour coding of the transcripts is the same as in fig. 3.3: *GFA1* blue, *MYO2* teal, *TRA1* purple.

3.6.2. SUPPLEMENTAL TABLES

Table 3.7: Gap closing effect on binding sites. Values are the binding-site distance in nm, taken as the transport threshold at which $\mu_{\text{binding}} - TH_{\text{transport}} = 0$ (fig. 3.3D); the four gap closing conditions tabulated here are shown in fig. 3.10. The interval in parentheses is the range of thresholds over which the uncertainty band of that curve crosses zero.

		Gap Closing Distance Tracking			
Location	**mRNA**	**2 Frames**	**5 Frames**	**10 Frames**	**15 Frames**
Nucleus	*GFA1*	74 (64–85)	75 (62–90)	75 (67–85)	72 (64–78)
	MYO2	89 (76–94)	78 (<49–86)	79 (<49–88)	100 (53–104)
	TRA1	63 (<49–76)	60 (<49–66)	67 (62–73)	71 (64–78)
Cytoplasm	*GFA1*	81 (51–88)	81 (51–86)	83 (78–90)	95 (82–>140)
	MYO2	73 (<49–82)	74 (57–82)	75 (67–82)	80 (71–86)
	TRA1	97 (57–131)	87 (78–96)	71 (61–85)	70 (60–83)

<49 / >140: the uncertainty-band intersection falls outside the scanned threshold range (49–140 nm).

Table 3.8: Effect of gap closing distance on export times for *GFA1*, *MYO2*, and *TRA1* mRNA. Values are characteristic dwell times in ms; the quoted uncertainty is that of the single-exponential fit to the complementary cumulative distribution.

		Gap Closing Distance Tracking			
Location	**mRNA**	**2 Frames**	**5 Frames**	**10 Frames**	**15 Frames**
Nuclear Dwell Time (ms)	*GFA1*	62 ± 1	82 ± 1	103 ± 2	124 ± 2
	MYO2	71 ± 1	71 ± 1	98 ± 2	136 ± 3
	TRA1	61 ± 1	66 ± 1	81 ± 2	100 ± 2
Cytoplasmic Dwell Time (ms)	*GFA1*	75 ± 2	82 ± 2	100 ± 2	115 ± 2
	MYO2	69 ± 2	71 ± 2	78 ± 2	85 ± 2
	TRA1	88 ± 1	91 ± 1	94 ± 2	98 ± 2
Total Export Time (ms)	*GFA1*	133 ± 6	159 ± 7	199 ± 6	235 ± 6
	MYO2	136 ± 6	140 ± 6	173 ± 6	219 ± 7
	TRA1	143 ± 6	154 ± 5	174 ± 5	195 ± 5

3.6.3. SUPPLEMENTAL NOTES

PROJECTING 2D MOTION ALONG ONE AXIS

The velocity of a freely moving particle in 2D can be decomposed into orthogonal components v_x and v_y. If these components are independent and identically distributed, the overall velocity v is:

$$v = \sqrt{v_x^2 + v_y^2} \tag{3.31}$$

$$\langle v_x^2 \rangle = \langle v_y^2 \rangle \tag{3.32}$$

Assuming isotropic motion, the expected values of the squared velocity components are equal:

$$\langle v^2 \rangle = \langle v_x^2 \rangle + \langle v_y^2 \rangle = 2\langle v_x^2 \rangle \tag{3.33}$$

Thus, the expected magnitude of the overall velocity is:

$$\langle v \rangle = \sqrt{2\langle v_x \rangle^2} \tag{3.34}$$

For a freely moving particle, the velocity projected onto any axis v_{proj} is related to the overall velocity by:

$$\langle v \rangle = \sqrt{2}\,\langle v_{\text{proj}} \rangle \tag{3.35}$$

This means that when we project the 2D motion of the particle onto any single axis, the expected ratio of the overall velocity to the projected velocity is $\sqrt{2}$.
In our analysis of mRNA movement, we observed that the ratio v/v_{proj} deviates from $\sqrt{2}$ near the central channel of the NPC. This deviation indicates confinement or that the motion is not isotropic, likely caused by the NPC structure.

POWER LOSS AND DENSITY IN YOKOGAWA CSU-X1 SPINNING DISK CONFOCAL MICROSCOPY

This is a back of the envelope calculation to estimate the power density in the sample plane, for with an input power of 100 mW at 488 nm on a spinning disk confocal microscope (Observer SD; Carl Zeiss) using a 100×/1.43 NA objective (Carl Zeiss). For the Yokogawa CSU-X1 spinning disk confocal microscopy, the power loss can be attributed to the additional components such as the spinning disk and the associated optics. Here is a breakdown of the factors contributing to power loss in a typical Yokogawa CSU-X1 spinning disk confocal system. In a communication with an imaging specialist from Zeiss, it was indicated that our back-of-the-envelope calculation likely provides an upper estimate of the power loss. In reality, the actual power loss could be approximately five times less. However, the only way to obtain an accurate measurement of the power density at the sample is by using a power meter.

- Laser Source and Coupling Efficiency:
  - Similar to confocal, assuming around 95% efficiency.
  - Loss: 5%.
- Beam Splitters and Dichroic Mirrors:
  - Typically, 90% to 95% efficiency.
  - Loss: 5% to 10% per component.
- Spinning Disk (Yokogawa CSU-X1):
  - The Yokogawa spinning disk with multiple pinholes typically transmits around 40% to 50% of the light.
  - Loss: 50% to 60%.
- Lenses and Objectives:
  - High-quality lenses and objectives with anti-reflective coatings.

  - Typical transmission efficiency: 95% to 98%.
  - Loss: 2% to 5% per lens.
- Mirrors:
  - High-reflective mirrors with around 99% efficiency.
  - Loss: 1% per mirror.

Assuming a typical Yokogawa CSU-X1 spinning disk confocal setup with one laser source, one beam splitter, one dichroic mirror, the spinning disk, three lenses, and two mirrors, we calculate the overall transmission efficiency as follows:

- Laser Source and Coupling: Efficiency: 95% (5% loss)
- Beam Splitter: Efficiency: 90% (10% loss)
- Dichroic Mirror: Efficiency: 95% (5% loss)
- Spinning Disk: Efficiency: 50% (50% loss)
- Lenses (three lenses): Efficiency per lens: 97% (3% loss per lens). Total for three lenses: $0.97 \times 0.97 \times 0.97 \approx 0.913$ or 91.3%
- Mirrors (two mirrors): Efficiency per mirror: 99% (1% loss per mirror). Total for two mirrors: $0.99 \times 0.99 = 0.98$ or 98%

Overall Efficiency Overall Efficiency:

$$0.95 \times 0.90 \times 0.95 \times 0.50 \times 0.913 \times 0.98 \approx 0.38 \text{ or } 38\% \tag{3.36}$$

If the initial laser power is 100 mW, the power reaching the sample can be calculated as:

$$\text{Power at sample} = \text{Initial Power} \times \text{Overall Efficiency} \tag{3.37}$$

$$\text{Power at sample} = 100\,\text{mW} \times 0.38 = 38\,\text{mW} \tag{3.38}$$

Assuming that an area covering approximately 1,000 pinholes on the lower Nipkow disk is illuminated:

$$\text{Power per spot} = \frac{38\,\text{mW}}{1000} = 0.038\,\text{mW} \tag{3.39}$$

Power Density Calculation for a 1.43 NA Objective The radius of the diffraction-limited spot, r, can be approximated by the equation:

$$r = \frac{0.61\lambda}{\text{NA}} \tag{3.40}$$

For a 488 nm laser with an NA of 1.43:

$$r = \frac{0.61 \times 488\,\text{nm}}{1.43} \approx 208\,\text{nm} \tag{3.41}$$

The area A of the spot can be calculated using the formula for the area of a circle:

$$A = \pi r^2 \tag{3.42}$$

Convert the radius to cm:

$$r = 208\,\text{nm} = 208 \times 10^{-7}\,\text{cm} = 2.08 \times 10^{-5}\,\text{cm} \tag{3.43}$$

Calculate the area in cm^2:

$$A = \pi(2.08 \times 10^{-5}\,\text{cm})^2 \approx 1.36 \times 10^{-9}\,\text{cm}^2 \tag{3.44}$$

Finally, the power density P_d is given by the total power per spot divided by the area:

$$P_d = \frac{0.038\,\text{mW}}{1.36 \times 10^{-9}\,\text{cm}^2} = \frac{0.038 \times 10^{-3}\,\text{W}}{1.36 \times 10^{-9}\,\text{cm}^2} \approx 2.8 \times 10^4\,\text{W/cm}^2 \tag{3.45}$$

Thus, the power density at the sample for a 100 mW confocal laser focused to a diffraction-limited spot with a 1.43 NA objective and considering the multiple spots illuminated in a Yokogawa CSU-X1 spinning disk confocal system would be approximately 2.8×10^4 W/cm^2.

BIBLIOGRAPHY

[1] Stefan Petrovic et al. “Architecture of the linker-scaffold in the nuclear pore”. In: *Science* 376 (2022), eabm9798.

[2] Pau Pascual-Garcia and Maya Capelson. “The nuclear pore complex and the genome: organizing and regulatory principles”. In: *Current Opinion in Genetics & Development* 67 (2021), pp. 142–150.

[3] Caterina Strambio-De-Castillia, Mario Niepel, and Michael P Rout. “The nuclear pore complex: bridging nuclear transport and gene regulation”. In: *Nature Reviews Molecular Cell Biology* 11.7 (2010), pp. 490–501.

[4] Arkaitz Ibarra and Martin W. Hetzer. “Nuclear pore proteins and the control of genome functions”. In: *Genes & Development* 29 (2015), pp. 337–349. DOI: 10.1101/gad.256495.114.

[5] Brian J. Natalizio and Susan R. Wente. “Postage for the messenger: designating routes for nuclear mRNA export”. In: *Trends in Cell Biology* 23 (2013), pp. 365–373.

[6] Abigail L. Buchwalter, Yun Liang, and Martin W. Hetzer. “Nup50 is required for cell differentiation and exhibits transcription-dependent dynamics”. In: *Molecular Biology of the Cell* 25 (2014), pp. 2472–2484.

[7] Jessica A Hurt and Pamela A Silver. “mRNA nuclear export and human disease”. In: *Disease Models & Mechanisms* 1.2-3 (2008), pp. 103–108.

[8] David Grünwald and Robert H Singer. “In vivo imaging of labelled endogenous β-actin mRNA during nucleocytoplasmic transport”. In: *Nature* 467.7315 (2010), pp. 604–607.

[9] Asaf Ashkenazy-Titelman et al. “RNA export through the nuclear pore complex is directional”. In: *Nature Communications* 13.1 (2022), p. 5881.

[10] Rakefet Ben-Yishay et al. “Imaging within single NPCs reveals NXF1’s role in mRNA export on the cytoplasmic side of the pore”. In: *Journal of Cell Biology* 218.9 (2019), pp. 2962–2981.

[11] Tim Kaminski, Jan Peter Siebrasse, and Ulrich Kubitscheck. “A single molecule view on Dbp5 and mRNA at the nuclear pore”. In: *Nucleus* 4.1 (2013), pp. 8–13.

[12] Carlas Smith et al. “In vivo single-particle imaging of nuclear mRNA export in budding yeast demonstrates an essential role for Mex67p”. In: *Journal of Cell Biology* 211.6 (2015), pp. 1121–1130.

[13] Mark-Albert Saroufim et al. “The nuclear basket mediates perinuclear mRNA scanning in budding yeast”. In: *Journal of Cell Biology* 211.6 (2015), pp. 1131–1140.

[14] Azra Lari et al. “Live-Cell Imaging of mRNP–NPC Interactions in Budding Yeast”. In: *Imaging Gene Expression: Methods and Protocols*. Springer, 2019, pp. 131–150.

[15] Sami Hocine et al. “Single-molecule analysis of gene expression using two-color RNA labeling in live yeast”. In: *Nature Methods* 10 (2013), pp. 119–121.

[16] Jeffrey A. Chao et al. “Structural basis for the coevolution of a viral RNA–protein complex”. In: *Nature Structural & Molecular Biology* 15 (2008), pp. 103–105.

[17] Weihan Li et al. “An improved imaging system that corrects MS2-induced RNA destabilization”. In: *Nature Methods* 19 (2022), pp. 1558–1562.

[18] Anthony P Schuller et al. “The cellular environment shapes the nuclear pore complex architecture”. In: *Nature* 598.7882 (2021), pp. 667–671.

[19] Paolo De Magistris. “The great escape: mRNA export through the nuclear pore complex”. In: *International Journal of Molecular Sciences* 22 (2021), p. 11767.

[20] Ben Montpetit et al. “A conserved mechanism of DEAD-box ATPase activation by nucleoporins and InsP6 in mRNA export”. In: *Nature* 472 (2011), pp. 238–242.

[21] Arvind Arjun Nellore Rajan, Ryoji Asada, and Ben Montpetit. “Gle1 is required for tRNA to stimulate Dbp5 ATPase activity in vitro and promote Dbp5-mediated tRNA export in vivo in Saccharomyces cerevisiae”. In: *eLife* 12 (2024), RP89835.

[22] Pierre Bensidoun et al. “Nuclear mRNA metabolism drives selective basket assembly on a subset of nuclear pore complexes in budding yeast”. In: *Molecular Cell* 82 (2022), pp. 3856–3871.

[23] Peter M Carlton et al. “Fast live simultaneous multiwavelength four-dimensional optical microscopy”. In: *Proceedings of the National Academy of Sciences* 107.37 (2010), pp. 16016–16022.

[24] Tyler Boothe et al. “A tunable refractive index matching medium for live imaging cells, tissues and model organisms”. In: *eLife* 6 (2017), e27240.

[25] Michael Reed et al. “The relative renal safety of iodixanol compared with low-osmolar contrast media: a meta-analysis of randomized controlled trials”. In: *JACC: Cardiovascular Interventions* 2.7 (2009), pp. 645–654.

[26] Peter A. McCullough and Jeremiah R. Brown. “Effects of intra-arterial and intravenous iso-osmolar contrast medium (iodixanol) on the risk of contrast-induced acute kidney injury: a meta-analysis”. In: *Cardiorenal Medicine* 1.4 (2011), pp. 220–234.

[27] Tingting Yu et al. “Rapid and prodium iodide-compatible optical clearing method for brain tissue based on sugar/sugar-alcohol”. In: *Journal of Biomedical Optics* 21 (2016), p. 081203. DOI: 10.1117/1.JBO.21.8.081203.

[28] Doyeon Lee et al. “High-fidelity optical diffraction tomography of live organisms using iodixanol refractive index matching”. In: *Biomedical Optics Express* 13 (2022), p. 6404. DOI: 10.1364/BOE.465066.

[29] Hao Zeng et al. “Study on the refractive index matching effect of ultrasound on optical clearing of bio-tissues based on the derivative total reflection method”. In: *Biomedical Optics Express* 5.10 (2014), pp. 3482–3493.

[30] Leonhard Möckl et al. “Accurate and rapid background estimation in single-molecule localization microscopy using the deep neural network BGnet”. In: *Proceedings of the National Academy of Sciences* 117.1 (2020), pp. 60–67.

[31] Steven M. Kay. *Fundamentals of Statistical Signal Processing*. Englewood Cliffs, N.J.: Prentice-Hall PTR, 1993.

[32] Carlas S Smith et al. “Probability-based particle detection that enables threshold-free and robust in vivo single-molecule tracking”. In: *Molecular Biology of the Cell* 26.22 (2015), pp. 4057–4062.

[33] Bernard Richards and Emil Wolf. “Electromagnetic diffraction in optical systems, II. Structure of the image field in an aplanatic system”. In: *Proceedings of the Royal Society of London. Series A. Mathematical and Physical Sciences* 253.1274 (1959), pp. 358–379.

[34] Philip J. Wyatt. “Cell wall thickness, size distribution, refractive index ratio and dry weight content of living bacteria (Staphylococcus aureus)”. In: *Nature* 226 (1970), pp. 277–279. DOI: 10.1038/226277a0.

[35] Robert E. Marquis. “Immersion refractometry of isolated bacterial cell walls”. In: *Journal of Bacteriology* 116 (1973), pp. 1273–1279. DOI: 10.1128/jb.116.3.1273-1279.1973.

[36] Daniel R. Rines et al. “Live Cell Imaging of Yeast”. In: *Cold Spring Harbor Protocols* 2011 (2011), pdb.top065482. DOI: 10.1101/pdb.top065482.

[37] Ulrich Kubitscheck et al. “Nuclear transport of single molecules: dwell times at the nuclear pore complex”. In: *Journal of Cell Biology* 168 (2005), pp. 233–243. DOI: 10.1083/jcb.200411005.

[38] Weidong Yang, Jeff Gelles, and Siegfried M. Musser. “Imaging of single-molecule translocation through nuclear pore complexes”. In: *Proceedings of the National Academy of Sciences* 101 (2004), pp. 12887–12892. DOI: 10.1073/pnas.0403675101.

[39] Pauli Virtanen et al. “SciPy 1.0: Fundamental algorithms for scientific computing in Python”. In: *Nature Methods* 17 (2020), pp. 261–272. DOI: 10.1038/s41592-019-0686-2.

[40] Seung Joong Kim et al. “Integrative structure and functional anatomy of a nuclear pore complex”. In: *Nature* 555 (2018), pp. 475–482. DOI: 10.1038/nature26003.

[41] Pieter Van Velde et al. “ZIMFLUX: Single molecule localization microscopy with patterned illumination in 3D”. In: *Optics Express* 31.25 (2023), pp. 42701–42722.

[42] S Stallinga and B Rieger. “Accuracy of the Gaussian point spread function model in 2D localization microscopy”. In: *Optics Express* 18 (2010), pp. 24461–24476.

[43] Yoav Benjamini and Daniel Yekutieli. “The control of the false discovery rate in multiple testing under dependency”. In: *Annals of Statistics* (2001), pp. 1165–1188.

[44] Zongwei Zhou et al. “UNet++: A nested U-Net architecture for medical image segmentation”. In: *Deep Learning in Medical Image Analysis and Multimodal Learning for Clinical Decision Support*. Springer, 2018, pp. 3–11.

[45] Daniel B. Allan et al. *soft-matter/trackpy: Python particle tracking toolkit*. 2023. DOI: 10.5281/zenodo.7670439.

[46] John C. Crocker and David G. Grier. "Methods of digital video microscopy for colloidal studies". In: *Journal of Colloid and Interface Science* 179 (1996), pp. 298–310.

[47] David Grünwald and Robert H. Singer. "Multiscale dynamics in nucleocytoplasmic transport". In: *Current Opinion in Cell Biology* 24 (2012), pp. 100–106. DOI: 10.1016/j.ceb.2011.11.011.

[48] David Grünwald, Robert H. Singer, and Michael Rout. "Nuclear export dynamics of RNA–protein complexes". In: *Nature* 475 (2011), pp. 333–341. DOI: 10.1038/nature10318.

[49] Siegfried M. Musser and David Grünwald. "Deciphering the Structure and Function of Nuclear Pores Using Single-Molecule Fluorescence Approaches". In: *Journal of Molecular Biology* 428 (2016), pp. 2091–2119. DOI: 10.1016/j.jmb.2016.02.023.

[50] Andreas Niedner et al. "Role of Loc1p in assembly and reorganization of nuclear ASH1 messenger ribonucleoprotein particles in yeast". In: *Proceedings of the National Academy of Sciences* 110 (2013), E5049–E5058.

[51] Agnese Kokina, Juris Kibilds, and Janis Liepins. "Adenine auxotrophy–be aware: some effects of adenine auxotrophy in Saccharomyces cerevisiae strain W303-1A". In: *FEMS Yeast Research* 14 (2014), pp. 697–707.

[52] Alessandro Rigano et al. "Micro-Meta App: an interactive tool for collecting microscopy metadata based on community specifications". In: *Nature Methods* 18 (2021), pp. 1489–1495. DOI: 10.1038/s41592-021-01315-z.

[53] James C Mullikin et al. "Methods for CCD camera characterization". In: *Image Acquisition and Scientific Imaging Systems*. Vol. 2173. Spie. 1994, pp. 73–84.

[54] B. Srinivasa Reddy and Biswanath N. Chatterji. "An FFT-based technique for translation, rotation, and scale-invariant image registration". In: *IEEE Transactions on Image Processing* 5 (1996), pp. 1266–1271.

[55] Michael A. Tycon et al. "Quantification of dye-mediated photodamage during single-molecule DNA imaging". In: *Analytical Biochemistry* 426 (2012), pp. 13–21. DOI: 10.1016/j.ab.2012.03.021.

[56] Stéfan Van der Walt et al. "scikit-image: image processing in Python". In: *PeerJ* 2 (2014), e453.

[57] Pavel Iakubovskii. *Segmentation models pytorch*. 2019.

[58] T. Y. Zhang and C. Y. Suen. "A fast parallel algorithm for thinning digital patterns". In: *Communications of the ACM* 27 (1984), pp. 236–239.

[59] Desta Fekedulegn, Maarten P. Mac Siúrtáin, and Jim J. Colbert. "Parameter estimation of nonlinear models in forestry". In: (1999).

[60] Donald W. Marquardt. “An algorithm for least-squares estimation of nonlinear parameters”. In: *Journal of the Society for Industrial and Applied Mathematics* 11 (1963), pp. 431–441.

[61] Pierre Vigier. *Perlin-NumPy: A fast and simple perlin noise generator using numpy*. 2018.

[62] Carlas S Smith et al. “Fast, single-molecule localization that achieves theoretically minimum uncertainty”. In: *Nature Methods* 7.5 (2010), pp. 373–375.

[63] Enrico Corradi, Walter Boscheri, and Marie-Laure Baudet. “SHOT-R: A next generation algorithm for particle kinematics analysis”. In: *bioRxiv* (2021), pp. 2021–12.

4

HIGH-THROUGHPUT QUANTIFICATION OF HUNTINGTIN mRNA EXPRESSION AND AGGREGATION IN MOUSE BRAIN USING AUTOMATED RNAscope IMAGING

Pieter VAN VELDE, Brian TRAN, Sarah ALLEN, Eric LUU, Raymond FURGAL, Ashley SUMMERS, Jillian BELGRAD, Emily KNOX, Anastasia KHVOROVA, David GRUNWALD

Huntington's disease (HD) is partly characterized by clustering of mutant huntingtin transcripts containing expanded CAG repeats, yet methods to quantify this RNA pathology at single-molecule resolution in tissue have been limited. Here we present a high-throughput RNAscope™ pipeline that combines automated confocal imaging with rigorous microscope characterization to quantify both single mRNA molecules and multi-transcript clusters in fixed mouse brain tissue. Using 3D Gaussian point-spread function (PSF) fitting calibrated on 200 nm fluorescent beads and pointillistic image features from tissue data, we establish per-slide intensity thresholds from negative controls and normalize experi-

This chapter has been published as a preprint on bioRxiv [1].

mental signals to single-molecule reference intensities. The critical validation of our approach operates at two scales: for single molecules, the linear relationship between bin-averaged spot intensity and spot size (Pearson $r^2 > 0.90$) reflects variable probe binding along transcripts; for clusters, the linear scaling between bin-averaged cluster mRNA content and cluster volume (ordinary least-squares fit, $R^2 > 0.98$) confirms uniform probe accessibility and enables quantitative conversion of fluorescence intensity to absolute mRNA counts. Applied to HttQ111+/- knock-in mice across multiple ages, we analyzed thousands of fields of view (FOVs), detecting >900,000 single mRNA molecules and segmenting >1.9 million mRNA clusters using two probes targeting mouse huntingtin (Htt): one detecting the spliced transcript that uses early cryptic polyadenylation sites in intron 1 (HTT1a), and one detecting full-length Htt (fl-HTT). Our analysis reveals considerable heterogeneity in mRNA accumulation: 16–62% of Q111 FOVs are classified as "extreme" (exceeding the 95th percentile of wildtype clustered mRNA levels), with striatum showing higher prevalence than cortex for both probes (HTT1a: 62% striatum, 31% cortex; fl-HTT: 44% striatum, 16% cortex). Extreme FOVs are characterized by elevated cluster numbers (2–6× more clusters per nucleus) and higher cluster density (1.3–1.7× more mRNA per μm^3). Cluster localization shows nuclear bias (~68%) in normal FOVs, but extreme FOVs exhibit a shift toward cytoplasmic localization, particularly for fl-HTT (48% nuclear vs 68% in normal FOVs), though the interpretation of this shift requires further investigation. Despite the large dataset at the cellular level, our study included only 11 mice (9 Q111, 2 wildtype), and this limited sample size precluded robust statistical inference at the animal level. Nevertheless, these quantitative metrics provide a framework for investigating disease mechanisms and evaluating therapeutic interventions using RNAscope in future studies with larger cohorts.

4.1. INTRODUCTION

RNAscope™ is an in situ hybridisation (ISH) method that addresses the long-standing trade-off between sensitivity and specificity in RNA detection. Conventional ISH often produces high background and limited sensitivity, whereas PCR-based methods lose spatial context. RNAscope pairs a stringent probe architecture with a branched amplification cascade: each "double Z" probe comprises two adjacent oligonucleotides that must bind contiguously to the target RNA before a pre-amplifier can attach, preventing amplification from partial or non-specific binding [2]. With this design, researchers visualise individual RNA molecules as discrete puncta using chromogenic or fluorescent readouts; the assay works on formalin-fixed tissue sections and supports multiplex detection of three to four targets per section [2, 3]. According to the manufacturer, each RNAscope punctate dot represents a single copy of an mRNA molecule; however, there is variation in dot intensity and size due to differences in the number of ZZ probes bound to each target molecule [4]. The manufacturer therefore recommends that "the number of dots is critical and not the intensity/size of the dot(s)." This guidance has shaped how the field uses RNAscope: current practice focuses on counting individual, well-separated puncta rather than measuring their intensities, which works well for single-molecule quantification but fails when multiple mRNAs cluster together. For mRNA clusters, ranging from just a few transcripts to dozens or even hundreds of co-localised molecules, simple dot counting cannot distinguish a single bright punctum from a cluster of many molecules, creating a fundamental measurement gap for pathologies driven by transcript clustering. In this work, we explicitly deviate from this manufacturer recommendation: our calibration framework validates that fluorescence intensity, when properly normalized, provides quantitative mRNA counts. This validation rests on three elements: (1) per-slide calibration using negative controls to establish detection thresholds, (2) modal intensity normalization using isolated single molecules as an internal standard, and (3) the resulting linear relationship between cluster volume and mean mRNA content (ordinary least-squares fit, $R^2 > 0.98$ on bin-averaged intensities), which would not hold if intensity were not quantitative. This calibrated intensity-based approach enables quantification of multi-transcript clusters that simple dot counting cannot resolve.

We apply RNAscope to Huntington disease (HD) models to demonstrate this approach. In HD, expanded CAG repeats in *HTT* transcripts cause aberrant splicing: the expanded repeat impairs normal splicing at the exon 1-intron 1 junction, leading to production of a truncated transcript that retains part of intron 1 and encodes a highly pathogenic exon 1 protein fragment [5, 6]. These mutant transcripts also form stable secondary structures that sequester RNA-binding proteins including muscleblind-like 1 (MBNL1), contributing to nuclear retention and foci formation [7, 8]. Similar MBNL1 sequestration by expanded repeat RNA occurs in myotonic dystrophy type 1 (DM1), where CUG repeats form nuclear foci that disrupt MBNL1 function [9]. Related RNA-mediated toxicity occurs in *C9orf72*-linked amyotrophic lateral sclerosis/frontotemporal dementia (ALS/FTD), where expanded G_4C_2 repeats form nuclear RNA foci [10]. Our model is the HttQ111+/- knock-in mouse, which carries a single expanded allele and exhibits progressive striatal-specific transcriptional dysregulation and neuronal intranuclear inclusions despite minimal neurodegeneration up to 12 months [11]. Beyond genotype, HD

pathology varies dramatically by anatomical location: in human post-mortem studies, striatal medium spiny neurons show early vulnerability while cortical pyramidal cells are relatively spared, and within each hemisphere, neurodegeneration progresses along a dorsal-to-ventral gradient within the striatum [12]. We therefore multiplex DARPP-32 labelling to mark medium spiny neurons (MSNs), the principal striatal neuron type, and combine it with DAPI nuclear counterstain to assess whether transcripts localize to the nucleus or cytoplasm. This cell-level and region-level heterogeneity demands comprehensive spatial sampling. Traditional approaches (manually selecting a handful of "representative" fields) risk systematic bias and cannot capture gradients of pathology across anatomical structures. Slide-scanner microscopy allows us to image entire sections, but this raises a practical question: is whole-brain coverage necessary, or can a few well-chosen slices suffice? By registering our data to the Allen Brain Atlas coordinate framework, we can test whether sub-sampling introduces artefacts and determine the minimal imaging strategy needed to reliably map regional vulnerability.

Here we present an end-to-end pipeline that integrates semi-automated slide-scanner imaging with a rigorous, quality-controlled analysis workflow to quantify mRNA clustering in HttQ111+/- mouse brain tissue using RNAscope. The primary contribution of this work is methodological: we describe a complete framework for quantifying both single mRNA molecules and multi-transcript clusters, with rigorous calibration and quality control at each stage. Each slide contains three adjacent brain sections: one hybridized with the experimental probe set targeting mouse *Htt* transcripts (a probe for the aberrantly spliced transcript that uses early cryptic polyadenylation sites in intron 1 [HTT1a] and a probe for full-length *Htt* [fl-HTT], along with DARPP-32 RNAscope probe for anatomical segmentation), one with positive control probes (POLR2A and UBC), and one with a negative control probe (non-mammalian bacterial DapB). This design enables within-slide technical validation, where positive controls establish assay sensitivity and dynamic range, while negative controls empirically determine detection thresholds for filtering background fluorescence. DARPP-32 staining in the experimental sections enables precise anatomical segmentation, distinguishing striatum from cortex and allowing region-specific analysis within each hemisphere along the rostro-caudal axis using atlas coordinates. Through high-throughput imaging of thousands of fields of view across anatomically defined cortical and striatal subregions, we first establish a single-molecule intensity calibration from isolated puncta, then characterize the transition from diffuse single molecules to high-intensity clusters using automated spot detection and spatial clustering. Our multi-tiered quality control (QC) framework filters out low-quality fields of view (FOVs) based on nuclear counts, computes slide-specific detection thresholds from negative control intensity distributions, cross-validates experimental measurements against positive control expression on the same slide, and traces outliers to distinguish technical failures from biological variation. We applied this pipeline to tissue from 9 HttQ111/+ mice (3 per age group at 2, 6, and 12 months) and 2 wildtype controls (at 2 and 12 months). We processed 30 slides total (with multiple non-continuous 40 μm-thick sections per animal), which were used for calibration and quality control analyses. After filtering slides with poor tissue quality, 18 slides remained for biological analysis: 15 Q111 slides and 3 wildtype slides. From these, we acquired 1,617 fields of view, each imaged in four color channels (DAPI nuclear stain, DARPP-32 striatal marker,

HTT1a, and fl-HTT), detected more than 900,000 single mRNA molecules, and segmented nearly 2 million mRNA clusters. We observe age-dependent increases in mRNA clustering for both fl-HTT and the pathogenic HTT1a splice variant, with substantial heterogeneity across tissue regions. However, we emphasize that while the dataset is large at the cellular level, the number of animals (particularly wildtype controls, n = 2) limits the strength of biological conclusions; the findings presented here should be considered preliminary observations that demonstrate the utility of the method rather than definitive characterization of HD progression. This approach combines statistical power from large-scale imaging with single-molecule resolution to map regional vulnerability and progression of huntingtin mRNA clustering in disease-relevant brain structures.

4.2. RESULTS

4.2.1. EXPERIMENTAL DESIGN AND DATA ACQUISITION

We imaged HttQ111+/- mice across multiple ages and anatomical regions. These mice were derived from control groups of a therapeutic study [13] and received either no treatment (2-month-old) or control injections (aCSF or NTC siRNA; see section 4.4.1 and Table 4.1). Each slide contained three coronal sections: one with experimental RNAscope probes, one with positive controls, and one with negative controls. The experimental probe configuration consisted of: C1: mm-HTT-intron1 conjugated to Alexa Fluor 488 (this probe targets intron 1 sequences, detecting both the aberrantly spliced HTT1a transcript and nascent pre-mRNA), C2: DARPP-32 conjugated to Alexa Fluor 647, C3: full-length mm-HTT (hereafter fl-HTT) conjugated to Alexa Fluor 546 (this probe targets the 3' UTR and detects full-length transcripts but not HTT1a), and a DAPI nuclear stain (probe target sequences in table S5 and Supplementary Note 4). Throughout this work, we refer to the 488 nm channel as the green channel and the 546 nm channel as the orange channel. These probes detect both wild-type (*mmHtt*) and mutant (*mmHtt1a*) transcripts, while DARPP-32 RNAscope signal provided anatomical segmentation. We observed that single-molecule detection was challenging in the Alexa 647 channel due to minimal intensity differences between specific signal and non-specific binding events in the negative control; therefore, we used DARPP-32 in this channel as a qualitative rather than quantitative measure. Positive control sections employed POLR2A in channel C1 (a low-abundance housekeeping gene), PPIB in channel C2 (a medium-abundance housekeeping gene), and UBC in channel C3 (a high-abundance housekeeping gene). Negative control sections utilized probes targeting the bacterial *dapB* gene, which has no mammalian targets. Each detection channel had its own negative control probe: dapB-C1, dapB-C2, and dapB-C3. We processed tissue from 9 Q111 mice (3 at 2 months, 3 at 6 months, 3 at 12 months) and 2 wildtype controls (1 at 2 months, 1 at 12 months), totaling 30 slides across all animals (1-4 slides per mouse). Each slide contained adjacent sections hybridized with different probe sets. All 30 slides had intact negative control sections, which were used to establish detection thresholds. Only 26 slides had intact experimental probe sections (HTT1a, fl-HTT, and DARPP-32), as tissue had fallen off during processing on 4 slides; these 26 slides were used for PSF calibration and single-molecule characterization (fig. 4.1). For biological analysis of mRNA expression and clustering (figs. 4.2 to 4.5), additional quality control filtering removed slides with insufficient tis-

sue integrity (torn tissue, scratched tissue, etc.), leaving 15 Q111 slides (from 8 mice) and 3 WT slides (from 2 mice), generating 1,334 Q111 and 283 wildtype unique imaging positions.

4.2.2. ESTABLISHING DETECTION THRESHOLDS THROUGH NEGATIVE CONTROL CALIBRATION

Quantifying mRNA at single-molecule resolution in fixed tissue presents unique challenges: probe hybridization efficiency varies between tissue types and preparation batches, autofluorescence contributes variable background, and the transition from isolated transcripts to multi-molecule clusters must be objectively defined. We address these challenges through a well-characterized, multi-stage pipeline that establishes per-slide control signals, distinguishes single molecules from clusters based on empirical size criteria, and controls for non-specific binding using negative controls (fig. 4.1).

The foundation of our quantitative approach is rigorous background characterization, based on detector characterization and conversion of grey levels to photons (see section 4.4.2). We computed per-slide, per-channel photon thresholds as the 95th percentile of integrated intensities from negative-control detections, i.e., spots detected on tissue sections hybridized with bacterial DapB probes that have no mammalian targets (n = 727,329 spots across 30 slides; see section 4.4.4 for detection pipeline details; fig. 4.1C; fig. S1). This threshold represents the intensity below which detected signals cannot be distinguished from non-specific binding and autofluorescence. Critically, we observed substantial slide-to-slide variation in these thresholds: coefficient of variation (CV) = 39.9% for the green channel (mean ± SD: 33,295 ± 13,301 photons) and CV = 43.1% for the orange channel (12,377 ± 5,337 photons). This variation motivated our per-slide normalization strategy: applying a global threshold would systematically bias results across slides. We validated that negative control thresholds showed no significant correlation with experimental mRNA expression levels across all four channel-region combinations (Pearson correlation): HTT1a in cortex ($r = -0.273$, $p = 0.345$), HTT1a in striatum ($r = -0.283$, $p = 0.307$), fl-HTT in cortex ($r = +0.255$, $p = 0.379$), and fl-HTT in striatum ($r = +0.284$, $p = 0.305$; mean $|r| = 0.274$, all $p > 0.3$; fig. S7). This weak/absent correlation is critical: it demonstrates that the biological variation we observe in HTT expression across slides is not driven by differences in negative control thresholds. Slides with higher background thresholds do not systematically show higher or lower HTT expression, confirming that observed differences in huntingtin transcript levels reflect true biological variation rather than technical artifacts of threshold determination.

For each slide, we imaged a subregion within the cortex and a subregion within the striatum, allowing us to examine whether background thresholds differed systematically between these brain regions. Comparing cortex and striatum thresholds within slides revealed no significant regional difference in either channel (paired t-test, n = 29 slides per channel: green $p = 0.451$, orange $p = 0.100$; fig. S14). Pooling both channels (58 slide–channel pairs, which are not independent and are shown for description only) gives cortex $23,057 \pm 14,660$ versus striatum $21,918 \pm 15,255$ photons (mean difference $+1,139 \pm 6,454$ photons; paired t-test $t = 1.344$, $p = 0.184$). Age showed no effect on thresholds (Pearson correlation, all $|r| < 0.1$, $p > 0.5$). Rostrocaudal position along the anterior-posterior axis also showed negligible correlations with thresholds in either re-

gion individually (Pearson correlation; cortex: $r = -0.054$, $p = 0.69$; striatum: $r = +0.086$, $p = 0.52$), indicating that the precise anatomical placement of the negative control imaging region does not meaningfully affect threshold determination. Given the absence of significant regional or positional effects, we merged the cortex and striatum measurements to compute a single per-slide threshold for subsequent analyses. An alternative cost-saving strategy (imaging negative controls on only a subset of slides and applying the pooled threshold to all slides) is evaluated in Supplementary Note 1 and figs. S22 to S24.

4.2.3. PSF CALIBRATION AND SINGLE-MOLECULE IDENTIFICATION

Initial PSF calibration from 200 nm fluorescent TetraSpeck microspheres yielded point-spread function widths of $\sigma_x = 185.0\,\text{nm}$, $\sigma_y = 187.0\,\text{nm}$ laterally, and $\sigma_z = 573.0\,\text{nm}$ axially for the green channel (40× oil objective, NA 1.3, spinning disk confocal; values for both green and orange channels in table S3). These values exceed the theoretical diffraction limit ($\sigma_{x,y} \approx \lambda/4\text{NA} \approx 99$ nm for 515 nm emission [14]), reflecting the finite bead size and non-optimal optical characteristics of the spinning disk system. However, RNAscope signals arise from branched amplification trees attached to ~20 ZZ probe pairs that bind along the target mRNA sequence. Unlike point-like fluorophores, these extended signal sources may produce spots with different characteristics than bead-derived PSFs. We therefore employed a two-stage empirical recalibration strategy, focusing on the experimental probe set (HTT1a and fl-HTT), to determine appropriate size criteria for single-molecule detection.

In the following, we illustrate the calibration procedure using the green channel (HTT1a); fig. 4.1D-I shows this channel only, with equivalent orange channel (fl-HTT) analysis in figs. S2 to S3. In the first stage, we used the bead-derived PSF ($\sigma_x = 185$ nm, $\sigma_y = 187$ nm, $\sigma_z = 573$ nm) as initial parameters for spot detection, then fitted each detected spot with a 3D Gaussian using flexible sigma values (see section 4.4.4 for detection and fitting details). Minimal filtering was applied at this stage: probability of false alarm (PFA) < 0.05 from the generalized likelihood ratio test (GLRT), and intensity above the per-slide negative control threshold. No size restrictions were applied. Raw integrated photon counts varied by 2-3× across slides due to differences in imaging parameters between sessions (tables S1 and S2), tissue autofluorescence, and probe hybridization efficiency (fig. 4.1E, inset). We normalized intensities per slide by identifying the modal intensity via kernel density estimation (KDE) [15, 16], then scaling all intensities such that this mode equals $N_{1\text{mRNA}} = 1.0$ (fig. 4.1E, main panel). Formally, the normalized intensity $\tilde{N}$ for each spot is:

$$\tilde{N} = \frac{N_{\text{raw}}}{N_{1\text{mRNA}}} \tag{4.1}$$

where N_{raw} is the integrated photon count from the 3D Gaussian fit, and $N_{1\text{mRNA}}$ is the per-slide modal intensity representing a single mRNA molecule. This normalization assumes that the most common detected signal corresponds to a single mRNA molecule, a reasonable assumption given that the detection pipeline is optimized for single spots. Plotting normalized intensity versus fitted spot size (fig. 4.1F, shown for the green channel using σ_x), we observed that intensity increases linearly from the bead PSF size toward larger spots, up to a certain point, which we term the breakpoint ($\sigma_x = 290.8$ nm for the

green channel). Beyond this breakpoint, further size increases yield no additional photon counts, a plateau reflecting model mismatch, where the Gaussian PSF model can no longer accurately describe larger structures. The breakpoint exceeds the bead PSF by 57%, reflecting the extended nature of RNAscope signal sources compared to point-like fluorophores. Figures S2 to S3 provide the complete breakpoint analysis for both channels (green and orange) across all three dimensions (σ_x, σ_y, σ_z).

In the second stage, we used the modal PSF sizes from Stage 1 as the new detection parameters, with the empirically-determined breakpoints as size upper bounds ($\sigma_x <$ 290.8 nm, $\sigma_y <$ 291.1 nm, $\sigma_z <$ 698.7 nm) and 80% of the bead-derived PSF as size lower bounds for all dimensions (spots smaller than this are likely noise or fitting artifacts). Applying these criteria to experimental tissue data (fig. 4.1H-I) yields intensity distributions that converge around $N_{1\text{mRNA}} = 1.0$ across all 26 slides (fig. 4.1H), confirming that our normalization procedure effectively removes technical variation. The size-intensity relationship (fig. 4.1I) shows a linear trend within the single-molecule regime, validating the breakpoint-based filtering. Detailed size and intensity distributions for single-molecule filtering are shown in fig. S4 (green channel) and fig. S5 (orange channel). Notably, the modal spot sizes after filtering differ between channels: the green channel (HTT1a) yields modes of $\sigma_x = 252$ nm, $\sigma_y = 258$ nm, $\sigma_z = 674$ nm, while the orange channel (fl-HTT) produces smaller modes of $\sigma_x = 239$ nm, $\sigma_y = 238$ nm, $\sigma_z = 667$ nm (5-8% smaller laterally). Since bead-derived PSF values are nearly identical between channels (table S3), this difference is not attributable to optical properties. Instead, it may reflect the shorter probe target region for fl-HTT (966 bp) compared to HTT1a (1,150 bp), with both target sequences detailed in table S5 and Supplementary Note 4, as 20 ZZ probe pairs distributed over a shorter mRNA segment would produce more spatially compact fluorescent signals. Other biological factors may also contribute, including differences in mRNA secondary structure, local folding environment, or probe binding efficiency along the target sequence. These refined single-molecule detections and the associated calibration parameters were used for all subsequent analyses.

This calibration framework enables quantitative intensity analysis of RNAscope data, a departure from conventional practice, which relies exclusively on counting discrete puncta. Within the single-molecule regime, we observe that larger spots exhibit proportionally higher fluorescence intensity, consistent with variable numbers of probe pairs binding to each target mRNA (the RNAscope amplification tree accommodates up to 20 double-Z probe pairs per target, but not all binding sites may be occupied on every transcript). Notably, the size distribution before breakpoint filtering (fig. 4.1F, bottom panel) exhibits a long tail extending toward larger sizes, reflecting unresolved clusters and model mismatch; after filtering (fig. 4.1I, bottom panel), the distribution becomes approximately normal, as expected for a homogeneous population of individual transcripts with stochastic variation in probe binding efficiency, further supporting our single-molecule assignment. By establishing per-slide control signals and empirically defining the boundary between single molecules and unresolved clusters, we can now convert integrated photon counts into absolute mRNA equivalents. This capability is essential for studying RNA clustering pathologies, where the biologically relevant signal lies not in the number of puncta but in the total transcript content of each cluster.

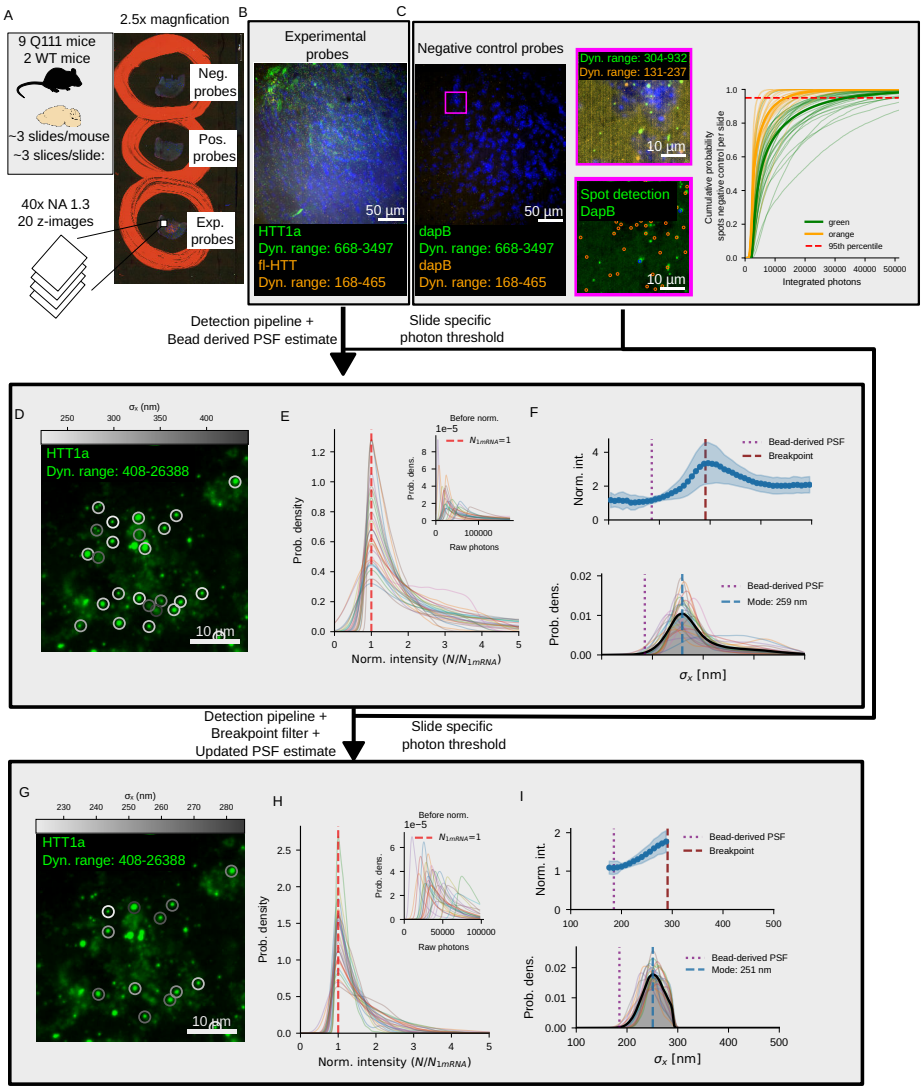

A
2.5x magnfication
9 Q111 mice
2 WT mice
~3 slides/mouse
~3 slices/slide:
Neg. probes
Pos. probes
Exp. probes
40x NA 1.3
20 z-images
B
Experimental probes
50 µm
HTT1a
Dyn. range: 668-3497
fl-HTT
Dyn. range: 168-465
C
Negative control probes
50 µm
dapB
Dyn. range: 668-3497
dapB
Dyn. range: 168-465
Dyn. range: 304-932
Dyn. range: 131-237
10 µm
Spot detection
DapB
10 µm
Cumulative probability spots negative control per slide
green
orange
95th percentile
Integrated photons
Detection pipeline + Bead derived PSF estimate
Slide specific photon threshold
D
σx (nm)
HTT1a
Dyn. range: 408-26388
10 µm
E
Before norm.
Prob. density
Raw photons
Norm. intensity (N/N1mRNA)
F
Norm. int.
Bead-derived PSF
Breakpoint
Prob. dens.
Mode: 259 nm
σx [nm]
Detection pipeline + Breakpoint filter + Updated PSF estimate
Slide specific photon threshold
G
σx (nm)
HTT1a
Dyn. range: 408-26388
10 µm
H
Before norm.
Prob. density
Raw photons
Norm. intensity (N/N1mRNA)
I
Norm. int.
Bead-derived PSF
Breakpoint
Prob. dens.
Mode: 251 nm
σx [nm]

Figure 4.1: **Establishing detection thresholds and single-molecule criteria through multi-stage calibration.** **(A)** Experimental design overview. Left: 9 Q111 and 2 WT mice, 1 to 4 slides per mouse, 3 tissue sections per slide, imaged at 40× (NA 1.3) with 20 z-planes per FOV (500 nm spacing). Right: 2.5× magnification overview showing slide layout with three adjacent coronal sections stained for negative control probes (bacterial DapB), positive control probes (housekeeping genes), and experimental probes (HTT). **(B)** Representative FOV from experimental probe section. HTT1a (green, 488 nm) and fl-HTT (orange, 548 nm) with DAPI nuclear counterstain (blue). Dynamic ranges indicated for each channel. Scale bar: 50 μm. **(C)** Negative control threshold determination. Left: FOV from DapB section displayed at same dynamic range as (B), showing minimal specific signal. Top-right inset: zoom at reduced dynamic range to visualize low-level background fluorescence. Bottom-right inset: same region with spot detection overlay; these detected spots are used to generate the CDF. Far right: CDFs of integrated photon counts from DapB sections (n = 727,329 spots, 30 slides). Faint lines: individual slides; bold lines: channel means (green = 488 nm; orange = 548 nm). Red dashed line: 95th percentile threshold. Thresholds computed per slide-channel to account for local imaging conditions. **(D-F)** *Stage 1: Initial detection using bead PSF.* Spots detected using bead-derived PSF (σ_x = 185 nm) as initial parameters, with minimal filtering (PFA < 0.05, intensity > threshold) and no size restrictions. **(D)** Representative FOV showing detected spots color-coded by fitted σ_x (250-400 nm range). Circles indicate all detected spots before size filtering, including both single molecules and unresolved clusters. Scale bar: 10 μm. **(E)** Normalized intensity distributions (n = 1,819,916 spots, 26 slides, green channel). Main: distributions with modal intensity set to $N_{1\text{mRNA}} = 1.0$. Inset: raw distributions showing 2-3× slide-to-slide variation before normalization. **(F)** Size-intensity relationship. Top: mean normalized intensity vs. σ_x showing increase from bead PSF to breakpoint, then plateau (model mismatch). Purple dotted line: bead PSF (185 nm); red dashed line: breakpoint. Bottom: σ_x probability density with mode at 259 nm. **(G-I)** *Stage 2: Detection with breakpoint filtering.* Spots detected with breakpoint-based size filtering (σ_x < 290.8 nm) to isolate single molecules. **(G)** Same FOV as (D) after applying size filter. Color scale now spans 230-280 nm, showing uniform single-molecule population. Larger clusters excluded. Scale bar: 10 μm. **(H)** Normalized intensity distributions (n = 249,526 spots, 26 slides, green channel). Successful collapse around $N_{1\text{mRNA}} = 1.0$. Inset: raw distributions before normalization. **(I)** Size-intensity relationship validates single-molecule identification. Top: intensity increases linearly with spot size below the breakpoint, as expected for single molecules with variable probe occupancy. Bottom: narrower σ_x distribution (mode 251 nm) after filtering. Technical parameters: pixel size 162.5 nm, slice depth 500 nm, size lower bounds 80% of bead-derived PSF for all dimensions ($\sigma_x \geq 148$ nm, $\sigma_y \geq 150$ nm, $\sigma_z \geq 458$ nm), PFA < 0.05. Figure S1 and Supplementary Note 1: per-slide vs. pooled threshold comparison. Figures S2 to S3: complete breakpoint analysis for both channels (green and orange) across all three dimensions (σ_x, σ_y, σ_z). Figures S4 to S5: detailed size and intensity distributions for single-molecule filtering in both channels.

4.2.4. QUANTIFYING MRNA CLUSTERS: LINEAR INTENSITY-VOLUME SCALING

Signals exceeding single-molecule size criteria cannot be resolved by PSF-based fitting and instead were captured by a 3D convolutional neural network trained to segment extended fluorescent regions (section 4.4.6). Crucially, single-molecule detection and cluster segmentation operate on the same images with overlapping sensitivity ranges, ensuring that no fluorescent signal is missed: isolated transcripts are captured by PSF fitting while extended clusters are captured by CNN segmentation. This overlap necessitates careful handling to prevent double-counting. We therefore implemented a conservative pruning strategy that serves as a double-safeguard: first, we catalog all potential signals comprehensively (including ambiguous cases during CNN training to maximize detection sensitivity), then we prune clusters that overlap with validated single-molecule coordinates. This two-stage approach (comprehensive cataloging followed by conservative pruning) ensures that single molecules are never double-counted as clusters while maintaining high sensitivity for genuine cluster detection. The pruning step removed 16.7% of green channel clusters (140,619/843,092) and 26.6% of orange channel clusters (499,176/1,875,933), indicating substantial spatial overlap between the detection modalities and validating the necessity of this safeguard. We then applied a two-stage intensity

filter: (1) the same negative control intensity threshold used for single-molecule filtering, and (2) a CV threshold on voxel intensities within each cluster (≥0.5) to remove homogeneous low-intensity regions likely arising from background fluorescence rather than true mRNA signal. This filtering discarded an additional 8.8% of green (62,153/702,473) and 2.8% of orange (38,849/1,376,757) clusters. The final dataset comprised 640,320 green channel clusters and 1,337,908 orange channel clusters across 15 Q111 slides (see section 4.2.1 for slide exclusion criteria; fig. 4.2).

For each retained cluster $\mathscr{C}$, we computed background-corrected integrated intensity using a local annular background estimate:

$$I_{\mathscr{C}} = \sum_{\mathbf{r}\in\mathscr{C}} I(\mathbf{r}) - \text{median}\{I(\mathbf{r}) : \mathbf{r} \in \text{dilate}(\mathscr{C}, r_0) \setminus \mathscr{C}\} \cdot n_{\mathscr{C}}, \tag{4.2}$$

where $\mathbf{r}$ is the spatial coordinate of a voxel, $I(\mathbf{r})$ is the fluorescence intensity at voxel $\mathbf{r}$, $n_{\mathscr{C}}$ is the number of voxels in the cluster, $\text{dilate}(\mathscr{C}, r_0)$ is the morphological dilation of $\mathscr{C}$ by radius r_0, and $\text{dilate}(\mathscr{C}, r_0) \setminus \mathscr{C}$ represents the annular region surrounding the cluster. This local background correction is critical in tissue, where fluorescence intensity can vary substantially over spatial scales of 10-20 μm due to cellular and subcellular structures. We then expressed cluster signal in single-molecule equivalents using the per-slide normalization factor from eq. (4.1):

$$\tilde{N}_{\mathscr{C}} = \frac{I_{\mathscr{C}}}{N_{1\text{mRNA}}}, \tag{4.3}$$

where $\tilde{N}_{\mathscr{C}}$ represents the mRNA content of cluster $\mathscr{C}$ in units of single-molecule equivalents. This normalization places clusters on the same quantitative scale as single mRNAs and enables direct comparison across slides despite photon-yield variations.

The critical validation of our quantitative approach is the relationship between cluster volume and mRNA content. If our single-molecule normalization correctly converts fluorescence intensity to mRNA equivalents, and if RNAscope probes uniformly access mRNA within clusters, we expect cluster mRNA content ($\tilde{N}_{\mathscr{C}}$) to scale linearly with volume. Deviation from linearity would indicate either (1) probe penetration limitations at larger cluster sizes (causing saturation), or (2) size-dependent variation in mRNA packing density (for example, if larger clusters were systematically more or less densely packed than smaller ones). We observed strong linear relationships for both channels: $\beta = 1.23$ mRNA/μm^3 for the green channel and $\beta = 1.03$ mRNA/μm^3 for the orange channel, with the slope fitted by ordinary least squares to all individual clusters within 0–30 μm^3 (fig. 4.2C-D). Across individual clusters, volume and mRNA content are strongly correlated (Pearson $r = 0.83$, $R^2 = 0.68$ for green, n = 616,100; $r = 0.89$, $R^2 = 0.79$ for orange, n = 1,314,992; Spearman $\rho = 0.89$ and 0.91), and the fitted line explains 98.8% and 99.7% of the variance of the bin-averaged intensities (R^2 on bin means, as displayed in fig. 4.2C-D). The gap between the two R^2 values reflects cluster-to-cluster scatter in mRNA content at a given volume rather than curvature of the mean relationship (fig. 4.2C-D).

This linearity has two important implications. First, it demonstrates that RNAscope probe amplification trees can access mRNA molecules throughout clusters regardless of cluster size; if probe penetration were limiting, we would observe saturation (sublinear scaling) at larger volumes. The consistent linearity across volumes spanning two

orders of magnitude (from sub-micron to >20 μm^3) indicates that even large clusters remain fully accessible to probe hybridization and branched amplification. Second, the similar slopes between channels (~1.1 mRNA/μm^3 average) suggest comparable mRNA packing density regardless of transcript type (exon 1 vs full-length), providing internal consistency validation.

Cluster volume and intensity distributions are shown in fig. 4.2E: both channels showed similar right-skewed distributions with intensity medians of 4.5 (HTT1a) and 4.3 (fl-HTT) mRNA equivalents.

We observed per-slide variation in the volume-intensity slope β (CV = 36% green, 26% orange), which represents mRNA packing density within clusters (fig. S6). This variation could potentially be explained by our choice of $N_{1\text{mRNA}}$ (the per-slide modal intensity we select as the single-molecule reference for normalization). If so, this would be problematic, as we would be introducing artificial variability through our normalization procedure rather than measuring true biological differences. To test this, we examined whether $N_{1\text{mRNA}}$ correlates with β. We observed no significant correlation between per-slide peak intensity and slope for either channel (Pearson correlation; green: $r = -0.37$, $p = 0.17$; orange: $r = 0.04$, $p = 0.89$). The observed inter-slide variability in β therefore reflects genuine biological or statistical variance across different tissue sections and animals, rather than artifacts of the normalization procedure.

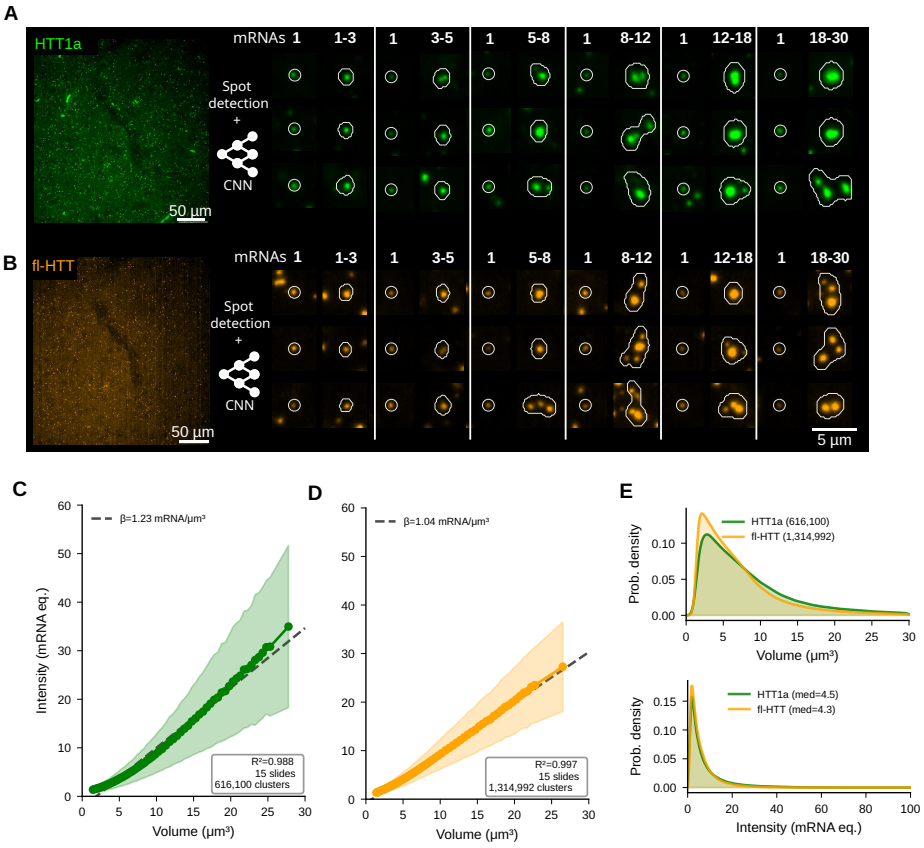


Figure 4.2: **Single mRNA detection and CNN-based cluster segmentation capture the full range of transcript aggregation states. (A)** HTT1a probe (488 nm, green). Left: representative FOV overview showing spatial distribution of mRNA signal. Scale bar: 50 μm. Right: paired comparisons of single mRNAs (left column of each pair, labeled "1") versus clusters of increasing mRNA content (right column, labeled by mRNA equivalents: 1-3, 3-5, 5-8, 8-12, 12-18, 18-30). Two rows show spot detection (circles) and CNN segmentation (white outlines). Single spots appear diffraction-limited while clusters show extended morphologies. Scale bar for zooms: 5 μm. **(B)** fl-HTT probe (548 nm, orange). Same layout as (A). **(C)** Green channel (HTT1a) cluster intensity (in mRNA equivalents) versus cluster volume. Each point represents the mean intensity of all clusters within a volume bin; shading shows ±1 SD across slides. Dashed line: linear fit with slope $\beta = 1.23$ mRNA/μm^3 fitted to the individual clusters (n = 616,100 of 640,320 clusters within 0 to 30 μm^3, 15 slides). $R^2 = 0.988$ evaluated on the binned means shown; on individual clusters Pearson $r = 0.83$ ($R^2 = 0.68$). Linear scaling validates quantitative mRNA counting and confirms probe accessibility throughout clusters. **(D)** Orange channel (fl-HTT) cluster intensity versus volume, same format as (C). Linear fit to individual clusters: $\beta = 1.03$ mRNA/μm^3 (n = 1,314,992 of 1,337,908 clusters within 0 to 30 μm^3, 15 slides). $R^2 = 0.997$ on the binned means shown; on individual clusters Pearson $r = 0.89$ ($R^2 = 0.79$). Similar slopes between channels suggest comparable mRNA packing density. **(E)** Distribution panels. Top: cluster volume distributions (KDE). Bottom: cluster intensity distributions in mRNA equivalents; medians of 4.5 (HTT1a) and 4.3 (fl-HTT). Data from Q111 animals only (15 slides). Cluster filtering: pruning removed 16.7% green (140,619/843,092) and 26.6% orange (499,176/1,875,933) clusters overlapping single-molecule spots; intensity/CV threshold removed 8.8% green (62,153/702,473, mean threshold 33,932 photons) and 2.8% orange (38,849/1,376,757, mean threshold 13,210 photons). Volume scaling: 0.0132 μm^3/voxel. Extended analyses in figs. S8 to S12.

4.2.5. REGIONAL EXPRESSION PATTERNS AND INDIVIDUAL VARIATION

Our analysis pipeline establishes a two-tier quantification strategy that captures the full spectrum of mRNA expression states. Single mRNAs are counted directly when they conform to tissue-calibrated PSF dimensions and pass stringent statistical filters ($p_{\text{FA}} < 0.05$, size within breakpoint thresholds, intensity above negative-control threshold). Clusters, detected through 3D segmentation and expressed in single-molecule equivalents via the per-slide normalization factor $N_{1\text{mRNA}}$, capture signal from densely packed or spatially unresolved transcript clusters (see section 4.4.6 for complete pipeline details). This slide-specific normalization ensures that both single molecules and clusters are quantified on a common, biologically interpretable scale that is robust to technical variation.

Throughout our analysis, we quantify three complementary measures of mRNA expression. For each region of interest $\mathscr{R}$ containing n single molecules and m clusters, we define:

$$N_{\text{single}}(\mathscr{R}) = n \quad \text{(single mRNA count)} \tag{4.4}$$

$$N_{\text{cluster}}(\mathscr{R}) = \sum_{j=1}^{m} \tilde{N}_{\mathscr{C}_j} \quad \text{(mRNA equivalents in clusters)} \tag{4.5}$$

$$N_{\text{total}}(\mathscr{R}) = N_{\text{single}}(\mathscr{R}) + N_{\text{cluster}}(\mathscr{R}) \quad \text{(total mRNA expression)} \tag{4.6}$$

where $\tilde{N}_{\mathscr{C}_j}$ is the intensity of cluster j expressed in single-molecule equivalents (eq. (4.3)). This framework enables direct comparison across experimental conditions, brain regions, and time points, as all measurements are normalized to a common molecular scale.

To convert total mRNA expression to per-nucleus values, we segment nuclei from DAPI-stained images using a residual 3D U-Net architecture (section 4.4.6). Direct counting of individual nuclei is challenging in brain tissue due to the densely packed cellular architecture, where overlapping nuclei prevent accurate instance segmentation. We therefore estimate the number of nuclei per field of view $\hat{N}_{\text{nuclei}}$ by dividing the total DAPI-stained volume by a mean nuclear volume of 716 μm^3, derived from manual diameter measurements (mean ± SEM: 10.6 ± 0.2 μm; SD = 2.3 μm; n = 120 nuclei; fig. S25; Supplementary Note 2). We then express mRNA per nucleus as:

$$\tilde{N}_{\text{mRNA}} = \frac{N_{\text{total}}(\mathscr{R})}{\hat{N}_{\text{nuclei}}} \tag{4.7}$$

This normalization controls for variation in cell density across FOVs and enables comparison of expression levels across tissue regions.

Having established this quantitative framework, we examined mRNA expression across brain regions (fig. 4.3). We analyzed expression across 9 anatomical subregions: 4 striatal quadrants (dorsomedial, dorsolateral, ventrolateral, ventromedial) definitively identified via DARPP-32 marker expression, and 5 cortical areas (motor, somatosensory upper limb, somatosensory nose, gustatory/insular, and piriform) assigned based on anatomical landmarks alone. Unlike the striatal subregions, where DARPP-32 immunoreactivity provides unambiguous molecular boundaries, cortical area assignments relied on visual comparison to the mouse brain atlas without cell-type-specific markers; consequently, there is inherent uncertainty in the precise cortical area designations, and some FOVs

may be misclassified. One-way ANOVA revealed no significant differences between subregions within cortex or within striatum for either transcript (all $p > 0.67$; Tukey HSD, all adjusted $p > 0.7$), and paired t-tests on slide means showed no difference between cortex and striatum as major regions (HTT1a $p = 0.555$, fl-HTT $p = 0.113$, n = 14 slides; fig. 4.3B; fig. S17). Given this uniformity, we combined all FOVs within each region for subsequent analyses. Rostrocaudal variation is examined separately below (fig. 4.3E).

We examined total mRNA expression across ages (2, 6, and 12 months) in Q111 mice (fig. 4.3D; fig. S18). To avoid pseudoreplication, we first averaged FOVs within each slide, then compared per-slide means across conditions. Although median expression values increased consistently with age across all conditions (e.g., Q111 striatum HTT1a: 5.4 mRNA/nucleus at 2 months, 17.0 at 6 months, 25.7 at 12 months), Mann-Whitney U tests between consecutive ages (2 vs 6 and 6 vs 12 months) did not reach statistical significance (all $p > 0.05$), likely due to limited statistical power with small sample sizes (n = 4-6 slides per age group). Similarly, comparisons between cortex and striatum within each age and genotype, and between Q111 and wildtype within each region and age, showed no significant differences (Mann-Whitney U tests on per-slide means, all $p > 0.26$). Note that with 1–2 wildtype slides per age the wildtype comparisons cannot reach $p < 0.33$ and are descriptive only. Median total mRNA levels in Q111 at 12 months: cortex HTT1a 25.3, fl-HTT 42.3 mRNA/nucleus; striatum HTT1a 25.7, fl-HTT 36.2 mRNA/nucleus.

Critically, examination of individual animals revealed substantial inter-mouse variability (fig. 4.3F; fig. S19): some Q111 mice showed expression levels comparable to wildtype, while others exhibited dramatically elevated mRNA accumulation (>50 mRNA/nucleus vs <10 in low-expressing mice). This variability suggests that mean expression values may obscure biologically important heterogeneity. The majority of HTT signal arose from clustered rather than single mRNA molecules: single mRNA contributed <10% of total expression (mean single mRNA: 0.39-0.49 mRNA/nucleus for HTT1a, 1.77-1.84 for full-length; figs. S12 to S13), indicating that most HTT signal arises from clusters, defined as any fluorescent signal above threshold that did not qualify as a single molecule according to our size criteria (section 4.4.5).

Given the limited number of slides per condition (n = 4-6) and even fewer mice, we lacked statistical power to draw firm conclusions about age or genotype effects at the animal level. To gain additional insight into HTT expression heterogeneity in Q111 mice, we therefore examined variation at the level of individual fields of view, focusing on clustered mRNA abundance and cluster properties.

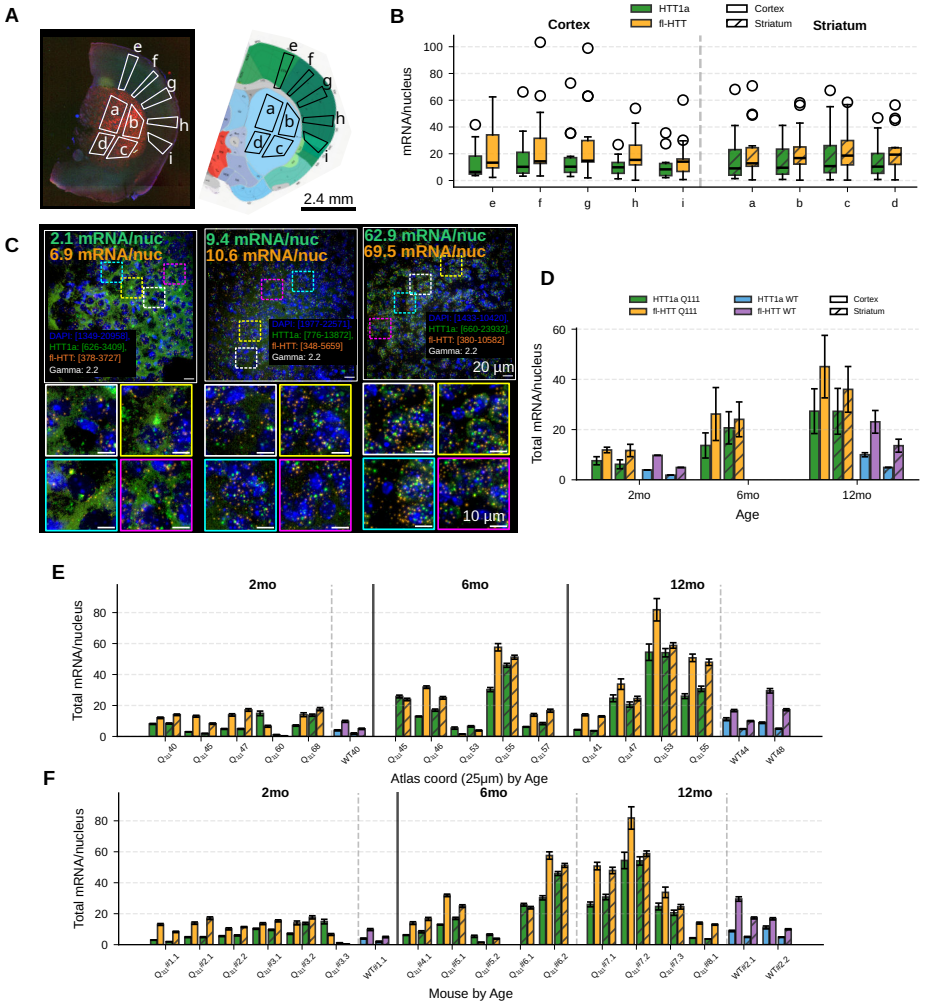

A
B
Cortex
Striatum
HTT1a
fl-HTT
mRNA/nucleus
2.4 mm
C
2.1 mRNA/nuc
6.9 mRNA/nuc
9.4 mRNA/nuc
10.6 mRNA/nuc
62.9 mRNA/nuc
69.5 mRNA/nuc
20 µm
10 µm
D
HTT1a Q111
fl-HTT Q111
HTT1a WT
fl-HTT WT
Total mRNA/nucleus
Age
2mo
6mo
12mo
E
Atlas coord (25µm) by Age
F
Mouse by Age

Figure 4.3: **Regional expression patterns and total mRNA quantification in Q111 and WT mice. (A)** Anatomical overview. Left: striatum (red) identified via DARPP-32 marker; yellow box shows imaging FOV locations. Right: schematic with subregion labels (a-i), adapted from the Allen Mouse Brain Atlas [17]. Striatal (DARPP-32 identified): a = dorsomedial, b = dorsolateral, c = ventrolateral, d = ventromedial. Cortical (approximate, no cell markers): e = motor (M1/M2), f = somatosensory upper limb (S1), g = somatosensory nose (S1), h = gustatory/insular, i = piriform. **(B)** Sub-regional expression (n = 250 measurements). X-axis: cortical (e-i, left of dashed line) and striatal (a-d, right) subregions. Box plots: median, IQR, 1.5×IQR whiskers. Green: HTT1a; orange: fl-HTT. Solid: cortex; hatched: striatum. **(C)** Representative FOV images: low, medium, high expression. Expression values annotated (green = HTT1a, orange = fl-HTT, mRNA/nucleus). DAPI nuclear stain in blue. Images displayed with gamma correction ($\gamma = 2.2$; $I_{\text{out}} = I_{\text{in}}^{1/\gamma}$) to enable simultaneous visualization of dim single molecules and bright clusters; the intensity scale is therefore non-linear, and bright spots are substantially brighter in the raw data than they appear. Dynamic ranges (raw image intensity values, not photon-corrected) shown at bottom of each panel. **(D)** Total mRNA by age (2, 6, 12 months). Each point represents one slide (per-slide mean of FOVs); bars show group median. Q111: green/orange; WT: blue/purple. Solid: cortex; hatched: striatum. Mann-Whitney U tests: no significant differences between ages, regions, or genotypes (all $p > 0.05$), likely due to limited sample sizes (n = 4-6 slides per group). **(E)** Expression by approximate atlas coordinate (assigned by visual comparison to Allen Mouse Brain Atlas coronal sections spaced at 100 μm intervals [17]), grouped by age. **(F)** Per-mouse breakdown, grouped by age. IDs: Q_{111}#1-Q_{111}#8, WT#1-WT#2; see Table 4.1 for mapping. Data: 1,334 Q111 FOVs (2,668 including both channels), 283 WT FOVs (566 including both channels). Extended analysis in figs. S12 to S13, figs. S17 to S19.

4.2.6. FOV-LEVEL ANALYSIS REVEALS HETEROGENEOUS MRNA ACCUMULATION

To move beyond mean expression values and characterize the distribution of mRNA accumulation at finer spatial resolution, we analyzed individual FOVs and compared Q111 distributions to wildtype (fig. 4.4A-C). We defined "extreme" FOVs as those with clustered mRNA per nucleus exceeding the 95th percentile (P95) of the wildtype distribution, a biologically grounded threshold that accounts for natural variation in healthy tissue. By definition, only ~5% of wildtype FOVs exceed this threshold, so any substantial deviation in Q111 mice indicates disease-associated mRNA accumulation.

We compared clustered mRNA per nucleus between Q111 and wildtype FOVs using Mann-Whitney U tests (fig. 4.4B-C). Wildtype P95 thresholds (dashed lines) were: HTT1a cortex 12.80, striatum 7.76 mRNA/nucleus; fl-HTT cortex 38.43, striatum 20.57 mRNA/nucleus. The lower striatal thresholds reflect lower baseline HTT expression in wildtype striatum.

This analysis revealed substantial heterogeneity in Q111 tissue. For HTT1a, 30.8% of cortical FOVs (215/697) and 62.0% of striatal FOVs (395/637) exceeded wildtype P95 thresholds, far exceeding the 5% expected by chance; the underlying expression distributions differ significantly between genotypes in both regions (Mann–Whitney U on FOVs, which are not independent observations: cortex $p = 7.6 \times 10^{-4}$, striatum $p < 10^{-30}$). For fl-HTT, 16.1% of cortical FOVs (112/697) and 43.5% of striatal FOVs (277/637) showed elevated clustering; here the genotype difference in the underlying distributions is significant in striatum ($p < 10^{-18}$) but not in cortex ($p = 0.80$). The higher prevalence of extreme FOVs in striatum is consistent with known striatal vulnerability in HD, where medium spiny neurons show selective susceptibility compared to cortical neurons [18, 19].

We examined factors contributing to this heterogeneity (fig. 4.4D and F). The proportion of extreme FOVs increased with age in Q111 mice, while remaining low in wildtype controls (fig. 4.4D). Individual mouse analysis revealed substantial animal-to-animal varia-

tion (fig. 4.4F): some Q111 mice showed >80% extreme FOVs while others remained near wildtype levels. However, given our limited sample size (8 Q111 and 2 wildtype mice, 15 slides after quality filtering), these trends should be interpreted with caution; larger cohorts will be needed to determine whether age, anatomical position, or other factors reliably predict mRNA accumulation phenotypes.

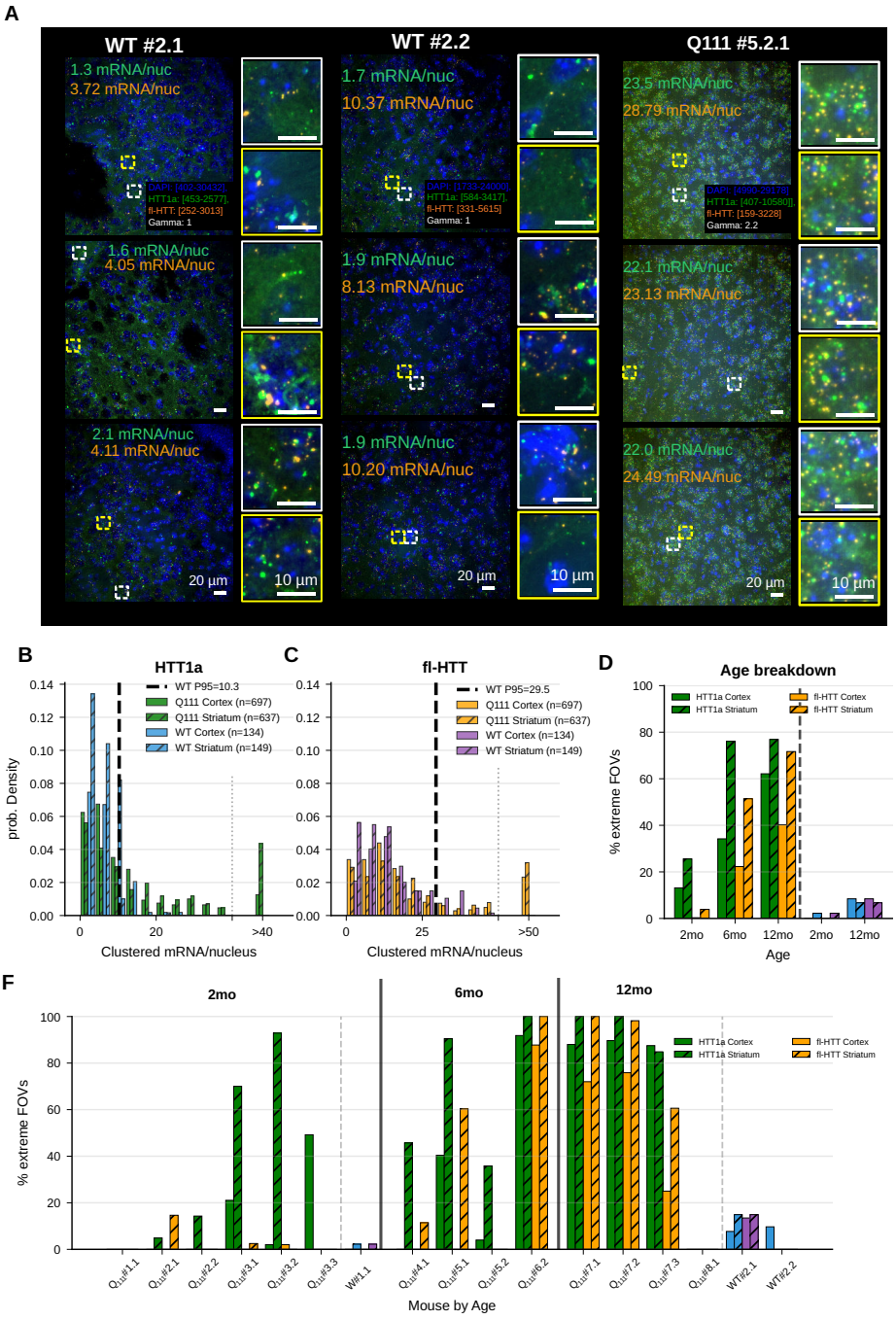

A
WT #2.1
WT #2.2
Q111 #5.2.1
1.3 mRNA/nuc
3.72 mRNA/nuc
1.7 mRNA/nuc
10.37 mRNA/nuc
23.5 mRNA/nuc
28.79 mRNA/nuc
1.6 mRNA/nuc
4.05 mRNA/nuc
1.9 mRNA/nuc
8.13 mRNA/nuc
22.1 mRNA/nuc
23.13 mRNA/nuc
2.1 mRNA/nuc
4.11 mRNA/nuc
1.9 mRNA/nuc
10.20 mRNA/nuc
22.0 mRNA/nuc
24.49 mRNA/nuc
20 µm
10 µm
B
HTT1a
WT P95=10.3
Q111 Cortex (n=697)
Q111 Striatum (n=637)
WT Cortex (n=134)
WT Striatum (n=149)
prob. Density
Clustered mRNA/nucleus
C
fl-HTT
WT P95=29.5
Q111 Cortex (n=697)
Q111 Striatum (n=637)
WT Cortex (n=134)
WT Striatum (n=149)
Clustered mRNA/nucleus
D
Age breakdown
HTT1a Cortex
HTT1a Striatum
fl-HTT Cortex
fl-HTT Striatum
% extreme FOVs
2mo
6mo
12mo
Age
F
2mo
6mo
12mo
% extreme FOVs
Mouse by Age

Figure 4.4: **FOV-level variance and extreme outlier analysis reveals heterogeneous mRNA accumulation.** **(A)** Representative FOV images comparing WT and extreme Q111 expression. Left two columns: WT mice (#2.1, #2.2) showing typical low-to-moderate expression (1-10 mRNA/nucleus). Right column: Q111 mouse (#5.2.1) showing an extreme FOV with elevated clustered mRNA (>20 mRNA/nucleus). Each column displays three FOVs with per-nucleus mRNA values annotated (green = HTT1a, orange = fl-HTT); insets show higher magnification of clusters. DAPI nuclear stain in blue. Q111 images displayed with gamma correction ($\gamma = 2.2$; $I_{\text{out}} = I_{\text{in}}^{1/\gamma}$) to enable simultaneous visualization of dim single molecules and bright clusters; the intensity scale is therefore non-linear, and bright spots are substantially brighter in the raw data than they appear. WT images displayed with linear scaling ($\gamma = 1.0$) as signal intensity is lower and does not require compression. Dynamic ranges (raw image intensity values, not photon-corrected) shown at bottom of each panel. Scale bars: 10 μm (main), 20 μm (insets). **(B)** HTT1a: clustered mRNA/nucleus distributions. Histograms with tail bin (>40) compressing outliers. Black dashed: WT P95 threshold, drawn as the mean of the two region-specific values (cortex 12.80, striatum 7.76 mRNA/nucleus); FOVs were classified as extreme against the region-specific threshold, not against this line. Q111 cortex: 30.8% extreme (215/697 FOVs), median 7.47; Q111 striatum: 62.0% extreme (395/637 FOVs), median 11.84. WT cortex: n = 134, median 7.47; WT striatum: n = 149, median 3.67. Mann-Whitney: cortex $p = 7.58 \times 10^{-4}$, striatum $p = 4.57 \times 10^{-31}$. **(C)** fl-HTT: same analysis. WT P95 thresholds: cortex 38.43, striatum 20.57. Q111 cortex: 16.1% extreme (112/697), median 13.52; striatum: 43.5% extreme (277/637), median 17.68. WT cortex median 13.47; WT striatum median 9.12. Mann-Whitney: cortex $p = 7.99 \times 10^{-1}$, striatum $p = 3.70 \times 10^{-19}$. **(D)** Extreme FOV % by age. Q111 left, WT right of dashed line. **(F)** Per-mouse extreme FOV %, grouped by age. IDs consistent with fig. 4.3F. Extreme = clustered mRNA/nucleus > WT P95 (per channel-region). Extended analysis in figs. S15 to S16.

4

4.2.7. CLUSTER PROPERTIES DISTINGUISH EXTREME FROM NORMAL FOVS

Having identified tissue regions with abnormal mRNA accumulation, we asked what distinguishes clusters in extreme FOVs from those in normal FOVs (fig. 4.5; figs. S20 to S21). Do extreme FOVs simply contain more clusters, or are individual clusters also different in size, density, or subcellular localization?

Extreme FOVs showed increased cluster abundance compared to normal FOVs (fig. 4.5B): for HTT1a, extreme FOVs had median 2.14 clusters/nucleus in cortex vs 0.81 in normal FOVs, a 2.6× fold change; striatum showed median 2.68 vs 0.46, a 5.8× fold change. For fl-HTT, cortex showed a 4.7× increase (median 7.74 vs 1.64); striatum 3.3× (5.69 vs 1.75). All four differences are significant (Mann-Whitney U on FOVs, $p < 10^{-50}$; fig. 4.5B; fig. S20 to fig. S21). Because extreme FOVs are defined by clustered mRNA per nucleus, which equals clusters per nucleus times mRNA per cluster, a difference in at least one of these two factors is expected by construction; the informative result is that cluster number accounts for most of the difference. This 2-6-fold increase in cluster number is the primary driver of elevated mRNA levels in extreme FOVs. Individual clusters in extreme FOVs also contained more mRNA (fig. 4.5C): the per-FOV mean cluster mRNA was 12.8 vs 6.2 mRNA equivalents in cortex and 9.8 vs 5.4 in striatum for HTT1a (medians across FOVs; Mann-Whitney U, both $p < 10^{-39}$), indicating that both cluster number and mRNA content per cluster contribute to elevated expression.

Beyond abundance and mRNA content, clusters in extreme FOVs differed in their mRNA packing density (fig. 4.5E): median cluster density was 1.3-1.7-fold higher in extreme compared to normal FOVs (HTT1a: 0.92 vs 0.55 mRNA/μm^3, 1.69× fold change; fl-HTT: 0.95 vs 0.74 mRNA/μm^3, 1.29× fold change). This indicates that clusters in extreme FOVs are not simply bigger; they contain more mRNA per unit volume.

Clusters showed nuclear bias in both extreme and normal FOVs (fig. 4.5D), with 67-68% located within the DAPI-stained nuclear region in normal FOVs (median distance to DAPI: −1.05 to −1.12 μm). However, extreme FOVs showed a significant shift toward

cytoplasmic localization, particularly for fl-HTT: extreme FOVs showed 45-49% nuclear clusters (median distance +0.12 to +0.34 μm, i.e., cytoplasmic) vs 68% in normal FOVs; the per-FOV nuclear fraction differed accordingly (Mann-Whitney U: $p = 2.2 \times 10^{-32}$ cortex, $p = 5.2 \times 10^{-35}$ striatum; fig. S21D and J). HTT1a showed a more modest shift (62-66% nuclear clusters in extreme vs 68% in normal FOVs; per-FOV nuclear fraction 61-66% vs 74-75%, $p = 1.7 \times 10^{-6}$ cortex, 7.0×10^{-15} striatum; fig. S20C, D, I and J).

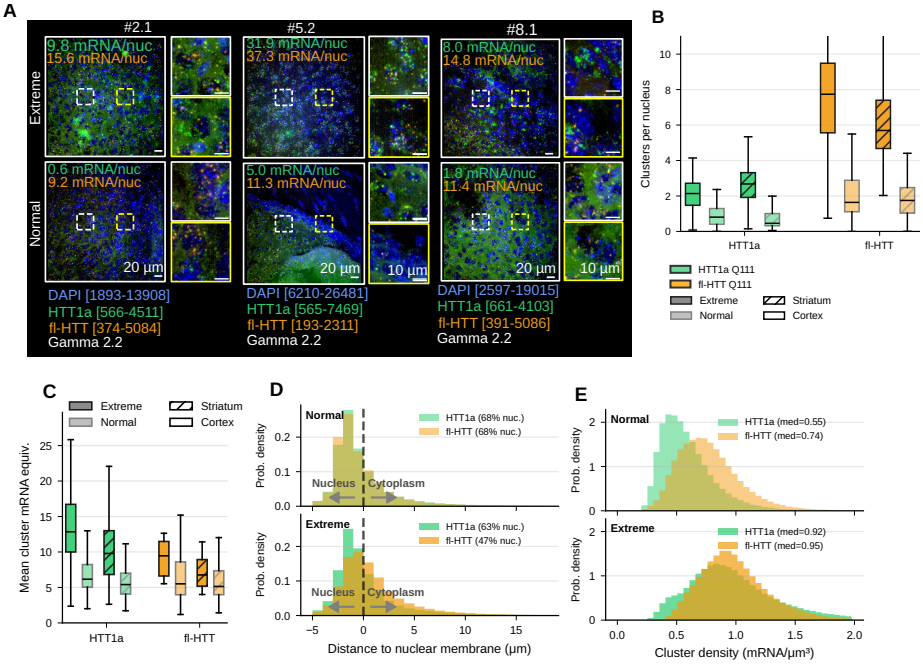


Figure 4.5: **Cluster properties in extreme vs normal FOVs reveal mechanistic insights.** **(A)** Representative FOV images comparing extreme (top row) vs normal (bottom row) Q111 expression across three mice (#2.1, #5.2, #8.1). Per-nucleus mRNA values annotated (green = HTT1a, orange = fl-HTT); insets show higher magnification of clusters. DAPI nuclear stain in blue. Images displayed with gamma correction ($\gamma = 2.2$; $I_{\text{out}} = I_{\text{in}}^{1/\gamma}$) to enable simultaneous visualization of dim single molecules and bright clusters; the intensity scale is therefore non-linear, and bright spots are substantially brighter in the raw data than they appear. Dynamic ranges (raw image intensity values, not photon-corrected) shown at bottom of each column. Scale bars: 20 μm (main), 10 μm (insets). **(B)** Clusters per nucleus. Box plots: extreme (dark, left) vs normal (light, right) Q111 FOVs. Sample sizes: HTT1a cortex normal n = 479, extreme n = 218; striatum normal n = 238, extreme n = 399; fl-HTT cortex normal n = 584, extreme n = 112; striatum normal n = 361, extreme n = 276. Mann-Whitney U test: HTT1a cortex extreme median = 2.137, normal = 0.807, $p = 2.86 \times 10^{-54}$; striatum extreme = 2.678, normal = 0.458, $p = 9.03 \times 10^{-91}$. Cluster number is the primary driver of elevated mRNA. **(C)** Mean cluster size (mRNA equivalents). Extreme FOVs have larger clusters. **(D)** Cluster localization (distance to DAPI edge, μm). Negative = nuclear; positive = cytoplasmic. Top: normal FOVs; bottom: extreme FOVs. Legend shows nuclear % (HTT1a: 67.9% normal, 63.0% extreme; fl-HTT: 67.9% normal, 47.5% extreme). **(E)** Cluster density (mRNA/μm^3). Top: normal; bottom: extreme. HTT1a median normal = 0.55, extreme = 0.92 (1.69×); fl-HTT median normal = 0.74, extreme = 0.95 (1.29×). Quality control: FOVs with <40 nuclei were excluded to ensure reliable per-nucleus normalization, removing 3,253 HTT1a clusters and 9,735 fl-HTT clusters relative to the unfiltered totals in fig. 4.2. Total clusters after filtering: HTT1a 637,067 (normal 218,402, extreme 418,665); fl-HTT 1,328,173 (normal 675,615, extreme 652,558). Extended analysis in figs. S20 to S21.

4.2.8. TECHNICAL VALIDATION AND CONTROL ANALYSES

Control analyses validated that experimental signals represent genuine biological variation rather than technical artifacts. Negative control thresholds showed no significant correlations with experimental mRNA expression (Pearson $|r| < 0.3$, $p > 0.3$ for all channel-region combinations; fig. S7). Positive control analysis quantified housekeeping gene expression: POLR2A (low-abundance) showed 16 ± 15 mRNA/nucleus in cortex and 17 ± 20 in striatum (paired t-test: $t = -0.91$, $p = 0.38$), while UBC (high-abundance) showed 89 ± 48 and 177 ± 105 mRNA/nucleus respectively (paired t-test: $t = -4.81$, $p = 0.0002$) (fig. S8). POLR2A showed strong correlations with experimental HTT probes (Pearson correlation; cortex $r = 0.81$, striatum $r = 0.98$ for HTT1a; fig. S9). A potential concern is that these correlations could be spurious: tissues with better RNA preservation might show higher counts for all transcripts, creating apparent correlations between any gene pair. To investigate this, we performed partial correlation analysis, statistically removing the effect of UBC (used here as a proxy for tissue quality) from both POLR2A and HTT measurements. If the original correlations were driven by tissue quality, partial correlations would be substantially reduced. Instead, correlations remained virtually unchanged (HTT1a striatum: original $r = 0.975$, partial $r = 0.977$; fig. S10). While this analysis has caveats (UBC may not perfectly capture all technical variation), the persistence of strong correlations after controlling for tissue quality is consistent with genuine biological coupling rather than a pure technical artifact. Comparison with bulk RNA-seq data from an independent Q111 mouse cohort (GSE65774 [20]) showed agreement in order of magnitude: the unit-independent UBC/POLR2A ratio had a similar mean in the two methods (44 ± 68 RNAscope, n = 16 slides, vs 54 ± 10 RNA-seq, n = 24 samples; Welch's t-test $p = 0.56$), but the RNAscope distribution is much wider and right-skewed, so its median is lower (22.5 vs 58.2; Mann–Whitney U $p = 0.002$; fig. S11). The higher RNAscope variance (CV 154% vs 18% for the ratio) likely reflects preserved cell-to-cell heterogeneity that bulk RNA-seq averages out [21]; sampling differences may also contribute, as our RNAscope approach examines thin tissue sections (40 μm) from specific anatomical locations, while the RNA-seq dataset used dissected striatum of unspecified volume.

4.3. DISCUSSION

We have developed and validated a high-throughput RNAscope imaging pipeline that quantifies both single mRNA molecules and their clusters in fixed brain tissue at single-molecule resolution. The key technical innovation is the establishment of a quantitative relationship between fluorescence intensity and absolute mRNA content, validated at two scales: for single molecules, the linear relationship between spot size and bin-averaged intensity (Pearson $r^2 > 0.90$) is consistent with variable probe binding along the transcript; for clusters, the linear scaling between cluster volume and mRNA equivalents (ordinary least-squares fit, $R^2 > 0.98$ on bin-averaged intensities) confirms uniform probe accessibility. Applied to HttQ111+/- knock-in mice, our analysis reveals several notable features of mutant huntingtin transcript biology: a substantial fraction of HTT mRNA exists in clusters rather than as single molecules, these clusters typically contain 4-5 transcripts, and considerable heterogeneity exists across tissue regions.

4.3.1. TECHNICAL ADVANCES: QUANTITATIVE MRNA COUNTING THROUGH VALIDATED LINEARITY

Our pipeline addresses key limitations of standard RNAscope analysis by establishing objective, reproducible methods for quantifying both single mRNA molecules and multi-transcript clusters. The critical validation is the linear relationship between cluster volume and mRNA content. This linearity is essential for three reasons: (1) it confirms that our per-slide modal normalization correctly converts arbitrary intensity units to absolute mRNA counts; (2) it demonstrates that RNAscope probe amplification trees access mRNA uniformly throughout clusters, with no saturation at larger cluster sizes; and (3) it provides a quantitative foundation for comparing mRNA accumulation across samples, slides, and experimental conditions.

For single-molecule detection, we use empirical PSF calibration that accounts for the ~57% larger effective spot dimensions arising from RNAscope probe cluster geometry compared to 200 nm fluorescent beads. The two-stage calibration (first establishing the size-intensity relationship on high-quality data to identify the breakpoint, then applying size-based filtering to isolate single molecules) provides an objective, data-driven approach to single-molecule identification that does not rely on arbitrary intensity thresholds.

For cluster quantification, we developed a neural network-based 3D segmentation approach combined with intensity normalization using the per-slide single-molecule reference. The two-stage cluster filtering (pruning overlaps with single molecules, then applying intensity and CV thresholds) prevents double-counting while removing background signals. The resulting intensity-volume relationship validates this approach: deviations from linearity would indicate probe penetration limitations, normalization errors, or systematic biases in cluster segmentation.

The per-slide normalization strategy is essential given the 2-3× variation in raw photon counts across slides (fig. 4.1E, inset). By identifying the modal intensity (the most common signal, corresponding to single mRNA molecules) via KDE and scaling each slide such that this mode equals $N_{1\text{mRNA}} = 1.0$, we center the intensity distributions around 1.0 (fig. 4.1E, main panel). After applying size-based filtering to isolate single molecules, the distributions sharpen further around $N_{1\text{mRNA}} = 1.0$ (fig. 4.1H), confirming that the filtering step successfully isolates a homogeneous population of single-molecule signals.

This quantitative intensity approach explicitly departs from manufacturer guidance, which emphasizes dot counting over intensity measurement. Our departure is justified by empirical validation: the strong linear relationship between cluster volume and normalized intensity (Pearson $r = 0.83$–0.89 across individual clusters; $R^2 > 0.98$ for the bin-averaged relationship) demonstrates that our calibration procedure successfully converts fluorescence intensity to absolute mRNA counts. Without this calibration framework, particularly the per-slide modal normalization and negative control thresholds, intensity-based quantification would indeed be unreliable due to the substantial slide-to-slide variation we observe (2-3× in raw photon counts). The manufacturer's conservative guidance reflects the challenges of intensity quantification without proper calibration, which our pipeline addresses.

SOURCES OF VARIANCE AND INFERENCE FRAMEWORK

Our measurements contain both technical and biological sources of variation. Technical variation arises from slide-to-slide differences in imaging parameters (2-3× variation in raw photon counts) and negative control thresholds (CV ≈ 40%). We address this through per-slide calibration: modal normalization removes photon-yield differences, and per-slide negative control thresholds account for local background conditions.

Biological variation occurs at multiple levels. Between animals, we observe substantial differences in mRNA accumulation (fig. 4.3F), with some Q111 mice showing expression levels comparable to wildtype while others exhibit dramatically elevated clustering. Within animals, different tissue regions show heterogeneous mRNA accumulation: the fraction of FOVs classified as "extreme" (exceeding wildtype P95 thresholds) varies by brain region and probe, ranging from 16% (fl-HTT in cortex) to 62% (HTT1a in striatum). Age effects trend upward but do not reach statistical significance with our current sample sizes.

Our study design samples at three nested levels: multiple FOVs per slide, multiple slides per mouse, and multiple mice per condition. For statistical comparisons, we average FOVs within each slide first, then compare slides across conditions. This avoids treating FOVs as independent observations (pseudoreplication) and ensures that the high FOV-to-FOV variability (~30% CV) is appropriately averaged rather than inflating our apparent statistical power. The biological variance between animals, not technical noise between FOVs, is what limits our ability to detect genotype and age effects.

4.3.2. BIOLOGICAL INSIGHTS: HETEROGENEOUS MRNA ACCUMULATION

A notable observation is not the prevalence of clustering per se, but rather the heterogeneous distribution of elevated clustering across tissue. Independent work using FISH has demonstrated widespread formation of mutant HTT mRNA clusters in HD mouse models, with 54-96% of striatal and cortical neurons containing clusters in YAC128 and BACHD-97Q-ΔN17 mice [22]; similar nuclear clustering was confirmed in YAC128 and BAC-CAG models [23]. Our FOV-level analysis reveals that 16-62% of Q111 FOVs exceed the 95th percentile of wildtype clustered mRNA, with considerable regional and individual variation. In striatum, 62.0% of Q111 FOVs showed extreme HTT1a clustering compared to only 30.8% in cortex; for fl-HTT, the corresponding values were 43.5% and 16.1%. This heterogeneity (where a substantial subset of tissue regions shows elevated mRNA accumulation) may be relevant to understanding disease pathogenesis and assessing therapeutic mechanisms, though larger sample sizes will be needed to confirm these patterns.

Although our per-slide analysis lacked statistical power to detect significant age effects (n = 4-6 slides per group), median mRNA expression values increased consistently with age across all conditions (e.g., Q111 striatum HTT1a: 5.4 at 2 months to 25.7 mRNA/nucleus at 12 months). This trend is consistent with the progressive pathology reported in Q111 mice, where neuronal intranuclear inclusions (NIIs) of mutant huntingtin protein increase from near-zero at 3 months to 28% of striatal neurons by 12 months, with inclusion size increasing over 40% between 9 and 12 months [11], and motor phenotypes emerge at 9 months and worsen progressively [24]. Future studies with larger sample sizes will be needed to determine whether the observed mRNA trends reach statistical

significance.

Our quantitative framework enables characterization of this heterogeneity. Extreme FOVs are characterized by: (1) elevated cluster numbers per nucleus (2-6× increase), indicating that cluster number is a primary driver of elevated total mRNA; (2) higher cluster density, i.e., more mRNA molecules packed per unit volume (1.3-1.7× higher); and (3) a shift toward cytoplasmic localization in extreme FOVs, particularly for fl-HTT (48% vs 68% nuclear). The interpretation of this cytoplasmic shift remains unclear. While mutant huntingtin has been shown to disrupt nuclear pore complex integrity [25], HD models typically show nuclear *retention* of mRNA rather than increased cytoplasmic accumulation [22]. The shift we observe could reflect altered nucleocytoplasmic transport dynamics, differences in cluster detection sensitivity between compartments, or other factors that will require further investigation. These specific metrics provide quantitative readouts that could potentially be used to assess therapeutic interventions targeting HTT expression or processing.

The mRNA clusters we characterize here are consistent with previous observations of mutant huntingtin mRNA forming nuclear clusters in HD mouse models, where these structures have been shown to exhibit phase-separation-like properties and resist therapeutic silencing [22, 23]. More broadly, nuclear mRNA foci containing repeat-expanded transcripts form through RNA-driven phase separation in a repeat length-dependent manner [26], and mutant huntingtin protein inclusions themselves behave as dynamic, phase-separated compartments [27]. Our 3D z-stack imaging enables direct volumetric density measurements (0.55-0.95 mRNA/μm^3), a metric not commonly reported in condensate studies. For example, Cochard et al. used smFISH with maximum intensity projections to quantify RNA recruitment to artificial protein condensates, reporting surface densities of 2-16 RNA/μm^2 and ~25-32 total RNAs per condensate (0.8-2.0 μm diameter) [28]. The total mRNA content per structure is in the same order of magnitude as our measurements (median 3.8-4.5, mean 6-9 mRNA equivalents per cluster), with the tail of our distribution extending beyond 20 mRNA equivalents (fig. 4.2E). However, converting their 2D surface density to volumetric density (by dividing total surface RNA by the sphere volume: $\frac{\rho_s \cdot 4\pi r^2}{(4/3)\pi r^3} = \frac{3\rho_s}{r}$) yields ~6-120 RNA/$\mu$m^3, substantially higher than our values. This difference may reflect distinct biology (native disease-associated mRNA clusters vs. engineered protein condensates), but also highlights that volumetric density depends critically on how cluster boundaries are defined. Defining boundaries consistently is non-trivial: we use local background correction, which makes total mRNA counts robust to boundary placement (a slightly larger boundary still yields accurate mRNA counts because background signal is subtracted), but the volume is directly affected by boundary choice, and thus so is the density. Consistent methodology, as applied here, is essential for meaningful comparisons across conditions. The observation that clusters in extreme FOVs show higher mRNA packing density could reflect concentration-dependent effects, where elevated local mRNA levels promote further condensation, though distinguishing active concentration mechanisms from passive crowding will require additional experiments.

Several mechanisms could contribute to this heterogeneity. First, transcription from the mutant allele may be stochastically variable, with some cells experiencing transcriptional bursts that generate high local mRNA concentrations [29, 5]. Second, CAG repeat-

containing transcripts form stable hairpin secondary structures that may impair degradation or export; in-cell studies show these hairpins remain largely folded under physiological conditions [8]. Third, regional differences in RNA binding protein expression could modulate HTT accumulation; expanded CAG repeats sequester MBNL1 and other splicing factors, leading to aberrant splicing and potentially altered transcript stability [7].

Critically, HTT1a arises from CAG repeat length-dependent incomplete splicing: the expanded repeat causes a block in splicing between exon 1 and exon 2, followed by cleavage and polyadenylation at a cryptic site in intron 1, producing a short mRNA encoding only exon 1 [5, 6]. The resulting exon 1 HTT protein fragment (containing the expanded polyglutamine tract) forms aggregates more readily than full-length protein and causes aggressive pathology; the R6/2 mouse, which expresses only this fragment, is the fastest-progressing HD model [30]. The uniform distribution of this pathogenic HTT1a species across cortex and striatum may be particularly relevant for understanding why striatal neurons (despite not having higher HTT1a levels) show selective vulnerability, supporting the hypothesis that intrinsic cellular factors rather than transcript abundance determine susceptibility [18].

Ideally, RNAscope imaging would be combined with immunofluorescence to assess protein localization and concentration in parallel with mRNA measurements. Such combined approaches would enable direct correlation between transcript accumulation and protein aggregation at the single-cell level, providing insight into whether mRNA clusters precede, coincide with, or follow protein inclusion formation. This would be particularly valuable for understanding the relationship between HTT1a mRNA clusters and the huntingtin protein inclusions that are hallmarks of HD pathology.

4.3.3. IMPLICATIONS FOR THERAPEUTIC DEVELOPMENT

The predominance of clustered mutant HTT mRNA raises important questions for ASO and siRNA therapeutics currently in clinical development for HD [31]. Recent studies have shown that huntingtin mRNA nuclear localization is cell-type specific, with approximately 50% of HTT mRNA localizing to the nucleus in neurons [32]. While ASOs can reduce both cytoplasmic and nuclear HTT mRNA (achieving ~90% and ~60% reduction respectively), siRNAs primarily eliminate cytoplasmic transcripts with minimal effect on nuclear mRNA [32]. Critically, nuclear mRNA clusters–which are specifically enriched in the aberrantly spliced HTT1a transcript [22]–are resistant to both siRNA and GapmeR ASO-based silencing [23], possibly explaining reduced efficacy in cases with ultralong CAG repeats where nuclear clusters are more prevalent. Our finding that the majority of mutant HTT signal exists in clusters and ~48-68% of these are nuclear therefore presents a therapeutic challenge, particularly for HTT1a which preferentially forms these resistant nuclear clusters. If nuclear clusters are resistant to current approaches, measuring cluster reduction (in addition to total mRNA knockdown) may be important for predicting clinical efficacy.

4.3.4. GENERALIZABILITY TO OTHER RNASCOPE APPLICATIONS

Several features of this pipeline should generalize beyond huntingtin mRNA to other RNAscope applications. The core principle, using isolated single molecules as an inter-

nal intensity standard for each slide, requires only that some fraction of target transcripts exist as resolvable single molecules, which is expected for most transcripts under most conditions. The key factors determining applicability include: (1) *Probe density*: our probes contain 20 ZZ pairs spanning ~1000 bp target regions, providing sufficient fluorescence for reliable single-molecule detection; transcripts with shorter target regions or fewer probe pairs may require sensitivity adjustments. (2) *Transcript structure*: the extended nature of RNAscope amplification trees (reflected in the ~57% larger PSF compared to point-like beads) may vary with target mRNA secondary structure; transcripts with extensive secondary structure might show different effective PSF dimensions. (3) *Clustering behavior*: our cluster quantification relies on the linear volume-intensity relationship, which requires uniform probe accessibility throughout clusters; transcripts forming dense phase-separated condensates with limited probe penetration might show saturation at large cluster sizes. (4) *Expression level*: transcripts expressed at very low levels may lack sufficient single molecules for reliable modal intensity estimation, while very high expression may cause extensive clustering that obscures single-molecule signals. For applications meeting these criteria, our calibration framework provides a validated approach to absolute mRNA quantification that extends RNAscope beyond simple dot counting.

4.3.5. LIMITATIONS AND FUTURE DIRECTIONS

Several limitations should be noted. Our wildtype sample size (n = 2) was insufficient for robust genotype comparisons. A major limitation is that we segmented DAPI signal per FOV and normalized by mean nuclear volume rather than performing individual nuclear segmentation. While we used DARPP-32 staining to identify the striatal region containing MSNs, this information was not incorporated into per-cell analysis; our approach cannot differentiate individual MSNs from other cell types (interneurons, glial cells) within the DARPP-32-positive region, which would require individual nuclear segmentation combined with cell-type-specific markers. Cell-type-specific analysis through individual nuclear segmentation combined with morphological or molecular markers would greatly enhance the biological interpretation of our findings. While we quantified nuclear vs cytoplasmic localization, we did not resolve sub-nuclear compartments. Sample preparation requires improvement: of 30 slides, 12 (~40%) were excluded due to poor tissue integrity, substantially reducing statistical power. Additionally, our slide selection did not systematically sample along the anterior-posterior axis, precluding rigorous analysis of spatial heterogeneity along this dimension. The substantial heterogeneity observed (both between animals and across tissue regions) suggests that sparse sampling may lead to unreliable estimates, motivating future studies to image large tissue areas per brain. Finally, our 3D Gaussian PSF model assumes a point-like emitter, but RNAscope probe binding regions span ~1000 bp of the target sequence, creating a spatially extended fluorescent source; replacing the point-source assumption with a model that accounts for this finite emitter size would enable deconvolution-based estimation of actual emitter dimensions and improve single-transcript classification. For example, a vectorial PSF model [33, 34, 35], which can also account for non-optimal optics, could be convolved with geometric primitives representing the probe binding region–a sphere for isotropic binding, or a rod-like structure aligned along the transcript to better approxi-

mate the ~1000 bp target sequence orientation. While individual FOV-level deviations can be large, we do not propagate this variability directly into mouse-level conclusions. When aggregating to the slide or mouse level (fig. 4.3), we observe consistent trends but lack statistical power with only 9 Q111 and 2 wildtype mice to detect significant differences. However, at the FOV level, significant differences emerge: Q111 FOVs show elevated mRNA accumulation compared to wildtype (fig. 4.4), and FOVs classified as extreme based on wildtype thresholds exhibit distinct cluster properties including elevated cluster numbers, higher packing density, and altered subcellular localization (fig. 4.5).
Future directions based on these limitations include: expanding sample sizes; implementing individual nuclear segmentation to enable cell-type-specific analysis; registering sections to a standardized mouse brain atlas; processing whole brains to capture full spatial heterogeneity; developing PSF models that incorporate finite emitter size; and applying the pipeline to evaluate therapeutic interventions using the cluster metrics identified here.

4.3.6. CONCLUSION

We present a high-throughput RNAscope imaging and analysis pipeline for quantifying mutant huntingtin mRNA in mouse brain at single-molecule resolution. The pipeline's key innovation is the establishment and validation of a linear relationship between cluster volume and mRNA content, enabling quantitative conversion of fluorescence intensity to absolute mRNA counts. Applied to HttQ111+/- mice, we observe considerable heterogeneity in mRNA accumulation: 16-62% of Q111 tissue regions show elevated clustering exceeding wildtype thresholds (HTT1a: 31% cortex, 62% striatum; fl-HTT: 16% cortex, 44% striatum). Extreme FOVs are characterized by elevated cluster numbers per nucleus (2-6× increase), higher cluster density (1.3-1.7×), and a shift toward cytoplasmic localization for fl-HTT (48% nuclear vs 68% in normal FOVs). While larger sample sizes will be needed to confirm these patterns, these quantitative metrics provide a framework for investigating disease mechanisms and evaluating therapeutic interventions. Importantly, having a validated analysis pipeline now justifies the investment in RNAscope probes and large-scale imaging: systematic studies across disease models, timepoints, and therapeutic interventions are now feasible. Combined with improvements in sample preparation to reduce tissue loss, this approach enables quantitative, high-throughput mRNA profiling for HD and other repeat expansion disorders characterized by RNA foci formation.

4.4. MATERIALS AND METHODS

4.4.1. SAMPLES AND TREATMENT

MOUSE MODELS

Brain tissue samples were obtained as described previously [13]. All mouse experiments were performed in alignment with the Institutional Animal Care and Use Committee at the University of Massachusetts Chan Medical School (protocol 202000010). Mice were bred and born at Jackson Labs (Farmington, CT) and transferred at 6 weeks of age to pathogen-free UMass Chan animal facilities, where they were housed with a 12h light:12h dark cycle at 23 ± 1°C and 50 ± 20% humidity with free access to food and water.

We used heterozygous HttQ111+/- mice (JAX Strain ID 370624, Mc_Q111 KI; C57BL/6J background) and wild-type C57BL/6J littermate controls. Tissue was collected after perfusion/fixation and processed identically across conditions to minimize batch effects. Mice in this study were derived from a separate therapeutic study investigating siRNA-mediated silencing of MSH3 and HTT [13]. That study administered treatments via intracerebroventricular (ICV) injection at 2 months of age. The mice used here were from control groups only: 2-month-old mice were untreated (UNT, prior to injection), while 6- and 12-month-old mice received either artificial cerebrospinal fluid (aCSF) or a non-targeting control siRNA (NTC). As these are standard control conditions not expected to alter HTT mRNA expression, we pooled all Q111 mice for analysis.

TISSUE PROCESSING

After transcardial perfusion and fixation, brains were sectioned coronally at 40 μm thickness using a vibratome. Sections were stored free-floating in PBS at 4°C prior to RNAscope staining.

Mouse ID Mapping. Anonymized mouse IDs used in fig. 4.3F and fig. 4.4F correspond to the following samples (Table 4.1):

ID	Sample	ID	Sample
Q_{111}#1	Q111 2mo #1 UNT	Q_{111}#6	Q111 6mo #3 NTC
Q_{111}#2	Q111 2mo #2 UNT	Q_{111}#7	Q111 12mo #1 aCSF
Q_{111}#3	Q111 2mo #3 UNT	Q_{111}#8	Q111 12mo #2 aCSF
Q_{111}#4	Q111 6mo #1 NTC	Q_{111}#9	Q111 12mo #3 aCSF
Q_{111}#5	Q111 6mo #2 NTC		
WT#1	WT 2mo #2 UNT	WT#2	WT 12mo #3 aCSF

Table 4.1: **Mouse ID mapping.** Anonymized IDs used in fig. 4.3F and fig. 4.4F correspond to individual mice. Q_{111}#1-Q_{111}#9 denote HttQ111+/- mice; WT#1-WT#2 denote wildtype controls. Treatment abbreviations: UNT = untreated, NTC = non-targeting control siRNA, aCSF = artificial cerebrospinal fluid (see text for details). Multiple slides per mouse are denoted with decimal notation (e.g., Q_{111}#1.1, Q_{111}#1.2).

STAINING PROTOCOL

RNAscope™ assays were performed according to the manufacturer's instructions (ACD Bio; detailed protocol in Supplementary Note 3, reagents in table S6). Typical probe sets comprised up to 20 ZZ pairs per target; one ZZ pair spans ~50 bases, yielding a tiled probe region of ~1000 bases and an estimated physical contour length of ~ 260 nm (assuming ~ 0.26 nm per base). Because this effective label extent approaches the lateral PSF, we acquired additional PSF calibration data with larger beads (see Section 4.4.3). For housekeeping control signals we used a ready-to-use mixture provided by the manufacturer containing three probes targeting POLR2A (channel C1), PPIB (channel C2), and UBC (channel C3).

SLIDE PREPARATION

After staining and amplification, samples were counterstained with DAPI and mounted in ProLong™ Glass Antifade Mountant (Thermo Fisher Scientific, P36982; refractive

index 1.52 after curing) with a No. 1.5 high-precision coverslip (Thorlabs, CG15KH1; 170 μm ± 5 μm thickness). Slides were cured flat at room temperature (30-60 min) and stored protected from light at 4°C until imaging.

4.4.2. OPTICAL SETUP & IMAGE ACQUISITION

Images were acquired sequentially on a TissueFAXS SL Q tissue cytometer (TissueGnostics, TG3-970 C), illuminated by a Lumencor Spectra III solid-state light engine with nominal excitation bands at 390/22 nm (mDAPI), 475/28 nm (sFITC), 555/28 nm (sCY3), and 637/12 nm (sCY5).
Two objectives were used:

- 2.5× (NA 0.085; Zeiss EC Plan-Neofluar M27) for whole-slide overview and ROI selection (2D).
- 40× oil (NA 1.3; Zeiss Plan-Apochromat Oil DIC (UV) VIS-IR) for 3D confocal imaging.

Following 2.5× overview scans, immersion oil (Immersol^{TM} 518F; refractive index 1.518 at 23°C) was applied before 40× confocal acquisitions. Emission was split using a SpectraSplit® 7 filter set (S-Split Blue, Green, Orange, Far-red), with central excitation/emission wavelengths (nm) of 374/425, 491/526, 543/570, and 648/688, respectively.
Fluorescence was detected on a Hamamatsu ORCA-Fusion BT sCMOS camera (C15440-20UP) with a physical pixel size of 6.5 μm. At 40× magnification, this yields an effective pixel size in the image plane of 6.5 μm/40 = 162.5 nm. Confocal sectioning used a Crest V2 spinning disk (15,000 rpm; pinhole diameter 60 μm, spacing 250 μm). All other optics (mirrors, lenses, collimation) were standard to the TissueFAXS SL Q system.
Acquisitions were controlled with TissueFAXS SL Viewer v7.1.131. Overview scans used exposure and power settings optimized for contrast. For confocal stacks, laser power and exposure were set such that the brightest signals remained below 40,000 ADUs; per-sample settings are listed in Supplementary Table S1. Laser powers were measured in situ (Thorlabs S170C; table S2). Illumination was restricted by a circular iris to a ∅485 μm area centered in the FOV. Each z-stack comprised 21 slices acquired at 500 nm axial spacing, providing a total imaging depth of 10 μm.
The Airy unit (AU) at Alexa 546 emission is 1 AU = 1.22 λ_{573}/NA ≈ 538 nm. With system magnification, the 60 μm pinhole corresponds to ~ 2.8 AU, maximizing signal collection at the cost of thicker optical sections. The confocal optical slice thickness is

$$\mathrm{OST} = \sqrt{\left(\frac{0.88\,\lambda_{\mathrm{em}}}{n - \sqrt{n^2 - \mathrm{NA}^2}}\right)^2 + \left(\frac{\sqrt{2}\,n\,PH}{\mathrm{NA}}\right)^2}, \tag{4.8}$$

with pinhole diameter PH and refractive index n [36]. For Alexa 546 in our system, OST ≈ 2.6 μm.

IMAGE PHOTON CALIBRATION

We recorded 1000 dark frames in complete darkness to estimate the camera offset: 101±6 ADU (mean ± SD across pixels). Photon calibration was performed by acquiring 1000

out-of-focus brightfield images of fixed cells at three illumination levels spanning the 16-bit range. The response was linear up to ~ 50,000 ADUs. The conversion gain (electrons/ADU) was obtained from a mean-variance fit [37], yielding 0.21 electrons/ADU (typical value ~ 0.24 for this sensor [38]). All analysis used images converted to photon (electron) counts.

4.4.3. IMAGING MODEL

We model the recorded intensity as the sum of an emitter signal convolved with the microscope PSF and a per-slice background term.

THREE-DIMENSIONAL GAUSSIAN PSF MODEL

We model the emitter as a separable integrated 3D Gaussian, which provides a reasonable approximation for spinning-disk confocal near focus [39]:

$$\mu_{ijk} = N\,E_x(X_i,\theta_x,\sigma_x)\,E_y(Y_j,\theta_y,\sigma_y)\,E_z(Z_k,\theta_z,\sigma_z) + bg_k, \tag{4.9}$$

where indices i, j denote pixel positions in the lateral plane and k denotes the slice index, with parameters $\boldsymbol{\theta} = [\theta_x,\theta_y,\theta_z,N,bg_{1..K},\sigma_x,\sigma_y,\sigma_z]^T$ and bg_k is the background level for slice k. The per-axis integrated Gaussians are

$$E_x = \tfrac{1}{2}\left[\operatorname{erf}\!\left(\frac{X_i-\theta_x+0.5}{\sqrt{2}\sigma_x}\right) - \operatorname{erf}\!\left(\frac{X_i-\theta_x-0.5}{\sqrt{2}\sigma_x}\right)\right], \tag{4.10}$$

$$E_y = \tfrac{1}{2}\left[\operatorname{erf}\!\left(\frac{Y_j-\theta_y+0.5}{\sqrt{2}\sigma_y}\right) - \operatorname{erf}\!\left(\frac{Y_j-\theta_y-0.5}{\sqrt{2}\sigma_y}\right)\right], \tag{4.11}$$

$$E_z = \tfrac{1}{2}\left[\operatorname{erf}\!\left(\frac{Z_k-\theta_z+0.5}{\sqrt{2}\sigma_z}\right) - \operatorname{erf}\!\left(\frac{Z_k-\theta_z-0.5}{\sqrt{2}\sigma_z}\right)\right], \tag{4.12}$$

analogous to the 2D integrated model [40].

Closed-form first derivatives are used for gradient and Hessian computations. For example,

$$\frac{\partial\mu}{\partial\theta_x} = N\frac{\partial E_x}{\partial\theta_x}E_yE_z, \quad \frac{\partial E_x}{\partial\theta_x} = \frac{1}{\sqrt{2\pi}\sigma_x}\left[e^{-\frac{(X_i-\theta_x-0.5)^2}{2\sigma_x^2}} - e^{-\frac{(X_i-\theta_x+0.5)^2}{2\sigma_x^2}}\right], \tag{4.13}$$

$$\frac{\partial\mu}{\partial N} = E_xE_yE_z, \qquad \frac{\partial\mu}{\partial bg_k} = 1, \tag{4.14}$$

with analogous expressions for θ_y,θ_z and $\sigma_{x,y,z}$.

OPTIMIZATION PROCEDURE (MLE USING LEVENBERG-MARQUARDT)

Parameters are estimated by Poisson MLE. Given observed intensities I_{ijk} and predictions μ_{ijk},

$$\log L(\boldsymbol{\theta}) = \sum_{i,j,k}\left[I_{ijk}\log(\mu_{ijk}) - \mu_{ijk}\right], \tag{4.15}$$

(up to an additive constant). The gradient is

$$\frac{\partial \log L}{\partial\theta_m} = \sum_{i,j,k}\frac{I_{ijk}-\mu_{ijk}}{\mu_{ijk}}\frac{\partial\mu_{ijk}}{\partial\theta_m}. \tag{4.16}$$

We use the Gauss-Newton approximation to the Hessian [41]:

$$H_{mn} \approx -\sum_{i,j,k} \frac{I_{ijk}}{\mu_{ijk}^2} \frac{\partial \mu_{ijk}}{\partial \theta_m} \frac{\partial \mu_{ijk}}{\partial \theta_n}. \tag{4.17}$$

Levenberg-Marquardt updates are

$$\boldsymbol{\theta}^{(n+1)} = \boldsymbol{\theta}^{(n)} - (\mathbf{H} + \lambda \operatorname{diag}(\mathbf{H}) + \epsilon \mathbf{I})^{-1} \nabla \log L(\boldsymbol{\theta}^{(n)}), \tag{4.18}$$

with $\lambda = 10^{-2}$ and $\epsilon = 10^{-6}$. In practice, we compute the pseudo-inverse via `torch.linalg.pinv` [42] to ensure robustness during batch processing: if any matrix in the batch is singular, the pseudo-inverse returns a valid result rather than causing the entire batch to fail. After each step we clip parameters to physically plausible bounds: $\theta_{x,y} \in [2, 10]$ pixels; $\theta_z \in [0, 30]$ slices; $N \in [1, 10^9]$ photons; $bg_k \in [1, 10^6]$ photons; $\sigma_{x,y} \in [0.2, 4]$ pixels; and $\sigma_z \in [0.2, 10]$ slices. Convergence is declared if all absolute parameter changes fall below 0.01 nm or 0.01 photons, or after 60 iterations. Fits violating bounds or failing to converge within 60 iterations are discarded.

4

PSF CALIBRATION ON BEADS

We calibrated $(\sigma_x, \sigma_y, \sigma_z)$ on TetraSpeck™ Fluorescent Microspheres Size Kit (Invitrogen™; $\varnothing 0.2\,\mu$m) with emission labels at 365/430 (blue), 505/515 (green), 560/580 (orange), and 660/680 nm (dark red). Beads are pre-mounted at the coverslip in ProLong™ Glass (refractive index 1.52; per manufacturer support for slides produced 2021-2025), matching the mounting conditions used for tissue samples. Across 20 fields of view per channel, we extracted > 6,000 bead volumes per channel (range 6,330-142,365) and fit 3D Gaussians following the procedure described in Section 4.4.3. The resulting σ_x, σ_y, and σ_z distributions were then fit with Gaussian functions (SciPy `curve_fit` [16]) to obtain mean PSF widths and standard errors. These values are summarized in Supplementary Table S3; the calibrated widths are used as priors and quality bounds in tissue fits.

4.4.4. DETECTION OF SINGLE SPOTS

We detect and validate single-molecule signals via a permissive candidate step followed by statistical and biological filtering.

INITIAL DETECTION

Candidates are detected on a maximum-intensity projection (MIP) of the z-stack using a difference-of-uniform-filters pipeline [43]: (i) apply uniform filters of width 6 and 12 pixels to the MIP and difference them; (ii) find local maxima exceeding 5 photons; (iii) enforce a 10-pixel minimum separation. The MIP provides robust 2D localization of candidates regardless of their axial position. For each detected candidate, we then extract a 12×12 pixel lateral ROI and a 10-slice axial sub-volume centered on the lateral center-of-mass for subsequent 3D Gaussian PSF fitting (Section 4.4.3).

DETECTOR FALSE POSITIVE PROBABILITY

After fitting, we compute a GLRT statistic between background-only (H_0) and signal-plus-background (H_1) [44]:

$$T_G = 2\left[\log L(\hat{\boldsymbol{\theta}}_{\text{signal+bg}}) - \log L(\hat{\boldsymbol{\theta}}_{\text{bg-only}})\right], \tag{4.19}$$

evaluated on each of 5 central slices using a 2D Gaussian PSF, as the 3D Gaussian model becomes less accurate further from focus [39]. P-values under H_0 are

$$p_{\mathrm{FA}} = 2\,\Phi\left(-\sqrt{T_G}\right), \tag{4.20}$$

with Benjamini-Yekutieli FDR control [45]. Candidates with any slice $p_{\mathrm{FA}} > 0.05$ are rejected.

BIOLOGICAL FALSE POSITIVE PROBABILITY

Negative-control slides (bacterial probes) were imaged each session to profile non-specific binding and free-dye fluorescence. For each channel we computed the 95th percentile of negative-control photon counts,

$$\mathrm{threshold}_{\mathrm{CDF}} = Q_{0.95}\left(\mathrm{photons}_{\mathrm{neg}}\right),$$

and accepted only candidates exceeding this threshold (per channel), complementing the detector-level filter and avoiding arbitrary cutoffs.

4.4.5. PSF CALIBRATION USING RNASCOPE DATA

RATIONALE

Bead-derived PSFs may under-estimate the effective width of RNAscope signals. Unlike point-source fluorescent beads, RNAscope amplification trees consist of branched DNA structures with fluorophores distributed across the amplification tree, spanning approximately 20 ZZ probe pairs (~50 base pairs each) that bind along the target mRNA. This spatial distribution of fluorophores effectively broadens the apparent PSF beyond the optical diffraction limit. We therefore refined the PSF constraints using tissue data directly.

TWO-PASS CALIBRATION PROCEDURE

We employed a two-pass approach to determine both the experimental PSF and the channel-specific breakpoints that distinguish diffraction-limited single-molecule signals from larger clusters (see fig. 4.1 for an overview):

Pass 1: Breakpoint determination with bead priors.

1. **Initial detection and fitting.** Using bead-derived PSF widths as initial values, we performed MLE fitting on all detected candidates with σ bounds set to $[0.2, 4]$ pixels laterally and $[0.2, 10]$ slices axially, allowing the fitted σ to vary freely within these bounds.

2. **Signal-width analysis.** We binned fitted spots by their recovered σ_x values and computed the mean integrated photon signal N within each bin. For true single molecules with consistent fluorophore stoichiometry, N should remain approximately constant regardless of fitted σ (with variation due to noise). Instead, we observed approximately linear increases in N with increasing σ up to a channel-specific inflection point, beyond which the relationship breaks down.

3. **Breakpoint identification.** The breakpoint σ_{bp} was defined as the σ value where the signal-width curve transitions from linear growth to plateau or deterioration. Below the breakpoint, larger fitted σ values reflect noise or minor optical aberrations in true single molecules; above the breakpoint, large σ values indicate spatially extended signals (clusters) where the Gaussian model is inappropriate. We identified the breakpoint using segmented linear regression (piecewise linear fits with one knot).

4. **Experimental PSF estimation.** To determine the effective RNAscope PSF width for each channel, we fitted a parabola to the five histogram bins surrounding the breakpoint and extracted the vertex. This represents the most probable σ for single-molecule signals in tissue, accounting for RNAscope amplification tree geometry.

Pass 2: Final detection with experimental PSF.

1. **Re-detection with calibrated priors.** We repeated the full detection pipeline (Section 4.4.4) using the experimentally determined PSF widths as initial values for MLE fitting, while still allowing σ to vary within bounds.

2. **Size-based rejection.** Fits were rejected from the single-molecule pipeline if any σ component fell outside the acceptable range: a minimum threshold of 80% of the bead-derived PSF width (to reject spuriously small fits likely caused by noise or fitting artifacts), and a maximum threshold at the channel-specific breakpoint (to reject spatially extended signals). Formally, fits were accepted only if $0.8\sigma_{bead} \leq \sigma \leq \sigma_{bp}$ for each axis. Signals exceeding the upper breakpoint are captured by the CNN-based cluster detection (Section 4.4.6).

SIGNAL PRESERVATION THROUGH OVERLAPPING PIPELINES

Importantly, the cluster detection pipeline is intentionally designed to overlap with single-molecule detection at the boundary. Clusters that spatially overlap with validated single spots are pruned from the cluster masks (16.7% of green clusters, 26.6% of orange clusters; see fig. 4.2), ensuring no double-counting while preserving all detected signal. This overlap guarantees that signals near the single-molecule/cluster boundary are captured by at least one pipeline, preventing signal loss at the transition.
Recalibrated breakpoint values are listed in Supplementary Table S4.

4.4.6. MRNA CLUSTER DETECTION

TRAINING DATA

We annotated clusters with LABKIT [46] in volumes of $512 \times 512 \times 21$ voxels for Alexa 488 and Alexa 546. Signals visually larger than diffraction-limited spots were labeled as clusters; ambiguous cases were included to ensure comprehensive detection (with later pruning to protect single-spot counts).

INFERENCE AND CLUSTER DEFINITION

A 3D CNN [47] produced voxelwise cluster probability maps (architecture in Supplementary Section 1). Binary masks were obtained at a predicted probability above 0.5. To

avoid double counting, cluster masks overlapping validated single spots were removed. Diffraction-limited signals (single or merged sub-diffraction emitters) remained in the single-spot pipeline (Sections 4.4.3-4.4.3).

SIGNAL ESTIMATION

For each cluster, we computed background-corrected photon counts on the photon-converted images:

$$I_{\text{corrected}} = \left(\sum_{\text{mask}} I_{\text{voxel}} \right) - \left(N_{\text{mask}} \times I_{\text{median background}} \right), \tag{4.21}$$

where $I_{\text{corrected}}$ is the background-corrected photon count for the cluster, I_{voxel} is the photon count at each voxel within the cluster mask, N_{mask} is the number of voxels in the cluster mask, and $I_{\text{median background}}$ is the median photon count in a local background shell formed by dilating the mask by 10 voxels in all dimensions and subtracting the original mask. Cluster centers-of-mass were retained for spatial analyses.

4.4.7. FLUORESCENT SIGNAL WITH RNASCOPE

The RNAscope™ technique employs probes designed to target mRNA transcripts, with up to 20 individual probe pairs per mRNA molecule. Following probe hybridization, two sequential amplification steps can generate up to 8000 fluorescent labels per transcript [2]. Each probe pair requires two adjacent binding events on the target mRNA, significantly increasing specificity. However, variability introduced during the amplification process can result in significant fluctuations in fluorescence intensity per transcript. Consequently, careful consideration of how estimated signal intensities are interpreted and categorized is essential for accurate quantification.

Two custom probes were used to detect mutant huntingtin transcripts: (1) the HTT1a probe (Mm-Htt-intron1-O2, Cat. No. 575581) targeting intron 1, which detects the aberrantly spliced transcript; and (2) the fl-HTT probe (Mm-Htt-No-XHs, Cat. No. 473001) targeting the 3' UTR (bp 9833-10798), which detects the canonical full-length transcript. Each probe consists of 20 ZZ pairs, with each ZZ pair covering approximately 40-50 nt, spanning roughly 1,000 nt of the target region. Full target sequences are provided in Supplementary Note 4 and table S5.

4.4.8. DAPI-BASED NUCLEAR SEGMENTATION

DAPI-stained nuclei were segmented in 3D using a residual 3D U-Net architecture [47], trained on manually annotated brain tissue volumes. Labeled regions were filtered by size (minimum 5,000 voxels, maximum 500,000 voxels) to remove noise and artifacts.

4.4.9. DISTANCE TO NUCLEAR BORDER

We computed the signed Euclidean distance from each cluster center-of-mass to the nearest nuclear boundary using anisotropic distance transform. Negative values indicate nuclear localization; positive values indicate cytoplasmic localization.

4.4.10. ATLAS REGISTRATION AND COORDINATE ASSIGNMENT

Anterior-posterior coordinates were assigned to each tissue section as a whole (not independently for striatum and cortex) by manual visual comparison with the Allen Mouse Brain Atlas [17]. For each slide, a trained observer compared the 2.5× overview image to coronal reference images from the Allen Reference Atlas (available at `https://mouse.brain-map.org`), identifying the best-matching atlas plane based on anatomical landmarks including corpus callosum shape, striatal boundaries, and cortical layering.

Within each section, FOV positions were assigned to striatal or cortical regions based on DARPP-32 signal (for striatum) or anatomical landmarks (for cortex). Striatal regions were definitively identified by positive DARPP-32 staining marking medium spiny neurons. Cortical region boundaries were more arbitrary, lacking cell-type-specific markers; cortical FOVs were positioned to sample all cortical layers in approximately equal proportions.

Coordinates are reported following the Allen atlas convention, where reference sections are spaced at 100 μm intervals. However, this visual matching procedure introduces substantial uncertainty: precise registration to the atlas coordinate system is not possible without computational image registration or fiducial markers. We estimate the uncertainty in anterior-posterior assignment to be on the order of ±200-400 μm (2-4 atlas sections), depending on how distinctively the anatomical landmarks differ between adjacent reference planes. Coordinates should therefore be interpreted as approximate rostrocaudal positions rather than precise atlas locations.

The anatomical schematic showing cortical and striatal subregion labels (Fig. 4.3A) was adapted from the Allen Reference Atlas coronal sections.

4.4.11. STATISTICAL ANALYSIS

All statistical analyses were carried out in Python with `scipy.stats`; post-hoc comparisons used `statsmodels`. The test applied to each comparison reported in this chapter is listed in table 4.2; the conventions that follow apply throughout.

Choice of test. Distributions of per-FOV and per-cluster quantities are strongly non-normal and heavy-tailed, so these are compared with the non-parametric Mann–Whitney U test in the main figures; the supplementary age-stratified panels additionally report unpaired t-tests and a one-way ANOVA with a Kruskal–Wallis check for comparability with common practice. FOVs and clusters from the same slide are not independent, so all FOV- and cluster-level p-values are descriptive. Comparisons of cortex and striatum across all slides are paired t-tests on slide means, because both regions are measured within the same physical section (fig. S17); within an age and genotype (fig. 4.3D), where only 1–6 slides are available, per-slide means are compared with the Mann–Whitney U test. All t-tests are Student's t-tests (equal variances assumed) except the RNAscope–RNA-seq comparison, where the variances differ by an order of magnitude and Welch's t-test is used.

Correlations. Coefficients denoted r are Pearson product-moment correlation coefficients, reported with the associated p-value; Spearman rank coefficients are used only where explicitly named. Partial correlations were computed by ordinary least-squares residualisation: each of the two variables of interest was regressed on the control vari-

able, and the Pearson correlation of the residuals is reported.

Linear fits. The slope β for the intensity–volume scaling relationship was obtained by unweighted ordinary least-squares regression over all individual clusters within the stated volume range; binning does not enter the fit. Two goodness-of-fit measures are reported: the Pearson correlation r (and $R^2 = r^2$) between volume and normalized intensity across individual clusters, and the coefficient of determination of the same line evaluated on the bin-averaged intensities (bins containing at least three slides), which is the value displayed in fig. 4.2. Plotted points show the mean intensity per volume bin with ±1 SD across slides. The per-slide calibration fits relating spot size to intensity are weighted least squares, with weights derived from the counts per bin.

Reported quantities and significance. All tests are two-sided. Summary values are given as mean ± standard deviation unless a median and interquartile range are named. The unit of n is stated with each test and is one of slides, animals, fields of view or clusters. A threshold of $p < 0.05$ is used throughout; where significance markers appear, they denote $^{*}\,p < 0.05$, $^{**}\,p < 0.01$ and $^{***}\,p < 0.001$, and "ns" denotes $p \geq 0.05$.

Multiple comparisons. Three corrections are applied where stated. Benjamini–Yekutieli false-discovery-rate control is used during spot detection, at the level of individual candidate emitters (section 4.4.4). Post-hoc pairwise comparisons between age groups at FOV level are Bonferroni corrected, and are computed only when the preceding one-way ANOVA is significant. Slide-level age comparisons (fig. 4.3D) are Mann–Whitney U tests between consecutive ages (2 vs 6 and 6 vs 12 months) and are not corrected, as none is significant. Comparisons between anatomical subregions use Tukey HSD, which controls the family-wise error rate across the subregion pairs. The remaining group comparisons reported in the Results are *not* corrected for multiple testing across regions, genotypes and transcripts. The differences on which our conclusions rest have p-values many orders of magnitude below the 0.05 threshold and are therefore unaffected by any standard correction; results with p close to 0.05 should be read as descriptive rather than confirmatory.

4.4.12. DATA AND CODE AVAILABILITY

Analysis scripts were executed per slide in parallel on a high-performance computing (HPC) cluster. The analysis code will be made publicly available after publication at `https://github.com/pvanvelde/rna_scope`. The complete imaging dataset totals multiple terabytes; a representative subset of processed data will be made available alongside the code. The complete dataset is available upon reasonable request.

4.4.13. USE OF AI

Generative AI tools were used during the preparation of this chapter for writing assistance and grammar checking, and to help locate errors in the analysis code. No data and no images were generated by AI: all measurements, image processing and figures derive from the experiments and analysis described above. All AI-assisted text and code was reviewed and verified.

4.5. SUPPLEMENTARY MATERIAL

SUPPLEMENTARY TABLES

Table S1: **Imaging parameters by session.** Laser intensity (Int., %) and exposure time (Exp., ms) settings for each fluorescence channel across imaging sessions. FITC (488 nm) was used for HTT1a detection; Cy3 (548 nm) was used for fl-HTT detection. The scanner is operated by imaging core staff, with settings chosen by the operator based on sample appearance. Parameter variations between sessions may partially contribute to the 2-3× variation in raw photon counts across slides, motivating per-slide intensity normalization.

	DAPI		FITC (HTT1a)		Cy3 (fl-HTT)		Cy5	
Session	Int.	Exp.	Int.	Exp.	Int.	Exp.	Int.	Exp.
1	50	150	50	500	50	50	50	100
2	50	150	70	500	50	150	50	500
3	50	100	80	500	50	100	50	100

Table 4.2: Statistical test used for each analysis reported in this chapter. Where a comparison is made at more than one level of aggregation, the level is stated, because it determines whether the samples are paired.

Comparison or quantity	**Test**
Calibration and controls	
Negative-control threshold, cortex vs striatum, within a slide	Paired t-test per channel (n = 29 slides); pooled slide–channel pairs shown descriptively
Threshold vs age, atlas coordinate or number of spots	Pearson correlation, with a least-squares trend line per channel
Per-slide threshold vs single-spot peak intensity	Pearson correlation
Positive controls (POLR2A, UBC), cortex vs striatum	Paired t-test (n = slides)
Positive control vs experimental probe	Pearson; partial correlation controlling for UBC
Quantification	
Cluster intensity vs cluster volume	Unweighted OLS over all individual clusters; Pearson r (R^2) on individual clusters and R^2 on bin means
Per-slide spot-size calibration fits	Weighted least squares
Expression	
Q111 vs wildtype, at FOV level	Mann–Whitney U; unpaired Student's t-test per age in the supplement (n = FOVs, descriptive)
Cortex vs striatum, all slides	Paired t-test (n = 14 slides). Within age × genotype: Mann–Whitney U on per-slide means
Across ages, at slide level	Mann–Whitney U on per-slide means, between consecutive ages only (2 vs 6 and 6 vs 12 months)
Across ages, at FOV level	One-way ANOVA with Kruskal–Wallis check; post-hoc Student's t-tests, Bonferroni corrected
Across anatomical subregions	One-way ANOVA; Tukey HSD, $\alpha = 0.05$
Extreme vs normal fields of view	
Clusters per nucleus, mean cluster mRNA, distance to the nuclear border, fraction nuclear	Mann–Whitney U (n = FOVs or clusters, as stated; descriptive, since extreme status is defined from the same clustered-mRNA quantity)
Method comparison	
RNAscope vs bulk RNA-seq, UBC/POLR2A ratio	Welch's t-test and Mann–Whitney U (both reported); Pearson vs age within each method

Table S2: **Laser power calibration.** Measured laser power (mW) at the sample plane as a function of software-controlled laser intensity (%) for each fluorescence channel. Measurements performed on TissueFAXS SL Q tissue cytometer (TissueGnostics, TG3-970 C) with Plan-Apochromat 40×/1.3 Oil DIC objective. Power measured using Thorlabs S170C photodiode sensor (S/N: 7010096) with Zeiss Immersol 518 F immersion oil. Illumination area restricted by circular iris to 485 μm diameter, centered at FOV center. All imaging data were acquired with the spinning disk active. FITC power was recorded with spinning disk on, showing ~5% transmission relative to direct illumination. Other channels exhibited similar reduction with spinning disk but were measured without it. Power measurements were performed once during the imaging period (~3 months); long-term stability and measurement uncertainty were not characterized.

Laser power (%)	DAPI (mW)	FITC* (mW)	Cy3 (mW)	Cy5 (mW)
10	0.7	0.3	0.4	0.5
20	1.3	0.5	0.7	1.2
30	1.9	0.7	1.1	1.9
40	2.4	0.9	1.4	2.6
50	3.0	1.1	1.7	3.3
60	3.6	1.3	2.1	4.1
70	4.1	1.5	2.5	4.7
80	4.7	1.7	2.8	5.4
90	5.3	2.0	3.2	6.1
100	5.9	2.2	3.5	6.8

*Spinning disk on; reduces power to ~5% of direct illumination.

Table S3: **Bead-based PSF calibration.** Mean ± SE of $\sigma_{x,y,z}$ per channel from 0.2 μm TetraSpeck microspheres.

Channel	σ_x (nm)	σ_y (nm)	σ_z (nm)
green	185 ± 2	187 ± 2	573 ± 8
orange	187 ± 1	191 ± 1	592 ± 9

Table S4: **Empirically-determined breakpoints.** Size thresholds separating single-molecule regime from cluster regime (see figs. S2 and S3).

Channel	$\sigma_{x,\text{break}}$ (nm)	$\sigma_{y,\text{break}}$ (nm)	$\sigma_{z,\text{break}}$ (nm)
green	290.8	291.1	698.7
orange	285.1	285.3	700.7

Table S5: **RNAscope probe target specifications.** Target region information for custom RNAscope probes used in this study. The HTT1a probe targets the 5' region of intron 1 of mouse *Htt*, which is retained in the aberrantly spliced Htt1a transcript. This region contains the cryptic polyadenylation sites used in incomplete splicing of mutant huntingtin mRNA. The fl-HTT probe targets the 3' UTR to detect the canonical full-length transcript. Full target sequences for both probes are provided in Supplementary Note 4 to document the exact genomic coordinates used for probe design, as reference genome annotations may change over time.

Probe	Target Region	ZZ Pairs	Notes
Mm-Htt-intron1-O2 (HTT1a)	Mouse *Htt* intron 1 (bp 41-1190, 1,150 bp)	20	Detects aberrantly spliced Htt1a; target sequence in Supplementary Note 4
Mm-Htt-No-XHs (fl-HTT)	Mouse *Htt* 3' UTR (bp 9833-10798, 966 bp)	20	Detects canonical full-length transcript; target sequence in Supplementary Note 4

SUPPLEMENTARY FIGURES

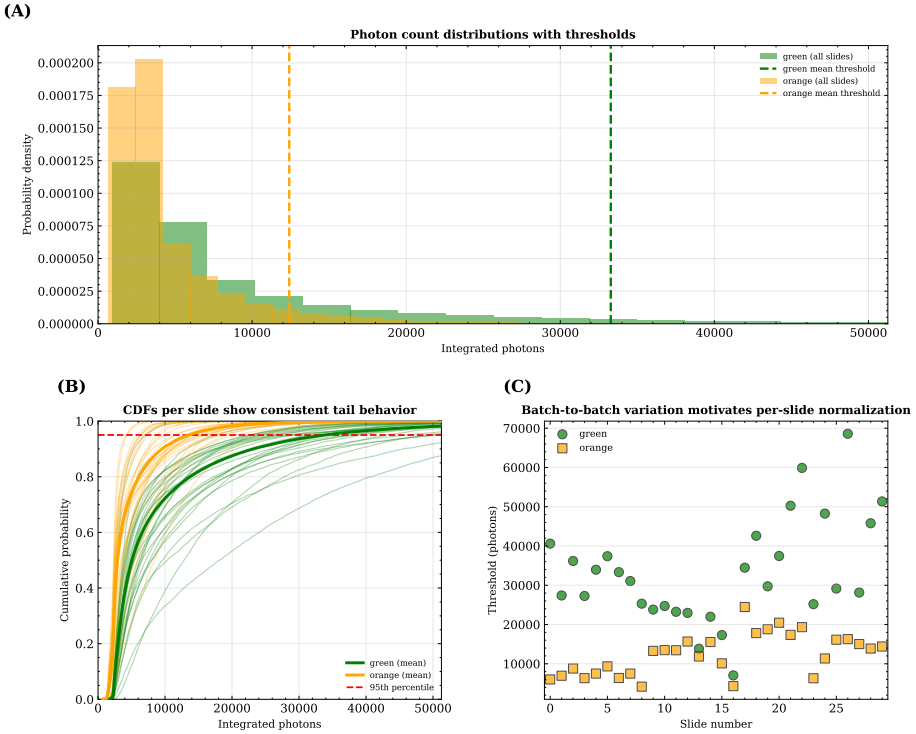


Figure S1: **Negative controls establish per-slide detection thresholds.** Analysis of 727,329 negative control spots (bacterial *DapB* probe, absent in mammalian tissue) across 30 slides (mean ± SD: 24,244 ± 7,748 spots/slide; 13,546 ± 7,748 green, 10,698 ± 6,113 orange). **(A)** Distributions of integrated photon counts from all negative-control detections (combined across slides). Mean ± SD of 95th percentile thresholds: 33,295 ± 13,301 photons (green); 12,377 ± 5,337 photons (orange). **(B)** Cumulative distribution functions (CDFs) per slide (thin lines) and mean CDF across all slides (bold) demonstrate consistent tail behavior despite variation in median background. Horizontal line at 0.95 marks the quantile used for thresholding. **(C)** Threshold values versus slide number (circles: green channel, squares: orange channel) reveal substantial slide-to-slide variation: CV_{green} = 39.9% (33,295 ± 13,301 photons); CV_{orange} = 43.1% (12,377 ± 5,337 photons). This motivates per-slide normalization to account for batch-to-batch variation in autofluorescence and staining efficiency. All values reported as mean ± SD across slides.

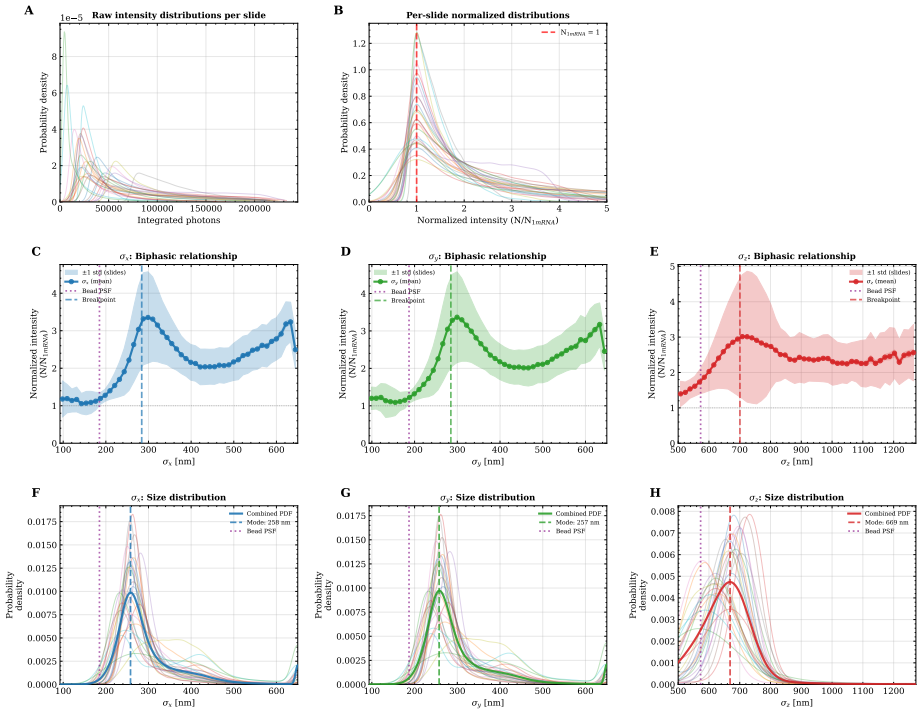


Figure S2: **Breakpoint analysis for green channel (HTT1a).** Analysis of 1,822,764 spots across 26 slides from Q111 mice (PFA < 1e-04). Median spots per slide: 70,106. **(A)** Raw intensity distributions per slide before normalization, showing 2-3× slide-to-slide variation in photon yield due to technical factors (tissue autofluorescence, fixation quality, probe hybridization efficiency, imaging conditions). **(B)** Per-slide normalized intensity distributions converging around $N_{1\text{mRNA}} = 1$ after modal normalization via kernel density estimation [15, 16]. Successful removal of technical variation while preserving biological signal (cluster tail). **(C-E)** Size-intensity relationships for σ_x, σ_y, σ_z. Bold line: mean from all pooled spots; light shaded region: ±1 SD across per-slide means; narrower dark bands: ±1 SEM. Purple dotted line: bead PSF (σ_x = 185 nm, σ_y = 187 nm, σ_z = 573 nm). Colored dashed line: empirically-determined breakpoint (σ_x = 284.1 nm, 53.6% larger than bead PSF; σ_y = 284.9 nm, 52.4% larger; σ_z = 700.8 nm, 22.3% larger). Piecewise linear regression: σ_x slope1 = 0.027 (single-molecule regime), slope2 = −0.005 (cluster regime). **(F-H)** Spot size distributions. Faint lines: per-slide KDE; thick line: combined PDF. Mode values from combined distributions (colored dashed): σ_x = 257.9 nm (39.4% larger than bead PSF), σ_y = 257.4 nm (37.7%), σ_z = 668.6 nm (16.7%). Size statistics: σ_x mean = 299.6 nm, median = 273.1 nm, SD = 90.9 nm. Modes define tissue-calibrated refined PSF values that supersede bead measurements for downstream analysis.

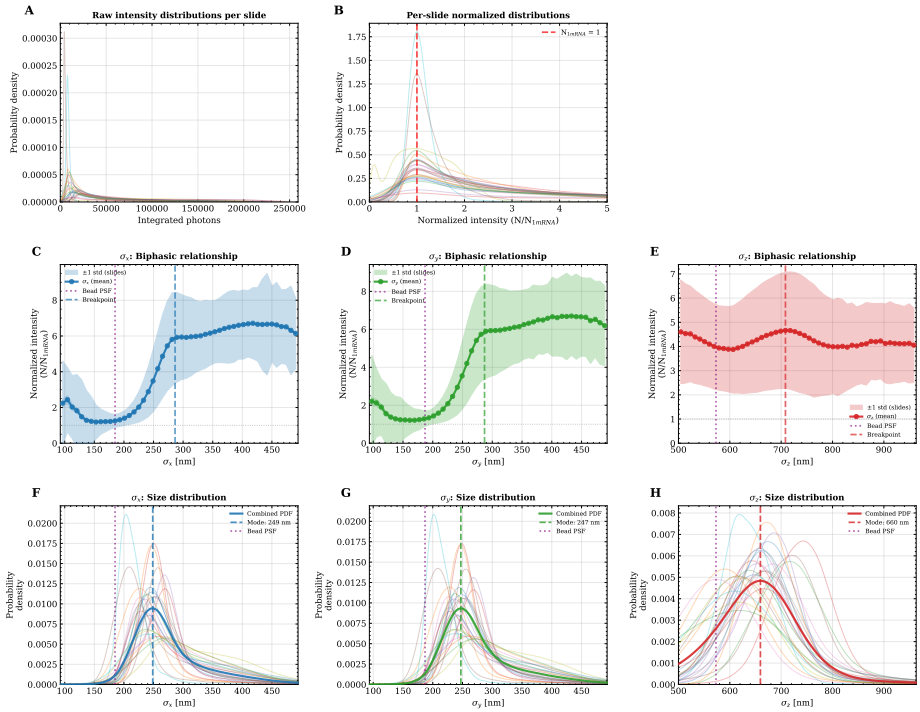


Figure S3: **Breakpoint analysis for orange channel (fl-HTT).** Analysis of 4,460,914 spots across 26 slides from Q111 mice (PFA < 1e-04). Median spots per slide: 171,573. **(A)** Raw intensity distributions per slide showing 2-3× slide-to-slide variation due to technical factors. **(B)** Normalized intensity distributions converging around $N_{1\text{mRNA}} = 1$ after per-slide modal normalization via KDE. **(C-E)** Size-intensity relationships. Breakpoints: σ_x = 286.1 nm (54.7% larger than bead PSF), σ_y = 286.8 nm (53.4% larger), σ_z = 708.4 nm (23.6% larger). Piecewise linear regression: σ_x slope1 = 0.060 (single-molecule regime), slope2 = 0.005 (cluster regime). **(F-H)** Spot size distributions. Mode values: σ_x = 248.6 nm (34.4% larger than bead PSF), σ_y = 247.2 nm (32.2%), σ_z = 659.6 nm (15.1%). Size statistics: σ_x mean = 281.2 nm, median = 262.1 nm, SD = 76.1 nm. Consistent breakpoint values between channels (~285 nm lateral, ~705 nm axial) validate the quantitative framework and reflect the physical extent of RNAscope probe clusters (~20 probe pairs) bound to target mRNA.

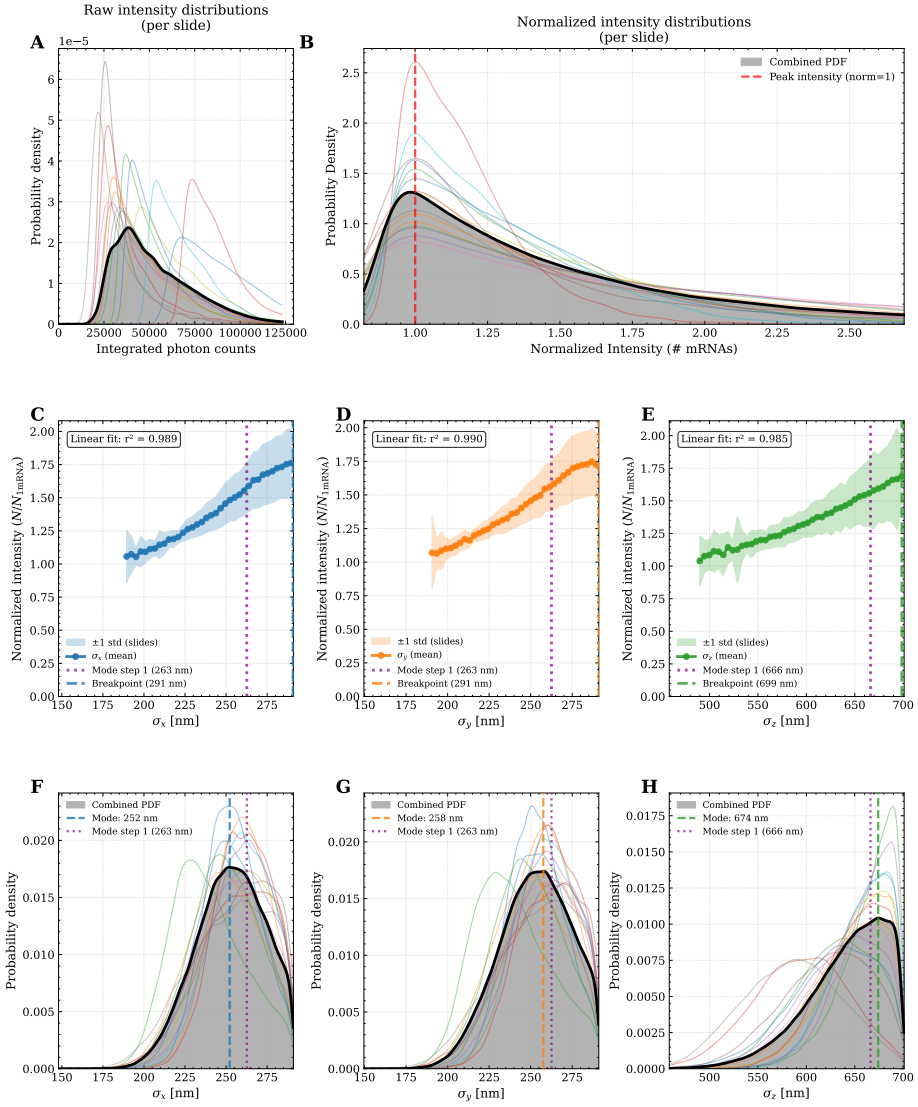

A
Raw intensity distributions
(per slide)
1e−5
Probability density
Integrated photon counts
B
Normalized intensity distributions
(per slide)
Combined PDF
Peak intensity (norm=1)
Probability Density
Normalized Intensity (# mRNAs)
C
Linear fit: r² = 0.989
Normalized intensity (N/N_mRNA)
±1 std (slides)
σx (mean)
Mode step 1 (263 nm)
Breakpoint (291 nm)
σx [nm]
D
Linear fit: r² = 0.990
Normalized intensity (N/N_mRNA)
±1 std (slides)
σy (mean)
Mode step 1 (263 nm)
Breakpoint (291 nm)
σy [nm]
E
Linear fit: r² = 0.985
Normalized intensity (N/N_mRNA)
±1 std (slides)
σz (mean)
Mode step 1 (666 nm)
Breakpoint (699 nm)
σz [nm]
F
Combined PDF
Mode: 252 nm
Mode step 1 (263 nm)
Probability density
σx [nm]
G
Combined PDF
Mode: 258 nm
Mode step 1 (263 nm)
Probability density
σy [nm]
H
Combined PDF
Mode: 674 nm
Mode step 1 (666 nm)
Probability density
σz [nm]

Figure S4: **Validation of single-molecule filtering (green channel, HTT1a).** All panels show data from the green channel (488 nm) corresponding to the HTT1a probe in Q111 transgenic mouse tissue. Analysis of orange channel (548 nm, fl-HTT) data yields similar results (fig. S5). **(A-B)** Per-slide intensity normalization demonstrates successful removal of technical variation. **(A)** Raw integrated photon counts for 15 slides (faint colored lines, 178,070 total spots) showing 2-3× variation; thick black line = combined PDF. **(B)** After per-slide normalization, all distributions converge around $N_{1\text{mRNA}} = 1$ (red dashed line) via kernel density estimation [15, 16]. **(C-E)** Biphasic relationships between normalized intensity and spot size after filtering validate the single-molecule regime. For each dimension, the bold line shows mean normalized intensity across 15 slides binned into 50 size bins (only bins with ≥100 spots shown). Purple dotted lines: tissue-calibrated modal spot sizes (σ_x = 263 nm, σ_y = 263 nm, σ_z = 666 nm; the bead-derived PSF is 185, 187 and 573 nm, table S3). Colored dashed lines: empirically-determined breakpoints (σ_x = 290.8 nm, σ_y = 291.1 nm, σ_z = 698.7 nm; 11%, 11%, 5% larger than the tissue modes and 57%, 56%, 22% larger than the bead PSF). Strong linear relationships between bin-averaged intensity and size below the breakpoint (Pearson $r^2 > 0.90$ across size bins) confirm the single-molecule regime. **(F-H)** Size distributions after filtering show tight clustering around modal values with clear truncation at breakpoints. Colored dashed lines mark modes defining tissue-calibrated refined PSF. **Quality filters:** (i) PFA < 5e-02, (ii) σ_i < breakpoint for all dimensions, (iii) intensity > slide-specific negative-control threshold, (iv) cluster CV ≥ 0.5. **Slides used (n=15):** m1a4, m1a5, m1b1, m2a2, m2a3, m2a4, m2a8, m2b1, m2b7, m3a1, m3a2, m3a3, m3a5, m3b2, m3b3. **Slides excluded:** poor tissue integrity or low positive control expression.

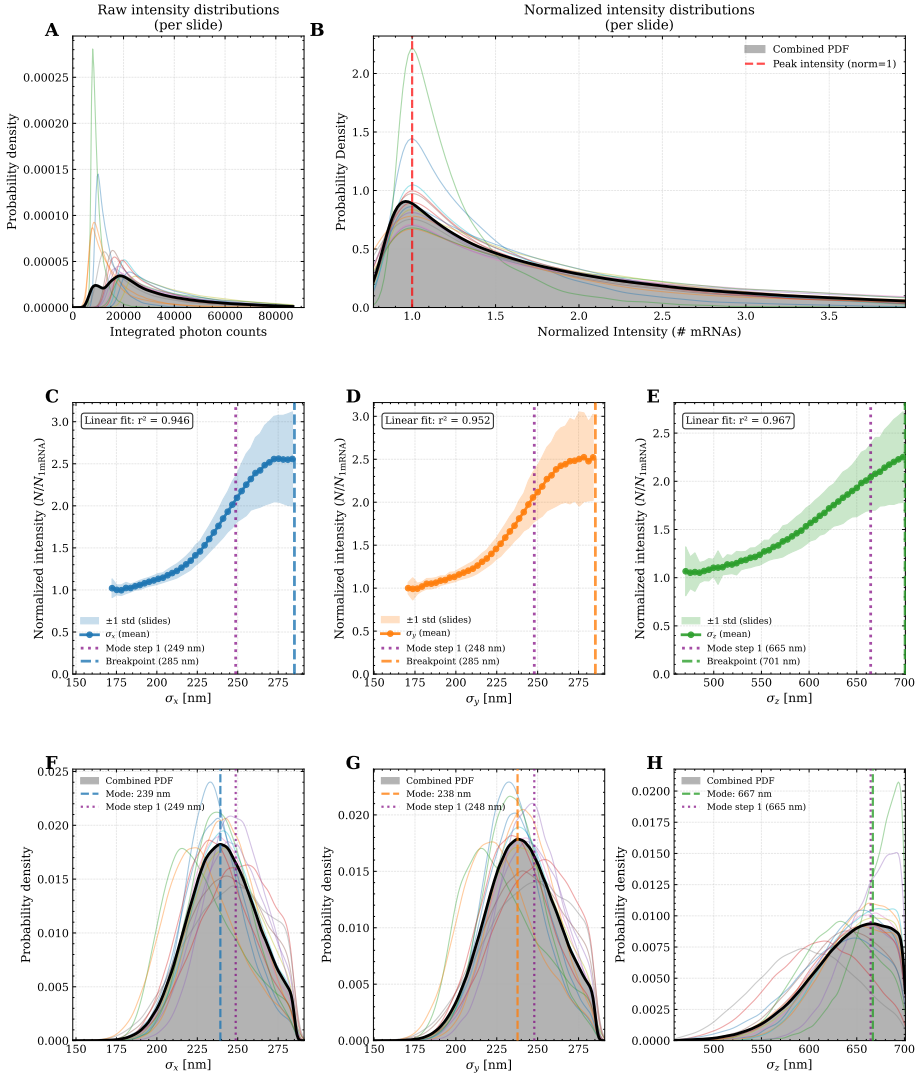

A
Raw intensity distributions
(per slide)
Probability density
Integrated photon counts
B
Normalized intensity distributions
(per slide)
Combined PDF
Peak intensity (norm=1)
Probability Density
Normalized Intensity (# mRNAs)
C
Linear fit: r² = 0.946
±1 std (slides)
σx (mean)
Mode step 1 (249 nm)
Breakpoint (285 nm)
Normalized intensity (N/N1mRNA)
σx [nm]
D
Linear fit: r² = 0.952
±1 std (slides)
σy (mean)
Mode step 1 (248 nm)
Breakpoint (285 nm)
σy [nm]
E
Linear fit: r² = 0.967
±1 std (slides)
σz (mean)
Mode step 1 (665 nm)
Breakpoint (701 nm)
σz [nm]
F
Combined PDF
Mode: 239 nm
Mode step 1 (249 nm)
Probability density
σx [nm]
G
Combined PDF
Mode: 238 nm
Mode step 1 (248 nm)
σy [nm]
H
Combined PDF
Mode: 667 nm
Mode step 1 (665 nm)
σz [nm]

Figure S5: **Validation of single-molecule filtering (orange channel, fl-HTT).** All panels show data from the orange channel (548 nm) corresponding to the fl-HTT probe in Q111 transgenic mouse tissue. Analysis of green channel (488 nm, HTT1a) data yields similar results (fig. S4). **(A-B)** Per-slide intensity normalization demonstrates successful removal of technical variation. **(A)** Raw integrated photon counts for 15 slides (faint colored lines, 746,805 total spots) showing 2-3× variation; thick black line = combined PDF. **(B)** After per-slide normalization, all distributions converge around $N_{1\text{mRNA}} = 1$ (red dashed line) via kernel density estimation [15, 16]. **(C-E)** Biphasic relationships between normalized intensity and spot size after filtering validate the single-molecule regime. For each dimension, the bold line shows mean normalized intensity across 15 slides binned into 50 size bins (only bins with ≥100 spots shown). Purple dotted lines: bead-derived PSF (σ_x = 249 nm, σ_y = 248 nm, σ_z = 665 nm). Colored dashed lines: empirically-determined breakpoints (σ_x = 285.1 nm, σ_y = 285.3 nm, σ_z = 700.7 nm; 15%, 15%, 5% larger than bead PSF). Strong linear relationships between bin-averaged intensity and size below the breakpoint (Pearson $r^2 > 0.90$ across size bins) confirm the single-molecule regime. **(F-H)** Size distributions after filtering show tight clustering around modal values with clear truncation at breakpoints. Colored dashed lines mark modes defining tissue-calibrated refined PSF. **Quality filters:** (i) PFA < 5e-02, (ii) σ_i < breakpoint for all dimensions, (iii) intensity > slide-specific negative-control threshold, (iv) cluster CV ≥ 0.5. **Slides used (n=15):** m1a4, m1a5, m1b1, m2a2, m2a3, m2a4, m2a8, m2b1, m2b7, m3a1, m3a2, m3a3, m3a5, m3b2, m3b3. **Slides excluded:** poor tissue integrity or low positive control expression.

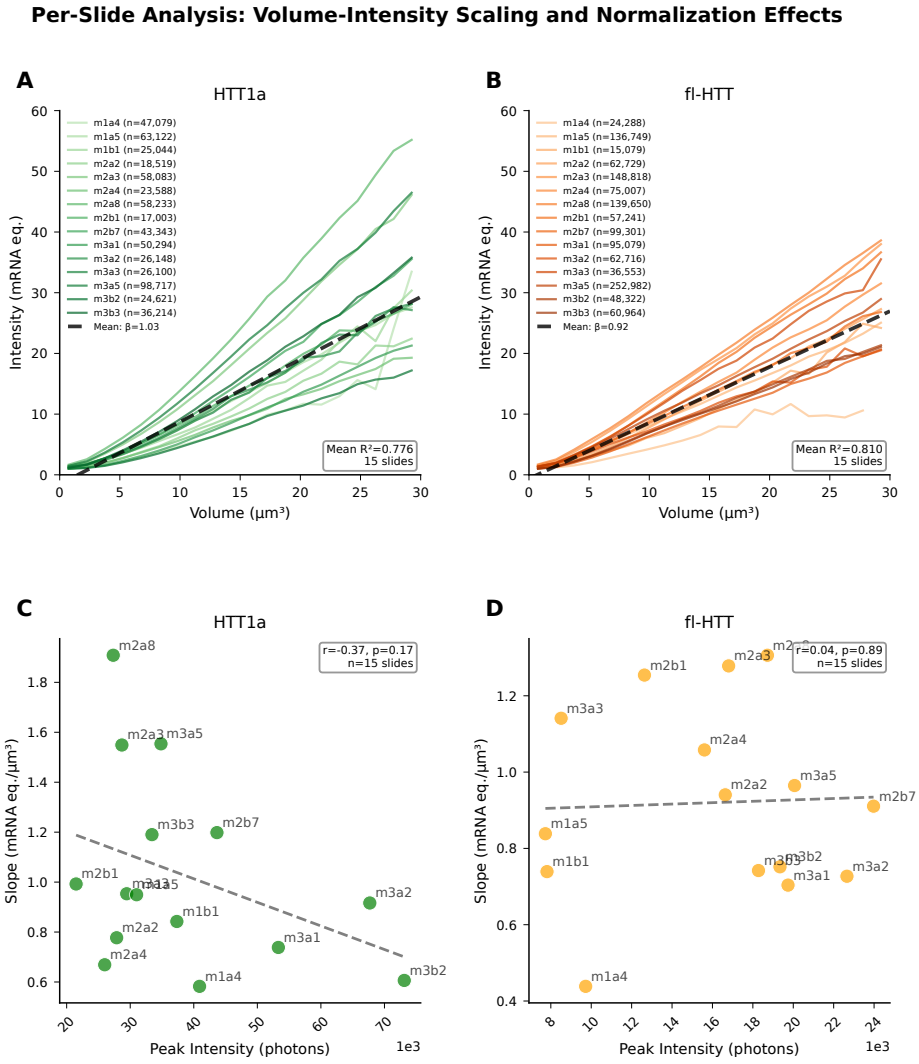


Figure S6: **Per-slide analysis of volume–intensity scaling.** Consistency of the volume–intensity relationship across individual slides, used to test whether per-slide normalization introduces a systematic bias. **(A)** Green channel (488 nm, HTT1a): per-slide binned mean intensity vs. cluster volume. Each colored line is one slide (n = 15 slides, 616,100 clusters within 0 to 30 μm^3; bins shown have ≥5 clusters). Dashed black line: mean slope $\beta = 1.03$ mRNA eq./μm^3. **(B)** Orange channel (548 nm, fl-HTT), same analysis: n = 15 slides, 1,314,992 clusters, mean slope $\beta = 0.92$ mRNA eq./μm^3. **(C, D)** Peak intensity (the modal single-molecule intensity $N_{1\text{mRNA}}$ used for normalization) vs. per-slide slope, for the green and orange channel respectively. Pearson $r = -0.37$, $p = 0.17$ (green) and $r = 0.04$, $p = 0.89$ (orange). **Slope statistics:** green mean = 1.03, SD = 0.37 mRNA eq./μm^3, CV = 36%, range 0.58–1.91; orange mean = 0.92, SD = 0.24 mRNA eq./μm^3, CV = 26%, range 0.44–1.31. **Per-slide R^2:** green mean = 0.78 (range 0.37–0.87); orange mean = 0.81 (range 0.43–0.89).

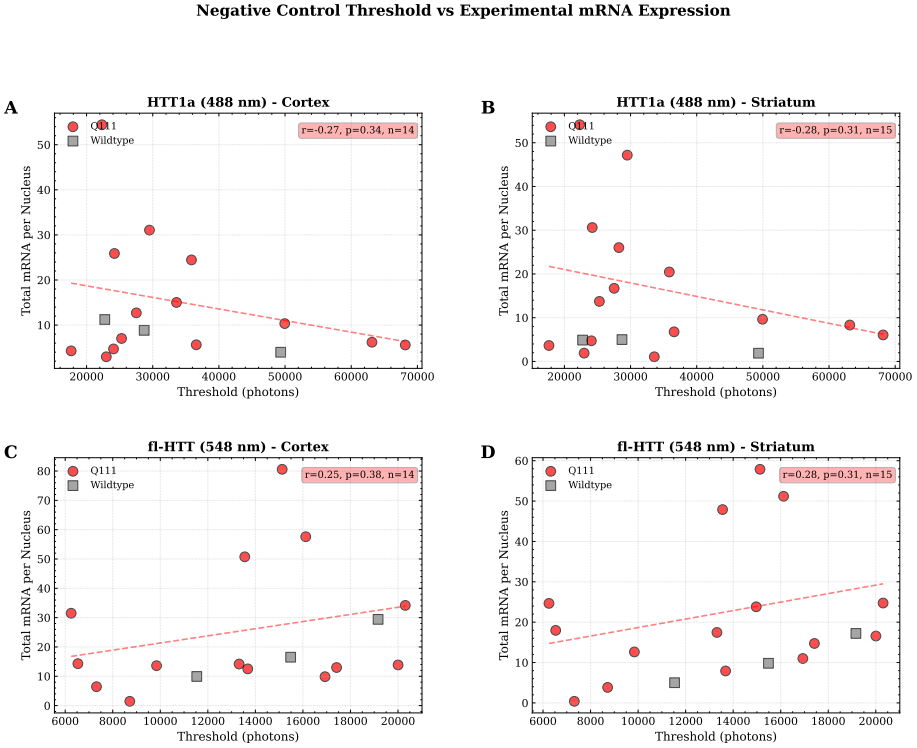


Figure S7: **Negative control thresholds show no correlation with experimental mRNA expression.** Validation that negative control background thresholds do not correlate with experimental mRNA expression levels. A *lack* of correlation validates that experimental signal represents true biological mRNA, not technical artifacts influenced by background. All correlations reported here are Pearson product-moment coefficients. **Dataset:** 18 unique slides (Q111 transgenic: 15, Wildtype: 3). Channels: HTT1a (488 nm, exon 1) and fl-HTT (548 nm). Regions: Cortex and Striatum. Merged threshold = average of Cortex and Striatum thresholds per slide (based on 95th percentile of DapB negative control intensities). **(A) HTT1a - Cortex:** Q111 n=14, Wildtype n=3. Q111 mRNA: 15 ± 15 mRNA/nucleus; Wildtype: 8 ± 4 mRNA/nucleus. Q111 correlation: $r = -0.273$, $p = 0.345$ (weak/no correlation). **(B) HTT1a - Striatum:** Q111 n=15, Wildtype n=3. Q111 mRNA: 17 ± 17 mRNA/nucleus; Wildtype: 4 ± 2 mRNA/nucleus. Q111 correlation: $r = -0.283$, $p = 0.307$. **(C) fl-HTT - Cortex:** Q111 n=14, Wildtype n=3. Q111 mRNA: 25 ± 23 mRNA/nucleus; Wildtype: 18 ± 10 mRNA/nucleus. Q111 correlation: $r = +0.255$, $p = 0.379$. **(D) fl-HTT - Striatum:** Q111 n=15, Wildtype n=3. Q111 mRNA: 22 ± 18 mRNA/nucleus; Wildtype: 10 ± 6 mRNA/nucleus. Q111 correlation: $r = +0.284$, $p = 0.305$. **Nuclear volume normalization:** Mean nuclear volume = 716 μm^3; mRNA counts normalized per nucleus to account for 3D sectioning of nuclei in tissue sections.

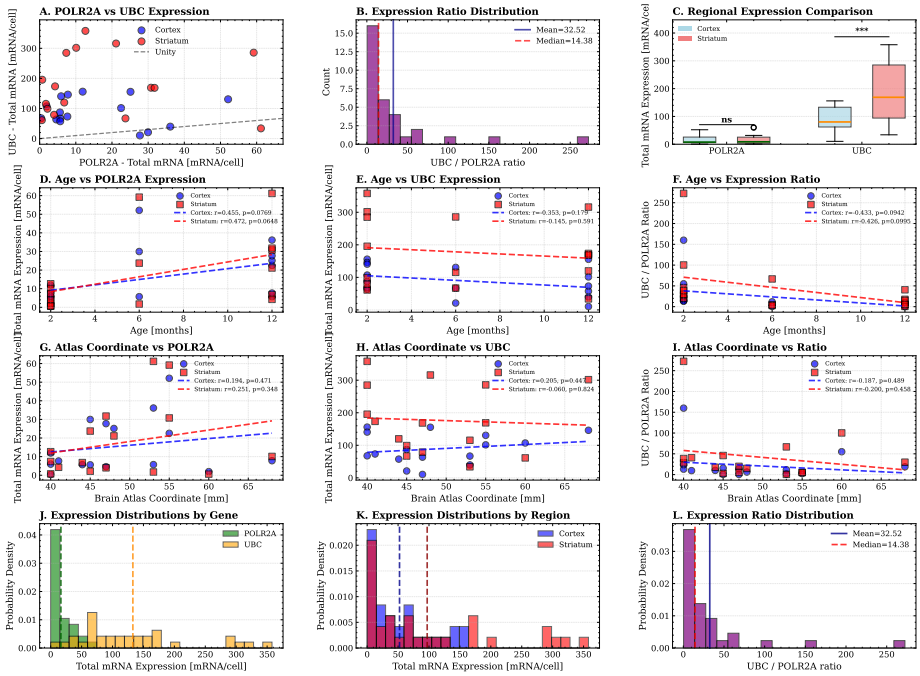


Figure S8: **Positive control analysis validates assay dynamic range.** Analysis of POLR2A (low-expression housekeeping gene, green channel) and UBC (high-expression housekeeping gene, orange channel) in positive control samples from Q111 and Wildtype mice. **Slides analyzed (n=16):** m1a4, m1b1, m2a2, m2a3, m2a4, m2a6, m2a8, m2b1, m2b6, m2b7, m3a1, m3a3, m3a4, m3a5, m3b2, m3b3. **Slides excluded:** poor tissue integrity. **Total FOVs:** 764; **Paired samples (slides with both Cortex and Striatum):** 16; **Age range:** 2-12 months; **Atlas coordinate range:** 40-68 (sections spaced at 100 μm intervals). **Row 1 (A-C):** Gene expression comparisons. (A) POLR2A vs UBC scatter plot colored by region. (B) UBC/POLR2A ratio histogram. (C) Regional comparison box plots. POLR2A: Cortex 15.78 ± 14.76 mRNA/cell (n=16 slides), Striatum 17.47 ± 19.49 mRNA/cell; paired t-test $t = -0.909$, $p = 0.38$. UBC: Cortex 89.34 ± 47.37 mRNA/cell, Striatum 177.28 ± 104.08 mRNA/cell; paired t-test $t = -4.809$, $p = 0.00023$. UBC/POLR2A ratio across both regions combined: mean 32.89 ± 57.05, median 14.10 (Cortex alone: 21.93; Striatum alone: 43.84). Note: the striatum-only ratio (43.84) is used in fig. S11 for comparison with striatum-derived RNA-seq data. **Row 2 (D-F):** Age dependencies for POLR2A, UBC, and UBC/POLR2A ratio with separate Cortex/Striatum regression lines. Non-significant correlations suggest robust normalization. **Row 3 (G-I):** Brain atlas coordinate dependencies with regional regressions. Tests for anterior-posterior expression gradients. **Row 4 (J-L):** Expression distributions by gene and region. UBC shows higher expression than POLR2A, as expected for a high-abundance housekeeping gene.

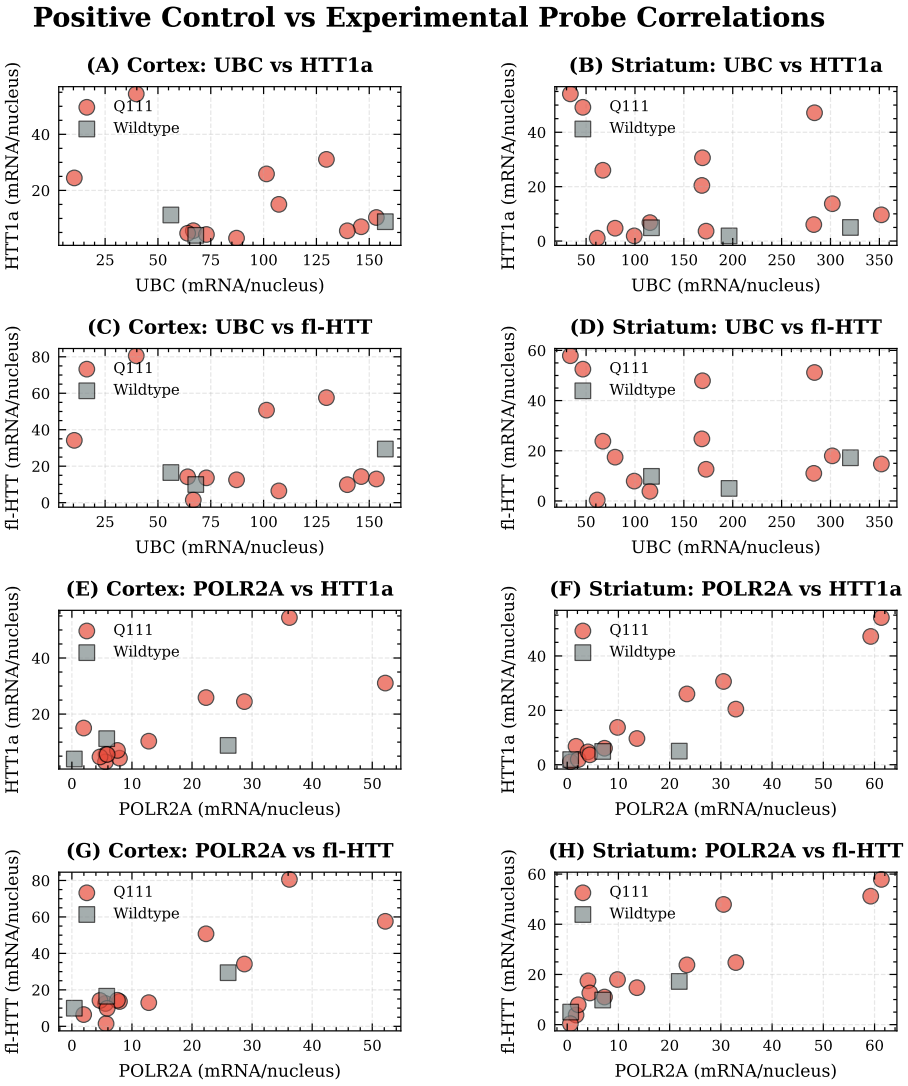


Figure S9: **Positive control correlations with experimental probes.** Tests whether variability in mHTT probes is driven by technical factors (tissue quality, RNA preservation) or true biological variation. All correlations in this figure are Pearson product-moment coefficients; significance markers denote $^{*}p < 0.05$, $^{**}p < 0.01$, $^{***}p < 0.001$. Each point = one slide (mean expression across all FOVs). Red circles: Q111; gray squares: wildtype. Sample sizes: Cortex n=12, Striatum n=13. **(A-B)** UBC vs mHTT1a. Cortex Q111: $r = -0.34$, $p = 0.29$; Striatum Q111: $r = -0.05$, $p = 0.86$. Weak correlations. **(C-D)** UBC vs fl-mHTT. Cortex Q111: $r = -0.28$, $p = 0.37$; Striatum Q111: $r = -0.00$, $p = 0.99$. Weak correlations. **(E-F)** POLR2A vs mHTT1a. Cortex Q111: $r = 0.81$, $p = 0.001^{**}$; Striatum Q111: $r = 0.98$, $p < 0.001^{***}$. Strong correlations. **(G-H)** POLR2A vs fl-mHTT. Cortex Q111: $r = 0.87$, $p < 0.001^{***}$; Striatum Q111: $r = 0.94$, $p < 0.001^{***}$. Strong correlations.

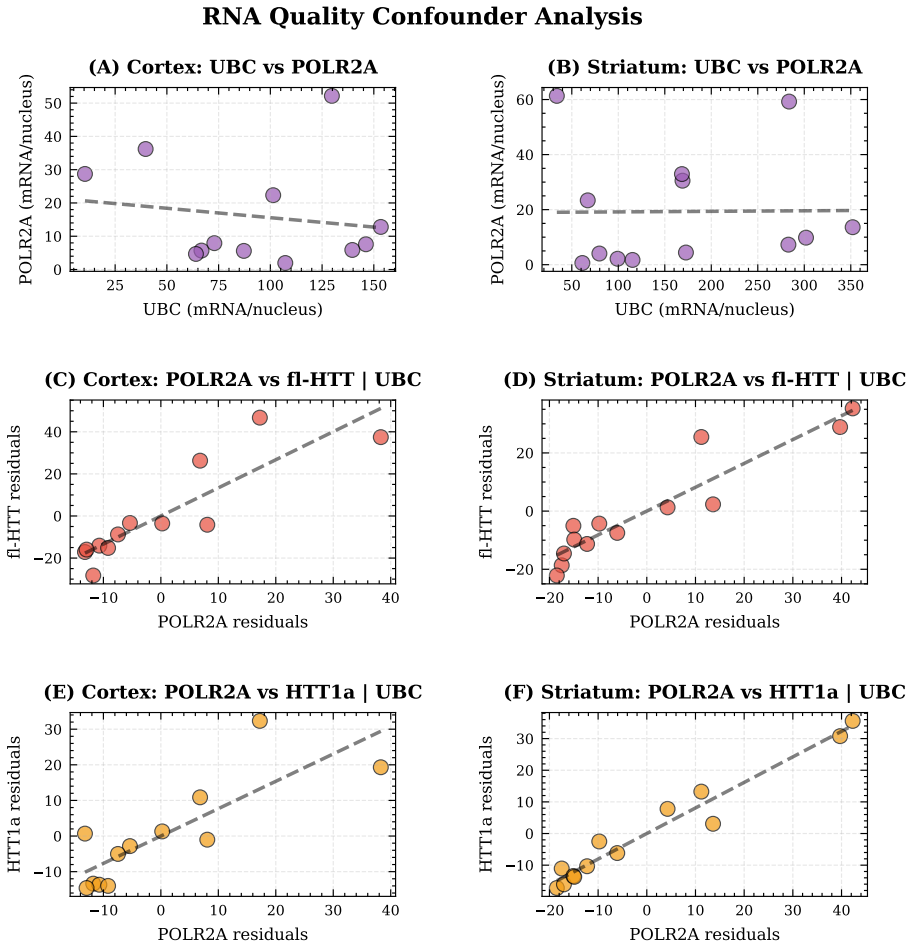


Figure S10: **Partial correlation analysis rules out RNA quality as major confounder.** Addresses whether strong POLR2A-mHTT correlations are spurious (driven by RNA quality) or reflect true biological coupling. Correlations are Pearson; partial correlations were obtained by ordinary least-squares residualisation on the control variable, followed by Pearson correlation of the residuals. Significance markers denote $^{*}\,p < 0.05$, $^{**}\,p < 0.01$, $^{***}\,p < 0.001$. Uses partial correlation controlling for UBC as a tissue quality proxy. Sample sizes: Cortex n=12, Striatum n=13. **(A-B)** UBC vs POLR2A correlation quantifies shared technical variance. Cortex: $r = -0.161$, $p = 0.62$; Striatum: $r = 0.010$, $p = 0.97$. Low correlations indicate UBC and POLR2A respond differently to tissue quality. **(C-D)** Partial correlation: POLR2A vs fl-mHTT | UBC. Cortex: original $r = 0.872$, partial $r = 0.873$, $p < 0.001^{***}$ (+0.1%); Striatum: original $r = 0.939$, partial $r = 0.939$, $p < 0.001^{***}$ (0.0%). **(E-F)** Partial correlation: POLR2A vs mHTT1a | UBC. Cortex: original $r = 0.809$, partial $r = 0.812$, $p = 0.001^{**}$ (+0.4%); Striatum: original $r = 0.975$, partial $r = 0.977$, $p < 0.001^{***}$ (+0.2%).

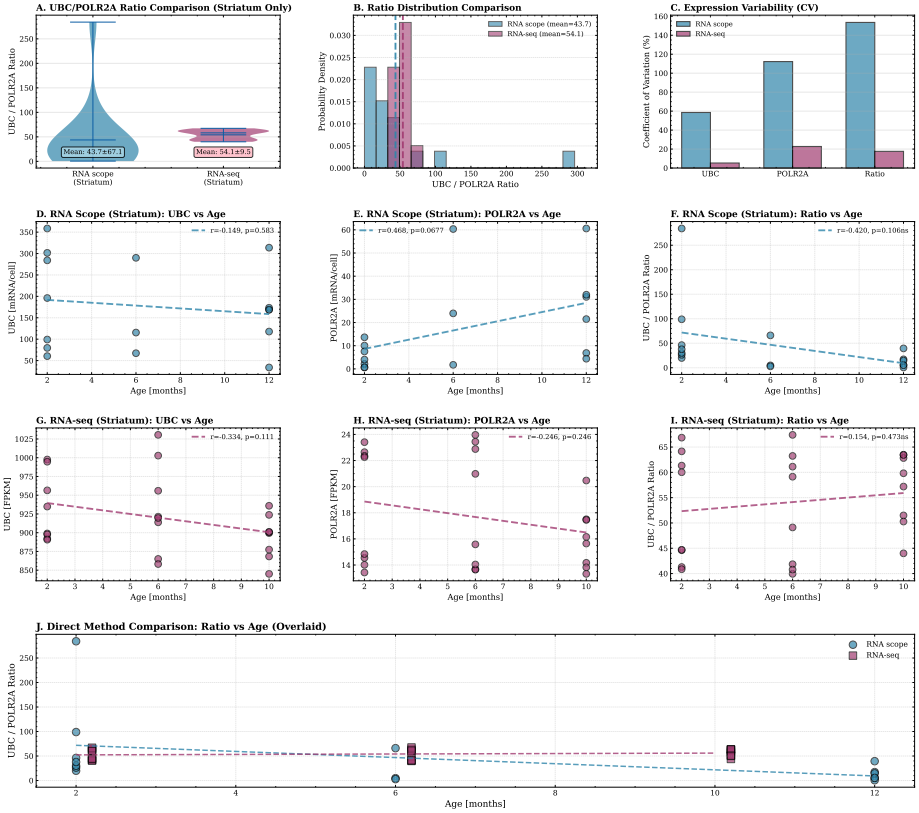


Figure S11: **Comparison of RNAscope and bulk RNA-seq validates housekeeping gene quantification.** Comparison between single-molecule RNAscope (this study; $n = 16$ slides from Q111 mice, ages 2-12 months, striatum only) and bulk RNA-seq (GSE65774 [20]; $n = 24$ Q111 striatum samples). **(A)** UBC/POLR2A ratio comparison (violin plots). This unit-independent ratio enables direct comparison despite different quantification approaches (mRNA/nucleus vs FPKM). RNAscope (striatum only): 44 ± 68; RNA-seq: 54 ± 10; fold difference of means $0.81\times$ (Welch's t-test: $t = -0.59$, $p = 0.56$); medians 22.5 (RNAscope) vs 58.2 (RNA-seq), Mann–Whitney U $p = 0.002$. Note: The RNAscope ratio here (43.8) is higher than the combined Cortex+Striatum ratio in fig. S8 (32.89) because this comparison uses striatum data only to match the RNA-seq dataset. **(B)** Overlaid histograms showing full distribution of UBC/POLR2A ratios; dashed lines indicate means. **(C)** Coefficient of variation comparison: UBC CV (RNAscope 58%, RNA-seq 5%), POLR2A CV (112% vs 23%), Ratio CV (154% vs 18%). Higher CV in RNAscope reflects biological heterogeneity at single-cell level that bulk RNA-seq averages out [21]. **(D-F)** RNAscope age correlations (striatum; Pearson): UBC vs age ($r = -0.14$, $p = 0.60$), POLR2A vs age ($r = 0.48$, $p = 0.06$), ratio vs age ($r = -0.42$, $p = 0.11$). **(G-I)** RNA-seq age correlations (Pearson): UBC vs age ($r = -0.33$, $p = 0.11$), POLR2A vs age ($r = -0.25$, $p = 0.25$), ratio vs age ($r = 0.15$, $p = 0.47$). **(J)** Direct method overlay showing both datasets on same axes.

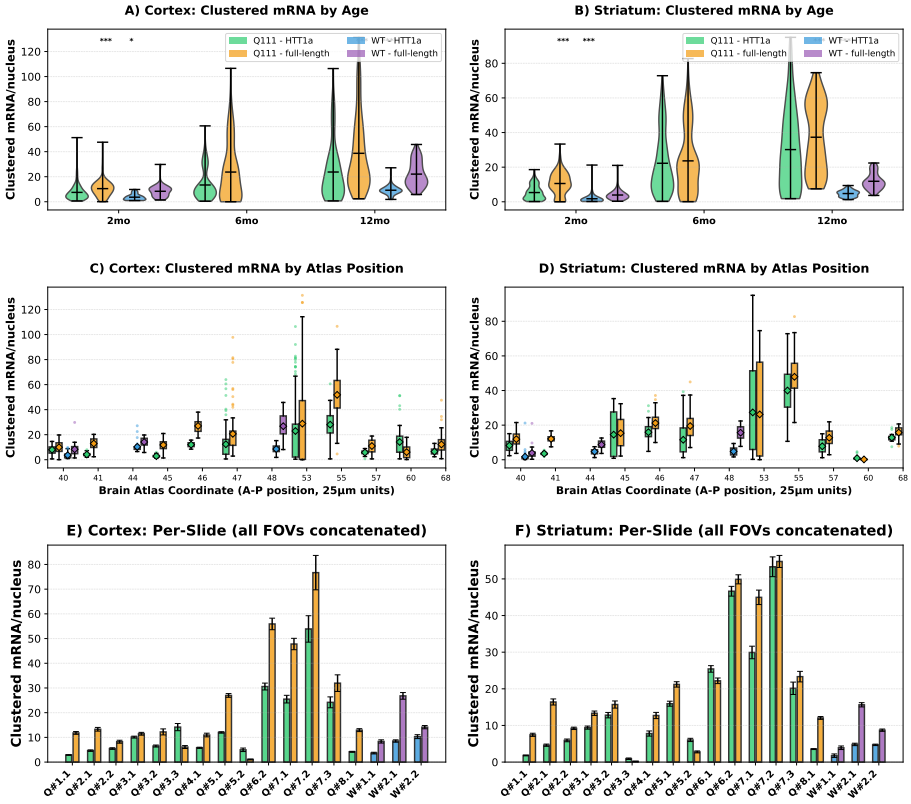


Figure S12: **Clustered mRNA expression dominates total signal.** Clustered mRNA represents clustered transcripts, quantified as $(I_{\text{cluster}}/I_{\text{peak}})/N_{\text{nuclei}}$. Dataset: 3,234 FOVs (Q111: 2,668; WT: 566). Cortex: 1,662 FOVs; Striatum: 1,572 FOVs. **(A-B) Age trends.** Violin plots showing clustered mRNA distribution across ages. Cortex: 2mo Q111 7.50 ± 6.79 mRNA/cell (n=335), 6mo 13.18 ± 11.28 (n=193), 12mo Q111 23.86 ± 22.17 (n=169); 12mo WT 9.19 ± 3.89 (n=83). Striatum: 2mo Q111 5.33 ± 4.19 (n=180), 6mo 21.85 ± 16.82 (n=284), 12mo Q111 30.24 ± 22.76 (n=173); 12mo WT 4.75 ± 1.88 (n=104). **Statistical tests (Q111 vs WT, unpaired t-test):** Striatum 2mo HTT1a: $t = 5.27$, $p < 0.0001$; Striatum 2mo fl-HTT: $t = 6.81$, $p < 0.0001$; Striatum 12mo HTT1a: $t = 11.39$, $p < 0.0001$; Striatum 12mo fl-HTT: $t = 13.04$, $p < 0.0001$. **(C-D)** Box plots showing expression across atlas coordinates (40-68, sections spaced at 100 μm intervals). Q111 HTT1a Striatum: mean 19.46 ± 19.02 mRNA/cell (n=637 FOVs); WT: 3.86 ± 2.74 (n=149 FOVs). **(E-F)** Per-slide bar plots showing mean±SEM expression, revealing inter-individual variability.

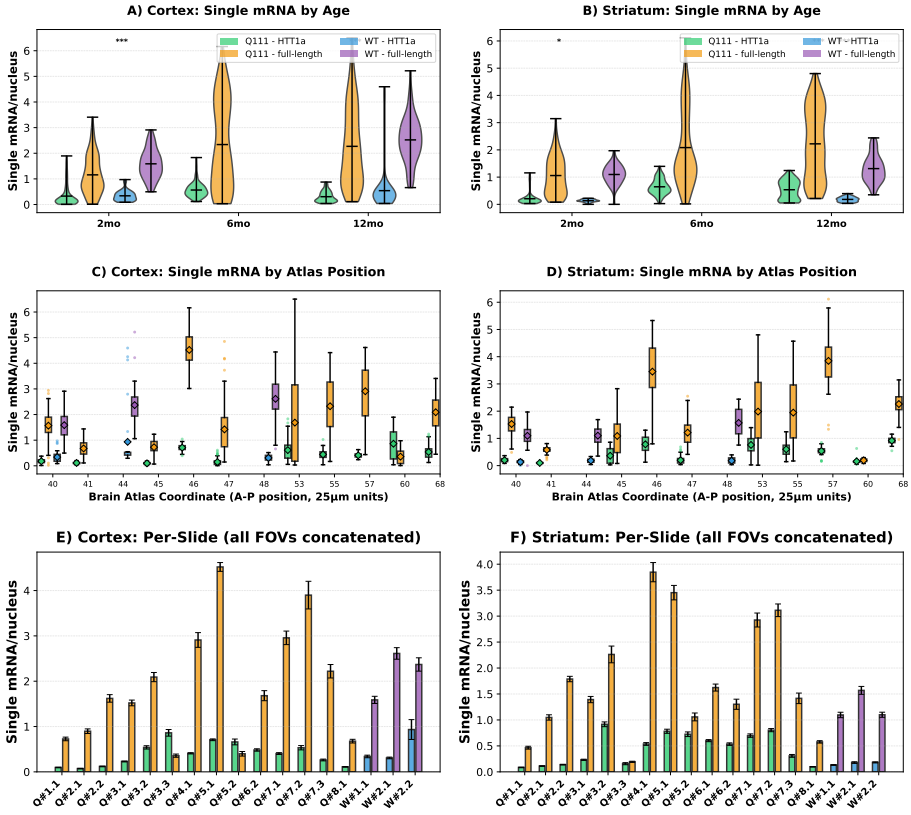


Figure S13: **Single mRNA expression analysis.** Single mRNA represents individual diffraction-limited spots, quantified as $N_{\text{spots}}/N_{\text{nuclei}}$ per nucleus. Dataset: 3,234 FOVs (Q111: 2,668; WT: 566). **(A-B) Age trends.** Violin plots showing distribution of single mRNA expression across ages. Cortex: 2mo Q111 HTT1a 0.33 ± 0.42 (n=335), WT 0.36 ± 0.21 (n=51); 6mo Q111 0.57 ± 0.29 (n=193); 12mo Q111 0.31 ± 0.21 (n=169), WT 0.54 ± 0.80 (n=83). Striatum: 2mo Q111 0.21 ± 0.23 (n=180), WT 0.14 ± 0.05 (n=45); 6mo Q111 0.65 ± 0.29 (n=284); 12mo Q111 0.54 ± 0.34 (n=173), WT 0.18 ± 0.09 (n=104). **Statistical tests (Q111 vs WT, unpaired t-test):** Striatum 2mo HTT1a: $t = 1.92$, $p = 0.056$ (ns); Striatum 2mo fl-HTT: $t = -0.05$, $p = 0.96$ (ns); Striatum 12mo HTT1a: $t = 10.49$, $p < 0.0001$; Striatum 12mo fl-HTT: $t = 7.34$, $p < 0.0001$. **(C-D)** Atlas coordinate trends. Box plots showing expression across approximate anterior-posterior coordinates (atlas sections spaced at 100 μm intervals). Q111 HTT1a: cortex 0.39 ± 0.36 (n=697), striatum 0.49 ± 0.34 (n=637). WT HTT1a: cortex 0.47 ± 0.65 (n=134), striatum 0.17 ± 0.08 (n=149). **(E-F)** Per-slide breakdown showing mean ± SEM for each slide (all FOVs concatenated per slide).

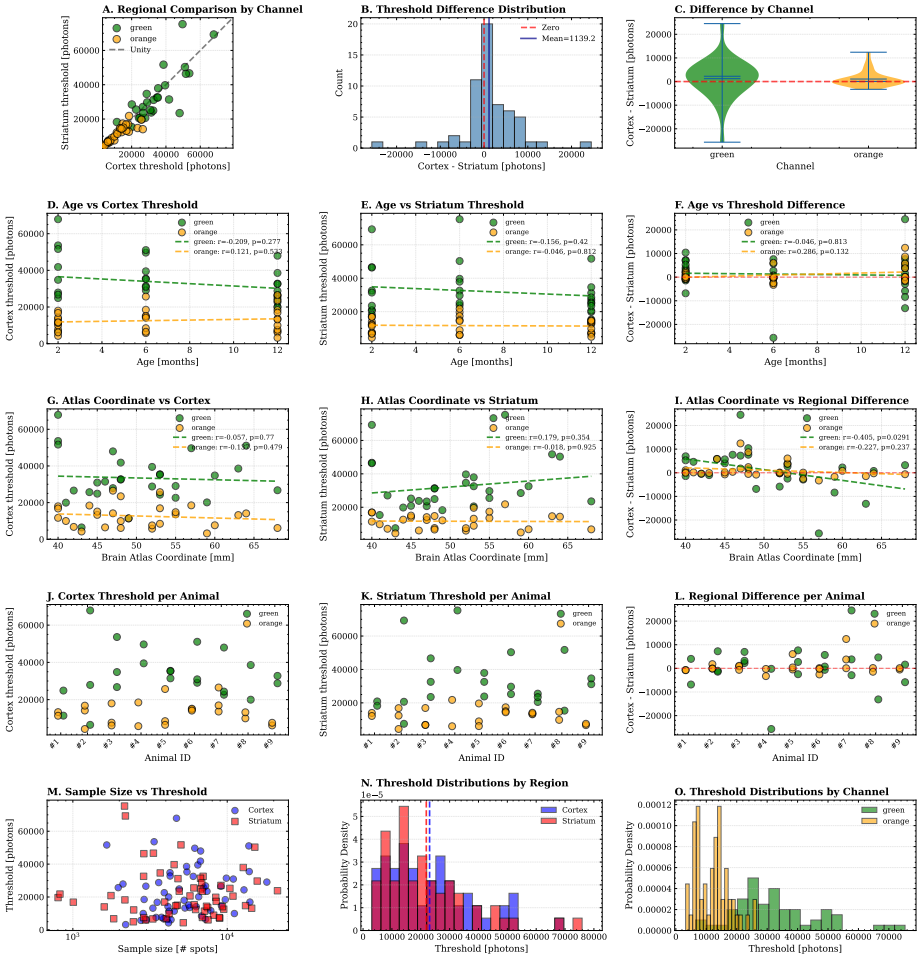

A. Regional Comparison by Channel
green
orange
Unity
Striatum threshold [photons]
Cortex threshold [photons]
B. Threshold Difference Distribution
Zero
Mean=1139.2
Count
Cortex - Striatum [photons]
C. Difference by Channel
Cortex - Striatum [photons]
green
orange
Channel
D. Age vs Cortex Threshold
green: r=-0.209, p=0.277
orange: r=0.121, p=0.5
Cortex threshold [photons]
Age [months]
E. Age vs Striatum Threshold
green: r=-0.156, p=0.42
orange: r=-0.046, p=0.817
Striatum threshold [photons]
Age [months]
F. Age vs Threshold Difference
green: r=-0.046, p=0.813
orange: r=0.286, p=0.132
Cortex - Striatum [photons]
Age [months]
G. Atlas Coordinate vs Cortex
green: r=-0.057, p=0.77
orange: r=-0.1
p=0.479
Cortex threshold [photons]
Brain Atlas Coordinate [mm]
H. Atlas Coordinate vs Striatum
green: r=0.179, p=0.354
orange: r=-0.018, p=0.925
Striatum threshold [photons]
Brain Atlas Coordinate [mm]
I. Atlas Coordinate vs Regional Difference
green: r=-0.405, p=0.0291
orange: r=-0.227, p=0.237
Cortex - Striatum [photons]
Brain Atlas Coordinate [mm]
J. Cortex Threshold per Animal
Cortex threshold [photons]
Animal ID
K. Striatum Threshold per Animal
Striatum threshold [photons]
Animal ID
L. Regional Difference per Animal
Cortex - Striatum [photons]
Animal ID
M. Sample Size vs Threshold
Cortex
Striatum
Threshold [photons]
Sample size [# spots]
N. Threshold Distributions by Region
Probability Density
Threshold [photons]
O. Threshold Distributions by Channel
Probability Density
Threshold [photons]

Figure S14: **Comprehensive negative control background threshold analysis across brain regions.** Analysis of regional differences in negative control thresholds (Cortex vs Striatum) and their relationships with age, sample size, and brain atlas coordinates. Negative control thresholds define the intensity cutoff above which spots are considered true mRNA. **Dataset:** 58 paired samples (slide-channel combinations), 29 unique slides. Channels: green (488 nm, HTT1a) and orange (548 nm, fl-HTT). Age range: 2-12 months. Brain atlas coordinates: 40-68 (sections spaced at 100 μm intervals). **Overall regional comparison:** Cortex threshold: $23,057 \pm 14,660$ photons; Striatum: $21,918 \pm 15,255$ photons. Mean difference (Cortex − Striatum): $+1,139 \pm 6,454$ photons. Paired t-test: $t = 1.344$, $p = 0.184$ (*no significant regional difference*). **Per-channel statistics:** Green (n=29): Cortex $33,430 \pm 13,272$, Striatum $32,215 \pm 15,244$ photons ($p = 0.451$). Orange (n=29): Cortex $12,684 \pm 6,202$, Striatum $11,622 \pm 4,663$ photons ($p = 0.100$). **Age correlations (Pearson):** Age vs Cortex threshold: $r = -0.068$, $p = 0.611$; Age vs Striatum: $r = -0.084$, $p = 0.530$; Age vs regional difference: $r = +0.044$, $p = 0.744$ (*no significant age effects*). **Rostrocaudal position (Pearson correlation):** Atlas coordinate vs Cortex threshold: $r = -0.054$, $p = 0.69$; Atlas coordinate vs Striatum threshold: $r = +0.086$, $p = 0.52$ (both negligible). The regional *difference* shows a modest correlation with atlas position ($r = -0.325$, $p = 0.013$), but this reflects small opposing trends that largely cancel when regions are merged. **Row 1 (A-C):** Regional comparison scatter, difference histogram, and violin plots by channel. **Row 2 (D-F):** Age dependencies for Cortex, Striatum, and their difference. **Row 3 (G-I):** Brain atlas coordinate dependencies for Cortex, Striatum, and their difference. **Row 4 (J-L):** Per-animal analysis for each animal (n=9), enabling assessment of inter-animal vs intra-animal variability. Panel J: Cortex threshold per animal. Panel K: Striatum threshold per animal. Panel L: Regional difference (Cortex − Striatum) per animal. **Row 5 (M-O):** Sample size effects (M) and threshold distributions by region (N) and by channel (O).

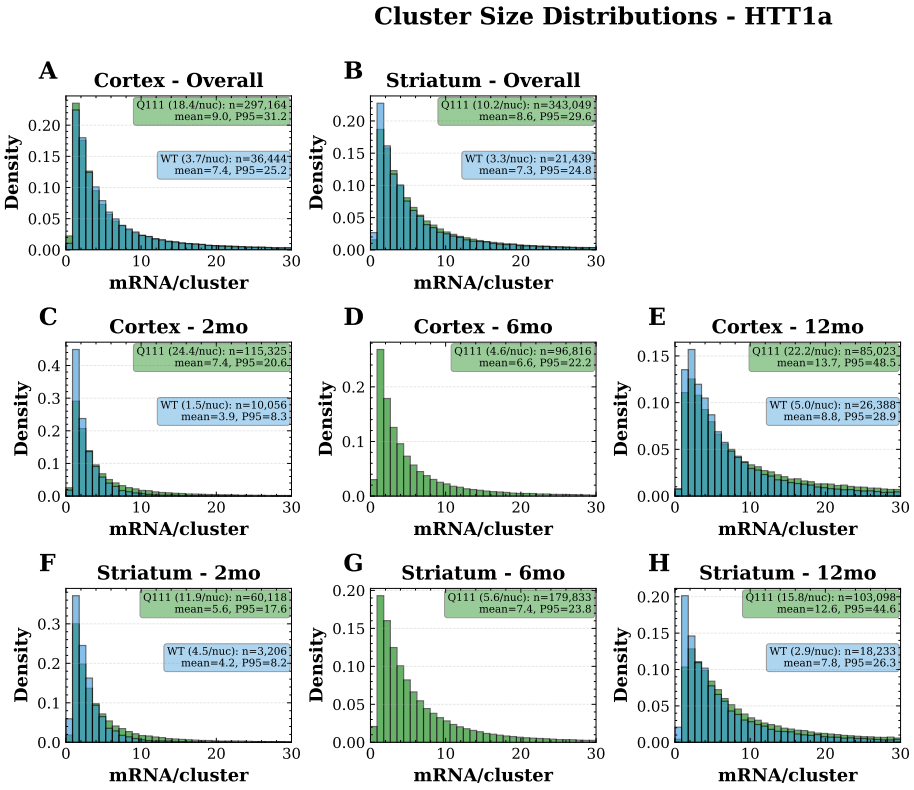


Figure S15: **Cluster size distributions for HTT1a.** Analysis of 698,169 clusters: Q111 640,320, WT 57,849. Cortex: 333,511 clusters; Striatum: 364,658 clusters. Slides with technical failures were excluded. **(A-B) Overall distributions.** Cortex Q111: n=297,099 clusters, mean 8.96 mRNA equiv., median 3.87, P95 31.21, 18.42 clusters/nucleus; WT: n=36,412, mean 7.40, median 3.90, P95 25.06, 3.71 clusters/nucleus. Striatum Q111: n=342,971, mean 8.64, median 4.54, P95 29.57, 10.19 clusters/nucleus; WT: n=21,437, mean 7.26, median 3.98, P95 24.78, 3.35 clusters/nucleus. **(C-H) Age stratification.** Cortex: 2mo Q111 n=115,329, mean 7.44, 24.37 cl/nucleus; 6mo n=96,749, mean 6.59, 4.62 cl/nucleus; 12mo Q111 n=85,021, mean 13.74, 22.16 cl/nucleus. Striatum: 2mo Q111 n=60,096, mean 5.64, 11.94 cl/nucleus; 6mo n=179,781, mean 7.40, 5.64 cl/nucleus; 12mo Q111 n=103,094, mean 12.54, 15.79 cl/nucleus. **(I-P)** Per-mouse distributions revealing inter-individual variability. Cluster size = cluster intensity / slide-specific single-spot peak intensity (mRNA equivalents). CV threshold ≥0.5; intensity threshold >95th percentile of negative control.

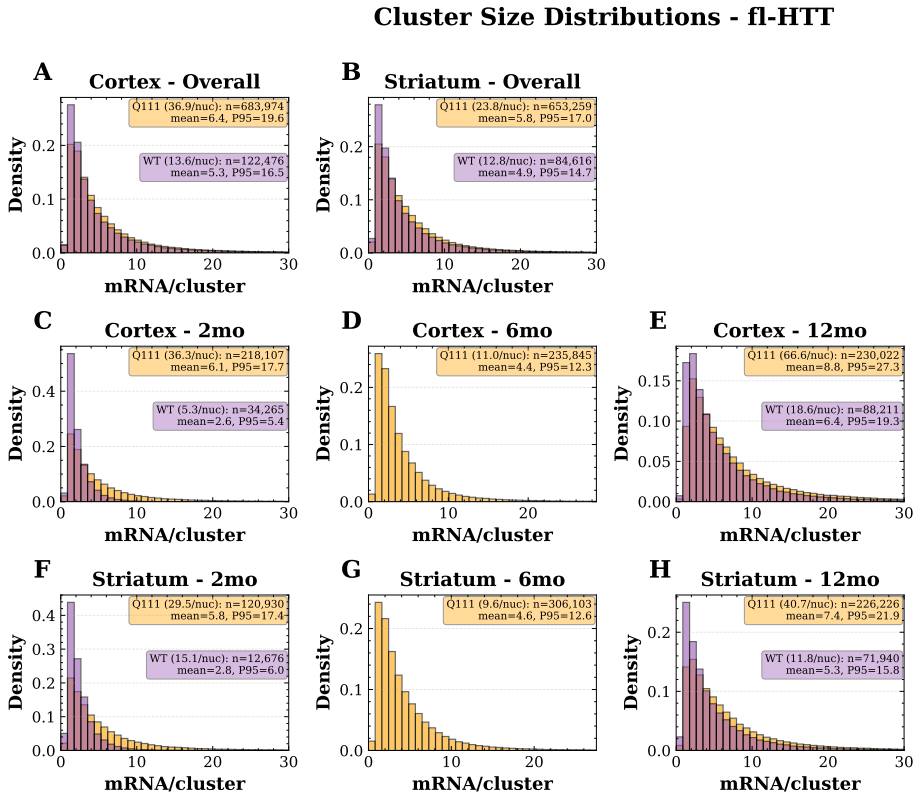


Figure S16: **Cluster size distributions for fl-HTT.** Analysis of 1,544,983 clusters: Q111 1,337,908, WT 207,075. Cortex: 806,405 clusters; Striatum: 738,578 clusters. Slides with technical failures were excluded. **(A-B) Overall distributions.** Cortex Q111: n=683,947 clusters, mean 6.42 mRNA equiv., median 3.77, P95 19.59, 36.85 clusters/nucleus; WT: n=122,458, mean 5.30, median 3.10, P95 16.47, 13.56 clusters/nucleus. Striatum Q111: n=653,230, mean 5.78, median 3.75, P95 17.02, 23.75 clusters/nucleus; WT: n=84,617, mean 4.88, median 3.03, P95 14.68, 12.83 clusters/nucleus. **(C-H) Age stratification.** Cortex: 2mo Q111 n=218,032, mean 6.14, 36.24 cl/nucleus; 6mo n=235,892, mean 4.38, 11.03 cl/nucleus; 12mo Q111 n=230,023, mean 8.79, 66.57 cl/nucleus. Striatum: 2mo Q111 n=120,905, mean 5.83, 29.48 cl/nucleus; 6mo n=306,100, mean 4.57, 9.63 cl/nucleus; 12mo Q111 n=226,225, mean 7.39, 40.68 cl/nucleus. **(I-P)** Per-mouse distributions revealing inter-individual variability. Cluster size = cluster intensity / slide-specific single-spot peak intensity (mRNA equivalents). CV threshold ≥0.5; intensity threshold >95th percentile of negative control.

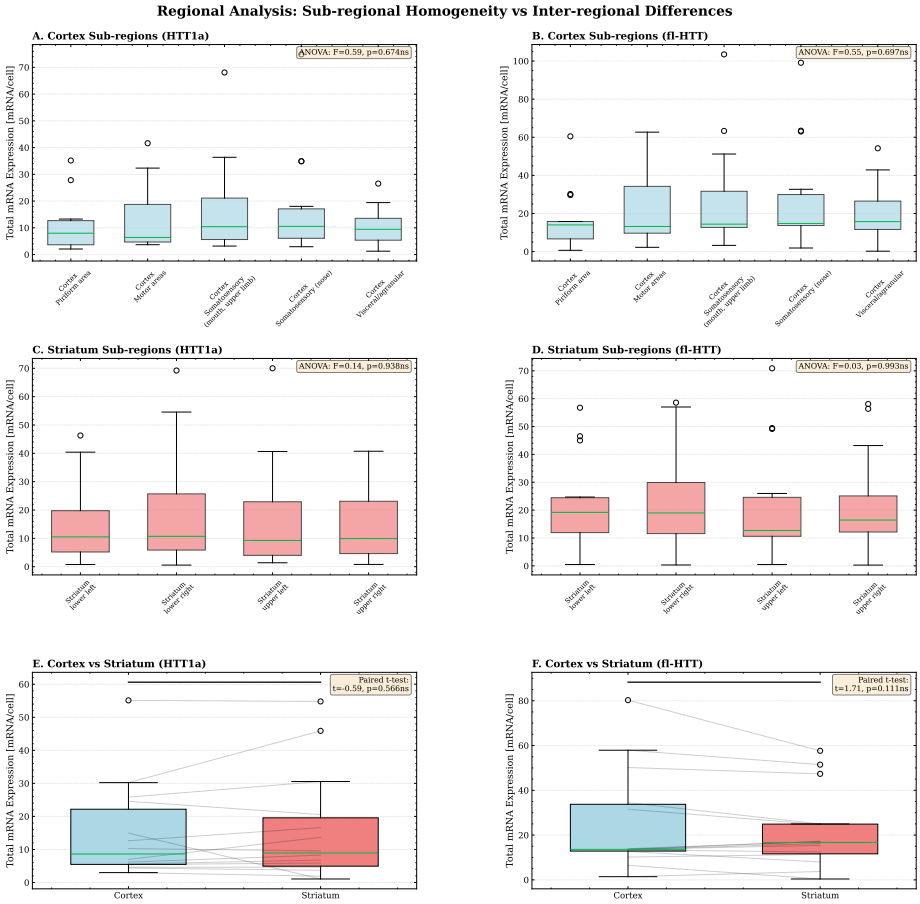
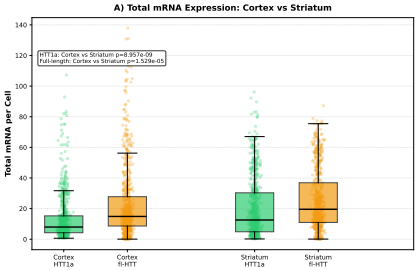
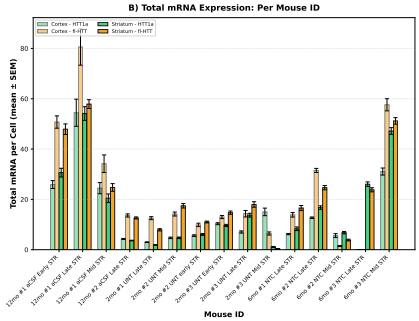
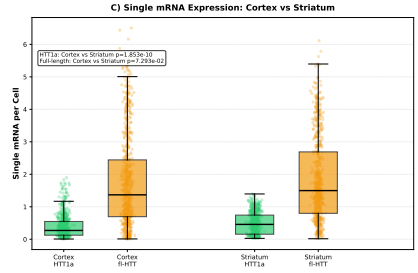
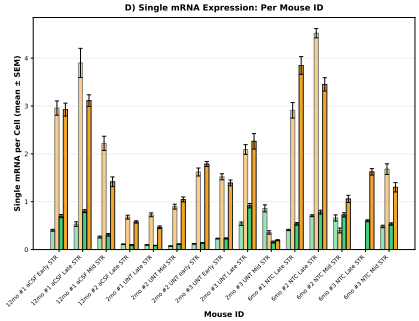


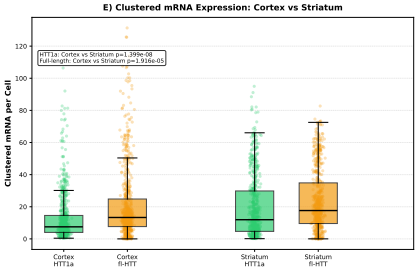
Figure S17: **Detailed regional expression analysis.** Sub-regional expression patterns analyzed using one-way ANOVA with Tukey HSD post-hoc tests (α = 0.05). **Dataset:** Q111 experimental samples, 15 slides, 2,668 FOVs total (Cortex: 1,394; Striatum: 1,274). Age range: 2-12 months; atlas coordinate range: 40-68 (sections spaced at 100 μm intervals). **Cortex subregions (n=5):** Piriform area, Primary/secondary motor areas, Primary somatosensory (mouth/upper limb), Supplemental/primary somatosensory (nose), Visceral/gustatory/agranular areas. **Striatum subregions (n=4):** Lower left, lower right, upper left, upper right quadrants. **Row 1 (A-B):** Cortex sub-regional analysis. **ANOVA, HTT1a:** $F = 0.579$, $p = 0.679$ (ns). **ANOVA, fl-HTT:** $F = 0.548$, $p = 0.702$ (ns). **Row 2 (C-D):** Striatum sub-regional analysis. **ANOVA, HTT1a:** $F = 0.135$, $p = 0.939$ (ns). **ANOVA, fl-HTT:** $F = 0.033$, $p = 0.992$ (ns). **Row 3 (E-F):** Inter-regional comparison with paired t-test and connecting lines. HTT1a: Cortex 14.91 ± 13.77 vs Striatum 15.95 ± 15.90 mRNA/cell, $t = -0.605$, $p = 0.555$ (ns, n=14 paired samples). Full-length: Cortex 25.30 ± 21.98 vs Striatum 22.08 ± 17.11 mRNA/cell, $t = 1.698$, $p = 0.113$ (ns).

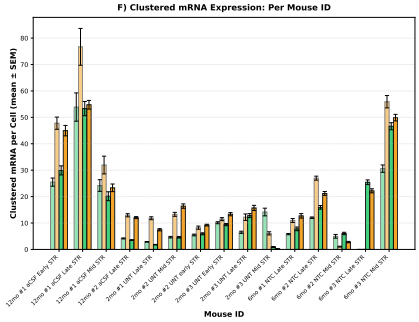

A) Total mRNA Expression: Cortex vs Striatum
HTT1a: Cortex vs Striatum p=8.957e-09
Full-length: Cortex vs Striatum p=1.529e-05
Total mRNA per Cell
Cortex HTT1a
Cortex fl-HTT
Striatum HTT1a
Striatum fl-HTT

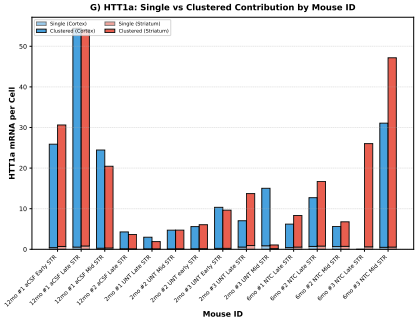

B) Total mRNA Expression: Per Mouse ID
Cortex - HTT1a
Cortex - fl-HTT
Striatum - HTT1a
Striatum - fl-HTT
Total mRNA per Cell (mean ± SEM)
Mouse ID


C) Single mRNA Expression: Cortex vs Striatum
HTT1a: Cortex vs Striatum p=1.853e-10
Full-length: Cortex vs Striatum p=7.293e-02
Single mRNA per Cell
Cortex HTT1a
Cortex fl-HTT
Striatum HTT1a
Striatum fl-HTT


D) Single mRNA Expression: Per Mouse ID
Single mRNA per Cell (mean ± SEM)
Mouse ID


E) Clustered mRNA Expression: Cortex vs Striatum
HTT1a: Cortex vs Striatum p=1.399e-08
Full-length: Cortex vs Striatum p=1.916e-05
Clustered mRNA per Cell
Cortex HTT1a
Cortex fl-HTT
Striatum HTT1a
Striatum fl-HTT


F) Clustered mRNA Expression: Per Mouse ID
Clustered mRNA per Cell (mean ± SEM)
Mouse ID


G) HTT1a: Single vs Clustered Contribution by Mouse ID
Single (Cortex)
Clustered (Cortex)
Single (Striatum)
Clustered (Striatum)
HTT1a mRNA per Cell
Mouse ID

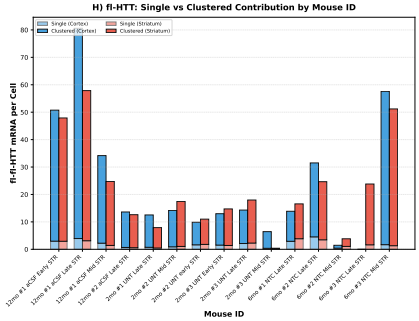

H) fl-HTT: Single vs Clustered Contribution by Mouse ID
Single (Cortex)
Clustered (Cortex)
Single (Striatum)
Clustered (Striatum)
fl-fl-HTT mRNA per Cell
Mouse ID

Figure S18: **Expression analysis across Q111 mice.** Detailed analysis of 2,668 FOVs from 15 Q111 slides. Cortex: 1,394 FOVs; Striatum: 1,274 FOVs. FOVs per mouse range from 86 to 250. **(A-B) Total mRNA.** Cortex: HTT1a mean 13.41 ± 14.88, median 7.98 mRNA/cell (n=697 FOVs); fl-HTT 22.80 ± 23.40, median 14.96. Striatum: HTT1a 19.96 ± 19.25, median 12.62; fl-HTT 25.37 ± 19.76, median 19.81. **(C-D) Single mRNA.** Cortex: HTT1a 0.39 ± 0.35, median 0.28; fl-HTT 1.77 ± 1.41, median 1.39. Striatum: HTT1a 0.49 ± 0.34, median 0.46; fl-HTT 1.84 ± 1.31, median 1.49. **(E-F) Clustered mRNA.** Cortex: HTT1a 13.02 ± 14.74, median 7.63; fl-HTT 21.03 ± 22.48, median 13.52. Striatum: HTT1a 19.48 ± 19.07, median 11.99; fl-HTT 23.53 ± 19.09, median 17.80. **Quality control:** Slides with poor tissue integrity were excluded; CV≥0.5 for cluster filtering; minimum 40 nuclei per FOV.

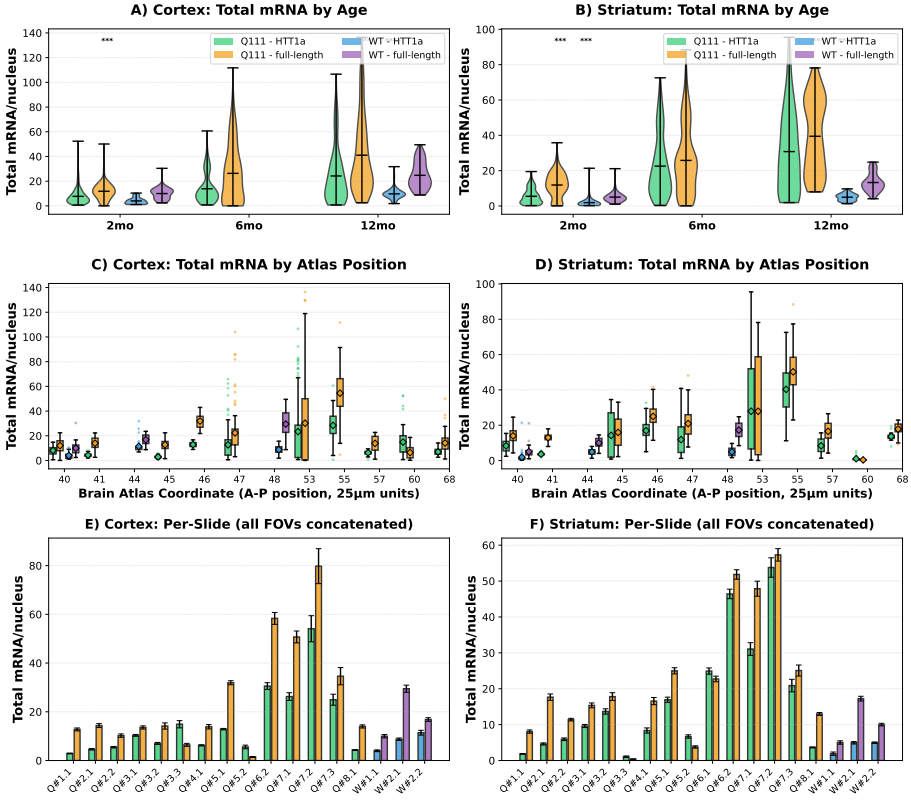


Figure S19: **Comprehensive total mRNA expression analysis.** Total mRNA combines single spots and clustered signal: $(N_{\text{spots}} + I_{\text{cluster}}/I_{\text{peak}})/N_{\text{nuclei}}$. Dataset: 3,234 FOVs (Q111: 2,668; WT: 566). **(A-B) Age trends.** Violin plots showing distribution of total mRNA expression. Cortex: 2mo Q111 HTT1a 7.83 ± 7.08 (n=335), WT 4.09 ± 2.62 (n=51); 6mo Q111 13.75 ± 11.31 (n=193); 12mo Q111 24.17 ± 22.36 (n=169), WT 9.73 ± 4.46 (n=83). Striatum: 2mo Q111 5.53 ± 4.35 (n=180), WT 1.93 ± 3.24 (n=45); 6mo Q111 22.50 ± 16.81 (n=284); 12mo Q111 30.78 ± 23.06 (n=173), WT 4.93 ± 1.96 (n=104). **Age-group comparisons (FOV level).** One-way ANOVA across the three ages, with the non-parametric Kruskal–Wallis test as a distribution-free check: cortex HTT1a $F(2,694) = 84.7$, $p < 0.0001$ (Kruskal–Wallis $H = 107.3$, $p < 0.0001$); cortex fl-HTT $F(2,694) = 120.3$, $p < 0.0001$ ($H = 162.1$, $p < 0.0001$); striatum HTT1a $F(2,634) = 106.5$, $p < 0.0001$ ($H = 205.6$, $p < 0.0001$); striatum fl-HTT $F(2,634) = 114.0$, $p < 0.0001$ ($H = 167.9$, $p < 0.0001$). Both tests agree in every case. Post-hoc pairwise comparisons between ages are Student's t-tests with Bonferroni correction (all adjusted $p < 0.0001$). **FOV-level statistical tests (Q111 vs WT, unpaired Student's t-test; the wildtype group at each age is a single mouse, and FOVs are not independent, so these tests are descriptive):** Striatum 2mo HTT1a: $t = 5.20$, $p < 0.0001$; Striatum 2mo fl-HTT: $t = 6.36$, $p < 0.0001$; Striatum 12mo HTT1a: $t = 11.40$, $p < 0.0001$; Striatum 12mo fl-HTT: $t = 12.73$, $p < 0.0001$. *Note:* FOV-level tests are more sensitive than per-slide tests but violate independence assumptions. **(C-D)** Atlas coordinate trends. Box plots showing expression across approximate anterior-posterior coordinates (atlas sections spaced at 100 μm intervals). Q111 HTT1a: cortex 13.43 ± 14.94 (n=697), striatum 19.95 ± 19.20 (n=637). WT HTT1a: cortex 7.58 ± 4.73 (n=134), striatum 4.03 ± 2.78 (n=149). **(E-F)** Per-slide breakdown showing mean ± SEM for each slide (all FOVs concatenated per slide). **Power note:** With n = 4-6 mice per age group, per-slide analyses may be underpowered (see main text).

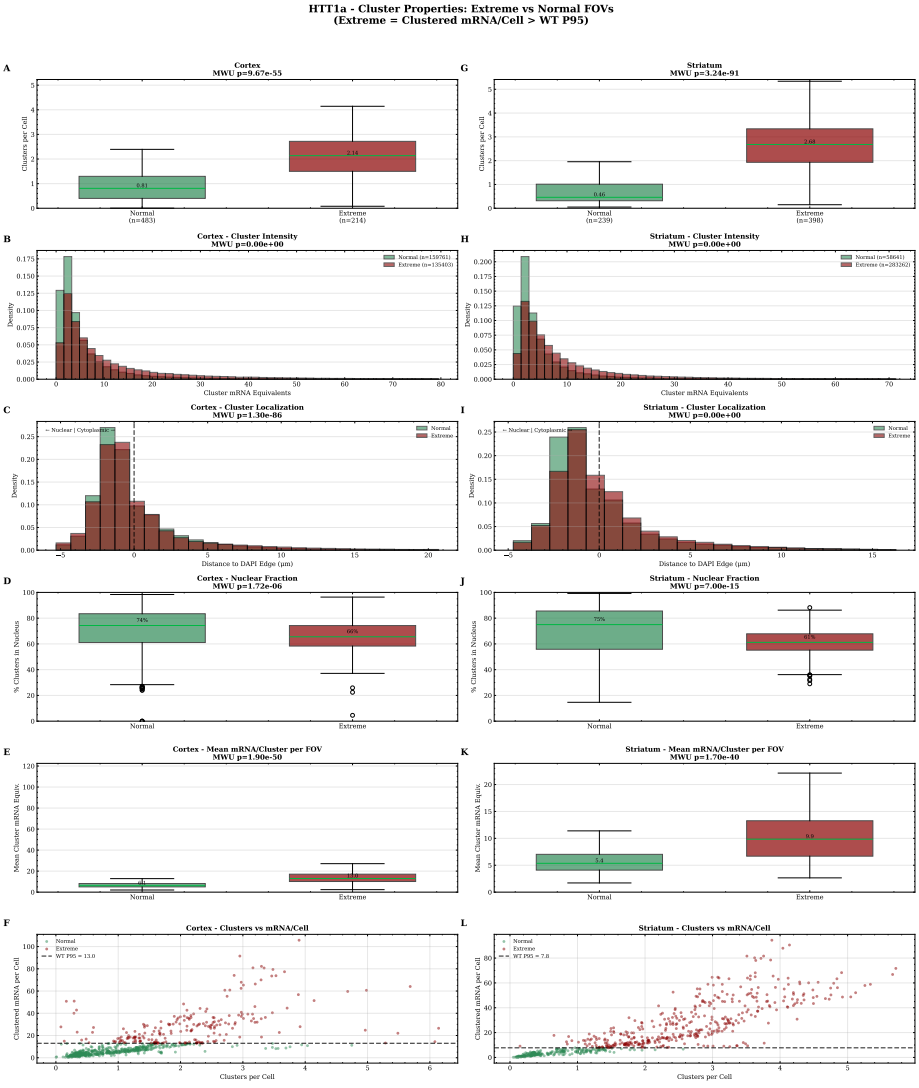

HTT1a - Cluster Properties: Extreme vs Normal FOVs
(Extreme = Clustered mRNA/Cell > WT P95)
A
Cortex
MWU p=9.67e-55
Clusters per Cell
0.81
2.14
Normal
(n=483)
Extreme
(n=214)
G
Striatum
MWU p=3.24e-91
Clusters per Cell
0.45
2.08
Normal
(n=239)
Extreme
(n=398)
B
Cortex - Cluster Intensity
MWU p=0.00e+00
Normal (n=159761)
Extreme (n=135403)
Density
Cluster mRNA Equivalents
H
Striatum - Cluster Intensity
MWU p=0.00e+00
Normal (n=586411)
Extreme (n=283262)
Density
Cluster mRNA Equivalents
C
Cortex - Cluster Localization
MWU p=1.30e-86
← Nuclear | Cytoplasmic →
Normal
Extreme
Density
Distance to DAPI Edge (µm)
I
Striatum - Cluster Localization
MWU p=0.00e+00
← Nuclear | Cytoplasmic →
Normal
Extreme
Density
Distance to DAPI Edge (µm)
D
Cortex - Nuclear Fraction
MWU p=1.72e-06
% Clusters in Nucleus
74%
66%
Normal
Extreme
J
Striatum - Nuclear Fraction
MWU p=7.00e-15
% Clusters in Nucleus
75%
61%
Normal
Extreme
E
Cortex - Mean mRNA/Cluster per FOV
MWU p=1.90e-50
Mean Cluster mRNA Equiv.
Normal
Extreme
K
Striatum - Mean mRNA/Cluster per FOV
MWU p=1.70e-40
Mean Cluster mRNA Equiv.
5.1
9.0
Normal
Extreme
F
Cortex - Clusters vs mRNA/Cell
Normal
Extreme
WT P95 = 13.0
Clustered mRNA per Cell
Clusters per Cell
L
Striatum - Clusters vs mRNA/Cell
Normal
Extreme
WT P95 = 7.8
Clustered mRNA per Cell
Clusters per Cell

Figure S20: **Cluster properties for HTT1a in extreme vs normal FOVs.** Extreme FOVs defined as exceeding WT P95 threshold (Q111 tissue only; WT data only used to define threshold). **Quality control:** FOVs with <40 nuclei were excluded to ensure reliable per-nucleus normalization, removing 3,253 clusters (0.5%) relative to the unfiltered dataset in fig. S15. **Dataset:** Cortex: WT P95 threshold 12.87 mRNA/cell, Extreme n=217, Normal n=480. Striatum: threshold 7.77 mRNA/cell, Extreme n=399, Normal n=238. Total clusters after filtering: 637,067. Color scheme: Sea Green = Normal, Dark Red = Extreme. **(A, G) Clusters per cell.** Box plots comparing cluster abundance; all extreme-versus-normal comparisons in this figure use the Mann-Whitney U test. Cortex: Extreme median 2.14 (IQR 1.24), Normal 0.81 (IQR 0.89), fold change 2.6×, Mann-Whitney $p = 9.67 \times 10^{-55}$. Striatum: Extreme 2.68 (IQR 1.39), Normal 0.46 (IQR 0.69), 5.9×, $p = 3.24 \times 10^{-91}$. **(B, H) Cluster mRNA equivalents.** Histograms of individual cluster sizes. Cortex: Extreme n=135,403 clusters, median 6.2 mRNA equiv.; Normal n=159,761, median 3.3; $p < 10^{-300}$. Striatum: Extreme n=283,262, median 5.8; Normal n=58,641, median 3.0; $p < 10^{-300}$. **(C, I) Nuclear localization.** Distribution of signed distance to DAPI edge (negative = nuclear). Cortex: Extreme median −0.91 μm, 65.8% nuclear; Normal −1.06 μm, 68.1% nuclear; $p = 1.30 \times 10^{-86}$. Striatum: Extreme −0.68 μm, 61.6%; Normal −1.05 μm, 67.7%; $p < 10^{-300}$. **(D, J) Fraction nuclear per FOV.** Cortex: Extreme median 65.5%, Normal 74.2%, $p = 1.72 \times 10^{-6}$. Striatum: Extreme 61.2%, Normal 75.1%, $p = 7.00 \times 10^{-15}$. **(E, K) Mean cluster mRNA.** Cortex: Extreme 12.9, Normal 6.1, $p = 1.90 \times 10^{-50}$. Striatum: Extreme 9.8, Normal 5.4, $p = 1.70 \times 10^{-40}$. **(F, L)** Scatter plots: clusters/cell vs mRNA/cell with WT P95 threshold (dashed line). **Cluster detection:** DBSCAN (eps=0.75 μm, min_samples=3), intensity > 2.5× peak.

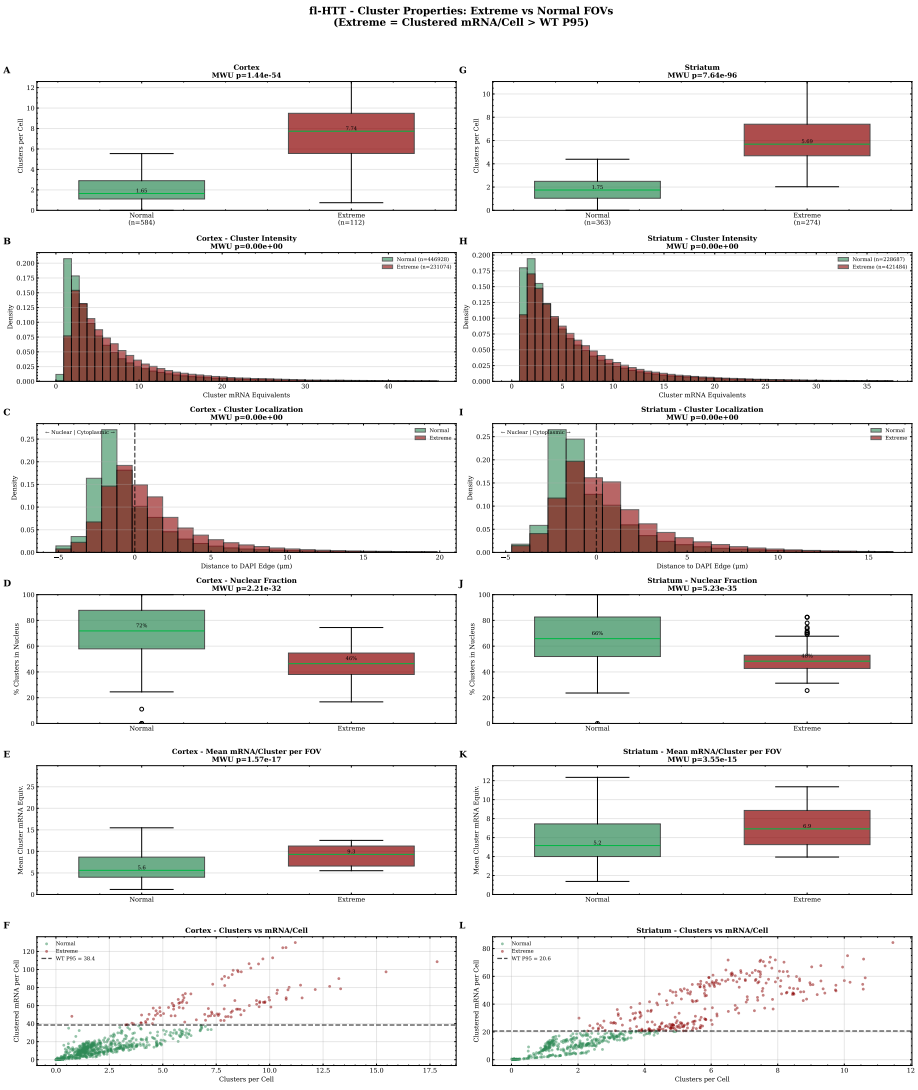

fl-HTT - Cluster Properties: Extreme vs Normal FOVs
(Extreme = Clustered mRNA/Cell > WT P95)
A
Cortex
MWU p=1.44e-54
Clusters per Cell
1.69
7.74
Normal
(n=584)
Extreme
(n=112)
G
Striatum
MWU p=7.64e-96
Clusters per Cell
1.75
5.69
Normal
(n=363)
Extreme
(n=274)
B
Cortex - Cluster Intensity
MWU p=0.00e+00
Normal (n=446928)
Extreme (n=231074)
Density
Cluster mRNA Equivalents
H
Striatum - Cluster Intensity
MWU p=0.00e+00
Normal (n=220687)
Extreme (n=421484)
Density
Cluster mRNA Equivalents
C
Cortex - Cluster Localization
MWU p=0.00e+00
Nuclear | Cytoplasm
Normal
Extreme
Density
Distance to DAPI Edge (µm)
I
Striatum - Cluster Localization
MWU p=0.00e+00
Nuclear | Cytoplasm
Normal
Extreme
Density
Distance to DAPI Edge (µm)
D
Cortex - Nuclear Fraction
MWU p=2.21e-32
% Clusters in Nucleus
72%
46%
Normal
Extreme
J
Striatum - Nuclear Fraction
MWU p=5.23e-35
% Clusters in Nucleus
66%
47%
Normal
Extreme
E
Cortex - Mean mRNA/Cluster per FOV
MWU p=1.57e-17
Mean Cluster mRNA Equiv.
5.8
9.2
Normal
Extreme
K
Striatum - Mean mRNA/Cluster per FOV
MWU p=3.55e-15
Mean Cluster mRNA Equiv.
5.2
6.9
Normal
Extreme
F
Cortex - Clusters vs mRNA/Cell
Normal
Extreme
WT P95 = 38.4
Clustered mRNA per Cell
Clusters per Cell
L
Striatum - Clusters vs mRNA/Cell
Normal
Extreme
WT P95 = 20.6
Clustered mRNA per Cell
Clusters per Cell

Figure S21: **Cluster properties for fl-HTT in extreme vs normal FOVs. Quality control:** FOVs with <40 nuclei were excluded to ensure reliable per-nucleus normalization, removing 9,735 clusters (0.7%) relative to the unfiltered dataset in fig. S16. **Dataset:** Cortex: WT P95 threshold 38.00 mRNA/cell, Extreme n=112, Normal n=585. Striatum: threshold 20.41 mRNA/cell, Extreme n=278, Normal n=359. Total clusters after filtering: 1,328,173. **(A, G) Clusters per cell.** All extreme-versus-normal comparisons in this figure use the Mann-Whitney U test. Cortex: Extreme median 7.67, Normal 1.64, 4.7×, $p = 1.44 \times 10^{-54}$. Striatum: Extreme 5.69, Normal 1.76, 3.2×, $p = 7.64 \times 10^{-96}$. **(B, H) Cluster mRNA equivalents.** Cortex: Extreme n=231,074 clusters, median 5.4; Normal n=446,928, median 3.8. Striatum: Extreme n=421,484, median 4.7; Normal n=228,687, median 3.9. **(C, I) Nuclear localization (notably stronger shift).** Cortex: Extreme median +0.34 μm (cytoplasmic), 45.4% nuclear; Normal -1.12 μm, 67.8% nuclear; $p < 10^{-300}$. Striatum: Extreme +0.12 μm, 48.7%; Normal -1.08 μm, 68.0%. **(D, J) Fraction nuclear per FOV.** Cortex: Extreme 46.4%, Normal 71.8%, $p = 2.21 \times 10^{-32}$ (25.4 pp difference). Striatum: Extreme 48.5%, Normal 66.0%, $p = 5.23 \times 10^{-35}$. **(E, K) Mean cluster mRNA.** Cortex: Extreme 9.5, Normal 5.6, $p = 1.57 \times 10^{-17}$. Striatum: Extreme 6.7, Normal 5.1. **(F, L)** Scatter plots: clusters/cell vs mRNA/cell with WT P95 threshold (dashed line).

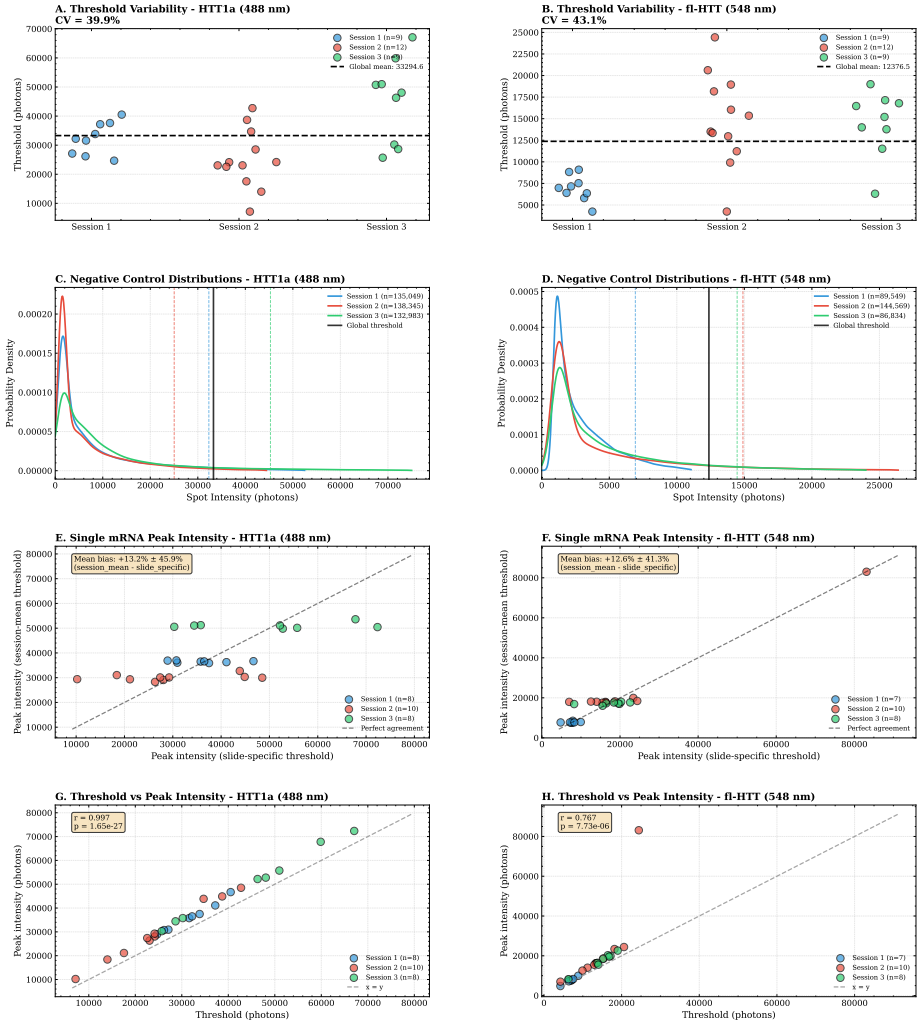


Figure S22: **Importance of per-slide negative control calibration.** Analysis across 3 imaging sessions, 30 slides with negative control. **Threshold variability:** HTT1a (488 nm): global threshold 33,295 ± 13,301 photons (CV = 39.9%, as in panel A); Session 1: 32,143 ± 5,005 (n=9), Session 2: 24,961 ± 10,002 (n=12), Session 3: 45,352 ± 15,045 (n=9). fl-HTT (548 nm): 12,377 ± 5,337 photons (CV = 43.1%). **Row 1 (A-B):** Per-slide thresholds by session. Each point = one slide's 95th percentile of negative control. Dashed line = global mean. **Row 2 (C-D):** KDE of negative control spot intensities by session. **Row 3 (E-F):** Single mRNA peak intensity: slide-specific vs pooled threshold. Mean difference (pooled − slide-specific): HTT1a +13.2% ± 45.9%; fl-HTT +12.6% ± 41.3%. Session 2 shows largest difference (+23.1% for HTT1a). **Row 4 (G-H):** Threshold vs peak intensity correlation showing relationship between background and signal levels.

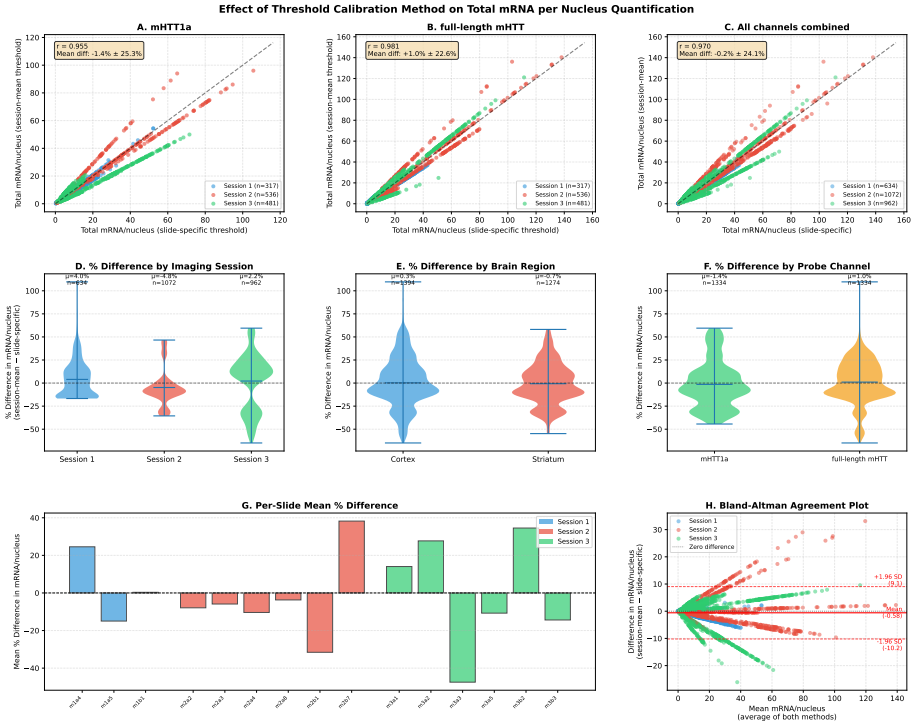
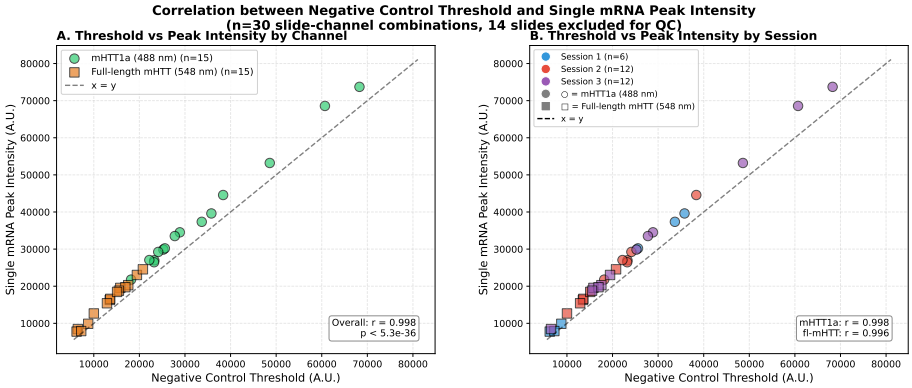


Figure S23: **Effect of threshold calibration method on total mRNA quantification.** Comparison of slide-specific (95th percentile per slide) vs pooled (average across slides within imaging batch) thresholds. **Dataset:** 2,668 FOVs (Session 1: n=634, Session 2: n=1,072, Session 3: n=962); Brain regions: Cortex n=1,394, Striatum n=1,274; Channels: HTT1a n=1,334, full-length n=1,334. Slides with poor tissue integrity were excluded. **Agreement:** Pearson $r = 0.9667$ ($p < 10^{-100}$), indicating near-perfect linear agreement; mean % difference 0% ± 25%; median −2.55% (IQR 30.08%). Paired comparison (pooled − slide-specific) across 2,668 FOVs: mean difference −0.65 mRNA/nucleus, $t = -6.39$, $p = 1.9 \times 10^{-10}$ (descriptive; FOVs within a slide are not independent), paired effect size $d_z = 0.12$ (negligible). **Bland-Altman:** Mean difference −0.647 mRNA/nucleus; 95% limits of agreement [−10.89, +9.59] mRNA/nucleus. **Individual variability:** 69.1% of FOVs differ >10%; 35.9% differ >20%; 5.2% differ >50%. Maximum individual difference: 98.2% (range −65.1% to +98.2%). 5th-95th percentile range: −33.9% to +45.3%. **Per-session breakdown:** Session 1: +4% ± 19%; Session 2: −5% ± 20%; Session 3: +2% ± 31%. **Per-slide variability:** 11/15 slides (73.3%) show >10% mean bias; 6/15 (40.0%) show >20% mean bias; max per-slide bias 48.2% (slide m3a3). **Row 1 (A-C):** Scatter plots comparing slide-specific (x) vs pooled (y) mRNA quantification by channel. Dashed line = perfect agreement. **Row 2 (D-F):** Violin plots of % differences by session, region, and channel. **Row 3 (G-H):** Per-slide mean difference (bar plot) and Bland-Altman plot (agreement analysis).



4

Figure S24: **Correlation between threshold and peak intensity.** Technical validation showing relationship between negative control thresholds (95th percentile of DapB intensities) and single-molecule peak intensities (KDE mode of experimental spot intensities) across slides. These metrics are independently derived from different probe populations (negative control vs experimental), providing internal consistency check.

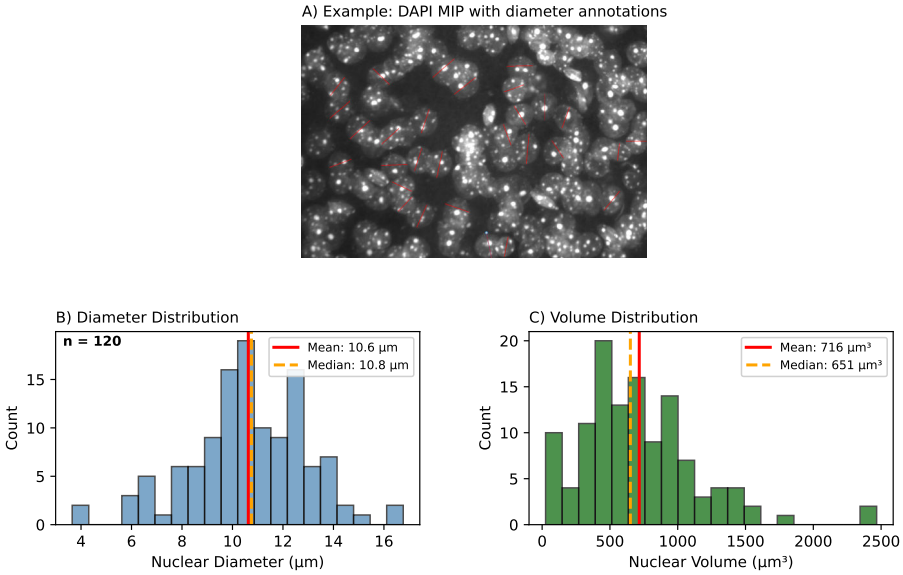


Figure S25: **Nuclear diameter calibration for per-nucleus mRNA quantification.** Manual measurement of nuclear diameters from DAPI-stained mouse brain tissue to establish mean nuclear volume for cell count estimation. **(A)** Representative maximum intensity projection (MIP) of DAPI-stained tissue with manual diameter annotations (red lines). Nuclei were selected to span cortical and striatal regions across multiple FOVs. **(B)** Distribution of measured nuclear diameters (n = 120 nuclei). Mean ± SEM = 10.6 ± 0.2 μm (SD = 2.3 μm); median = 10.8 μm. Range spans 3.6-16.8 μm, reflecting natural variation in nuclear size across cell types and tissue regions. **(C)** Derived nuclear volume distribution assuming spherical geometry ($V = \frac{4}{3}\pi r^3$). Mean ± SEM = 716 ± 39 μm^3 (SD = 432 μm^3); median = 651 μm^3. The mean value (716 μm^3) is used throughout this study for converting total DAPI volume to estimated nuclear counts. *Rationale:* The spherical approximation, while simplifying actual ellipsoidal nuclear morphology, provides consistent estimates across tissue regions. Deviations from sphericity average out across the many nuclei per FOV (typically 50-200), and the resulting per-nucleus mRNA values show strong correlation with direct nuclear counts (Pearson $r = 0.94$).

SUPPLEMENTARY NOTE 1: PER-SLIDE VERSUS POOLED NEGATIVE CONTROL CALIBRATION

Including a dedicated negative control section on every experimental slide increases reagent costs and uses tissue sections that could otherwise be used for experimental imaging. A practical alternative is to image negative controls on only a subset of slides and apply a pooled threshold to all slides. Here we evaluate the trade-offs of this approach.

In our experimental design, each slide contains tissue sections from a single animal, with the negative control (DapB probe) applied to a separate section on the same slide as the experimental probes. Imaging proceeds slide-by-slide, with all fields of view from one slide acquired before moving to the next. This design means that within-slide variation reflects local factors such as tissue properties and staining uniformity, while between-slide variation could reflect either technical factors (imaging drift, illumination changes) or biological differences between animals.

We compared per-slide thresholds (95th percentile of DapB spot intensities) against pooled thresholds for 30 slides spanning 3 imaging sessions on separate days. Between-session variation was substantial: Session 3 thresholds were ~1.8× higher than Session 2 for the green channel (fig. S22). This magnitude of difference clearly reflects technical variation and demonstrates that per-session calibration is essential. Within-session variation was also considerable (CV ~15-33%), but we cannot definitively determine whether this reflects technical drift during the session or biological animal-to-animal differences in tissue autofluorescence. We lack ground truth to distinguish these sources. Figure S14 (panels J-L) shows per-animal threshold distributions. The absence of significant regional differences within slides (panels A-C, paired t-test $p = 0.184$) and lack of age effects (panels D-F) suggests the threshold variation occurs at the slide level rather than reflecting systematic biological gradients.

The negative control threshold directly affects the single-molecule peak intensity estimate: after applying the threshold, only spots above this cutoff contribute to the intensity distribution, and the mode of this distribution defines the single-molecule reference intensity. As shown in fig. S24 (panels A and B), there is a positive linear correlation between threshold and peak intensity across slides. This relationship is expected–a higher threshold excludes more dim spots, shifting the intensity distribution toward brighter values. When using pooled thresholds instead of per-slide values, individual slides show mean differences of $+13.2\% \pm 45.9\%$ in peak intensity for mHTT1a and $+12.6\% \pm 41.3\%$

for fl-mHTT (fig. S22, rows E-F).
Figure S23 (panels A-C) directly compares total mRNA per nucleus calculated using slide-specific versus pooled thresholds across 2,668 FOVs. The scatter plots show a linear relationship ($r = 0.967$) with negligible mean difference (−0.07%), indicating that for population-level comparisons, the two calibration methods yield similar results. However, individual FOV-level variability is substantial (36% differ by >20%), and Bland-Altman analysis (panel H) shows 95% limits of agreement spanning ±10 mRNA/nucleus. We cannot prove that per-slide calibration is more accurate than session-pooled calibration. If the within-session threshold variation is primarily biological, then per-slide calibration might over-correct by attributing biological variation to technical noise. Conversely, if the variation is primarily technical, per-slide calibration appropriately accounts for slide-to-slide drift. For the present study, we used per-slide calibration as a conservative approach: per-session calibration is clearly required given the 1.8× between-session differences, and per-slide calibration cannot make results worse if the variation is technical. However, for applications where absolute quantification matters less than relative comparisons within a single session, pooled calibration may be adequate and offers cost savings by reducing the number of negative control sections required.

SUPPLEMENTARY METHODS: MODEL ARCHITECTURE AND TRAINING

The identification of mRNA clusters in the 3D microscopy images was performed using a deep learning approach, specifically employing a residual 3D U-Net architecture based on an existing, publicly available implementation [47].
The selected model, *ResidualUNet3D*, extends the classical 3D U-Net by integrating residual connections within its convolutional blocks, enabling deeper architectures and improved convergence. The network architecture is characterized by:

- An encoder-decoder structure with skip connections to preserve spatial context.
- Residual blocks consisting of Group Normalization, Convolution, and ReLU activations arranged in the order: GroupNorm → Conv3D → ReLU.
- A sequence of four hierarchical layers with increasing feature channels (32, 64, 128, 256) to capture multi-scale spatial features.
- A sigmoid activation applied at the output layer to produce voxel-wise probability maps of mRNA clusters.

Model training was configured as follows:

- **Loss Function**: Binary cross-entropy loss with logits (*BCEWithLogitsLoss*).
- **Optimizer**: Adam optimizer with a learning rate of 2×10^{-4} and weight decay of 10^{-5}.

- **Learning Rate Scheduler**: A plateau-based scheduler (*ReduceLROnPlateau*) was employed, reducing the learning rate by a factor of 0.2 after no improvement over eight validation cycles.
- **Training Protocol**: Training was performed for a maximum of 800 epochs (15,000 iterations), with validation every 500 iterations and TensorBoard logging every 30 iterations.

Data Preprocessing and Augmentation. The input training data consisted of volumetric patches (8 × 256 × 256 voxels), which were normalized (standardization) and augmented to enhance generalizability. Augmentation included:

- Random flipping and 90-degree rotations.
- Random rotations (±30°), specifically in the ZY-plane, to make the model robust for different spacing between z-slices.
- Elastic deformation for realistic shape variability.

Inference and Post-processing. At inference, the trained residual U-Net produced probability maps highlighting potential mRNA clusters. The predicted clusters were thresholded (set at a probability of 0.5) to yield binary masks.

SUPPLEMENTARY NOTE 2: MEAN NUCLEAR VOLUME ESTIMATION

Converting total mRNA expression to per-nucleus values requires estimating the number of nuclei per field of view. Direct counting of individual nuclei via instance segmentation is challenging in brain tissue due to the densely packed cellular architecture: overlapping and touching nuclei (particularly prevalent in striatum and deep cortical layers) cause standard segmentation algorithms (watershed, deep learning-based instance segmentation) to either merge adjacent nuclei into single objects or fragment single nuclei into multiple objects. Rather than attempting unreliable direct counting, we estimate nuclear number by dividing the total DAPI-stained volume by a mean nuclear volume derived from manual diameter measurements (fig. S25).

We manually measured nuclear diameters from DAPI maximum intensity projections, selecting well-separated nuclei across cortical and striatal regions (n = 120 nuclei). The measured diameter distribution showed mean ± SEM of 10.6 ± 0.2 μm (SD = 2.3 μm; median = 10.8 μm; range 3.6-16.8 μm; fig. S25B). Assuming spherical geometry ($V = \frac{4}{3}\pi r^3$), this yields a mean nuclear volume of 716 ± 39 μm^3 (SD = 432 μm^3; median = 651 μm^3; fig. S25C). We use the mean value (716 μm^3) throughout this study for converting total DAPI volume to estimated nuclear counts.

This nuclear diameter is consistent with published measurements for mouse striatal neurons. Medium spiny neurons (MSNs), which constitute >95% of striatal neurons, have nuclear diameters of 10-11 μm in adult mice [48]. We assume spherical nuclear geometry for volume estimation. Other cell types (interneurons, glia) may have different

nuclear sizes, making this volume-based approach less accurate than individual nuclear segmentation. However, since we apply the same mean nuclear volume across all conditions, relative comparisons between genotypes and brain regions remain valid.

Table S6: **RNAscope reagent list.** Complete list of reagents used for RNAscope™ experiments, including reference numbers and storage conditions.

Reagent	Ref./Cat. No.	Qty	Comments
Stored at 4° C			
RNAscope H_2O_2 and Protease Reagents	322381	2	3 mL squeeze-dropper bottles
Hydrogen Peroxide	322335	2	-
Protease III	322337	2	For prefixed tissues
Protease IV	322336	2	For fresh frozen tissues
RNAscope Probes			
3-plex Positive Control Probe - Mm	320881	1	C1: ~29 μL/slice
3-plex Negative Control Probe	320871	1	-
Mm-Htt-intron1-O2 (HTT1a)	575581	1	Mouse HTT intron 1
Mm-Htt-No-XHs-C3 (fl-HTT)	473001-C3	3	Full-length mouse HTT
Mm-Pp1r1b-C2 (DARPP-32)	405901-C2	1	Striatal marker
Hs-HTT-intron1-No-XMm-O1-C2	561441-C2	3	Human HTT intron 1
HS-HTT-no-X-MmOa-ver2	420231	3	Full-length human HTT
RNAscope V2 Fluorophores			
Alexa Fluor 488 tyramide reagent	B40953	2	-
Alexa Fluor 546 tyramide reagent	B40955	2	-
Alexa Fluor 647 tyramide reagent	B40958	2	-
RNAscope Multiplex TSA buffer	322809	1	-
RNAscope Multiplex Fluorescent Detection v2			
Detection Reagents v2 (Box)	323110	4	3 mL squeeze-dropper bottles
AMP 1	323101	1	-
AMP 2	323102	1	-
AMP 3	323103	1	-
HRP C1	323104	1	-
HRP C2	323105	1	-
HRP C3	323106	1	-
HRP Blocker	323107	3	-
DAPI	323108	1	-
Stored at Room Temperature			
RNAscope Wash Buffer (Box)	310091	4	4 bottles per box
RNAscope Target Retrieval (Box)	322000	8	4 bottles per box
ProLong Glass Antifade Mountant	P36984	2	-
DMSO	J66650.AD	-	-
Ethanol	BP2818-4	-	-
SSC Buffer 20×	S6639-1L	-	-
10% Neutral Buffered Formalin	-	-	-
Other Materials			
High precision coverslips #1.5	CG15KH1	1	-
Hydrophobic barrier pen	H-4000	1	-

SUPPLEMENTARY NOTE 3: RNASCOPE PROTOCOL FOR PREFIXED MOUSE BRAIN TISSUES

The following protocol was used for RNAscope™ staining of mouse brain tissues that had been prefixed for more than 48 hours in PFA/NBF.

SECTION PREPARATION

1. Set the oven to 60°C.
2. Prepare a petri dish with deionized water (DI water) and thin brushes for transferring brain slices.
3. Using a thin brush, move the brain slice from the plate into the petri dish. Gently unfold the brain slice as much as possible.
4. Pipette 100 μL of DI water onto the slide for mounting. Treat the slide as three sections: top, middle, and bottom, large enough to fit 3 brain samples.
5. Carefully transfer the brain slice using the thin brush to move it into the water droplet on the slide.
6. Continue to unfold the brain slice while gently wiping excess water with a Kimwipe until the sample is completely flat. Avoid directly touching the sample with Kimwipe.
7. Using the thin brush, orient the brain slices in the same manner with image processing purposes in mind.
8. Bake the slides at 60°C for 30 min in the humidity tray (maximum 20 slides) with the tray lid off and no wet paper towels. After incubation, adjust the temperature to 40°C.
9. During this incubation, prepare 1× wash buffer by mixing 60 mL of 50× RNAscope wash buffer (Ref. No. 320058) with 2.94 L milli-Q water.

FIXATION AND DEHYDRATION

1. Place prefixed tissues into the slide rack and immerse slides in 10% Neutral Buffer Formalin (NBF). Place the container on ice for 15 min.
2. Prepare ethanol standards:

Percentage	EtOH (mL)	DI water (mL)
50%	50	50
70%	70	30
100%	100	0

3. Immerse slides in 50% EtOH for 5 min at room temperature (RT).

4. Immerse slides in 70% EtOH for 5 min at RT.

5. Immerse slides in 100% EtOH for 5 min at RT. Repeat with fresh 100% EtOH.

6. Remove excess liquid by gently flicking slides and wiping around the sample. Allow to dry for 5 min at RT.

PRETREATMENT

1. Add 5 drops of hydrogen peroxide (Ref. No. 322335) to cover each sample and incubate at RT for 10 min.

2. Prepare 1× Target Retrieval Buffer by mixing 70 mL of 10× Target Retrieval Buffer (Ref. No. 322001) with 700 mL DI water in a 1 L glass beaker and boil on a hot plate.

3. Wash slides in DI water by moving the slide rack up and down 5 times. Repeat with fresh DI water.

TARGET RETRIEVAL

1. Submerge slides in boiling liquid for 5 min, ensuring the temperature is >99°C and <105°C.

2. Immediately transfer hot slide rack into RT DI water.

3. Wash slides in DI water (5 times). Repeat with fresh DI water.

4. Wash slides in 100% EtOH (5 times).

5. Remove excess liquid and allow to dry for 5 min at RT.

6. Draw 1-2 circles with hydrophobic barrier pen (Cat. No. H-4000) around each sample without touching it. Allow to dry for 5 min.

7. Insert slides into humidity tray.

8. Add 1 drop of Protease III to cover each section.

9. Incubate at 40°C for 30 min.

10. During incubation, dilute probes to RT before use:

# Experiments	C1 (μL)	C2 (μL)	C3 (μL)
6	240	5	5
10	480	10	10
20	960	20	20

11. Wash slides in DI water (5 times). Repeat with fresh DI water.

PROBE HYBRIDIZATION

1. Remove excess liquid and insert slides into humidity tray.
2. For negative control probe (Ref. No. 320871) and positive control probe (Ref. No. 320881), add 1 drop to cover corresponding samples. For experimental probe mixture, pipette 30 μL to cover samples.
3. Incubate in humidity tray for 2 hours at 40°C.
4. Submerge in wash buffer for 2 min at RT, agitating slightly. Repeat with fresh wash buffer.
5. Transfer slides to slide rack and submerge in 5× SSC (Ref. No. S6639-1L) overnight. Prepare by adding 25 mL of 20× SSC to 75 mL DI water.

SIGNAL AMPLIFICATION (AMP 1-3)

1. Line humidity tray with paper towels, fill with DI water, pour out excess, and place into oven at 40°C.
2. Transfer slides to humidity tray.
3. Wash off 5× SSC by submerging in wash buffer for 2 min at RT. Repeat.
4. Remove excess liquid.
5. Add 1 drop of Amp 1 (Ref. No. 323101) to cover each sample and incubate at 40°C for 30 min.
6. Wash in wash buffer for 2 min. Repeat.
7. Add 1 drop of Amp 2 (Ref. No. 323102) and incubate at 40°C for 30 min.
8. Wash in wash buffer for 2 min. Repeat.
9. Add 1 drop of Amp 3 (Ref. No. 323103) and incubate at 40°C for 15 min.
10. Wash in wash buffer for 2 min. Repeat.

HRP-C1 SIGNAL DEVELOPMENT

1. Add 1 drop of HRP-C1 (Ref. No. 323104) to cover each sample.
2. Incubate at 40°C for 15 min.
3. During incubation, prepare fluorophores: resuspend Alexa Fluor reagents (dry pellet) in 150 μL DMSO (Ref. No. J66650.AD), then dilute 1:100 in TSA buffer (Ref. No. 322809):

# Slides	Alexa Fluor (μL)	TSA Buffer (mL)
6	10	0.99
10	20	1.98
20	40	3.96

4. Wash in wash buffer for 2 min. Repeat.
5. Add 30 μL of corresponding diluted Alexa dye to cover each sample.
6. Incubate at 40°C for 30 min.
7. Wash in wash buffer for 2 min. Repeat.
8. Add 1 drop of v2 HRP blocker (Ref. No. 323107) to cover each sample.
9. Incubate at 40°C for 15 min.
10. Wash in wash buffer for 2 min. Repeat.

HRP-C2 AND HRP-C3 SIGNAL DEVELOPMENT

Repeat the HRP-C1 development steps for HRP-C2 (Ref. No. 323105) and HRP-C3 (Ref. No. 323106), using the corresponding Alexa dyes for each channel. For HRP-C3, retrieve ProLong Glass Antifade reagent (Ref. No. P36984) and thaw at RT for 1 hour before use to prevent bubbles.

MOUNTING

1. Add 1 drop of DAPI (Ref. No. 323108) to cover each sample.
2. Incubate for 10 min at RT.
3. Wash slides in 1× PBS (5 times). Repeat with fresh PBS.
4. Remove excess liquid and allow samples to dry for 5 min at RT.
5. Set pipette to 60 μL and slowly draw up ProLong Glass Antifade reagent (Cat. No. P36984). Slowly add reagent on each sample, avoiding bubbles.
6. Carefully place a #1.5 coverslip (Ref. No. CG15KH1) on each slide while avoiding bubbles.
7. Allow mounting reagent to harden overnight in the dark at RT, then seal with nail polish.
8. Store at 4°C until imaging. Samples are most stable for 2 weeks.

SUPPLEMENTARY NOTE 4: RNASCOPE PROBE TARGET SEQUENCES

Custom RNAscope probes were designed by Advanced Cell Diagnostics (ACD Bio) for detection of mouse huntingtin (*Htt*) transcripts. Each probe consists of 20 ZZ pairs, with each ZZ pair covering approximately 40-50 nt, spanning roughly 1,000 nt total in the target region.

FL-HTT PROBE: MM-HTT-NO-XHS (CAT. NO. 473001)

This probe targets the 3' untranslated region (3' UTR) of the canonical full-length mouse *Htt* mRNA. It consists of 20 ZZ pairs targeting region 9833-10798 of NM_010414.2 (966 bp).

Target sequence:

>NM_010414.2:9833-10798 Mus musculus huntingtin (Htt), mRNA

CCTGGTATGTGGATCAGAAGTCCTAGCTCTTGCCAGATGGTTCTGAGCCCGCCTGCTC
CACTGGGCTGGAGAGCTCCCTCCCACATTTACCCAGTAGGCATACCTGCCACACCAGT
GTCTGGACACAAAATGAATGGTGTGTGGGGCTGGGAACTGGGGCTGCCAGGTGTCCA
GCACCATTTTCCTTTCTGTGTTTTCTTCTCAGGAGTTAAAATTTAATTATATCAGTAAAG
AGATTAATTTTAATGTAACTTTTCCTATGCCCGTGTAAAGTGTGTGACTTGGCAAGGCC
TGTGCTGCATGTGACAAAGTTTATGGAAGTGGAGGGGCCTTCTGGCCGCCACTCCCTC
TCCTGTAGCTACTCAGTCTAGTCGGGCAGGTCCCTCCTGTAGCCCTCCCAACACCCTG
TGGCACTTGCACTTCATACAGCTCCCTTTTCTTATGCATTCCATTAAGCCAGCACAGAG
AGAGGTGTTGGTATTGACTGCCTGTGTGAGAATCCTGCCTGTGGCCTAACTGAGGAAC
TGAAAAACTGACTTCCACTGTTAGAGTTATAAGGAGGCTTGCCCTGTGGCAGCTGCCCT
CCTCTCCCCTTCCCAGGCATGACTGTCAAGCTATCTCCTCCCTGGTGTTGATGCACTCT
CCTAGTCTCTCAGCCTGGGTAGAAACAGCATCTGCTGGACCCAAAGTGGCTATCCCAA
TAACCTCATCCCTGGTTGTGGCTGACCTGCACTGTAGCCTGCCCACACACCAGCTGAC
CATTGTGGATGCTGTCTGTCCCTTTGTATCTTCTGCATGGTTGGGACCTGAGAAGTGCT
GACCTGATTACCCCAAAGGTGTCTCTGAGCTATGGTTTGTTGGTTTGTCTCAGTTTCTC
ATAGTCAAGGGAAAGCTTGGTGTCCTAGCAACAGTTAAGAATGGACCCAGAGCCTCTTT
TGCCCCTTCCCATCTTGCCTTCTGTCAGCCC

HTT1A PROBE: MM-HTT-INTRON1-O2 (CAT. NO. 575581)

This probe targets the 5' region of intron 1 of mouse *Htt*, which is retained in the aberrantly spliced Htt1a transcript. This region contains the cryptic polyadenylation sites used in incomplete splicing of mutant huntingtin mRNA. The target sequence is retained in the Htt1a transcript but is absent from the canonical full-length Htt mRNA. The probe consists of 20 ZZ pairs targeting region 34919494-34920643 of NC_000071.7 (1,150 bp).

Target sequence:

>NC_000071.7:34919494-34920643 Mus musculus strain C57BL/6J chromosome 5, GRCm39

CCTGGCCTGCGTGCTGGGCATGGCCAACACTGTTCCCTGTCCAGAGGGTCGCGGTAC
CTCCCTGAGGCCAGGCTTTCCCGGCCCGGGCCCTCGTCTTGCGGGGTCTCTGGCCTC
CCTCAGAGGAGACAGAGCCGGGTCAGGCCAGCCAGGGACTCGCTGAGGGGCGTCACG
ACTCCAGTGCCTTCGCCGTTCCCAGTTTGCGAAGTTAGGGAACGAACTTGTTTCTCTCT
TCTGGAGAAACTGGGGCGGTGGCGCACATGACTGTTGTGAAGAGAACTTGGAGAGGCA
GAGATCTCTAGGGTTACCTCCTCATCAGGCCTAAGAGCTGGGAGTGCAGGACAGCGTG
AGAGATGTGCGGGTAGTGGATGACATAATGCTTTTAGGAGGTCTCGGCGGGAGTGCTG
AGGGCGGGGGAGTGTGAACGCATCCAATGGGATATTCTTTTTCCAAGTGACACTTGAA
GCAGCCTGTGACTCGAGGCACTTCGTACTCTCCTGGCGTTTCATTTAGTTTGTGGTGT
AGTGTAGTTAAACCAGGTTTTAAGCATAGCCAGAGAGGTGTGCTTCTGTGTGTCTGCAG
GCAGTTGGATGAGTTGTATTTGTCAAGTACATGGTGAGTTACTTAGGTGTGATTATTAA
TAAAAAACTATATGTGTGCATATATATGAAAGAGTCGACTTATACTTAACTGCCTATCGA

TTTTTTGTTCTATATAAAACGGATACATTGGTGGTGCTCAGTTTTCACCGGGGAATGAA
TTTTACTAGTGTTGCAGACAGGCTTGTTTTAGAACATAGGCCACTCTGACTCTGACTTT
GTGCCAGTAAAAGTTCCTGTTTAGTTCTTTGCTGACATCTTATAGATCTTTGGAAGCTA
GCTGCTTGTGACTGGAGAGAATATTGAAACAGAAGAGAGACCATGAGTCACAGTGCTC
TAAGAGAAAAGAGACGCTCAAAACATTTCCTGGAAATCCATGCTGAGTGTTGAGCCCTG
TGCTCTCTTGCAGCTCAGTCCTTTCTCTCAACTCTGGGCATTTTATTTCTAATCTGGATT
TGTATAATTAATAAGGAGAACTTTTGGGAACAACCTACTAAAGAATGTCATCATTAAAAC
TCACTTAGAAAATAAGTGTTCTGGTGATATCATTGAGC

BIBLIOGRAPHY

[1] Pieter van Velde et al. “High-throughput quantification of huntingtin mRNA expression and aggregation in mouse brain using automated RNAscope imaging.” In: *bioRxiv* (2026), pp. 2026–02.

[2] F Wang et al. “RNAscope: a novel in situ RNA analysis platform for formalin-fixed, paraffin-embedded tissues”. In: *The Journal of Molecular Diagnostics* 14 (2012), pp. 22–29.

[3] S Atout et al. “Evaluation of the suitability of RNAscope as a technique to measure gene expression in clinical diagnostics: A systematic review”. In: *Molecular Diagnosis & Therapy* 26 (2022), pp. 19–37.

[4] Advanced Cell Diagnostics. *RNAscope Frequently Asked Questions*. 2023. URL: https://acdbio.com/technical-support/solutions/faq.

[5] K Sathasivam et al. “Aberrant splicing of HTT generates the pathogenic exon 1 protein in Huntington disease”. In: *Proceedings of the National Academy of Sciences* 110 (2013), pp. 2366–2370.

[6] Andreas Neueder et al. “The pathogenic exon 1 HTT protein is produced by incomplete splicing in Huntington’s disease patients”. In: *Scientific Reports* 7.1 (2017), p. 1307.

[7] X Sun et al. “Nuclear retention of full-length HTT RNA is mediated by splicing factors MBNL1 and U2AF65”. In: *Scientific Reports* 5 (2015), p. 12521.

[8] A Hautke et al. “CAG-repeat RNA hairpin folding and recruitment to nuclear speckles with a pivotal role of ATP as a cosolute”. In: *Journal of the American Chemical Society* 145 (2023), pp. 9571–9583.

[9] K Yum, E T Wang, and A Kalsotra. “Myotonic Dystrophy: Disease Repeat Range, Penetrance, Age of Onset, and Relationship Between Repeat Size and Phenotypes”. In: *Current Opinion in Genetics & Development* 44 (2017), pp. 30–37.

[10] M DeJesus-Hernandez et al. “Expanded GGGGCC hexanucleotide repeat in noncoding region of C9ORF72 causes chromosome 9p-linked FTD and ALS”. In: *Neuron* 72 (2011), pp. 245–256.

[11] R M Bragg et al. “Motivational, proteostatic and transcriptional deficits precede synapse loss, gliosis and neurodegeneration in the B6.HttQ111/+ model of Huntington’s disease”. In: *Scientific Reports* 7 (2017), p. 41570.

[12] I Han et al. “Differential vulnerability of neurons in Huntington’s disease: the role of cell type-specific features”. In: *Journal of Neurochemistry* 113 (2010), pp. 1073–1091.

[13] J Belgrad, A Summers, C Landles, et al. “Blocking somatic repeat expansion and lowering huntingtin via RNA interference synergize to prevent Huntington’s disease pathogenesis in mice”. In: *bioRxiv* (2025), p. 2025.06.24.661398.

[14] Jelmer Cnossen et al. “Localization microscopy at doubled precision with patterned illumination”. In: *Nature Methods* 17.1 (2020), pp. 59–63.

[15] D W Scott. *Multivariate Density Estimation: Theory, Practice, and Visualization*. New York: John Wiley & Sons, 1992.

[16] Pauli Virtanen et al. “SciPy 1.0: Fundamental algorithms for scientific computing in Python”. In: *Nature Methods* 17 (2020), pp. 261–272. DOI: 10.1038/s41592-019-0686-2.

[17] E S Lein et al. “Genome-wide atlas of gene expression in the adult mouse brain”. In: *Nature* 445 (2007), pp. 168–176. URL: https://mouse.brain-map.org.

[18] M E Ehrlich. “Huntington’s disease and the striatal medium spiny neuron: cell-autonomous and non-cell-autonomous mechanisms of disease”. In: *Neurotherapeutics* 9 (2012), pp. 270–284.

[19] G Bergonzoni, J Döring, and M Biagioli. “D1R- and D2R-medium-sized spiny neurons diversity: insights into striatal vulnerability to Huntington’s disease mutation”. In: *Frontiers in Cellular Neuroscience* 15 (2021), p. 628010.

[20] P Langfelder et al. “Integrated genomics and proteomics define huntingtin CAG length-dependent networks in mice”. In: *Nature Neuroscience* 19 (2016), pp. 623–633.

[21] S Kwon. “Single-molecule fluorescence in situ hybridization: quantitative imaging of single RNA molecules”. In: *BMB Reports* 46.2 (2013), pp. 65–72.

[22] S Ly et al. “Mutant huntingtin messenger RNA forms neuronal nuclear clusters in rodent and human brains”. In: *Brain Communications* 4 (2022), fcac248.

[23] Sarah Allen et al. “mRNA nuclear clustering leads to a difference in mutant huntingtin mRNA and protein silencing by siRNAs in vivo”. In: *Nucleic Acid Therapeutics* 34.4 (2024), pp. 164–172.

[24] E Yhnell, S B Dunnett, and S P Brooks. “A longitudinal motor characterisation of the HdhQ111 mouse model of Huntington’s disease”. In: *Journal of Huntington’s Disease* 5 (2016), pp. 149–161.

[25] J C Grima et al. “Mutant huntingtin disrupts the nuclear pore complex”. In: *Neuron* 94 (2017), 93–107.e6.

[26] A Jain and R D Vale. “RNA phase transitions in repeat expansion disorders”. In: *Nature* 546 (2017), pp. 243–247.

[27] F Aktar et al. “The huntingtin inclusion is a dynamic phase-separated compartment”. In: *Life Science Alliance* 2 (2019), e201900489.

[28] A Cochard et al. “RNA at the surface of phase-separated condensates impacts their size and number”. In: *Biophysical Journal* 121 (2022), pp. 1675–1690.

[29] A J M Larsson et al. “Genomic encoding of transcriptional burst kinetics”. In: *Nature* 565 (2019), pp. 251–254.

[30] L Mangiarini et al. “Exon 1 of the HD gene with an expanded CAG repeat is sufficient to cause a progressive neurological phenotype in transgenic mice”. In: *Cell* 87 (1996), pp. 493–506.

[31] S J Tabrizi et al. “Targeting huntingtin expression in patients with Huntington’s disease”. In: *The New England Journal of Medicine* 380 (2019), pp. 2307–2316.

[32] M C Didiot et al. “Nuclear localization of huntingtin mRNA is specific to cells of neuronal origin”. In: *Cell Reports* 24 (2018), 2553–2560.e5.

[33] S Stallinga and B Rieger. “Accuracy of the Gaussian point spread function model in 2D localization microscopy”. In: *Optics Express* 18 (2010), pp. 24461–24476.

[34] Marijn Siemons et al. “High precision wavefront control in point spread function engineering for single emitter localization”. In: *Optics Express* 26.7 (2018), pp. 8397–8416.

[35] Pieter Van Velde et al. “ZIMFLUX: Single molecule localization microscopy with patterned illumination in 3D”. In: *Optics Express* 31.25 (2023), pp. 42701–42722.

[36] H Mao, P Bhola, P Bhola, et al. *Introduction to Spinning Disk Confocal Microscopy*. 2023. URL: https://zeiss-campus.magnet.fsu.edu/articles/spinningdisk/introduction.html.

[37] James C Mullikin et al. “Methods for CCD camera characterization”. In: *Image Acquisition and Scientific Imaging Systems*. Vol. 2173. Spie. 1994, pp. 73–84.

[38] Hamamatsu Photonics. *ORCA-Fusion BT Digital CMOS Camera Technical Note*. 2021.

[39] B Zhang et al. “Gaussian approximations of fluorescence microscope point-spread function models”. In: *Applied Optics* 46 (2007), pp. 1819–1829.

[40] Carlas S Smith et al. “Fast, single-molecule localization that achieves theoretically minimum uncertainty”. In: *Nature Methods* 7.5 (2010), pp. 373–375.

[41] A Ranganathan. *The Levenberg-Marquardt Algorithm*. Tutorial. 2004.

[42] A Paszke et al. “PyTorch: An imperative style, high-performance deep learning library”. In: *Advances in Neural Information Processing Systems*. Vol. 32. 2019, pp. 8026–8037.

[43] Fang Huang et al. “Simultaneous multiple-emitter fitting for single molecule super-resolution imaging”. In: *Biomedical Optics Express* 2.5 (2011), pp. 1377–1393.

[44] Carlas S Smith et al. “Probability-based particle detection that enables threshold-free and robust in vivo single-molecule tracking”. In: *Molecular Biology of the Cell* 26.22 (2015), pp. 4057–4062.

[45] Yoav Benjamini and Daniel Yekutieli. “The control of the false discovery rate in multiple testing under dependency”. In: *Annals of Statistics* (2001), pp. 1165–1188.

[46] M Arzt et al. “LABKIT: Labeling and Segmentation Toolkit for Big Image Data”. In: *Frontiers in Computer Science* 4 (2022), p. 777728.

[47] A Wolny et al. “Accurate and versatile 3D segmentation of plant tissues at cellular resolution”. In: *eLife* 9 (2020), e57613. URL: https://github.com/wolny/pytorch-3dunet.

[48] M Matamales, J Bertran-Gonzalez, L Salomon, et al. “Striatal medium-sized spiny neurons: identification by nuclear staining and study of neuronal subpopulations in BAC transgenic mice”. In: *PLOS ONE* 4 (2009), e4770.

5

CONCLUSION

This thesis developed quantitative fluorescence microscopy methods that extract molecular-level information from imaging data at three biological scales. The common thread is a deliberate transfer of principles from computational optics and single-molecule biophysics into increasingly complex biological contexts. A vectorial PSF model enables nanometer-precision localization in Chapter 2. Statistical detection theory, combined with neural-network-based background estimation, enables live-cell mRNA tracking through nuclear pore complexes in Chapter 3. PSF-informed calibration and likelihood-based detection underpin molecular-unit RNA quantification in dense brain tissue in Chapter 4. In each chapter, optical modeling and statistical inference convert raw fluorescence images into quantitative measurements that answer biological questions.

5.1. UNIFYING APPROACH

The three chapters are not three separate studies that happen to share some authors. They trace a progression in which the same core ideas are applied to different fields: PSF modeling, photon-statistics-based inference, and computational compensation for imaging imperfections. This progression is the thesis.

ZIMFLUX (Chapter 2) operates in a controlled regime. Isolated fluorophores on DNA-origami nanostructures produce well-defined signals against a relatively uniform background. The challenge is physical: refractive index mismatch distorts the PSF at depth, degrading axial precision [1, 2]. The solution combines a vectorial PSF model that accounts for aberrations, supercritical angle fluorescence, and depth-dependent changes [3] with three-dimensional structured illumination. Together, the accurate PSF model and the modulation pattern achieve a 1.5-fold improvement in axial precision. It self-calibrates the illumination pattern from the data.

The yeast mRNA imaging framework (Chapter 3) takes these principles into a far more demanding environment. Live cells scatter light. The cell wall introduces refractive index mismatch. Short exposure times and low laser power produce dim signals. The background is no longer uniform but structured: it varies across the cell, between nucleus

and cytoplasm, and from frame to frame. Despite these complications, the underlying detection problem is the same: fit a PSF model to candidate emitters and decide whether each detection is real. A generalized likelihood ratio test, grounded in photon statistics, makes that decision [4, 5].

The Huntington's disease pipeline (Chapter 4) extends this approach to tissue-scale imaging. Brain sections introduce depth-dependent signal attenuation, autofluorescence, and probe hybridization variability across slides. Here the PSF model serves a different purpose: it defines what a single mRNA molecule looks like. Bead-calibrated PSF parameters set the initial detection criteria. Empirical recalibration on RNAscope signals refines these for the extended sources produced by branched amplification. The result is a quantitative intensity-to-count calibration spanning single molecules to clusters containing dozens of transcripts.

A striking parallel connects the biological chapters. Both yeast cells and fixed brain tissue present inhomogeneous backgrounds that confound standard detection. In yeast, the background varies spatially due to out-of-focus fluorescence and cell-wall scattering. In brain tissue, it varies due to autofluorescence, tissue density, and depth-dependent optical effects. In both cases, the solution separates background estimation from signal detection. This separation is the methodological core that unifies Chapters 3 and 4. Without it, false positive rates in yeast reach 40%. Without it, intensity-based mRNA quantification in tissue conflates background with biological signal.

The evolution across chapters represents a transfer of measurement-science principles from optical engineering into biology. PSF modeling, developed for precise single-molecule localization, scales to contexts where the signal is weaker and the background is structured. It works even when the questions demand large-scale quantification rather than nanometer positioning. These approaches are transferable. The same detection theory works in a yeast cell and in a brain section. The same PSF calibration philosophy applies to isolated fluorophores and to extended RNAscope amplification trees. Quantitative microscopy is a field in its own right. The methods developed here show that its principles produce biological insight across very different systems.

5.2. IMPLICATIONS FOR QUANTITATIVE COMPUTATIONAL MICROSCOPY

A defining methodological choice in this thesis is to combine machine learning with classical statistical testing, applying the two in sequence. Neural networks excel at pattern recognition and learn complex, spatially varying structures from data. Statistical tests provide principled decision boundaries with controllable error rates. Neither alone is sufficient for the imaging conditions encountered here. The combination, using each where it is strongest, defines the computational approach of this thesis.

5.2.1. DECISION MAKING SUPPORTED BY STATISTICS

In Chapter 3, a convolutional neural network estimates the fluorescence background in each frame [6]. It was trained on synthetic data with realistic noise, non-uniform background, and simulated Gaussian emitters. The CNN estimates structured background that varies across the cell without requiring an analytical model of its spatial structure.

The detection decision, however, is not made by the network. A generalized likelihood ratio test makes that decision. It compares the likelihood of the data under two hypotheses: signal plus background versus background alone. The GLRT threshold is set by the desired significance level, not by the training data. This provides a statistical guarantee that a purely neural-network-based detector cannot offer.

Why does this matter? A detector that relies on a neural network for the entire pipeline ties its false positive rate to the training set. If the training data under-represent certain background conditions, the detector produces false positives in those regions. If the labeling is inconsistent, the decision boundary shifts in ways that are difficult to diagnose. By separating estimation from decision, the framework places the CNN where it adds value: capturing spatial patterns too complex for parametric models. The GLRT handles the step where statistical control matters most, at the boundary between signal and noise.

Chapter 4 applies the same philosophy. A residual 3D U-Net identifies and masks potential mRNA clusters but does not determine their molecular content. That determination rests on PSF-informed Gaussian fitting and photon-calibrated intensity measurement, where integrated photon counts are normalized to a per-slide single-molecule reference intensity derived from the modal detected signal. The neural network handles a task difficult to specify in a parametric model: recognizing irregularly shaped clusters in three-dimensional confocal data. The quantification derives from an optical model with known parameters. Molecular counts remain traceable to physical quantities rather than learned associations.

The GLRT deserves emphasis because it fixes the false-alarm rate at a chosen level and, subject to that limit, detects as many true emitters as the data allow [4]. In Chapter 3, the CNN-GLRT combination allows the test to be used without a parametric model for the background. In Chapter 4, GLRT-based spot detection on negative-control samples achieves a per-slide calibrated photon threshold. In both cases, the decision to accept or reject a candidate detection is grounded with statistics and not by an arbitrary threshold.

5.2.2. TRANSFERABILITY OF THE HYBRID APPROACH

Transferability is a key advantage of the statistical approach. A classifier requires retraining when imaging conditions change. The GLRT does not, because its decision boundary derives from the physics of photon detection rather than a specific training set. New conditions change signal and background levels but not the statistical framework. The detection approach is portable across experimental setups.

The broader principle is that machine learning is most valuable when it handles nuisance variation such as background structure, morphological diversity, and registration artifacts. Statistical testing is most valuable when a wrong decision has quantifiable consequences. A false mRNA detection inflates transport statistics. A false cluster assignment distorts molecular counts. Combining them assigns each method to the task it handles best. This is distinct from the trend of replacing classical image analysis with end-to-end deep learning. The goal is not automation for its own sake. It is quantitative measurement with defined error properties.

5.3. ENABLING IMPACT OF OPTICAL MODELING

Each chapter demonstrates that optical models are not merely tools for image formation. They are enabling methods that determine what biological questions can be answered. The PSF model in ZIMFLUX achieves resolution through elegant physics. The PSF model in the HTT pipeline achieves measurement through careful boundary definition. Both show that the value of a model lies not in its complexity but in how well its assumptions match the context. How explicitly its limits are defined matters just as much.

5.3.1. UNBIASED ESTIMATION USING VECTORIAL PSF MODELING

In ZIMFLUX (Chapter 2), the vectorial PSF model is not new [3], but it is the enabler. It accounts for refractive index mismatch, supercritical angle fluorescence, and optical aberrations simultaneously. This produces unbiased localizations at depth, which can be verified internally: the illumination pattern estimated from the data must be consistent with the PSF-based position estimates. If the two disagree, the model assumptions, such as the refractive index profile or aberration coefficients, need to be revised. In practice, the self-calibration converges when the model is adequate, providing a built-in consistency check. Existing modulation-enhanced methods such as ModLoc and ROSE-Z use simpler PSF descriptions that break down under depth-dependent aberrations [7, 8]. The vectorial model makes the method robust to sample-specific variations: coverslip tilt, refractive index profiles, imaging depth.

5.3.2. SIMPLE MODELS WITH CAREFULLY DEFINED PARAMETER BOUNDS

In the Huntington's disease pipeline (Chapter 4), the optical model is simpler: a three-dimensional Gaussian PSF calibrated from fluorescent beads. The challenge does not lie in the model itself but in defining the parameter bounds where it applies within the biological context. RNAscope signals do not arise from point-like emitters. They come from branched amplification trees distributed along the target mRNA. The effective signal source is extended, producing spots that exceed the diffraction-limited PSF. The breakpoint analysis identifies the sigma value beyond which the Gaussian model can no longer represent the shape of the image feature. This defines where single-molecule detection ends and cluster identification begins. This boundary emerges from the data as the point where the optical model breaks down.

The Gaussian PSF is an approximation at two levels. First, even for a true point source it underestimates the collected signal by omitting the tails of the diffraction pattern [9]. Second, RNAscope amplification trees are not point sources: probe pairs bind along the target mRNA, so the observed image is the PSF convolved with an extended source structure. Probe pairs can be spaced up to 1000 base pairs apart along the transcript, but the three-dimensional folding of the mRNA is unknown, so the spatial extent of the source cannot be predicted from the sequence alone. A more sophisticated description would convolve the PSF with a spatial model of the amplification tree, but such a model would vary between mRNA transcripts and probe sets, adding complexity that was not warranted for the current analysis. The breakpoint analysis addresses this by defining where the Gaussian approximation is still adequate and where it is not. Below the breakpoint, the spot size and intensity grow together as more probes bind, and the Gaussian fit remains a reasonable description. The systematic errors it introduces cancel in the

per-slide comparison, if the same error is made consistently. Above the breakpoint, the mismatch between the Gaussian and the true image feature becomes too large for the fit to be meaningful, which defines the transition to the cluster regime. There, the pipeline switches to integrated intensity, which scales linearly with cluster volume ($R^2 > 0.98$), confirming that probes access mRNA throughout the cluster regardless of size. The two regimes connect through the same per-slide normalization to single-molecule equivalents. The biological conclusions, including spatial heterogeneity across brain regions, striatal vulnerability, and an age-dependent trend that does not reach significance at our sample size, rest on this calibration. Without it, the pipeline produces images rather than measurements.

The conditions across slides are not the same. Background levels vary. Probe hybridization efficiency differs. Tissue quality changes from section to section. Yet the pipeline aggregates measurements across all of them. The per-slide normalization, anchored in the PSF model and negative-control calibration, accounts for these differences. The measurements become comparable not because the conditions are identical but because the optical model and statistical framework define what "comparable" means.

5.3.3. FROM FEASIBILITY TO DEPENDABILITY

Both the vectorial model in ZIMFLUX and the Gaussian model in the HTT pipeline share a lesson. An elegant model applied within its valid regime produces reliable measurements. A complex model applied beyond its boundaries produces numbers without meaning. Defining those boundaries is as important as building the model.

This thesis establishes feasibility. Molecular-unit RNA measurement in dense brain tissue is possible. Live-cell mRNA tracking through NPCs with controlled false positives is achievable. Depth-invariant single-molecule localization with self-calibrating structured illumination works. The next step is dependability. The transition requires defining the operating range: the conditions under which measurements remain stable across preparers, slides, and imaging sessions. Detection is no longer the limiting factor. Dependability is. This step converts research tools into transferable measurement platforms that enable cross-laboratory comparison and, eventually, clinical application.

5.3.4. BIOLOGICAL DISCOVERIES ENABLED BY THESE METHODS

The methodological contributions are not ends in themselves. They enable biological findings inaccessible without quantitative measurement.

The yeast imaging framework reveals that mRNA transport through the NPC is not a simple unidirectional process. Of 1,953 *GFA1* transport traces, fewer than half classify as a clean export; 817 remain undefined, meaning that within the precision of the measurement neither the direction of travel nor whether the mRNA crossed the nuclear envelope could be established. *MYO2* and *TRA1* show the same pattern. Import, although a minority, is a consistent fraction across all three transcripts, and different transcripts exhibit distinct docking site positions and transport dynamics. These observations challenge the textbook view of strictly unidirectional mRNA export [10], and are consistent with recent MINFLUX measurements showing overlapping import and export pathways within the NPC central channel [11]. None of these findings would be possible without the CNN-GLRT framework that keeps false positives under control at low signal-to-noise

ratios.
The Huntington's disease pipeline reveals spatial heterogeneity that bulk measurements cannot capture. In Q111 mice, 16–62% of fields of view show extreme mRNA clustering. The striatum is consistently more affected than the cortex [12]. Between animals, the fraction of extreme fields ranges from near zero to over 80%. These differences reflect genuine biology: somatic mosaic expansion of the CAG repeat, regional gene regulation, and cell-type-specific vulnerability [12]. The pipeline preserves this variation because the PSF-based calibration and per-slide normalization provide comparable molecular counts across all imaging positions.
The two biological chapters connect through a concrete mechanistic link. Mutant huntingtin protein disrupts nuclear pore complex integrity by sequestering nucleoporins, leading to impaired nucleocytoplasmic transport [13]. In our yeast data, 7 to 11% of transport traces are imports. Even modest changes in NPC function could therefore shift the balance between export and import. The cytoplasmic localization shift we observe in extreme FOVs of HD tissue may reflect exactly this kind of disruption. The yeast framework could be applied to models expressing expanded-repeat huntingtin constructs. This would directly test whether NPC disruption changes mRNA transport dynamics. Such an experiment would bridge these two chapters at the mechanistic level. One measures how mRNA moves through the pore. The other measures the downstream consequences when the pore is compromised.

5.4. IMPLICATIONS FOR SOCIETY

5.4.1. TOWARD UNDERSTANDING AND TREATING HUNTINGTON'S DISEASE

The most direct societal relevance lies in the Huntington's disease research. HD affects approximately 5.70 per 100,000 individuals in Europe, North America, and Australia [14]. No curative treatment exists. RNA-targeted therapies, including antisense oligonucleotides and small interfering RNAs, represent a promising strategy for reducing toxic mutant huntingtin transcript levels.
The quantitative framework of Chapter 4 provides tools for evaluating such therapies at tissue level with single-molecule resolution. Researchers can assess whether an intervention reduces not only overall mRNA levels but also pathological clustering. Existing silencing strategies appear effective against single cytoplasmic mRNAs but less so against clustered aggregates [15]. The choice of target sequence, closer to the 5' or 3' end, may determine therapeutic access to mRNA within clusters. These questions are now testable with the calibrated pipeline. The cluster-level metrics established here include mRNA count per cluster, spatial distribution, and subcellular localization. Together, they provide the readout needed to evaluate whether treatments reach the most relevant aggregates.

5.4.2. ADVANCING FUNDAMENTAL UNDERSTANDING

The insights into mRNA transport dynamics through nuclear pore complexes advance our understanding of gene expression regulation. Disruptions in mRNA export have been implicated in cancer and neurodegenerative disorders [16]. The bidirectional transport we observe suggests that NPC dysfunction could alter the balance between ex-

port and import. Mutant huntingtin protein sequesters nucleoporins [13], which may change mRNA availability for translation. The quantitative framework captures both successful and failed transport, providing data for kinetic models of mRNA trafficking.
The advances in single-molecule localization microscopy provide tools applicable to many biological questions requiring nanometer-scale 3D resolution: protein complex structure, chromatin organization, synapse architecture, and signaling molecule arrangement on cell membranes.

5.4.3. OPEN SCIENCE AND ACCESSIBILITY

The methods in this thesis use widely available hardware, commercial reagents, and computational approaches suitable for open-source implementation. ZIMFLUX requires a standard astigmatic lens combined with a digital micromirror device. The yeast framework uses standard widefield equipment. The RNAscope pipeline uses commercial reagents and automated confocal microscopes available in core facilities. This accessibility is important for standardizing methods across laboratories and clinical trials.

5.5. FUTURE PERSPECTIVES

Several directions emerge from this thesis.
The natural extension of ZIMFLUX is to increase the modulation frequency. Generating the excitation field with two opposing objectives produces interference pitches up to a factor of two smaller than achievable with a single objective, improving precision. This principle has been applied in isoFLUX, achieving spatially invariant isotropic resolution [17]. 4Pi-SIMFLUX takes this further by integrating structured illumination with 4Pi interferometric detection [18]. While 4Pi-SMLM already provides excellent axial precision, its lateral resolution remains the bottleneck. Adding structured illumination doubles the lateral precision, achieving near-isotropic 2–3 nm localization in three dimensions.
The question of where cargo passes through an individual NPC channel has been addressed by techniques such as MINFLUX, which achieve the nanometer-scale precision needed to resolve transport routes within the ~40 nm-wide, ~70 nm-deep central channel [19]. Sau et al. resolved distinct import and export paths of importin α using two-colour MINFLUX in permeabilized cells [11]. mRNA has not yet been tracked at this resolution. It is a substantially larger cargo than a single protein, so its path through the central channel may differ. Combining MINFLUX-type approaches with a dual-label strategy, placing fluorophores at both the 5' and 3' ends of the mRNA, could reveal whether the molecule threads through the NPC 5' end first [20] and how the two ends separate in time and space during transit. However, MINFLUX is limited to one or a few emitters at a time, making it difficult to collect the statistics needed to compare transport across many pores within the same cell. More fundamentally, any technique that improves precision by concentrating excitation light faces a phototoxicity ceiling in live cells. Carlton et al. showed that at a power density of ~480 W/cm^2, yeast cells already exhibit a serious decrease in doubling rate and viability [21]. The phototoxicity threshold depends on exposure time, wavelength, and labeling strategy, and differs between organisms, but it fundamentally limits what can be observed in living cells.
A widefield approach sacrifices the nanometer resolution within a single channel but

captures the entire nuclear envelope simultaneously, providing the throughput to ask a biologically distinct question: not where within a pore transport occurs, but *which* pores are active. Our current framework models the nuclear envelope as a continuous ring and assigns each mRNA detection to the nearest point on that ring, without resolving individual NPCs. A haploid yeast nucleus contains 65–182 NPCs depending on cell cycle stage, at an average density of ~12 NPCs/μm^2, with nearest-neighbor distances that can be as small as ~120 nm, below which very few NPCs are observed [22]. To reliably assign a transport event to an individual pore, the three-dimensional co-localization precision must be substantially smaller than this spacing. For a given three-dimensional co-localization precision σ_{3D}, the isotropic per-axis precision is $\sigma_{3D}/\sqrt{3}$. For nearest neighbors separated by 120 nm, a σ_{3D} of ~52 nm (per-axis ~30 nm) would give a misassignment probability of approximately 2%. Our current lateral co-localization precision of ~49 nm at 20 ms frame intervals is close to this regime in two dimensions, but no axial information is available, and the two-dimensional projection compresses NPCs at different depths onto the same image plane. NPC density varies across species and cell types, so the precision required to distinguish individual pores is organism-specific. Brighter labeling strategies, such as HaloTag-JaneliaFluor dyes, which are approximately 2–2.5 times brighter per molecule than EGFP [23], combined with an axial encoding scheme such as astigmatism, biplane detection [24], or structured illumination, could make single-pore assignment feasible.

Resolving individual pores would open qualitatively new questions. NPCs are not static: they diffuse laterally in the nuclear envelope, switching between immobile, slow, and fast diffusive states with diffusion coefficients ranging from 0.001 to 0.03 μm^2/s [25]. Nuclear basket proteins regulate this mobility; in their absence, NPCs spend more time in the fast diffusive state and redistribute across the envelope [25]. Moreover, nuclear baskets, the nucleoplasmic structures that recruit mRNA for export, assemble on only a subset of NPCs in a transcription-dependent manner [26]. Not all pores carry baskets at all times, implying that individual NPCs differ in their transport competence. If transport events could be mapped to single pores, the framework developed in Chapter 3 could directly test whether mRNA export is concentrated at basket-bearing NPCs or distributed across the nuclear envelope, whether the import events we observe preferentially involve basket-free pores, and whether NPC mobility itself correlates with transport activity.

For the Huntington's disease pipeline, the most pressing need is defining the operating range for routine quantitative use. This means establishing sampling stability for rare-event inference, minimal control density for reliable null estimation, and detection stability bounds under realistic perturbations. Application to larger cohorts and therapeutic studies would directly evaluate RNA-targeted treatments.

A key assumption in the intensity-to-count calibration is that RNAscope probes access mRNA uniformly within clusters. Berrevoets et al. used automated 3D STED microscopy to resolve the architecture of NEAT1_2 transcripts within paraspeckle nuclear bodies [27]. Different transcript regions occupy distinct radial positions within the condensate. If huntingtin mRNA clusters adopt similarly heterogeneous conformations, probe accessibility may vary with position. The strong volume-intensity linearity we observe ($R^2 > 0.98$) suggests that probe access is not yet a major limitation at the cluster sizes in our dataset. Larger or denser aggregates may not follow this trend. Super-resolution

methods that resolve individual molecules within clusters could refine this calibration by accounting for the physical arrangement of transcripts in dense aggregates.
This also raises questions for siRNA-based therapeutics. If mRNA within clusters is organized in a shell-like structure, drugs may reach the periphery while the interior remains protected [15]. The choice of target sequence, closer to the 5' or 3' end, may determine whether the siRNA can access its binding site. Imaging of HTT mRNA organization within clusters, combined with siRNA treatment, could test this directly.
Extension to other repeat expansion disorders, such as amyotrophic lateral sclerosis and myotonic dystrophy [28, 29], would test whether the measurement framework generalizes.
The bottleneck in quantitative microscopy has never been acquisition alone. Even as imaging hardware improves in resolution and throughput, the interpretation of the data determines whether images become measurements. Computational frameworks that model the physics of image formation, quantify uncertainty, and define the regime of validity of each measurement are as important as the microscopes themselves. The methods in this thesis embed statistical testing and optical modeling into the measurement pipeline rather than applying them post hoc. Quantitative microscopy depends as much on how we model and test our measurements as on how we acquire them.

BIBLIOGRAPHY

[1] Yiming Li et al. “Depth-dependent PSF calibration and aberration correction for 3D single-molecule localization”. In: *Biomedical Optics Express* 10.6 (2019), pp. 2708–2718.

[2] Marijn Siemons et al. “High precision wavefront control in point spread function engineering for single emitter localization”. In: *Optics Express* 26.7 (2018), pp. 8397–8416.

[3] S Stallinga and B Rieger. “Accuracy of the Gaussian point spread function model in 2D localization microscopy”. In: *Optics Express* 18 (2010), pp. 24461–24476.

[4] Steven M. Kay. *Fundamentals of Statistical Signal Processing*. Englewood Cliffs, N.J.: Prentice-Hall PTR, 1993.

[5] Carlas S Smith et al. “Probability-based particle detection that enables threshold-free and robust in vivo single-molecule tracking”. In: *Molecular Biology of the Cell* 26.22 (2015), pp. 4057–4062.

[6] Leonhard Möckl et al. “Accurate and rapid background estimation in single-molecule localization microscopy using the deep neural network BGnet”. In: *Proceedings of the National Academy of Sciences* 117.1 (2020), pp. 60–67.

[7] Pierre Jouchet et al. “Nanometric axial localization of single fluorescent molecules with modulated excitation”. In: *Nature Photonics* 15.4 (2021), pp. 297–304.

[8] Lusheng Gu et al. “Molecular-scale axial localization by repetitive optical selective exposure”. In: *Nature Methods* 18.4 (2021), pp. 369–373.

[9] Rasmus Ø. Thorsen et al. “Impact of optical aberrations on axial position determination by photometry”. In: *Nature Methods* 15.12 (2018), pp. 989–990. DOI: 10.1038/s41592-018-0227-4.

[10] Sami Hocine, Robert H Singer, and David Grünwald. “RNA processing and export”. In: *Cold Spring Harbor Perspectives in Biology* 2.12 (2010), a000752.

[11] Abhishek Sau et al. “Overlapping nuclear import and export paths unveiled by two-colour MINFLUX”. In: *Nature* 640.8059 (2025), pp. 821–827. DOI: 10.1038/s41586-025-08738-0.

[12] Robert E Handsaker et al. “Long somatic DNA-repeat expansion drives neurodegeneration in Huntington disease”. In: *bioRxiv* (2024), pp. 2024–05.

[13] J C Grima et al. “Mutant huntingtin disrupts the nuclear pore complex”. In: *Neuron* 94 (2017), 93–107.e6.

[14] Tamara Pringsheim et al. “The incidence and prevalence of Huntington’s disease: a systematic review and meta-analysis”. In: *Movement Disorders* 27.9 (2012), pp. 1083–1091.

[15] Sarah Allen et al. “mRNA nuclear clustering leads to a difference in mutant huntingtin mRNA and protein silencing by siRNAs in vivo”. In: *Nucleic Acid Therapeutics* 34.4 (2024), pp. 164–172.

[16] Jessica A Hurt and Pamela A Silver. “mRNA nuclear export and human disease”. In: *Disease Models & Mechanisms* 1.2-3 (2008), pp. 103–108.

[17] Lu Yin, Yile Sun, and Hongfei Zhu. “isoFLUX: three-dimensional modulation-enhanced localization microscopy with spatially invariant isotropic resolution”. In: *Chinese Optics Letters* 23.7 (2025), p. 071101.

[18] Qian Wang et al. “4Pi-SIMFLUX: 4Pi single-molecule localization microscopy with structured illumination”. In: *Nature Methods* (2025), pp. 1–8.

[19] Seung Joong Kim et al. “Integrative structure and functional anatomy of a nuclear pore complex”. In: *Nature* 555 (2018), pp. 475–482. DOI: 10.1038/nature26003.

[20] Asaf Ashkenazy-Titelman et al. “RNA export through the nuclear pore complex is directional”. In: *Nature Communications* 13.1 (2022), p. 5881.

[21] Peter M Carlton et al. “Fast live simultaneous multiwavelength four-dimensional optical microscopy”. In: *Proceedings of the National Academy of Sciences* 107.37 (2010), pp. 16016–16022.

[22] Mark Winey et al. “Nuclear pore complex number and distribution throughout the *Saccharomyces cerevisiae* cell cycle by three-dimensional reconstruction from electron micrographs of nuclear envelopes”. In: *Molecular Biology of the Cell* 8.11 (1997), pp. 2119–2132. DOI: 10.1091/mbc.8.11.2119.

[23] Jonathan B. Grimm et al. “A general method to improve fluorophores for live-cell and single-molecule microscopy”. In: *Nature Methods* 12.3 (2015), pp. 244–250. DOI: 10.1038/nmeth.3256.

[24] Sripad Ram et al. “High accuracy 3D quantum dot tracking with multifocal plane microscopy for the study of fast intracellular dynamics in live cells”. In: *Biophysical Journal* 95.12 (2008), pp. 6025–6043. DOI: 10.1529/biophysj.108.140392.

[25] Jonas Zsok et al. “Nuclear basket proteins regulate the distribution and mobility of nuclear pore complexes in budding yeast”. In: *Molecular Biology of the Cell* 35.11 (2024), ar143. DOI: 10.1091/mbc.E24-08-0371.

[26] Pierre Bensidoun et al. “Nuclear mRNA metabolism drives selective basket assembly on a subset of nuclear pore complexes in budding yeast”. In: *Molecular Cell* 82.20 (2022), pp. 3856–3871. DOI: 10.1016/j.molcel.2022.09.019.

[27] Enya S. Berrevoets et al. “Smart 3D super-resolution microscopy reveals the architecture of the RNA scaffold in a nuclear body”. In: *Nature Communications* 16.1 (2025), p. 10689. DOI: 10.1038/s41467-025-65723-x.

[28] Veronique V Belzil, Tania F Gendron, and Leonard Petrucelli. “RNA-mediated toxicity in neurodegenerative disease”. In: *Molecular and Cellular Neuroscience* 56 (2013), pp. 406–419.

[29] R Nalavade et al. “Mechanisms of RNA-induced toxicity in CAG repeat disorders”. In: *Cell Death & Disease* 4.8 (2013), e752–e752.

EPILOGUE

Looking back at the work in this thesis, a recurring theme emerges: the interplay between technological innovation and biological discovery. Each chapter began with a biological question that required a new approach. Each method that was developed in turn revealed unexpected biological insights.

The ZIMFLUX project started from a clear optical physics challenge: how to improve axial localization precision when imaging deep into samples. The solution required combining concepts from structured illumination and PSF engineering in a new way. Seeing the method validated on biological nanostructures was particularly satisfying. The theoretical improvements translated into practical gains.

The yeast mRNA imaging project taught a different lesson. Sometimes the most impactful contribution is not a dramatic new technique, but a careful framework that makes existing methods more accessible and robust. We traded some signal quality for biological relevance by avoiding cell wall digestion and working at low laser powers. The computational methods we developed to compensate for this trade-off became a central part of the work.

The Huntington's disease project was perhaps the most eye-opening. Analyzing over 900,000 single mRNA molecules and 1.9 million clusters revealed a level of heterogeneity that was hard to appreciate from smaller-scale studies. Certain brain regions show dramatically different mRNA clustering patterns. Answering the questions this raises will require much larger cohorts. The quantitative framework developed here provides the tools to do so.

ACKNOWLEDGEMENTS

A doctoral dissertation bears one name on the cover, but many people make it possible. First and foremost, I would like to thank my daily supervisor, David Grunwald. His scientific guidance shaped this thesis in many ways. Beyond research, he welcomed me when I immigrated to a different continent. Being able to stay with his family during my first months helped me build a life in Massachusetts.
I am equally grateful to my promotor, Bernd Rieger, for his honest and clear feedback. He kept me on track by setting clear boundaries and expectations. I also want to thank Carlas Smith, who supervised me during my master's thesis and first introduced me to David. When my US visa was delayed at the start of my PhD, Carlas allowed me to work in his lab so I could begin my research before traveling to David's group.
Once in the US, the members of the Grunwald lab made me feel at home. I thank them for their help, feedback, and many lab meetings. Back in Delft, the members of Bernd Rieger's lab were equally welcoming during my short stays.
Finally, I am grateful for the new friends I made in Massachusetts, who made my time in Worcester a good one.

Pieter

CURRICULUM VITÆ

Pieter Fop VAN VELDE

13 July 1996	Born in Groningen, the Netherlands.

EDUCATION

2014–2018	BSc Applied Physics Rijksuniversiteit Groningen
2018–2021	MSc Applied Physics Technische Universiteit Delft
2022–2026	PhD. Applied Physics Technische Universiteit Delft *Thesis:* Quantitative Fluorescence Microscopy for RNA Imaging: From Single Molecules to Tissue *Promotors:* Prof.dr. B. Rieger, Dr.ir. C.S. Smith and Dr. D. Grünwald

EXPERIENCE

2014–2018	Speed skater, iSkate Participated in the Dutch national championships single distances (1500 m), 2017
2018–2019	Fuel Cell Engineer Eco-Runner Team Delft
2019–2020	Teaching Assistant, Electronic Instrumentation Technische Universiteit Delft
2019—	Farmer, Hunsingo Dairy Kantens, Groningen
2021	Graduate Intern, later Consultant Corporate & Institutional Banking — Energy Europe ABN AMRO Bank N.V., Amsterdam
2022–2026	Graduate research, Grünwald laboratory UMass Chan Medical School, Worcester, USA
2025—	Co-founder, Farm Solutions AI Groningen

LIST OF PUBLICATIONS

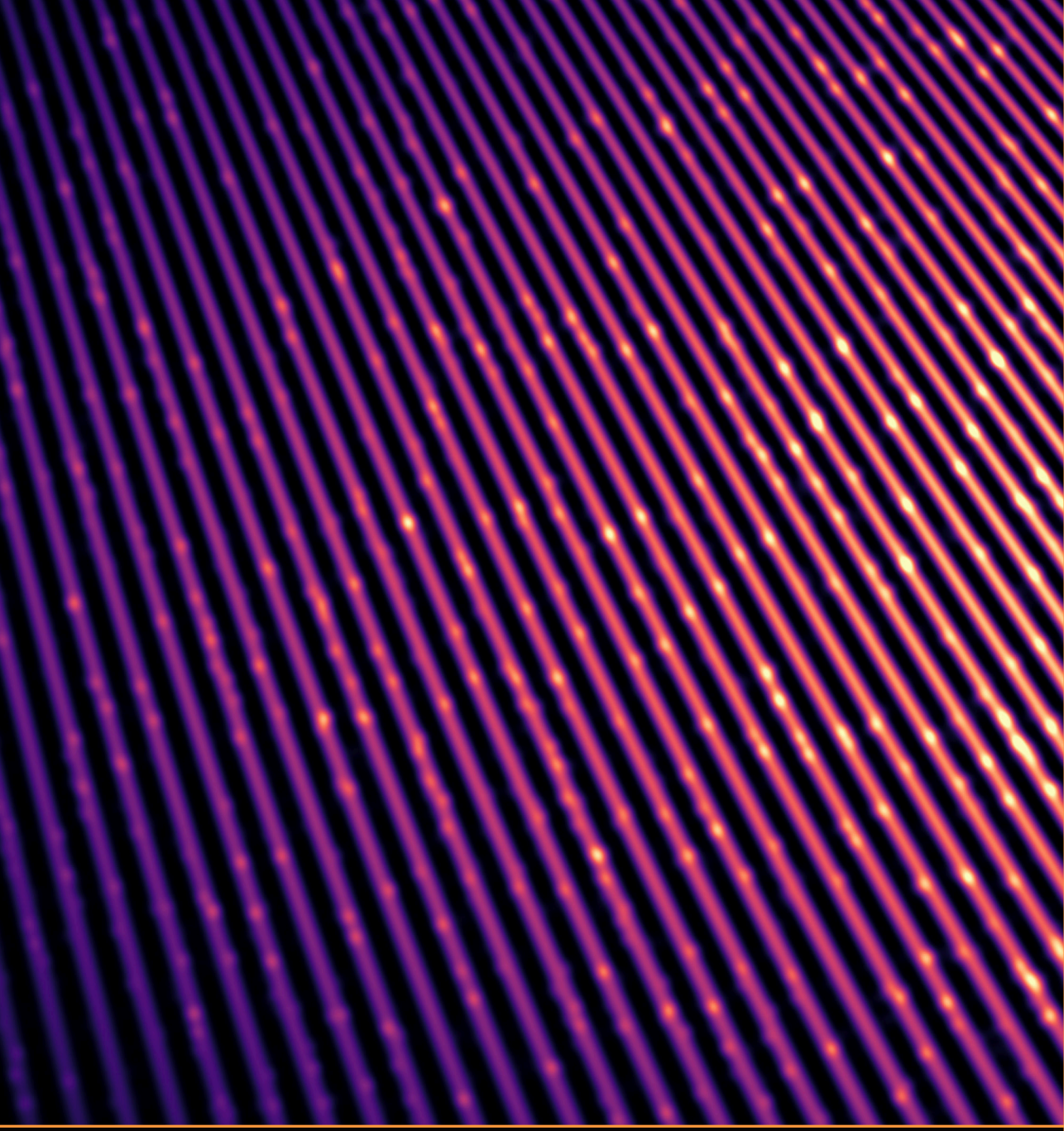
5. Y. Wang, **P. van Velde**, S.-T. Hung, M.O. Held, R. Huo, K. Grußmayer, D. Grunwald, N.H. Dekker, C.S. Smith, *TIRFscan: enhancing axial localization precision through multi-angle evanescent-field modulation*, Manuscript in preparation (2026).

4. **P. van Velde**, B. Tran, S. Allen, E. Luu, R. Furgal, A. Summers, J. Belgrad, E. Knox, A. Khvorova, D. Grunwald, *High-throughput quantification of huntingtin mRNA expression and aggregation in mouse brain using automated RNAscope imaging*, bioRxiv (2026).

3. **P. van Velde**, M. Hammer, A. Rossouw, B. Tran, A.E. Li, G. Latino, A. Lari, B. Rieger, B. Montpetit, D. Grunwald, *Live cell mRNA imaging in yeast: framework for studying mRNA transport through the nuclear pore complex*, Manuscript in preparation.

2. **P. van Velde**, B. Rieger, T. Hinsdale, J. Cnossen, D. Fan, S.-T. Hung, D. Grunwald, C. Smith, *ZIMFLUX: Single molecule localization microscopy with patterned illumination in 3D*, Optics Express **31**(25), 42701–42722 (2023).

1. J. Mitchell, C.S. Smith, J. Titlow, N. Otto, **P. van Velde**, M. Booth, I. Davis, S. Waddell, *Selective dendritic localization of mRNA in Drosophila mushroom body output neurons*, eLife **10**, e62770 (2021).



Fluorescence microscopy has become indispensable for studying biology at the molecular level, yet quantitative measurements of RNA expression and location demand continued innovation in optical methods and computational image analysis. This dissertation presents three contributions at different biological scales: ZIMFLUX, which combines astigmatic PSF engineering with structured illumination to improve axial precision in three-dimensional single-molecule localization; a live-cell framework for imaging mRNA transport through the nuclear pore complex in yeast; and a calibrated RNAscope pipeline that quantifies huntingtin mRNA clustering in mouse brain tissue.

ISBN 978-94-6518-401-2